

Dissertation zur Erlangung des Doktorgrades
der Fakultät für Chemie und Pharmazie
der Ludwig-Maximilians-Universität München

**Synthetic Investigations in
Borates, Borate Germanates, Gallium
Oxonitrides, and Intermetallic Phases
at Extreme Conditions**

Dipl.-Chem. Gunter Heymann

aus

Wolfratshausen

2007

Erklärung

Diese Dissertation wurde im Sinne von § 13 Abs. 3 bzw. 4 der Promotionsordnung vom 29. Januar 1998 von Herrn Priv.-Doz. Dr. H. Huppertz betreut.

Ehrenwörtliche Versicherung

Diese Dissertation wurde selbständig, ohne unerlaubte Hilfe erarbeitet.

München, den 24.06.2006



Gunter Heymann

Dissertation eingereicht am 25.06.2007

1. Gutachter: Priv.-Doz. Dr. H. Huppertz

2. Gutachter: Prof. Dr. R. Pöttgen

Mündliche Prüfung am 26.07.2007

To my parents

Acknowledgements

First of all, I would like to express my gratitude to PD Dr. H. Huppertz for giving me the opportunity to work in his group, for the freedom of research paired with continuous advertence and support, as well as for his stimulating enthusiasm. Thanks a lot for the fine and interesting COST meetings, where I was allowed to be present.

Special thanks go to Prof. Dr. W. Schnick for the excellent research conditions, the unhesitant acceptance in his group, and for support in all chemical questions.

I am indebted to Prof. Dr. R. Pöttgen for the final corrections of this thesis and for the excellent cooperation with his group. I would like to thank him for the fruitful discussions, ideas, and in particular for his encyclopaedic knowledge in the field of intermetallic phases. Thank you very much also for being co-referee of this thesis.

For the steady supply of intermetallic precursors, as well as for the close cooperation, starting with literature support till to the enormous staying power in tiny single crystal picking, I would like to thank Dipl.-Chem. J. F. Riecken. I wish you the best for your PhD thesis.

I am thankful to Prof. Dr. R. Pöttgen, Prof. Dr. J. Winterlin, Prof. Dr. D. Johrendt, and Prof. Dr. K. Karaghiosoff for their attendance as examiners in my *viva-voce*.

My colleagues Stefanie Jakob and Christian Schmolke, as well as my ex-colleagues Florian Stadler, Oliver Schön, and Christoph Krininger I would like to thank for the great years of study and that they always had an open ear for chemical and much more important, for private questions. The time passed by much too fast. Good luck for your future.

Special thanks go to my comrade of the laboratory D2.102 Johanna Knyrim for the calm and concentrated working atmosphere. But I will also thank her for the numerous funny moments, which created variety and let a day pass by very quickly.

My thank is due to the press team namely, Cordula Braun, Stefanie Hering, Dr. Friedrich Karau, Johanna Knyrim, and Florian Pucher for their collegiality and excellent team work. I also want to keep in mind and thank the famous technicians Stephan Landerer, Markus Kutschka, Harald Ober, and Helmut Ober of our workshop, as well as all HiWi's Sandra Christian, Yvonne Floredo, Jana Friedrichs,

Stephanie Neumair, Max Pitscheider, and Theresa Soltner for preparing the countless assembly parts.

For carrying out innumerable measurements, as well as for their postprocessing, I would like to thank Sandra Albrecht, Dr. Sascha Correll, Dr. Rolf-Dieter Hoffmann, Dr. Bettina Lotsch, Juliane Kechele, Thomas Miller, Christian Minke, Dr. Peter Mayer, Dr. Oliver Oeckler, Dr. Sudhindra Rayaprol, Dr. Ernst-Wilhelm Scheidt, and Wolfgang Wünschheim.

Special thanks go to my bachelor and research students Nina Behrmann, Cordula Braun, Sandra Christan, Almut Haberer, and Theresa Soltner for their excellent work. All of you were able to contribute a special part to this thesis. Good speed for your future.

For technical support, as well as with hardware or software problems and their quick elimination I would like to thank Wolfgang Wünschheim.

For financial support, I would like to thank the Deutsche Forschungsgemeinschaft (DFG, Bonn).

Last but not least, for a particularly convenient working atmosphere throughout the last years and for all sorts of technical, scientific, and personal support, I would like to thank my present and past colleagues Yamini Avadhut, Dr. Ulrich Baisch, Dr. Sabine Beyer, Daniel Bichler, Cordula Braun, Dr. Sascha Correll, Stefanie Hering, Dr. Holger Emme, Cora Hecht, Elsbeth Hermanns, Stefanie Jakob, Petra Jakubcová, Dr. Friedrich Karau, Juliane Kechele, Johanna Knyrim, Robert Kraut, Dr. Alexandra Lieb, Catrin Löhnert, Dr. Bettina Lotsch, Thomas Miller, Christian Minke, Helen Müller, Dr. Abanti Nag, Dr. Oliver Oeckler, Sandro Pagano, Dr. Regina Pocha, Florian Pucher, Dr. Stefan Rannabauer, Rebecca Römer, Andreas Sattler, Dr. Jörn Schmedt auf der Günne, Christian Schmolke, Stefan Sedlmaier, Jan Sehnert, Lena Seyfarth, Theresa Soltner, Dr. Florian Stadler, Dr. Johannes Weber, Wolfgang Wünschheim, and Martin Zeuner.

Above all, I am indebted to my parents and my brother, who continuously supported me and made a carefree study possible. Thank you very much for the encouragement of all of my ideas and plans.

*„Die Wissenschaft besteht nur aus Irrtümern. Allerdings diese
muß man begehen. Es sind die Schritte zur Wahrheit.“*

(Jules Verne)

Contents

1 Introduction	1
2 Experimental Methods	9
2.1 Precursor Preparation	9
2.2 Multianvil High-Pressure Equipment	10
2.2.1 Modified Walker-Module	10
2.2.2 The 1000 t Press	13
2.2.3 Preparation of Experiments	16
2.2.4 Pressure Calibration	23
2.2.5 Temperature Calibration	25
2.2.6 Recovering the Sample	26
2.2.7 Experimental Dangers	28
3 Analytical Methods	29
3.1 X-Ray Diffraction	29
3.1.1 X-Ray Diffraction and Crystal Structure Analysis	29
3.1.2 X-Ray Powder Diffraction	31
3.1.3 Temperature-programmed X-Ray Powder Diffraction	31
3.1.4 Single Crystal Diffraction	32
3.1.5 Computer Programs	32
3.2 Energy Dispersive Analyses of X-Rays	33
3.3 Elemental Analysis	34
3.4 Infrared Spectroscopy	34
3.5 Magnetic and Heat Capacity Measurements	35
3.6 Lattice Energy Calculation	36
3.7 Bond-Length Bond-Strength Calculation	36
3.8 Calculation of the Charge Distribution	37
3.9 Cycle-Class Spectra	37
4 Experimental Section	39
4.1 Rare-Earth Borates	39
4.1.1 Introduction	39
4.1.2 Starting Materials	45
4.1.3 The Borate α -Nd ₂ B ₄ O ₉	45
4.1.3.1 Synthesis	45
4.1.3.2 Crystal Structure Analysis	46

4.1.3.3	Crystal Structure Description.....	50
4.1.3.4	Theoretical Calculations.....	53
4.1.4	The <i>meta</i> -Borate β -Nd(BO ₂) ₃	54
4.1.4.1	Synthesis	54
4.1.4.2	Crystal Structure Analysis	54
4.1.4.3	Crystal Structure Description.....	57
4.1.5	The <i>meta</i> -Borates δ -RE(BO ₂) ₃ (RE = La, Ce)	60
4.1.5.1	Synthesis	60
4.1.5.2	Crystal Structure Analysis	61
4.1.5.3	Crystal Structure Description.....	65
4.1.5.4	IR Spectroscopy	69
4.1.5.5	Thermal Behaviour.....	70
4.1.5.6	Theoretical Calculations.....	71
4.1.6	The Oxoborate Pr ₄ B ₁₀ O ₂₁	73
4.1.6.1	Synthesis	73
4.1.6.2	Crystal Structure Analysis	73
4.1.6.3	Crystal Structure Description.....	78
4.1.6.4	IR Spectroscopy	80
4.1.6.5	Thermal Behaviour.....	82
4.1.7	Discussion.....	83
4.2	Rare-Earth Borate Germanates.....	87
4.2.1	Introduction	87
4.2.2	Starting Materials	90
4.2.3	The Rare-Earth Borate Germanate Ce ₆ (BO ₄) ₂ Ge ₉ O ₂₂	90
4.2.3.1	Synthesis	90
4.2.3.2	Crystal Structure Analysis	91
4.2.3.3	Crystal Structure Description.....	94
4.2.3.4	Thermal Behaviour.....	98
4.2.3.5	Theoretical Calculations.....	98
4.2.3.6	Conclusion	100
4.3	Gallium Oxonitrides.....	101
4.3.1	Introduction	101
4.3.2	The Spinel Type Structure of Ga _{2.81} O _{3.57} N _{0.43}	102
4.3.2.1	Synthesis	102
4.3.2.2	Analytical Methods	103
4.3.2.3	Results and Discussion	105

4.3.2.4	Conclusion	109
4.4	Ternary Intermetallic Phases Synthesized at HP/HT-Conditions.....	111
4.4.1	Introduction	111
4.4.2	Starting Materials	114
4.4.3	The Stannides $REPtSn$ ($RE = La-Nd, Sm$).....	114
4.4.3.1	Introduction	114
4.4.3.2	Syntheses	116
4.4.3.3	Crystal Structure Analysis.....	118
4.4.3.4	Crystal Structure Description.....	126
4.4.3.5	Thermal Behaviour.....	131
4.4.3.6	Magnetic Properties and Heat Capacity Measurements.....	133
4.4.3.7	Electronic Structure Calculation	143
4.4.4	The Stannides $REPdSn$ ($RE = La, Ce$)	145
4.4.4.1	Introduction	145
4.4.4.2	Syntheses	146
4.4.4.3	Crystal Structure Analysis.....	146
4.4.4.4	Crystal Structure Description.....	150
4.4.4.5	Thermal Behaviour.....	152
4.4.4.6	Magnetic Properties.....	153
4.4.5	The Stannides $RENiSn$ ($RE = La, Ce, Sm$).....	156
4.4.5.1	Introduction	156
4.4.5.2	Syntheses	156
4.4.5.3	Crystal Structure Analysis.....	157
4.4.6	The Stannide $ErAgSn$	160
4.4.6.1	Introduction	160
4.4.6.2	Synthesis.....	160
4.4.6.3	Crystal Structure Analysis.....	161
4.4.6.4	Crystal Structure Description.....	164
4.4.7	Discussion.....	166
4.4.8	The System $RE-Ag-Ge$	170
4.4.8.1	Introduction	170
4.4.8.2	Synthesis of $Ce_4Ag_3Ge_4O_{0.5}$	172
4.4.8.3	Crystal Structure Analysis of $Ce_4Ag_3Ge_4O_{0.5}$	173
4.4.8.4	Crystal Structure Description.....	177
4.4.8.5	Thermal Behaviour.....	179

4.4.8.6	Magnetic Properties.....	180
4.4.8.7	Electronic Structure Calculation	181
4.4.8.8	Synthesis of $Ce_3Ag_4Ge_4$	182
4.4.8.9	Crystal Structure Analysis.....	183
4.4.8.10	Crystal Structure Description.....	185
4.4.8.11	Discussion.....	187
4.4.9	The System <i>RE</i> -Au-Ge	190
4.4.9.1	Introduction	190
4.4.9.2	Synthesis of $Ce_7Au_{13.34(2)}Ge_{9.66(2)}$	191
4.4.9.3	Crystal Structure Analysis.....	192
4.4.9.4	Crystal Structure Description.....	194
4.4.9.5	Discussion.....	198
4.5	Further Cooperations	201
4.5.1	New preparation process for ^{57}Fe doped $LaCuO_3$ [373]	201
4.5.2	$SrRu_{1-x}Cr_xO_3$ perovskites: Solid solutions between two itinerant electron oxides [381].....	203
4.5.3	An organometallic <i>chimie douce</i> approach to new $Re_xW_{1-x}O_3$ phases [389]	206
5	Prospects	209
6	Summary	213
6.1	Multianvil High-Pressure / High-Temperature Synthesis	213
6.2	Rare-Earth Borates	213
6.3	Rare-Earth Borate Germanate	216
6.4	Gallium Oxonitrides.....	217
6.5	Ternary Rare-Earth Transition Metal Stannides	218
6.6	Ternary Rare-Earth Transition Metal Germanides.....	220
6.7	Further Cooperations	222
7	Appendix	225
7.1	List of Abbreviations.....	225
7.2	Publications.....	226
7.2.1	Conference contributions	226
7.2.2	Papers.....	226
7.3	CSD-Numbers.....	228
7.4	Curriculum Vitae	229
7.5	References.....	230

1 Introduction

Daily life of people on Earth takes place at pressure conditions of ~ 1013 mbar ($1.013 \cdot 10^{-4}$ GPa) at sea level. In general, we do not feel this pressure and we do not care much about the parameter pressure and its influence. But in fact our body is very sensible against pressure changes. We feel a force on the drumheads when leaving sea level up into higher regions or descent below sea level in deeper areas of the water. At a depth of 10 m the pressure has doubled and one and the same amount of gas suddenly fills half the volume as before, which means that the gaseous state is highly compressible. This reflects the general comprehension of people concerning the parameter pressure.

As solid-state chemists, we are interested in much higher pressures and its effect on materials. By the time, a typical solid or liquid has to be compressed to several hundred thousand atmospheres, before its molar volume is reduced by approximately 50%. Once the megabar range (1 Mbar = 1,000 kbar = 100 GPa \approx 1,000,000 atm.) is reached, average interatomic distances can be decreased by up to a factor of two [1]. Most of our chemical knowledge has been gained from studies carried out at or near one atmosphere pressure at the Earth's surface, while plenty of the matter in the universe exists under much higher pressure conditions, deep inside of the Earth, planets, and stars. For that reason, also geologist and astronomers are very interested in high-pressure technologies next to chemists and physicists.

Modern high-pressure experiments are enabled by various types of high-pressure devices, ranging from mechanical presses developed by *Bridgeman* and subsequent generations of high-pressure researchers, through the hand-held diamond anvil cells (DAC's), that allow experiments to be carried out in the laboratory into the multimegabar range ($P > 100$ GPa) combined with *in-situ* analytical methods, to specially designed windowed pressure cells for chemical and biological experiments in the low-pressure range [2]. Dynamic shock-wave experiments are currently the method of choice to reach the most extreme P - T conditions, which even allow sampling of deep planetary interiors including the gas giants and small stars, and also conditions experienced during thermonuclear explosions [2, 3]. More technical details concerning high-pressure facilities can be found in the cited references as well as in a special review about multianvil synthesis in solid-state chemis-

try [4]. In the following, the focus should be set on the effects of high-pressure and its possibilities in materials chemistry, which are described on the basis of selected examples. Fortunately, many solids synthesized at high-pressures can be quenched to ambient conditions, where they are thermodynamically metastable, yet remain indefinitely kinetically stable. *Demazeau et al.* [5] analyzed in a recent review two different approaches of materials chemistry under high-pressures. Hence, for a given composition with characteristic chemical bonds, high-pressures can induce structural transformations, and in contrast to that, high-pressures can also lead to the formation of new materials through the formation of new chemical bonds starting from different precursors, which do not react under ambient pressure conditions.

Structural transformations induced by high-pressures are characterized by a negative ΔV which means that the increase in pressure during the synthesis leads to a more dense structure than observed under normal-pressure conditions. As already mentioned, high-pressure causes a decrease of the average distances between atoms participating in the involved structures. This results in an increase of electrostatic repulsion between the most highly charged cations or anions and causes instabilities. In order to reduce these adverse effects, the structure is changed to another one involving higher coordination numbers of the atoms often associated with larger interatomic distances. Other reasons for a structural transformation under high-pressure conditions are different compressibilities of the involved chemical bonds. An example for such a behaviour in structural transformation is observed for the *RETSn* stannides ($RE = \text{La-Nd, Sm, T} = \text{Ni, Pd, Pt}$) described in detail later on in this thesis (Chapter 4.4).

When the target chemical bonds do not already exist in the precursors, then high-pressure allows the synthesis of new materials. In general, high-pressure syntheses are influenced from two sets of parameters, which are of thermodynamical nature or of the reactivity of the precursors. Thermodynamic effects associated with the specificities of the pressure parameter can be related to “Le Chatelier’s rule” reducing the formation of gas or liquid phases under pressure conditions. The densification effect, leading to a negative ΔV value, can be seen also as a specific case of “Le Chatelier’s rule”.

The synthesis of the new first nitridic clathrate $[\text{P}_4\text{N}_4(\text{NH})_4](\text{NH}_3)$ using a high-pressure / high-temperature reaction at 600 °C and 11 GPa in a Walker-type multianvil assembly by *Karau et al.* [6] was only possible in taking advantage of “Le Chatelier’s rule”. The thermolysis of ammonium azide NH_4N_3 under high-pressure and high-temperature was used to provide the high partial pressures of both N_2 and NH_3 , which were concurrently necessary for an ammonolysis reaction and thermal

stabilization of P_3N_5 . Under normal-pressure conditions NH_4N_3 decomposes into NH_3 and HN_3 at 133 °C and P_3N_5 dissociates into the elements at temperatures higher than 850 °C. Under the extreme synthetic conditions of $P_4N_4(NH)_4(NH_3)$, NH_3 apparently is incorporated into the growing $PN(NH)$ framework structure and therefore acts as a template molecule. Figure 2.1-1 displays the crystal structure of the new nitridic clathrate.

High N_2 partial pressures, generated *in-situ* by thermolysis of azides, were frequently used in the synthesis of metal containing nitridophosphates, starting from the respective metal azide and P_3N_5 .

Another important phosphorus nitride compound synthesized through the densification effect, which is in most cases accompanied by an increase of the coordination number, was the synthesis of the high-pressure phase γP_3N_5 at 11 GPa and 1800 K [7]. γP_3N_5 crystallizes in a three-dimensional network structure built up from corner sharing PN_4 tetrahedra and trans-edge-sharing distorted PN_5 square pyramids (see Figure 2.1-2). These tetragonal PN_5 pyramids represent a novel structural feature, previously not known in solid-state compounds. Additionally, *Kroll* and *Schnick* proposed that γP_3N_5 transforms into a δP_3N_5 with *kyanite* type structure at pressures exceeding 43 GPa [8].

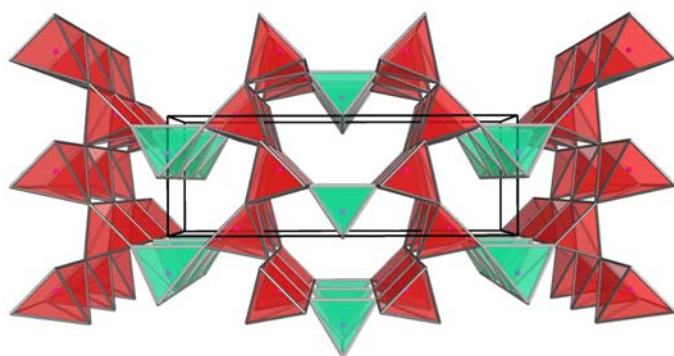


Figure 2.1-2: Crystal structure of γP_3N_5 , view along [010].

importance of βSi_3N_4 as a ceramic material, the new cubic modification (see Figure 2.1-3) attracted widespread interest [11]. Predictions that γSi_3N_4 must be signifi-

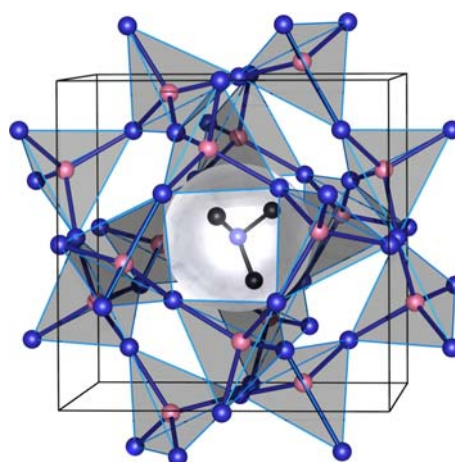


Figure 2.1-1: Crystal structure of cubic $[P_4N_4(NH)_4](NH_3)$, view approximately along [001]; blue spheres: N, pink spheres: P, dark gray spheres: H [6].

In connection with the synthesis of γP_3N_5 , another important nitride and its transformation into a cubic modification under high-pressures has to be mentioned. The normal-pressure α and βSi_3N_4 modifications contain exclusively SiN_4 units, while the high-pressure γSi_3N_4 structure (*spinel* type) exhibits Si in two different types of coordination, *i.e.* SiN_4 and SiN_6 units [9, 10]. Due to the im-

cantly harder than the two known polymorphs α - and β - Si_3N_4 and even harder than the hardest known oxide (*stishovite*) came true. Large-volume syntheses and shock-wave experiments with high γ - Si_3N_4 yields of 80% confirmed the prediction as third hardest material after diamond and cubic boron nitride. Diamond anvil cell studies indicate that at 34 GPa a further Si_3N_4 modification forms: δ - Si_3N_4 [12].

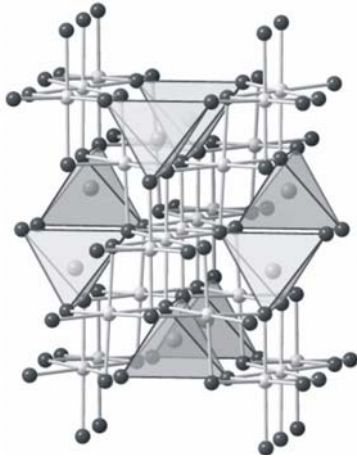


Figure 2.1-3: Crystal structure of the high-pressure modification γ - Si_3N_4 (black spheres: N; light spheres: Si).

At this point, it is a good occasion to summarize the efforts of high-pressure / high-temperature chemistry in the important field of superhard materials synthesis. Since the first successful synthesis of diamond by the Swedish ASEA-team, the dream of a harder material than diamond has been born. One important example is the intense interest in the high-pressure synthesis of the covalent cubic compound C_3N_4 , theoretically predicted by *Cohen* and co-workers. A hardness comparable with or exceeding that of diamond is assumed for that compound [13]. Nevertheless, the recent research for new superhard materials indicates that the search for materials harder than diamond is futile [14]. Instead, other materials with

similar hardness but better technical properties are in the focus of the present research. The system B-C-N is such a promising candidate. *Solozhenko et al.* reported about a phase with the composition BC_2N , which was discovered in a diamond anvil cell exhibiting a diamond like structure. A large volume synthesis at 18 GPa and 2200 K in a multianvil system at the Bayerisches Geoinstitut in Bayreuth, Germany [15], delivered enough substance for hardness measurements, which showed that BC_2N exhibits a value of hardness between diamond and cubic boron nitride. Accordingly, it is possible that this substance could be the second hardest material after diamond, but up till now it exists a controversial discussion if it is a new compound or only a mixture of c-BN besides diamond.

The icosahedral boride class of superhard materials with structures related to α -rhombohedral boron was intensively investigated by *McMillan et al.* Syntheses of B_6O_{1-x} at pressures between 1 and 10 GPa using a Walker-type multianvil apparatus and a B_2O_3 -enriched environment yielded in a material close to the nominal composition (up to $\text{B}_6\text{O}_{0.96}$) [16-19]. The large class of superhard metal carbides, which have already found broad technical application, should be leaved out in the context of this short summary.

After this brief excursion, we will focus back on the synthesis of novel materials through the densification effect. One large field of research in our group deals with

the high-pressure study of the systems RE_2O_3 - B_2O_3 . It was possible to prepare new compositions of rare-earth borates depending on the size of the rare-earth metal. Common ground of all high-pressure compounds is a negative ΔV value if one compares the $\Sigma V/Z$ of the precursors to the V/Z of the high-pressure phases. A more detailed introduction into the various rare-earth borates synthesized at extreme conditions is given in Chapter 4.1 of this thesis.

Often a decrease in volume, caused by applying high-pressure, is accompanied by a rise of the coordination number as already mentioned. On the other way round, high-pressures can be used to stabilize high coordination numbers. During the last forty years, when high-pressures were used in materials chemistry, the synthesis of new perovskites ABO_3 was an important domain [20, 21]. Coordination numbers of 12 or CN 8 + 4, as a common distortion for the larger cation A, and CN 6 for the smaller cation B were not realizable for smaller cations under ambient pressure. For example, the high-pressure synthesis of $SeMO_3$ perovskites with $M^{2+} = Mn, Co, Ni, Cu,$ and Zn helps to minimize the electronic anisotropy induced by the lone pair of Se and favours the stabilization of a strongly distorted perovskite structure with an abnormally high tilting effect of the MO_6 octahedra. In fact, Se^{4+} as a $4s^2$ cation is too small to occupy the A site in the perovskite structure. But Se^{4+} is very close to 3 oxygen atoms (instead of 12) and therefore a pyramidal selenite group SeO_3^{2-} can be defined. Thus, the octahedra are highly tilted, with strongly bent M-O-M angles, and the residual space is filled through the Se^{4+} lone pair [22]. For the preparation of solid solutions of two perovskites, from which one is only attainable using the parameter pressure, pressure is also needed to obtain the mixed perovskites (see Chapter 4.5.2 of this thesis).

A further advantage of high-pressures is the possibility to synthesize materials through the compressibility of atoms. The compressibility of an atom is modified by its electronic configuration and is thus determined by its position in the Periodic Table. New materials can be stabilized regarding the modification of the ionic radii r_A / r_B ratio of the corresponding atoms. In the $RE_2M_2O_7$ pyrochlore structure, the limit of stability is defined by $r_A / r_B \sim 1.55$. Nevertheless, it is possible, due to the difference in compressibility between RE^{3+} and Ge^{4+} , to prepare the $RE_2Ge_2O_7$ series with the pyrochlore structure under high-pressure conditions although the r_A / r_B ration being close to 1.8 under normal conditions [23].

If the pressure is high enough the reactivity of a given element can be modified through a change of the electronic configuration of its orbitals. For example, potassium shows an electronic configuration under normal-pressure conditions of s^1d^0 , but under pressures exceeding the 10 GPa region the configuration changes and the d orbitals are stabilized. Consequently, the electronic configuration becomes s^0d^1

and potassium acquires chemical properties comparable to a transition metal. This phenomenon can explain the formation of intermetallic compounds of the composition K_xAg_y under very high-pressures generated by using diamond anvil cells [24, 25].

The wide field of high-pressure chemistry also includes reactive pressures to stabilize the highest oxidation states of transition metals. These pressures comprise on one side high gaseous pressures in the several hundred MPa range and on the other side *in-situ* generated gaseous pressures through thermal decomposition of for example Na_2O_2 or $KClO_3$. Many unusual formal oxidation states were stabilized in oxides (for example: Fe^{4+} , Fe^{5+} , Co^{3+} , Co^{4+} , Ni^{3+} , Cu^{3+} , Ir^{5+} , and Ir^{6+}) by this technique.

If we focus finally on the kinetics of chemical reactions, one can say that high-pressures obviously have a strong influence onto this parameter. The following example clearly reveals the effect of the kinetics on materials preparation. The synthesis of $LaFeO_3$, starting from the educts La_2O_3 and Fe_2O_3 , requires at normal-pressure and 1000 °C about 70 h. Using a pressure close to 5 GPa and the same temperature, only 10 min are necessary to obtain a pure perovskite phase [26]. These effects are not well understood, whereas the general belief would expect a decrease of kinetics with increasing pressure, which is in fact observed for many cases. This introduction presented several effects caused by the parameter pressure, but which one turns the balance, depends extremely on the chemical system. It has been shown that high-pressure in combination with high-temperature is a powerful tool to create new materials. For generating the required pressures and temperatures, the Walker-type multianvil technique is the best compromise, covering a wide range of pressures in combination with a sufficient amount of sample. This technique was used within this thesis to investigate various chemical systems, often performed in cooperation with other European groups. A multiplicity of interesting new compounds were discovered, which are presented in the following.

The first part of this thesis deals with the primary field of research of our working group and investigates the synthesis of oxoborates with the large rare-earth cations ($RE = La-Nd$) in a pressure range between 3.5 and 5.5 GPa. In the following Chapter, introductory experiments into the field of rare-earth germanates are presented, which resulted in a new borate germanate compound. Chapter 4.3 treats the substance class of gallium oxonitrides at high-pressure conditions and was executed in the context of an application for a research grant within the new DFG priority program SPP1236. Chapter 4.4 contains the main experimental part of this thesis and deals with high-pressure / high-temperature investigations of selected ternary intermetallic phases and their broad chemical and physical characterization. The

last Chapter gives a short survey about other projects performed in European cooperations during the experimental part of this PhD thesis. Altogether, this thesis delivers a wide insight in the successful application of the parameter pressure in the synthesis of new materials.

2 Experimental Methods

2.1 Precursor Preparation

The precursor preparation of the intermetallic phases took place in cooperation with the group of Prof. Dr. R. Pöttgen, Institut für Anorganische und Analytische Chemie, Universität Münster and was performed by Dipl.-Chem. J. F. Riecken during his PhD work.

All precursors employed in this work were synthesized by arc-melting [27]. The advantages of this technique are short reaction times and high temperatures (~3000–4000 K). Therefore the metals are placed in a conical water-cooled copper crucible. A non-consumable cerium dioxide doped tungsten electrode is used in combination with a welding generator, equipped with a high frequency supply (Handy-TIG 210-DC, Lorch, Auenwald-Mittelbrüden). Figure 2.1-1 shows the arc-melting chamber with the copper crucible and the tungsten electrode. The melting procedure is carried out under an argon atmosphere of about 800 mbar, which was purified over molecular sieves, silica gel, and titanium sponge (900 K). Starting materials for the syntheses are ingots, wires, granules, or powders of the corresponding metals. In a first step the ingots are cut into smaller pieces and arc-melted to small buttons, powders are cold-pressed to pellets (\varnothing 6 mm) and in the following the ideal atomic ratio is arc-melted. Air sensitive metals are handled under paraffin oil and subsequently washed with *n*-hexane. The paraffin oil and *n*-hexane were dried over sodium wire. In order to ensure homogeneity, the samples are turned over and remelted three times. The weight loss after the various melting procedures is generally smaller than 0.5%.



Figure 2.1-1: Arc-melting furnace

2.2 Multianvil High-Pressure Equipment

The high-pressure / high-temperature experiments presented in this thesis were performed in a 1000 t press (Voggenreiter, Mainleus, Germany) and a modified Walker-Module [28]. Figure 2.2-1 gives a look at the press with the hydraulic control-unit on the right side and the temperature control-unit on the left side. In the following sections a detailed description of the high-pressure facility (Chapter 2.2.1), the preparation of experiments (Chapter 2.2.3), and calibration methods (Chapter 2.2.4; 2.2.5) is given.



Figure 2.2-1: 1000 t press with heating- (left side) and control-unit (right side).

2.2.1 Modified Walker-Module

To fulfil the requirements like a realization of high-pressures and high-temperatures in combination with large sample volumes at reasonable costs, the best compromise can be found in a multianvil module as it has been developed by *Walker et al.* in 1990 [28]. On the basis of these plans and the experiences of *Frost*

et al. [29], the original Walker-Module was scaled up to a maximum load of 1000 t and fabricated in cooperation with the company Voggenreiter (Mainleus, Germany).

Figure 2.2-2 shows the schematic construction of the module. The six tool steel wedges (C_{1-6}) including the cubes (D) plus the pressure medium (red octahedron) are positioned in the containment ring (B). The latter is surrounded with a safety ring (A). The loading of the module is accomplished through pressure-distribution plates (E). For security reasons, the stability range of the containment ring (HSM, 1.2343, $R_c = 52$, 17.8 cm (inner diameter), 33.8 cm (outer diameter), total height 19.4 cm) and the surrounding safety ring (Höver, 1.4541, 33.8 cm (inner diameter), 37.8 cm (outer diameter) total height 19.4 cm) are dimensioned with a factor of 2.5, which means that the module holds a load of 2500 t without any failure [30].

The wedges are made from tool steel (HSM, 1.3343) hardened to $R_c = 62$ and exhibit a square face side with the dimensions of 6.00 cm \times 6.00 cm (for 32 mm tungsten carbide cubes), with an angle of $35^\circ 26'$ to the axis of the module. The lowest corner of the square face has a distance of 2.00 cm from the basis. Figure 2.2-3 gives a view of one of the 98 mm high wedges with the square face in front and wiring channels on both sides. Three assembled wedges with a small gap of approximately 1 mm in between fit perfectly into the 17.8 cm diameter cylindrical cavity of the containment ring. Figure 2.2-4 shows a photograph of the massive containment ring surrounded by the safety ring incorporating three wedges with wiring ports.

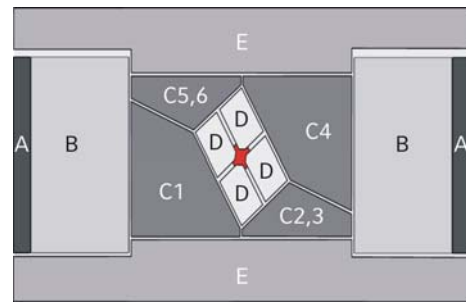


Figure 2.2-2: Cross section of the walker module [30].



Figure 2.2-3: Single tool steel wedge with wiring channels.

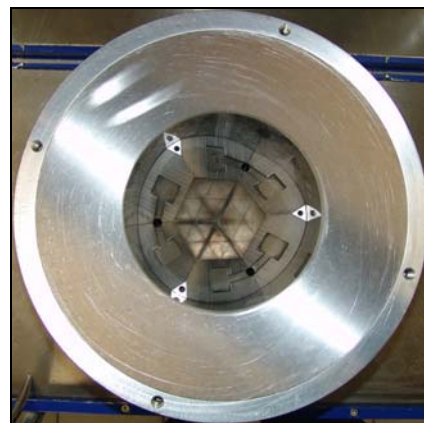


Figure 2.2-4: Containment ring with three wedges inside.

On top and bottom the containment ring is sealed with two pressure-distribution plates (37.8 cm in diameter, 3.9 cm thick) made from an Al alloy (Alimex, AMP 8000). The raised part of the plate, which directly lies on the wedges, is made of tool steel (Höver, 1.4548.4). For cooling a spiral cooling was milled into the top and the bottom pressure-distribution plates and sealed by the tool steel plates (Figure 2.2-5). Additionally, the pressure-distribution plates (Figure 2.2-6) and wedges show several tunnels and shafts to bring wiring between the wedges, which is necessary for pressure and temperature calibration.

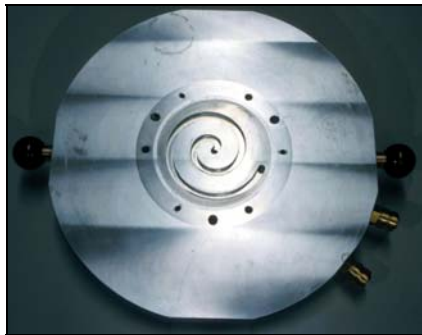


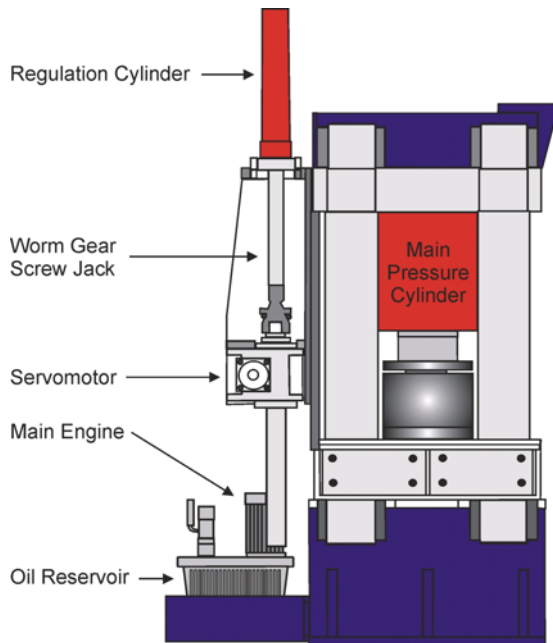
Figure 2.2-5: Spiral cooling inside the pressure distribution plate [30].



Figure 2.2-6: Top and bottom pressure distribution plate [30].

2.2.2 The 1000 t Press

The 1000 t press was constructed from the company Voggenreiter (Mainleus, Germany). Figure 2.2-7 gives a schematic side view of the press and the hydraulic system. It can be divided into three parts:



- The main pressure cylinder (CCR-10002, Enerpac, Columbus, WI, USA).
- An additional regulation cylinder with a worm gear screw jack driven by a servomotor.
- The main engine with the oil reservoir.

Figures 2.2-9 to 2.2-12 show photographs of these compounds. Under the top covering above the top plate the main valve for the main pressure cylinder and the lock valves for the regulation cylinder are mounted (Figure 2.2-10). Figure 2.2-8 gives a diagram of the oil circuit divided in the three mentioned parts by a red line.

Figure 2.2-7: Side view of the 1000 t press and the hydraulic unit [30].

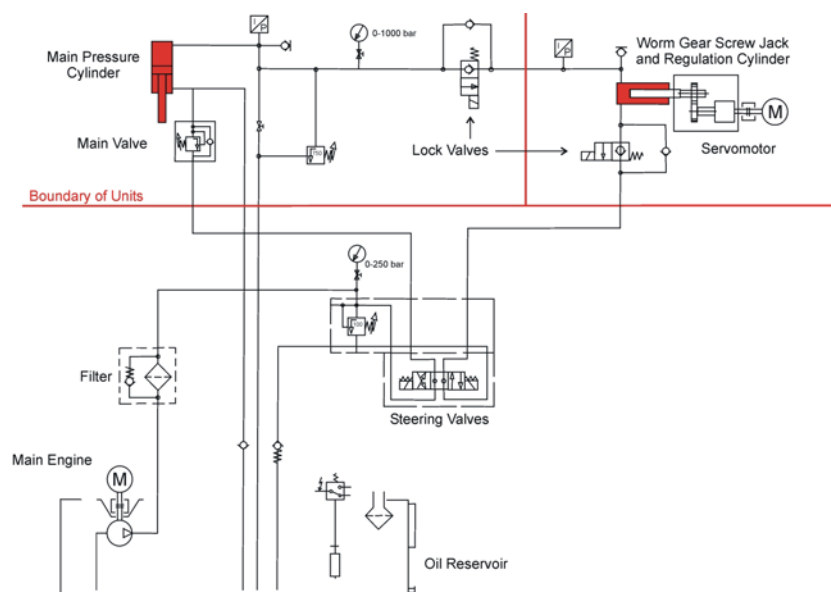


Figure 2.2-8: Oil circuit diagram of the 1000 t press [30].



Figure 2.2-9: Main hydraulic unit and oil reservoir



Figure 2.2-10: Hydraulic valves and oil pipes on the top plate of the 1000 t-press [30].



Figure 2.2-11: Worm gear screw jack



Figure 2.2-12: Servomotor for slow pressure changes.

After moving the Walker-type module beneath the main pressure cylinder, the gap of 1 cm between ram and top pressure distribution plate is closed in 20 seconds, using the main engine with high velocity. To avoid a hard put down, induction switches (Figure 2.2-13) stop the driving of the ram just before the distance piece touches the pressure distribution plate. The following more precise regulation of the oil pressure in the main cylinder is ensured by the servomotor, through moving the worm gear screw jack into the outer regulation cylinder. Up to an oil pressure of 10 bar, which corresponds to a load of 14.3 t, the compression of the module takes place in a relatively fast time of approximately 20 min, closing all gaps between the wedges, cubes, and the octahedral cavity. Further compression is predetermined by the ramp given for the experiment. Typically, the compression rate has a maximum value of 100 t per hour, whereas the decompression time requires the three-



Figure 2.2-13: Induction switches

fold time.

It is possible to control the main engine, servomotor, and the valves *via* a SPS (Simatic S7-300) equipped with a serial RS232C interface. The essential information concerning the experimental profile is transferred from a second control unit (Windows PC). Therefore the program PRESSCONTROL [31] was employed, which is able to transfer the pressure and temperature ramps to the SPS, read out the current system pressure, and control all actions of the SPS. Figure 2.2-14 shows the graphical surface of the program. Experimental parameters, which typically have to be entered, are type and size of the octahedron, type of furnace, and the way of heating. For heating, the program distinguishes between temperature-controlled heating *via* a thermocouple and predetermined power/temperature curves for the corresponding assembly without thermocouple. In the next step, the pressure/temperature ramp has to be entered including the intended times for each step. The maximum load of 1000 t corresponds to 700 bar oil pressure, which is used as input parameter for the intended load. After entering the experimental details, the pressure ramp as well as the temperature ramp is shown as yellow lines in two diagrams. During the course of an experiment the actual oil pressure and temperature given by the thermocouple are continuously read out and displayed on the screen. In the case of a rapid loss of pressure (blow-out), security functions were programmed to ensure the stopping of the experiment. Also routines for recording calibration curves were integrated in the program PRESSCONTROL [31].

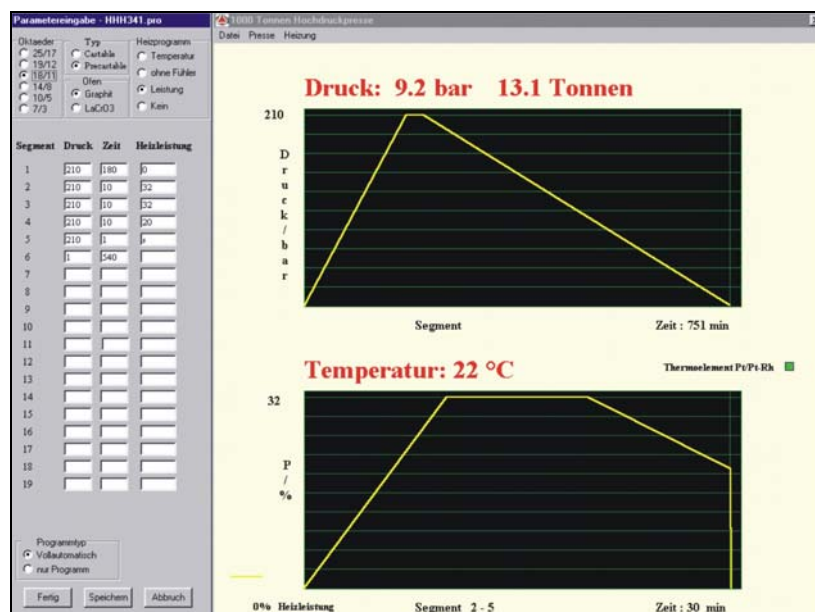


Figure 2.2-14: Graphical surface of the program PRESSCONTROL [31].

2.2.3 Preparation of Experiments

As already described in Chapter 2.2.1, the multianvil Walker-Module is based on the six wedges compressing a cubic arrangement of eight inner anvils. These inner anvils are made from sintered tungsten carbide (edge length: 32 mm) and exhibit truncated corners forming a triangular face. Thus, by arranging eight cubes with truncated corners, an octahedral cavity is formed, wherein the pressure cell (octahedron) is located. There exist several different assemblies, which are clearly defined by their octahedral edge length (OEL) and truncation edge length (TEL) of the corresponding tungsten carbide cube. For instance, an 18/11 assembly describes an octahedron with an edge length of 18 mm surrounded by eight tungsten carbide cubes exhibiting truncated triangular faces with an edge length of 11 mm. The choice of the appropriate assembly depends on the required sample pressure. A detailed description of the different assemblies and reachable pressure ranges is given later in this Chapter. First, the assembling of the octahedron and its fitting inside of the tungsten carbide cube arrangement is described.

The pressure medium is a prefabricated and sintered magnesium oxide octahedron (Ceramic Substrates & Components Ltd., Newport, Isle of Wight) doped with 5 % magnesium chromite. In the next step, a hole has to be drilled between opposite faces of the octahedron for sample loading. Figure 2.2-15 displays a general survey about all the different parts of the octahedral assembly. The sample is located directly in the centre of the octahedron inside of a hexagonal boron nitride (HeBoSint® S100, Henze, Kempten, Germany) crucible (g) and closed with a h-BN plate (h). The choice fell on hexagonal boron nitride as a crucible material because of its chemical inertness under high-pressure / high-temperature conditions. For heating we used cylindrical graphite (RW403, SGL Carbon, Bonn, Germany) resistance heaters (e, f) surrounding the h-BN capsule. An arrangement of two distinct and telescoped furnaces with a stepped wall thickness ensured a low thermal gradient along the sample [32]. To centre the sample capsule inside of the furnaces, two MgO-rods (Magnorite MN399CX, Saint-Gobain Industrial Ceramics, Worcester, MA, USA) were positioned on the bottom and top side (c). For thermal insulation of the furnace against the MgO octahedron, an additional zirconia sleeve (Ceramic Substrates & Components LTD., Newport, Isle of Wight) surrounds the inner part (d). The furnace is contacted *via* two molybdenum plates (b) (Mo007905, Goodfellow, Bad Nauheim, Germany) at the bottom and at the top, fitting directly into the MgO-rings (a). Figure 2.2-16 shows a cross section of the octahedral pressure cell. All the mentioned capsules and plates for the pressure cell are made by ourselves on a lathe (Opti D480, Collrep GmbH, Maintal, Germany).

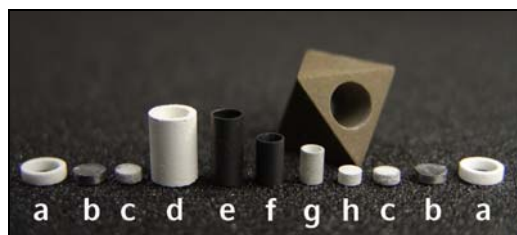


Figure 2.2-15: General survey about the assembly parts.

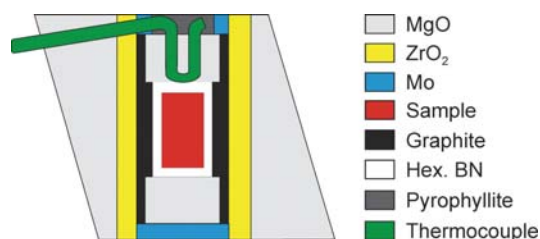


Figure 2.2-16: Cross section of the octahedral pressure cell [30].

After the insertion of the inner assembly parts inside of the octahedron, the eight tungsten carbide cubes are arranged around it as seen schematically in Figure 2.2-18. The triangular faces of the truncated cubes fit on the faces of the octahedron, whereby the cubes are kept on distance through pyrophyllite gaskets between them (Ceramic Substrates & Components Ltd., Newport, Isle of Wight). Figure 2.2-19 shows a photograph of an octahedron already surrounded by five cubes. To achieve a complete sealing of the octahedral cavity inside of the eight tungsten carbide cubes, pyrophyllite gaskets are arranged around the truncated edges as illustrated in Figure 2.2-17. The first cube is equipped with three short pyrophyllite gaskets, the second cube exhibits two short gaskets and a long one, the third two long and one short, and the fourth three long bars. To fix the gaskets on the tungsten carbide cubes small dots of UHU instant adhesive (UHU GmbH & Co. KG, Bühl) are used as adhesive. At elevated temperatures the glue acts like a lubricant and too much glue can lead to blowouts. Therefore a careful dosage is definitely important.

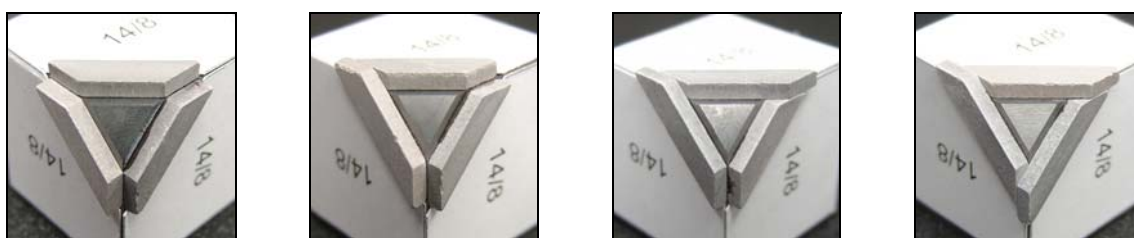


Figure 2.2-17: Different arrangements of the pyrophyllite gaskets around the truncated corners.

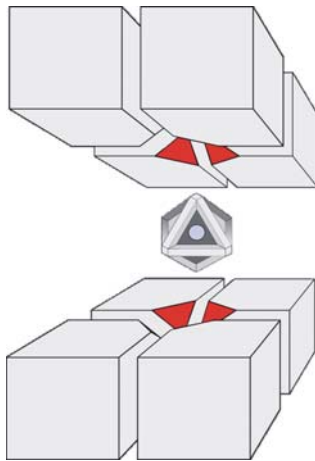


Figure 2.2-18: Truncated cubes to compress the central octahedron [30].



Figure 2.2-19: Octahedron already surrounded from five tungsten carbide cubes.

As seen from Figure 2.2-19, half of the cubes are laminated with cardboards (Bristolkarton, 369 g/m^3) at three faces, while the other half is provided with PTFE-tape (SKAP 130, Beichler & Grünenwald GmbH, Löchgau, Germany). The cubes are alternately arranged, so each cube, pasted with cardboards, is neighbored to a cube with PTFE-tape and vice versa. The main function of the covering is to slow down and stabilize the extruding of the crushed gaskets.

The quality, technical specifications, and suitability of the tungsten carbide used for the inner anvils, produced by different manufactures, are highly variable [33]. Currently, the best qualities are Toshiba "F" grade (Langenfeld, Germany), Kennametal "THM-U", "THM-F" (Mistelgau, Germany), and Ceratizit "TSM10" (Reutte, Austria). Cubes applied in this work were Kennametal "THM-U", "THM-F" and Ceratizit "TSM10".



Figure 2.2-20: Completely assembled cube

For stabilization the cubes are stuck to pads of fiber glass (Type 2372.4, Menzel & Seyfried, Gröbenzell, Germany) with a thickness of 0.8 mm (Figure 2.2-20). The top and the bottom pad show an incision with a threaded copper stripe (about $1.5 \text{ cm} \times 3.0 \text{ cm}$, thickness: 0.1 mm) to ensure a current flow from the wedges via the pads onto the two opposite cubes, whose truncated faces lie directly on the molybdenum plates. Figure 2.2-21 demonstrates schematically the procedure of positioning the assembled cubes into the Walker-type module.

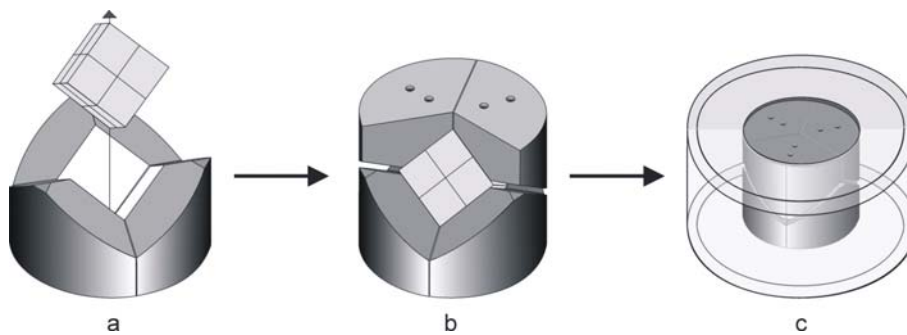


Figure 2.2-21: Graphical illustration of the assemblage of the Walker-Module [30].

The left picture illustrates the cubic arrangement placed along its threefold axis in a nest of three wedges. Afterwards, the top wedges, as seen at the picture in the middle, take their positions on top of the cube, leaving a gap between top and bottom wedges. To stabilize the complete setup, it is located in the containment ring (right-picture), which is not shown at the previous pictures for reasons of clarity. Figure 2.2-22 gives a view inside of the containment ring. Between the wedges and the containment ring, there is a gap of 0.125 mm filled with two sheets of PET-foil (BO-PET IA, D-K Kunststoff-Folien GmbH, Dessau, Germany). One large sheet (thickness: 0.75 mm) covers the complete inner containment ring and juts out 1.5 cm above the containment ring. Other individual plastic sheets (thickness: 0.50 mm) covers the outside of each wedge. Both plastic foils are fixed with polytetrafluoroethylen (PTFE) spray, which furthermore acts as a lubricant.

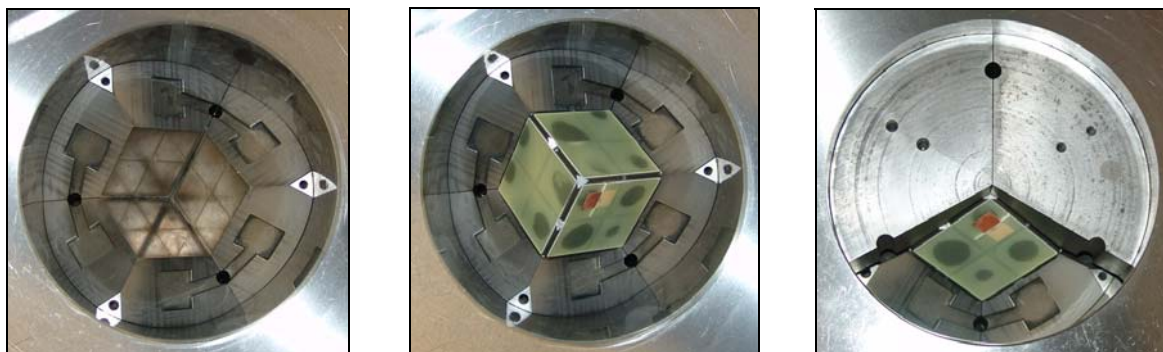


Figure 2.2-22: Stepwise mounting of the cube inside the nest of the three tool steel wedges and subsequent closing with the upper wedges.

The plastic sheets fulfill several functions: The lubrication solvent between the containment ring, wedges, and plastic foil ensures the mobility of the anvils and their optimal alignment. The plastic sheets provide electrical insulation of the containment ring from the wedges. Furthermore, the sheets absorb stress concentrations and compensate surface flaws as well as roughness of the wedges and the

containment ring, respectively. When putting on the top pressure distribution plate to finish the assembling of the Walker-Module, one has to act very carefully, so that the sticking out plastic sheet is not damaged.



Figure 2.2-23: Loaded Walker-Module with fixed water cooling.

In the last step, the Walker-type module is moved from the preparation table directly under the hydraulic ram of the 1000 t press. Figure 2.2-23 shows the press with the complete module under the ram. On the left side of the pressure distribution plates the adapters for the water cooling are visible. The wherewithal electric connection for heating occurs *via* a small metal extension (right side of the bottom pressure distribution plate), which moves directly into a small shoe connecting the plate with one pole of the electrical circuit. The second pole is fixed on the backside of the distance piece (aluminium) between the ram and the top pressure distribution plate.

Assembly variations

Different chemical systems require various materials for crucibles or furnaces. Also the parameter pressure affects the choice of the assembly. Depending on the achievable pressure range there exists an optimal assembly. Table 2.2-1 gives an overview about the different assembly sizes, their maximum pressures and sample amount. All other parts required for sample loading are depending on the choice of the assembly size. Figure 2.2-24, Figure 2.2-25, and Figure 2.2-26 show the dimensions of the pieces for the inner octahedral part of an 18/11, 14/8, and an 10/5 assembly, which were used for the syntheses in this work by default.

Up to pressures of 10 GPa and temperatures of 1500 °C, graphite can be used successfully as the heater material. Above these limits, the material starts to convert to diamond and its performance collapses. As an alternative, LaCrO₃ (Cherry-O, Amagasaki-City, Japan) can be used as a heater material to generate temperatures up to 3000 K.

Some chemical systems may necessitate a change in capsule materials. Other possible capsule materials are copper, molybdenum, platinum, or gold. In this work mainly h-BN and some times molybdenum capsules were used.

Table 2.2-1: Overview about the different assemblies; *OEL: Octahedral Edge Length, TEL: Truncation Edge Length

25/17	18/11	14/8	10/5
25 mm OEL*	18 mm OEL	14 mm OEL	10 mm OEL
			
			
17 mm TEL*	11 mm TEL	8 mm TEL	5 mm TEL
Max. pressure: 4.0 GPa	Max. pressure: 10.0 GPa	Max. pressure: 13.0 GPa	Max. pressure: 16.0 GPa
crucible volume: ~ 80 mm ³	crucible volume: ~ 35 mm ³	crucible volume: ~ 9 mm ³	crucible volume: ~ 4 mm ³
sample amount: ~ 60 – 100 mg	sample amount: ~ 30 – 50 mg	sample amount: ~ 20 – 30 mg	sample amount: ~ 10 – 15 mg

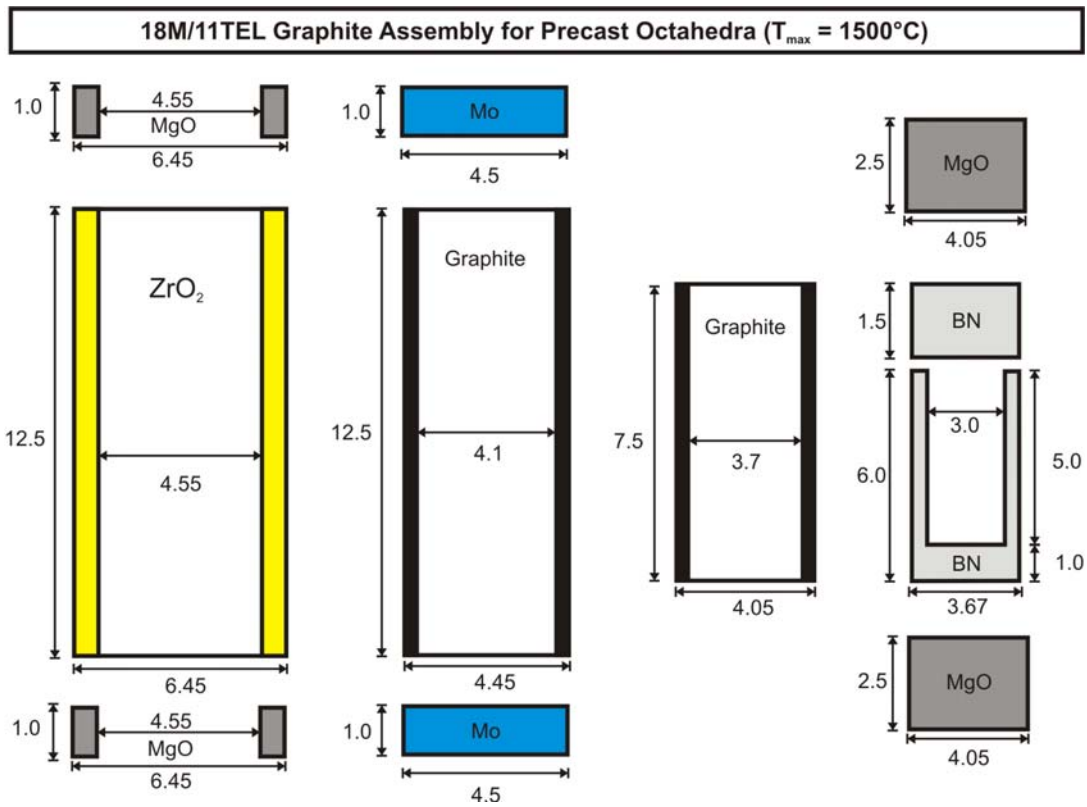


Figure 2.2-24: Dimensions /mm of the pieces for the inner octahedral part of an 18/11 assembly using precast octahedra with pyrophyllite gaskets.

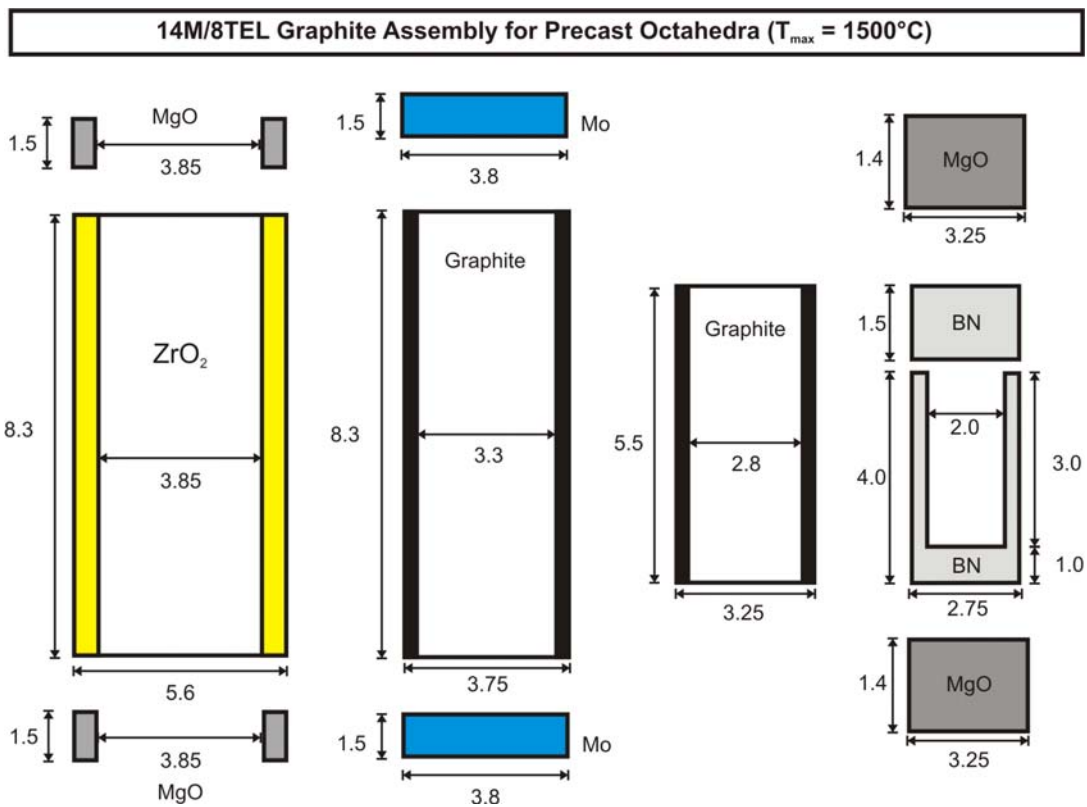


Figure 2.2-25: Dimensions /mm of the pieces for the inner octahedral part of an 14/8 assembly using precast octahedra with pyrophyllite gaskets.

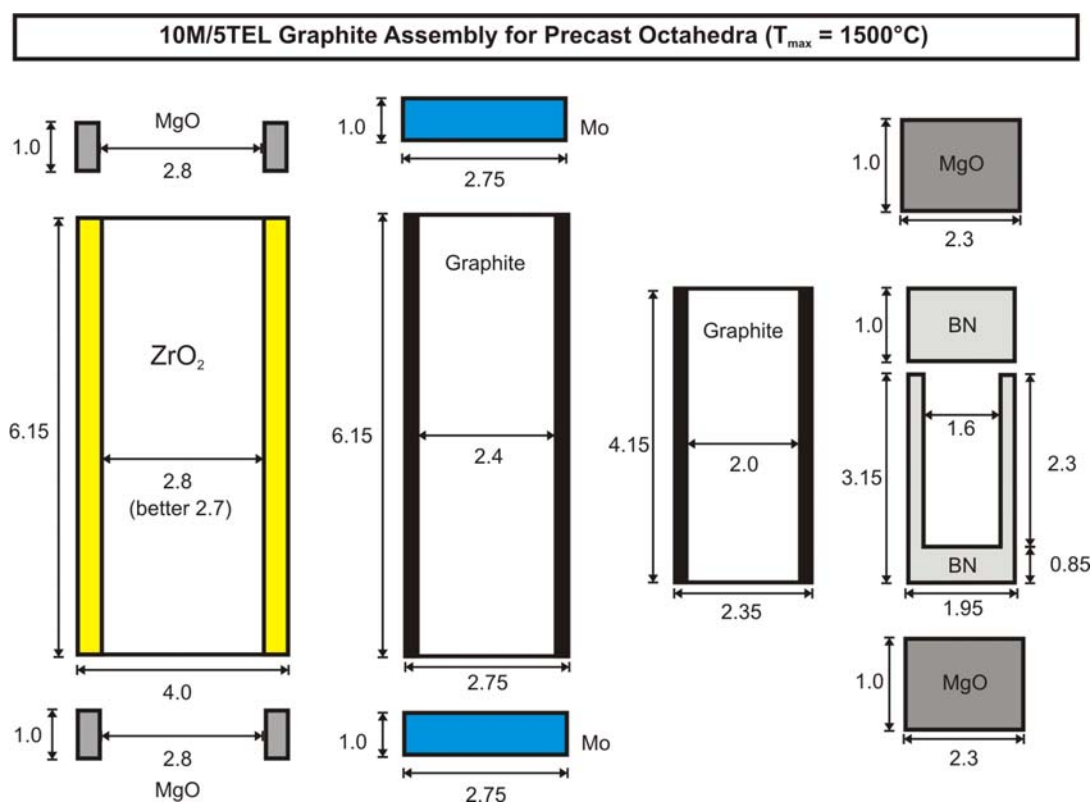


Figure 2.2-26: Dimensions /mm of the pieces for the inner octahedral part of an 10/5 assembly using precast octahedra with pyrophyllite gaskets.

2.2.4 Pressure Calibration

Using a multianvil setup, the calculation of the effective pressure inside the sample, depending on the applied force, is nearly impossible. Fixed points are known from diamond anvil cell investigations, where actual pressures can easily be calculated or determined *via* the ruby luminescence. These calibrations are the basis for estimating the created pressure, because the necessary gasketing and side-support arrangements always absorb a sizable fraction of the force applied to the sample. The pressures, generated in multianvil devices are calibrated as a function of hydraulic oil pressure. Commonly used transitions for calibrating the assemblies up to a pressure of 13 GPa are the I-II, II-III, and III-V transitions in Bi (at 2.55, 3.15, and 7.70 GPa, respectively) representing one of the most studied elements at high-pressure [34-45] and semi-conductor to metal transitions in ZnTe (6 GPa - anomaly - LPP - HPP1 at 9.6 GPa, and HPP1 - HPP2 at 12.1 GPa) [46-50].

For recording the bismuth resistance plot, a hole was drilled between opposite faces of the octahedron and filled with a 3.8 mm long and 1.7 mm in diameter cylinder of Bi metal. The remaining drill hole from both sides of the octahedron was furthermore filled with copper electrodes, each provided with two cable connections from copper wire, to allow electrical communication between the bismuth and the

resistance measuring circuit outside the press. Figure 2.2-27 gives a schematic view of the octahedron including the Bi calibration setup.

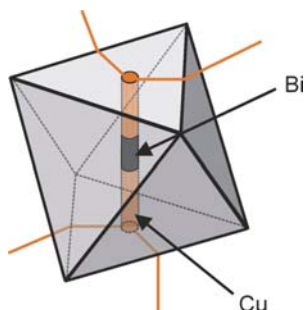


Figure 2.2-27: Bi calibration setup [30]

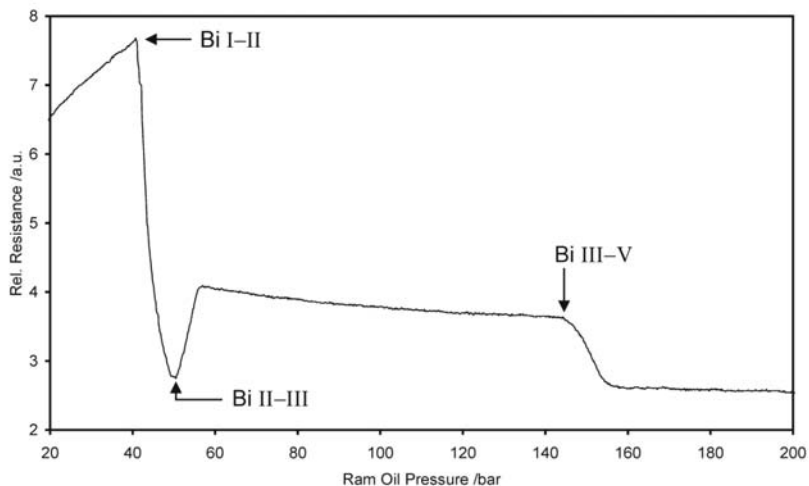


Figure 2.2-28: Relative resistance of Bi in dependence of the ram oil pressure in a 14/8 chrome magnesia octahedron [30].

This setup permits a current free detection of the resistance in dependence upon the ram oil pressure. Figure 2.2-28 shows a typical chart for the relative resistance of Bi in a 14/8 precast octahedron. The diagram clearly exhibits three sharp resistance changes due to the phase transformations I-II, II-III, and III-V. Concerning the structures, rhombohedral Bi-I (isotypic to As) transforms into Bi-II with a monoclinic structure, followed by Bi-III being composed of a tetragonal host structure and an interpenetrating guest component, which is incommensurate with the host [45]. Further increase in pressure results in a phase transformation to the body-centred cubic phase Bi-V above 7.7 GPa.

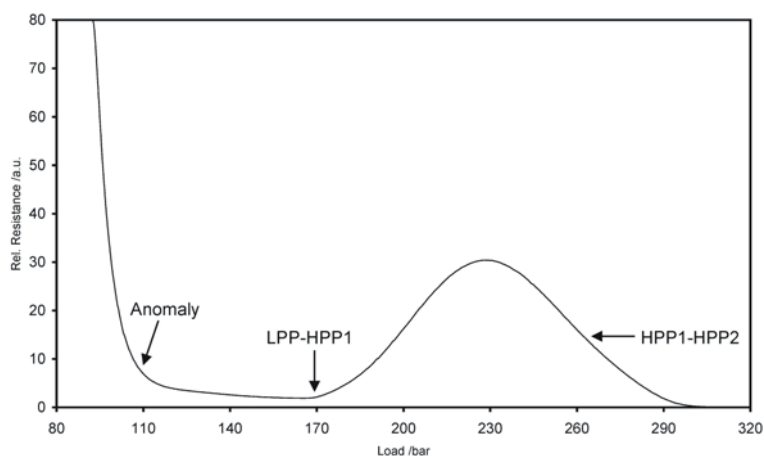


Figure 2.2-29: Relative resistance of ZnTe in dependence on the ram oil pressure in a 14/8 chrome magnesia octahedron [30].

For calibrations with ZnTe (99.998 %, Alfa Aesar), powdered samples with a thickness of 1.9 mm and 1.6 mm in diameter, contacted analogously to the Bi calibration, were used. As the resistance of ZnTe (semiconductor) is much larger than the resistance of tungsten carbide, the cubes were

part of the circuit. The three anomalies shown at the pressure resistance plot in Figure 2.2-29 can be attributed *(i)* to a change of the band gap in the zinc blende type ZnTe (around 6 GPa), *(ii)* followed from a transformation to a semiconducting *cinnabar* type phase (~9.5 GPa) [48, 49], *(iii)* and ends up with a transition to a metallic orthorhombic (*Cmcm*) phase at about 12.0 GPa [50], which can be regarded as a distorted rock salt structure.

Furthermore, possible calibration systems are the metals cerium (0.77 GPa [51-53]), barium (5.5 GPa [54-56]), and thallium (3.65 GPa [57]). Figure 2.2-30 represents the pressure calibration curves for these 18/11, 14/8, and 10/5 assemblies but now in dependence of the applied load.

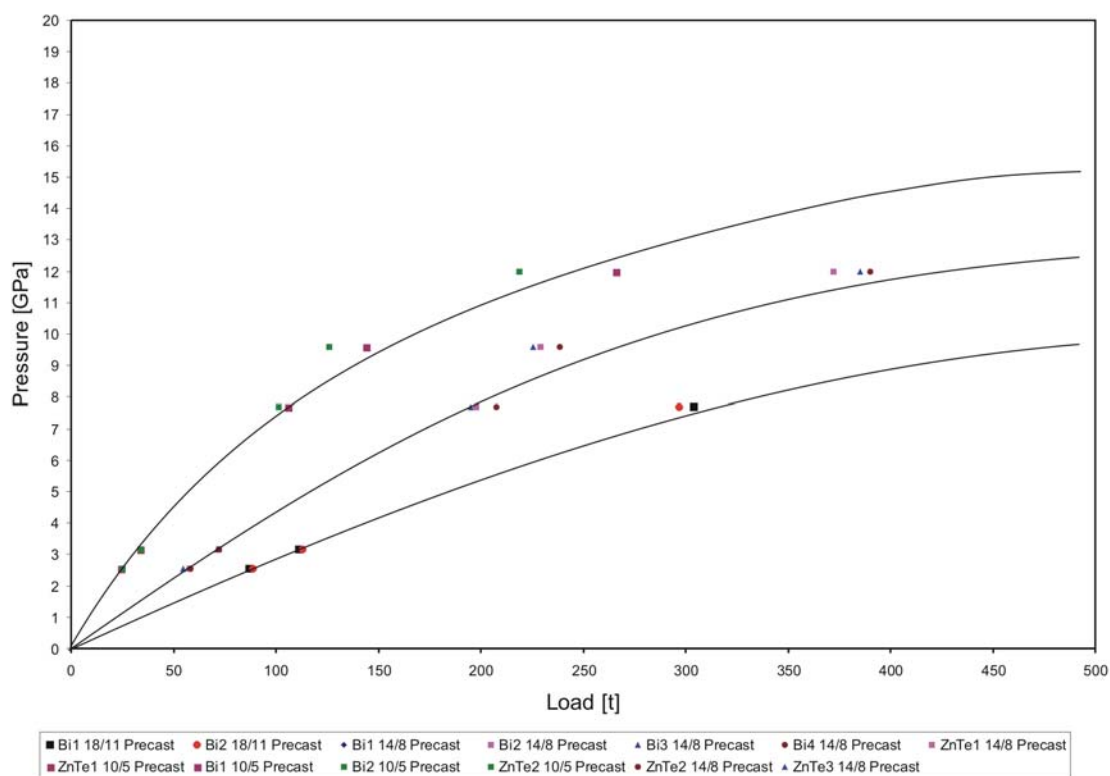


Figure 2.2-30: Pressure calibration curves for the 18/11, 14/8, and the 10/5 assembly.

2.2.5 Temperature Calibration

Besides an exact pressure calibration, an appropriate temperature calibration is just as important. The temperature is measured using a thermocouple (Figure 2.2-31), which can be inserted perpendicular to the heater or along the axis as shown in Figure 2.2-32. This thermocouple is directly connected to an Eurotherm 2404 temperature controller (Limburg a. d. Lahn, Germany). As thermocouple types, Pt-Pt₈₇Rh₁₃ was used for temperatures up to 1500 °C, and W₃Re₉₇-W₂₅Re₇₅ above

1500 °C (SPPL-010, SP13RH-010, W3W25-010, Newport Omega, Deckenpfronn, Germany). For the installation of a thermocouple the assembly setup has to be changed. At one side the MgO and Mo plates are replaced by corresponding rings, to create a way out for the wiring. Measuring the temperature along the heater axis enables the use of a thermocouple in combination with a sample. But the temperature of the axially inserted thermocouple, fixed on top of the sample, offers a source of uncertainty resulting from the thermal gradient, that exists primarily along the sample length.



Figure 2.2-31: Axial thermocouple with copper coils, alumina sleeves and Mo ring [30].

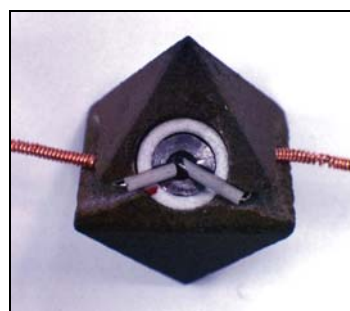


Figure 2.2-32: Axial thermocouple mounted in an octahedron [30].

Other uncertainties arise from the pressure effect on the thermocouple electromotive force (emf) [58]. Experimental difficulties prevented the clear measurement of this effect. Recorded temperatures are therefore affected by several effects. Curves of the measured temperatures in dependence of the heating power for every assembly and different loads were recorded. So it is possible to perform experiments without fitting a thermocouple into the assembly every time.

2.2.6 Recovering the Sample

After decompression, the Walker-type module has to be moved out from the hydraulic ram to the preparation table. In the following the top pressure distribution plate is lifted, the three top wedges are removed, and the eight inner cubic anvils with the octahedron inside are carefully raised out of the nest. Figure 2.2-33 shows the cube after an experiment. To clearly demonstrate the function of cardboards, PTFE-tape, and pyrophyllite gaskets, two cubes are carefully removed revealing the octahedron in the centre. The recovered experimental octahedron was broken apart, and the sample carefully separated from the surrounding hexagonal boron nitride and furnace material. The following pictures give a view of two different chemical

systems. Figure 2.2-34 shows a borate compound and Figure 2.2-35 an intermetallic phase inside the BN capsule. Both samples exhibit no reaction with the crucible material.

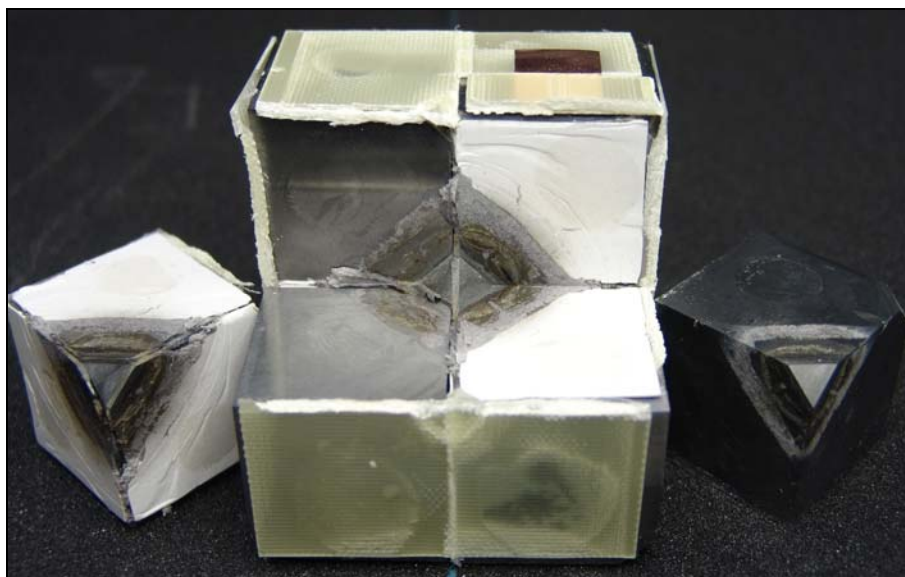


Figure 2.2-33: Cube after the high-pressure / high-temperature experiment.

On the other side, boron nitride can react with the sample depending on the chemical system and reaction temperature. Especially at temperatures above 1200 °C hexagonal boron nitride starts to react with several materials.



Figure 2.2-34: BN capsule with a borate compound [30].



Figure 2.2-35: Intermetallic phase in a BN capsule [30].



Figure 2.2-36: Separation of an intermetallic phase from a BN capsule [30].

2.2.7 Experimental Dangers

Due to the robustness of the two Walker-type modules, which have been constructed up to a maximal load of 2500 t, no reason for experimental dangers with regard to ruptures is given. Nevertheless, during the heating phase of an experiment, it is required to wear ear protectors owing to the risk of a blow-out. A blow-out can be caused by the failure of one of the gaskets (Figure 2.2-37) and manifests in an explosive loss of pressure.

A second danger arises from the eight truncated cubic anvils. In the course of an experiment at high-temperatures and high-pressures, the tungsten carbide cubes start to sinter, which leads to tensions inside the cubes. Under normal pressure conditions these tensions can result in an explosive destruction of the cube (Figure 2.2-39) or less violent in cracked cubes (Figure 2.2-38). Therefore, it is necessary to wear goggles while working with used cubes, and to keep the cubes under a protective shield, if not in use.



Figure 2.2-37: Octahedron after a blow-out [30].



Figure 2.2-38: WC cube with crack [30].

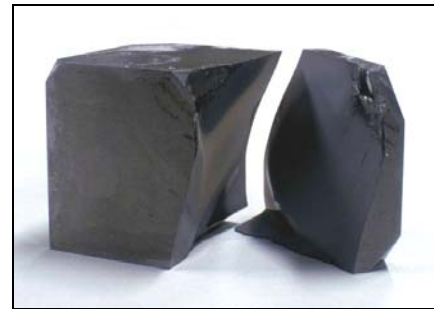


Figure 2.2-39: Broken WC cube [30].

3 Analytical Methods

3.1 X-Ray Diffraction

3.1.1 X-Ray Diffraction and Crystal Structure Analysis

Because of the particular importance to this work a brief introduction in X-ray diffraction and single crystal structure analysis is given in the following. For a more detailed disquisition on this subject, the reader is referred to standard works in the literature [59, 60].

Preconditions for the observation of diffraction phenomena are lattices in dimensions of X-ray radiation. The therefore preferred radiations are $\text{CuK}_{\alpha 1}$ with $\lambda = 154.18$ pm and $\text{MoK}_{\alpha 1}$ with $\lambda = 71.073$ pm. In this range, also the distances of lattice planes belonging to the same family of organic and inorganic crystals are located. The periodically arranged atoms or ions in a crystal consequently built up a three dimensional diffraction grating for the X-ray photons. To achieve constructive interference, the retardation between two waves must be an integer multiple of the wavelength. This connection is given in the *Bragg* equation (1) the central equation of diffraction phenomena.

$$n\lambda = 2d_{hkl}\sin\theta_{hkl} \quad (1)$$

It correlates the interplanar spacing d_{hkl} of lattice planes belonging to the same family with the diffraction angle θ_{hkl} . Figure 3.1-1 shows a graphical illustration of the *Bragg* equation.

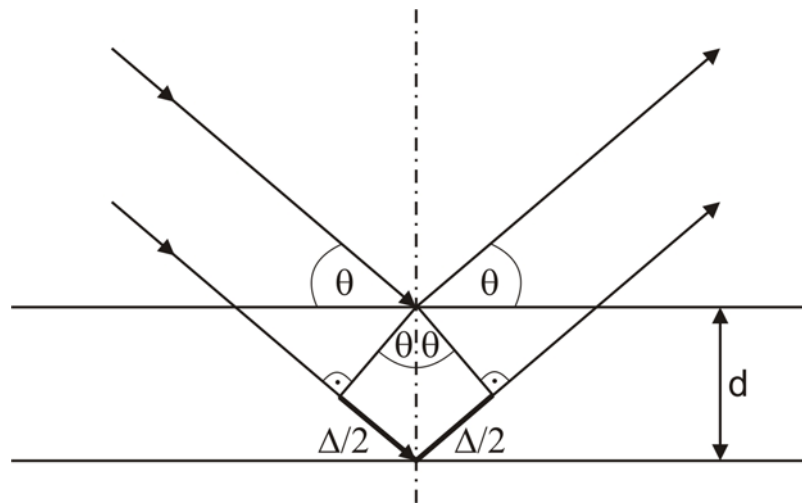


Figure 3.1-1: Reflection of X-rays from two lattice planes belonging to the same family. d is the interplanar spacing.

For X-rays, the scattered total intensities I_{hkl} are proportional to the square of the structure amplitude, taking into account several correction terms during data reduction (equation (2)).

$$I_{hkl} \propto L \cdot P \cdot |F_{hkl}|^2 \quad (2)$$

(L = Lorentz factor, P = polarization factor, F_{hkl} = structure amplitude)

The structure amplitude F_{hkl} depends as well from the atom position as from its scattering factor f_j . This allows a summation over all j atoms of the cell (equation (3)).

$$F_{hkl} = \sum_j f_j e^{2\pi i(hx_j + ky_j + lz_j)} \quad (3)$$

(x_j, y_j, z_j = atom positions)

As follows from equation (2), the structure amplitude F_{hkl} is directly proportional to the total intensities I_{hkl} . If the structure factors are known in modulus and phase, the atomic positions are unequivocally determinable. Indeed, according to equation (4) the electron density function ρ_{xyz} and therefore finally the crystal structure can be calculated by Fourier transformation of the structure amplitude F_{hkl} .

$$\rho_{xyz} = \frac{1}{V} \sum_{hkl} F_{hkl} \cdot e^{-2\pi i(hx+ky+lz)} \quad (4)$$

Unfortunately, as shown in equation (2), only the moduli $|F_{hkl}|$ can be obtained from diffraction intensities because the corresponding phase information is lost. This is the so-called crystallographic phase problem. How to identify the atomic positions starting only from the moduli $|F_{hkl}|$ is a question for which the *Direct methods* and the *Patterson method* were developed. [61, 62] The refinement occurs by optimizing the model on full-matrix least-squares on F^2 . Additional atoms are assigned to residual peaks by difference Fourier synthesis with associated refinement until no significant residual peaks remain.

3.1.2 X-Ray Powder Diffraction

Powder diffractometric methods were generally used for a fast identification of the synthesized samples. The diffraction experiments on powder samples were conducted on two STOE Stadi P diffractometers (STOE & Cie, Darmstadt) or on a Guinier diffractometer G670 (Huber Diffractionstechnik GmbH & Co. KG, Rimsting), respectively.

The STOE Stadi P diffractometers are constructed in focussing geometry using Ge(111)-monochromatized $\text{CuK}_{\alpha 1}$ ($\lambda = 154.18 \text{ pm}$) or Ge(111)-monochromatized $\text{MoK}_{\alpha 1}$ ($\lambda = 71.073 \text{ pm}$) radiation, respectively. Measurements were performed in Debye-Scherrer (capillary) or transmission geometry (between acetate films). The diffraction intensities were collected by a position sensitive detector (PSD) with an opening angle of $2\theta = 5^\circ$.

The advantage of the Huber Guinier diffractometer is the high resolution of the X-ray film technique with the sensitivity of an imaging plate system in combination with short exposure times. Inside one box, the instrument combines the camera unit, the scan device, and an erasure lamp. Flat powder samples were measured in transmission geometry in the range $3^\circ \leq 2\theta \leq 100^\circ$ with quartz monochromatized $\text{CuK}_{\alpha 1}$ radiation and SiO_2 as standard.

3.1.3 Temperature-programmed X-Ray Powder Diffraction

The temperature-programmed *in-situ* X-ray diffractometry was performed on a STOE Stadi P powder diffractometer ($\text{MoK}_{\alpha 1}$; $\lambda = 71.073 \text{ pm}$) with a computer-controlled STOE furnace. An electrically heated graphite tube held the sample capil-

lary (silica glass capillaries, Fa. Hilgenberg, $\varnothing_{\text{ext.}}$ 0.1–0.5 mm) vertical with respect to the scattering plane. Bores in the graphite tube permitted unobstructed pathways for the primary beam as well as for the scattered radiation. The temperature, measured by a thermocouple in the graphite tube, was kept constant within 0.2 °C. The samples were heated from room temperature to 1100 °C in steps of 50 °C or 100 °C, respectively. The heating rate between different temperature steps was set to 50 °C/min and the data acquisition started directly after reaching the next temperature step. Caused through the construction of the furnace, the data collection was restricted to a 2θ range of approximately 3–21°.

3.1.4 Single Crystal Diffraction

Small single crystals were isolated using a polarization microscope MZ12 (Leica, Bensheim) by mechanical fragmentation from a crop of crystals covered by a thin film of paraffine on a glass carrier. The small crystals were fixed on a thin glass fiber with beeswax or instant glue. Afterwards, the quality of the preselected single crystals were checked using a Laue or Precession camera in Laue mode (Buerger Precession camera 205, Huber Diffraktionstechnik GmbH, Rimsting) operating with white Mo radiation (Röntgengenerator Kristalloflex 760, Siemens). Imaging Plates [63] coated with a photosensitive material (e.g. BaFX:Eu²⁺, X = Cl, Br, I) were applied for recording the diffracted X-rays. For the readout, a laser scanner (BAS-2500 Bio Imaging Analyser, Fuji Photo Film Corporation, Japan) was employed.

Single crystal intensity data were collected at temperatures between 200 and 293 K from irregularly shaped crystals by use of a STOE IPDS detector diffractometer (Fa. STOE & Cie, Darmstadt), or on a Kappa CCD diffractometer (Bruker AXS / Nonius, Karlsruhe) equipped with a rotating anode and graphite monochromatized MoK_α radiation (71.07 pm). In general, a raw data reduction was performed with instrumental specific software, typically accounting for Lorentz-, polarization-, and isotropic extinction corrections.

3.1.5 Computer Programs

The programs BASREAD [64] and TINA [65] were used for evaluating the Laue diagrams. Powder diffractograms were recorded and handled with the STOE program package WinXPOW [66]. By means of the embedded programs TREOR [67–69], ITO [70], DICVOL [71], and THEO [72] indexing of recorded powder patterns and simulation of powder patterns on the basis of single crystal data were possible.

The integrated search routine „SEARCH-MATCH“ [73], referred to the JCPDS - database [74], was used for phase analyses.

Data reduction and absorption correction of single crystal data occurred with the programs X-RED [75], X-SHAPE [76], and HABITUS [77]. Analysis of the data sets, including determination of the possible space groups, were carried out with the program XPREP [78], which was also used for semi-empirical absorption corrections, if applicable. The crystal structures were solved by *Direct-* or *Patterson-methods* using the program SHELXS-97 [79] and refined on F^2 by applying the full-matrix least-squares method implemented in SHELXL-97 [80]. Both programs are combined in the X-STEP32 [81] user interface. Evaluation and verification of the structure models including the selected space groups was done with the program PLATON (including ADDSYMM) [82].

For visualization of the crystal structures, the program DIAMOND [83] was employed.

3.2 Energy Dispersive Analyses of X-Rays

To investigate the morphology and composition of crystals, an electron scanning microscope (JSM-6500F with field emission source, Jeol, USA; maximum resolution: 1.5 nm) was used. The EDX-technique (Energy Dispersive Analysis of X-rays) enables a qualitative and semi-quantitative analysis of the composition on the basis of the characteristic X-ray emissions of elements (EDX detector: model 7418, Oxford Instruments). With high voltages accelerated electrons knock K-, L-, or M-shell electrons out of the sample. This is possible if the energy of the electron beam is higher than the ionisation energy of the elements contained in the sample. The resulted electron hole is occupied instantaneously by an electron of a higher shell and the difference in energy is emitted through element characteristic X-ray radiation. In addition to that, elastic and inelastic scattering gives information about the topology and morphology of the sample.

For best results and most exact conclusions concerning the composition, the sample should be orientated orthogonal to the electron beam. This could be realized by grinding and polishing of in synthetic resin imbedded samples. A few intermetallic samples were investigated by this method with regard to their phase compositions. Because of the fact that the samples were not grinded to plain surfaces, an elemental analysis *via* EDX can only be considered as a semi-quantitative way. Table 3.2-1 gives an overview about the fault tolerances depending on the concentration c

of the investigated element by conventional EDX analysis. Furthermore, the analysis is much more precise for heavier elements than for light elements.

Table 3.2-1: Fault tolerance of EDX analysis after lit. [84] for elements heavier than sodium.

Concentration c of an element in the sample	Expected relative failures	Maximum absolute failure in the centre of the concentration range
$50\% \leq c \leq 100\%$	1 – 5%	$71.25\% \leq c \leq 78.75\%$
$10\% \leq c \leq 50\%$	5 – 10%	$27\% \leq c \leq 33\%$
$1\% \leq c \leq 10\%$	10 – 70%	$1.5\% \leq c \leq 8.5\%$
$c \leq 1\%$	> 70%	any

For the EDX sample preparation some small single crystals, smithereens of bulk material, or powdered sample material were placed on a messing sample holder and fixed with hot-melt adhesive (Pattex, Henkel, Düsseldorf) or self-adhesive carbon plates (Plano, Wetzlar). To avoid charge effects and to ensure conductivity, the samples were sputtered with carbon (Sputter device: BAL-TEC MED 020, BAL-TEC AG, Balzers, Netherlands). In the case of intermetallic phases a sputtering of the sample was not necessary, if self-adhesive carbon plates were used.

The data collection as well as the evaluation took place with the INCA [85] program package.

3.3 Elemental Analysis

Concerning the composition, the produced samples were primarily investigated *via* EDX analysis. To verify the chemical constitution particularly with regard to the O/N - content, selected samples were sent to the microanalytical laboratory *Pascher* (Remagen, Germany). A carrier hot gas extraction method was used after pyrolysis of the sample in a graphite crucible. The detection was carried out by an IR/thermal conductivity measurement.

3.4 Infrared Spectroscopy

IR spectroscopy is a very useful method for the characterisation of molecular arrangements, whereby typical vibrations with the aid of databases could be assigned reliably. At highly condensed solid-state compounds a correlation between certain absorption bands and typical lattice vibrations is not so easy to verify. Never-

theless, it is possible to distinguish between specific atom groups. So, in borate chemistry, the IR spectroscopy is a very useful tool to differentiate among $[\text{BO}_3]^{3-}$ and $[\text{BO}_4]^{5-}$ groups.

Infrared (IR) spectra were recorded on a Bruker IFS66/v FTIR spectrometer (Bruker Analytik GmbH, Ettlingen) in an evacuated cell between 400 and 4000 cm^{-1} (DLATGS detector). The samples were thoroughly mixed with dried KBr (5 mg sample, 500 mg KBr) in a glove box (MBraun, MB150-GI and UniLab, $\text{O}_2 < 1$ ppm, $\text{H}_2\text{O} < 1$ ppm, Garching) under dried argon atmosphere (purity grade 4.8, Messer Griesheim, Germany). Afterwards, KBr pellets of samples were prepared by pressurizing, using a hand press with a press capacity of 10 kN.

The program OPUS (Bruker Analytik GmbH) [86] served for evaluation of the spectra.

3.5 Magnetic and Heat Capacity Measurements

The magnetic and heat capacity measurements were carried out on a Quantum Design Physical Property Measurement System (PPMS) in cooperation with Dr. R.-D. Hoffmann and Dr. S. Rayaprol, Universität Münster, using AC-, DC-MS and heat capacity options.

For magnetization measurements, the samples (about 10–35 mg) were enclosed in thin-walled gelatin capsules. The lowest achievable temperature inside the PPMS system was 3 K, and hence all the measurements were performed down to 3 K, with magnetic flux densities up to 80 kOe. The samples were magnetized by a constant magnetic field and the magnetic moment of the samples was measured by an induction technique, producing a DC magnetization curve $M(H)$. Inductive measurements were performed by moving the sample through a set of copper pickup coils. The induced signal was analyzed with a digital signal processor (DSP) to determine the sample's magnetic moment.

Using the measured magnetization M_p of the sample, the molar mass of the compound M_{mol} , the magnetic induction B , and the mass of the sample m_p , the molar susceptibility can be calculated using the following formula:

$$\chi_{mol} = \frac{M_p \cdot M_{mol}}{B \cdot m_p} \quad (5)$$

(χ_{mol} = molar susceptibility, M_p = measured magnetization, M_{mol} = molar mass, B = magnetic induction, m_p = sample mass)

For the specific heat measurements (C_p) the samples were glued to the platform of a pre-calibrated heat capacity measuring puck with *Apiezon N* grease. The C_p measurements were carried out with a relaxation technique, using a sophisticated *two-tau model* to simulate the effect of the heat flow between the microcalorimeter platform and the sample (*tau2*) as well as the heat flow between the platform and puck stage (*tau1*).

3.6 Lattice Energy Calculation

An appropriate method to check crystal structures with regard to their plausibility are calculations of the Madelung Part of Lattice Energy (MAPLE) [87-89]. These computations consider the electrostatic interactions of ions in a crystal structure, depending on the distance, and calculate the coordinative contribution of ligands around a central atom. For each crystallographic layer one obtains partial MAPLE-values, giving the total MAPLE-value of the compound by summing up the partial ones. MAPLE-values are additive with high accuracy, which means that the sum of the total MAPLE-values of the starting materials are comparable to the total MAPLE-value of the product.

3.7 Bond-Length Bond-Strength Calculation

In solid-state compounds, the correlation of bond-length and bond-strength permits a prediction of bond distances with given valences. The concept is based on *Pauling's* defined bond-grade [90], mainly used for the description of metals or intermetallic phases. *Brown* [91], as well as *Brese* and *O'Keeffe* [92] generalized the concept for a multiplicity of compounds.

Contrary, it is possible to calculate backwards valence sums from bond distances derived from crystal structure determinations. This method is a helpful tool to check crystal structure determinations on their plausibility. The bond valence v_{ij} between the atoms i and j is defined as:

$$v_{ij} = \exp \left[\frac{(R_{ij} - d_{ij})}{b} \right] \quad (6)$$

(v_{ij} = bond valence, R_{ij} = bond valence parameter, d_{ij} = bond distance, b = constant (37 pm))

For each elemental combination exists a specific bond valence parameter R_{ij} , which can be found in the literature [92,93]. b is an empirical parameter with a value of 37 pm. The total valence sum V_i is equivalent to the totalized valences v_{ij} of all bonds starting from the atom i .

$$V_i = \sum_j v_{ij} \quad (7)$$

3.8 Calculation of the Charge Distribution

Calculations concerning the charge distribution were performed with the program CHARDI (Charge Distribution in Solids) [94, 95]. This method is a combination of Pauling's bond-grade [90] and the effective coordination number (ECoN). In contrast to MAPLE, which is based on an ionic approach, CHARDI considers anion-anion- and cation-cation-interactions, too.

The ECoN contribution $\Delta E(ij \rightarrow k)$ is calculated from the average weighted distance $d(ij \rightarrow k)$ of all cations K_i , located on the crystallographic layer j , to all anions A_k . The summation about all these values yield for all cations K_{ij} in a partial effective coordination number $\Delta(\text{ECoN})$ with the anions A_k as ligands. Taking into account the number of anions A_k surrounding K_{ij} , the charge distribution $\Delta q(ij \rightarrow k)_{\text{cation}}$ results. Equations (8) and (9) give the summed up charge of i atoms on j layers.

$$Q_{\text{cation}} = -\sum_i \sum_j \Delta q(ij \rightarrow k)_{\text{cation}} \quad (8)$$

$$Q_{\text{cation}} = -\sum_k \Delta q(k \rightarrow ij)_{\text{anion}} \quad (9)$$

($\Delta q(ij \rightarrow k)_{\text{cation}}$ = charge distribution of cation K_{ij} with respect to anion A_k , $\Delta q(k \rightarrow ij)_{\text{anion}}$ = charge distribution of anion A_k with respect to cation K_{ij} , $i = i^{\text{th}}$ cation, $j = \text{crystallographic layer}$, $k = k^{\text{th}}$ anion)

3.9 Cycle-Class Spectra

For the characterisation and for comparison reasons of three dimensional condensed crystal structures Cycle-Class Spectra according to Klee were calculated [96]. That is a topological analysis of networks concerning the frequency of for example B_nO_n -rings in the unit cell. The program TOPOLAN was used to perform the calculations [97].

4 Experimental Section

4.1 Rare-Earth Borates

4.1.1 Introduction

Boron, element number five and located as a group 13 element in the Periodic Table has properties, which are borderline between metals and non-metals. It is a semiconductor rather than a metallic conductor. Chemically it is closer to silicon than to aluminum, gallium, indium, and thallium. Furthermore, it is an electron deficient element, possessing a vacant p-orbital, which causes Lewis acidity. The reactions of boron are dominated by a requirement for electrons. Also, boron is the least electronegative non-metal, meaning that it is usually oxidized in reactions. For that reason, boron does not appear in nature in elemental form but is found combined in *borax* ($\text{Na}_2\text{B}_4\text{O}_5(\text{OH})_4 \cdot 8\text{H}_2\text{O}$), *boric acid* (H_3BO_3), *colemanite* ($\text{Ca}_2\text{B}_6\text{O}_8(\text{OH})_6 \cdot 2\text{H}_2\text{O}$), *kernite* ($\text{Na}_2\text{B}_4\text{O}_6(\text{OH})_2 \cdot 3\text{H}_2\text{O}$), *ulexite* ($\text{NaCaB}_5\text{O}_6(\text{OH})_6 \cdot 5\text{H}_2\text{O}$), and other borates. The natural frequency of boron in the Earth's crust lies around 0.001% and separates into sedimentary deposits or water dissolved borates with low concentrations [98]. This water solubility is seen as one of the main reasons for the accumulation of borates at high concentrations in shallow or surface deposits. Boron-rich waters, from springs along fault zones due to volcanic activity, concentrated on the surface at high evaporation rates precipitating borate minerals. These sedimentary borate minerals have appreciable water solubility, typically protected by a layer of clay. Nowadays, the main continental borate deposits are located in the western United States (Boron and Death Valley, California and in the western Turkey), supplying > 80% of the world demand for borates.

Worldwide, the annual consumption of B_2O_3 for various industrial borate containing products is larger than 1 million tons [98]. The largest single customer is the glass industry which needs huge amounts of B_2O_3 for fiberglass production, low-expansion borosilicate glasses, or glass frits used in the ceramic industry. Borates, like sodium peroxyborate, used as a whitening agent in laundry products, amount the second largest consumption of borates. As the third largest consumer of borates

the fertilizer production is considered. Beside these main fields of application, which take nearly 75% of the world demand, there are reams of smaller end-use applications.

Today, the synthesis, structural characterization, materials processing, and device optimization of synthetic borates plays an increasing role. The usage as phosphor, for example $\text{SrB}_4\text{O}_7:\text{Eu}$ in UV-emitting medical lamps, $\text{GdMgB}_5\text{O}_{10}:\text{Ce}$, Tb as the green emitting component in fluorescent lamps, or $(\text{Y,Gd})\text{BO}_3:\text{Eu}$ as the red-emitting component in plasma display panels for high-definition television are only few examples of high-tech applications of borates. Also in the field of NLO-materials, great progress has been made since the advent of an era about 20 years ago with the first borate material $\beta\text{-BaB}_2\text{O}_4$ (BBO), suitable for laser systems [99, 100]. Borate crystals such as LiB_3O_5 (LBO) and $\text{CsLiB}_6\text{O}_{10}$ (CLBO) have enabled the reliable production of laser light at wavelengths and power levels, that were previously unattainable with solid-state systems [101, 102]. In our working group, we were able to establish a new non-centrosymmetric modification of BiB_3O_6 (BIBO) synthesized under high-pressure / high-temperature conditions [103]. The structure of $\delta\text{-BiB}_3\text{O}_6$ is isotypic to $\gamma\text{-CeB}_3\text{O}_6$ and further investigations concerning NLO effects are in progress.

As mentioned at the beginning of this Chapter, the crystal chemistry of borates is in some aspects comparable to silicon due to the close relationship between boron and silicon. In nature, boron is always found covalently bonded to oxygen, forming an especially strong bond with oxygen. Stronger bonds were only formed with fluorine [104]. Usually, boron compounds resemble other non-metals, notably silica. For example, B_2O_3 and SiO_2 are similar in their acidic nature, and their melts readily dissolve metallic oxides to form borates and silicates that, in cooling, give glasses being difficult to crystallize.

The main structural differences between silicates and borates is the result of the formation of tetrahedral $[\text{BO}_4]^{5-}$ as well as trigonal planar $[\text{BO}_3]^{3-}$ groups in borate chemistry, whereas the silicates are exclusively built up from tetrahedral $[\text{SiO}_4]^{4-}$ groups. Despite the apparent simplicity of these fundamental units, borate structures often consist of quite complex combinations of these components. They may exist as isolated anions, link together by sharing oxygen to form rings and cages, or further polymerize into chains, sheets, or extended networks. Furthermore, borate anions interact with cations in complex ways and often display extensive hydrogen-bonding integrating their structures.

Threefold coordinated oxygen atoms are also not observed in silicate chemistry up to now. Following the pressure coordination rule [192], an increase of pressure can lead to higher coordinated boron as well as oxygen atoms. For example, the normal-pressure modification of B_2O_3 -I [105] is exclusively built up from trigonal $[BO_3]^{3-}$ groups (see Figure 4.1-1), whereas in the high-pressure phase B_2O_3 -II [211] all boron atoms are coordinated tetrahedrally (see Figure 4.1-2) and $\frac{2}{3}$ of the oxygen atoms are in a threefold coordination.

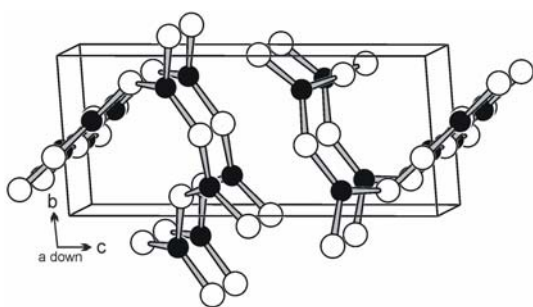


Figure 4.1-1: Crystal structure of trigonal B_2O_3 -I (boron: black spheres; oxygen: white spheres) [30]

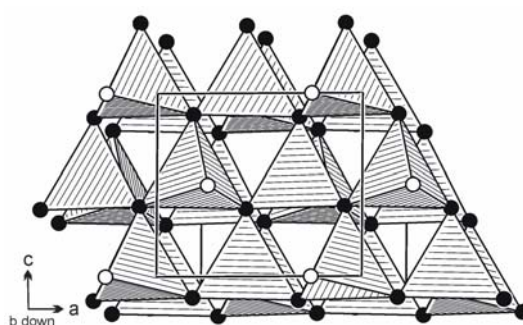


Figure 4.1-2: Crystal structure of orthorhombic B_2O_3 -II ($O^{[2]}$: white spheres; $O^{[3]}$: black spheres) [30]

The application of high pressures and high temperatures during borate syntheses resulted in one more remarkable structural feature. In the year 2002 *Huppertz et al.* were able to synthesize edge-sharing $[BO_4]^{5-}$ tetrahedra for the first time [113, 114, 137, 138]. In the following a short overview about the structural variability of borates is given, without any claim of completeness due to the huge number of compounds.

At the moment, over 1100 borate crystal structures are listed in the Inorganic Crystal Structure Database ICSD [106]. High-pressure investigations are rare and were mainly performed from the geological point of view. Starting in the year 1999, systematic high-pressure experiments up to maximum pressures of 16 GPa have been carried out by *Huppertz et al.* The focus of these experiments was set on rare-earth metal borates and later on, transition metal borates followed. In principle, only the compositions $RE_2O_3:B_2O_3 = 1:1, 1:3,$ and $3:1$ were known, resulting in the compositions $REBO_3, REB_3O_6,$ and $RE_3BO_6,$ which can be synthesized directly from the rare-earth oxides and boron oxide. In contrast to the orthoborates $REBO_3$ and the *meta*-borates $REB_3O_6,$ there exist some uncertainties concerning the compositions of the rare-earth oxoborates RE_3BO_6 ($RE = La, Y, Gd$) [107, 108]. The latest results adopt different compositions with the idealized formulas $RE_{26}(BO_3)_8O_{27}$ ($RE = La$)

and $RE_{17.33}(BO_3)_4(B_2O_5)_2O_{16}$ ($RE = Y, Gd$) [109, 110]. Other authors confirmed the initial composition again, so there are still controversies left.

In the context of the investigations into the high-pressure / high-temperature synthesis of new rare-earth and transition metal oxoborates, several new high-pressure polymorphs of known compositions, e.g. β - MB_4O_7 ($M = Ca$ [206], Zn [205], Hg [207]), χ - $REBO_3$ ($RE = Dy, Er$) [111], and ν - $DyBO_3$ [112] were discovered. Additionally, new compositions were realized, whose successful syntheses were indisputably based on the pressure parameter. For example, all attempts to produce rare-earth metal(III) oxoborates with the ratio $RE_2O_3:B_2O_3 = 2:3, 1:2,$ and $3:5$ under normal-pressure conditions were in vain. In contrast, the corresponding high-pressure experiments led in most cases to phase pure rare-earth metal(III) oxoborates $RE_4B_6O_{15}$ ($RE = Dy, Ho$) [113-115] and α - $RE_2B_4O_9$ ($RE = Sm-Ho$) [116, 137, 138], exhibiting the former described rare structural unit of edge-sharing tetrahedra. Chapter 4.1.3 of this thesis describes the synthesis of α - $Nd_2B_4O_9$, the new initial compound with the largest cation in this series. The corresponding polymorphs β - $RE_2B_4O_9$ ($RE = Dy, Gd$) [117, 118] did not show $[BO_4]^{5-}$ tetrahedra with common edges. Latest experiments yielded in a third compound exhibiting edge-sharing tetrahedra. The special feature of the compound β - NiB_2O_4 [119] is that in contrast to the first two compounds all tetrahedra are linked to each other *via* one common edge and two common corners. Figure 4.1-3 gives an overview of the three crystal structures with edge-sharing $[BO_4]^{5-}$ tetrahedra.

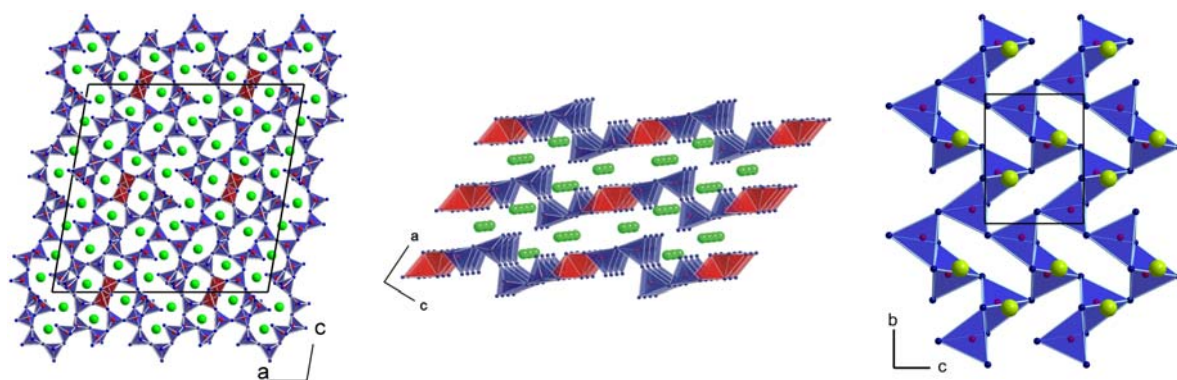


Figure 4.1-3: Overview about the crystal structures with edge-sharing tetrahedra: α - $RE_2B_4O_9$ (left), $RE_4B_6O_{15}$ (middle), β - NiB_2O_4 (right).

The former mentioned structural relationship between borates and silicates was clearly realized for the new composition $RE_3B_5O_{12}$ ($RE = Tm-Lu$) [120] and β - HfB_2O_5 [121], which crystallize in the silicate analogue structures of *semenovite* and *datolite*, respectively.

In recent years, a systematic investigation of rare-earth *meta*-borates with the composition $RE(BO_2)_3$ [122-127] under ambient- and high-pressure conditions led to the discovery of new modifications and the clarification of the stability ranges. The series starts with the well-characterized monoclinic phases α -La(BO_2)₃ [154, 155], α -Ce(BO_2)₃ [193], α -Pr(BO_2)₃ [152], α -Nd(BO_2)₃ [128, 129], α -Sm(BO_2)₃ [130], α -Eu(BO_2)₃ [123], α -Gd(BO_2)₃ [130], and α -Tb(BO_2)₃ [131], crystallizing in the space group $I2/a$ (non-standard setting of: $C2/c$). Figure 4.1-4 (left) gives a view of the crystal structure of the α -type modification. These compounds are characterized by chains of tetrahedral $[BO_4]^{5-}$ and triangular $[BO_3]^{3-}$ units, which may be regarded as anionic $\infty^1\{[B_3O_6]^{3-}\}$ chains, running along the c axis and built up on the regular succession of $[BO_4]^{5-}$ tetrahedra, which share four corners with monodentate $[BO_3]^{3-}$ triangles. These chains are separated from each other by RE^{3+} cations surrounded by 10 oxygen atoms, forming distorted bicapped tetragonal antiprisms. Starting with Tb^{3+} , the *meta*-oxoborates exhibit a second structure variation of orthorhombic β -Tb(BO_2)₃, solved by *Nikelski* and *Schleid* in 2003 [209] for the first time (Figure 4.1-4, middle). Continuing the research with smaller rare-earth metal ions led to the insight that only the dysprosium compound was attainable under normal-pressure conditions. For the synthesis of the remainder β - $RE(BO_2)_3$ series with $RE = Ho-Lu$, high-pressure / high-temperature conditions of 7.5 GPa and 1000 °C were necessary [208]. Interestingly, the thulium, ytterbium, and lutetium representatives crystallized only as by-products during the formation of compounds with the formula $RE_3B_5O_{12}$ ($RE = Er-Lu$) [120]. A detailed description of the crystal structure is given in connection with the discussion of the new neodymium representative in Chapter 4.1.4.

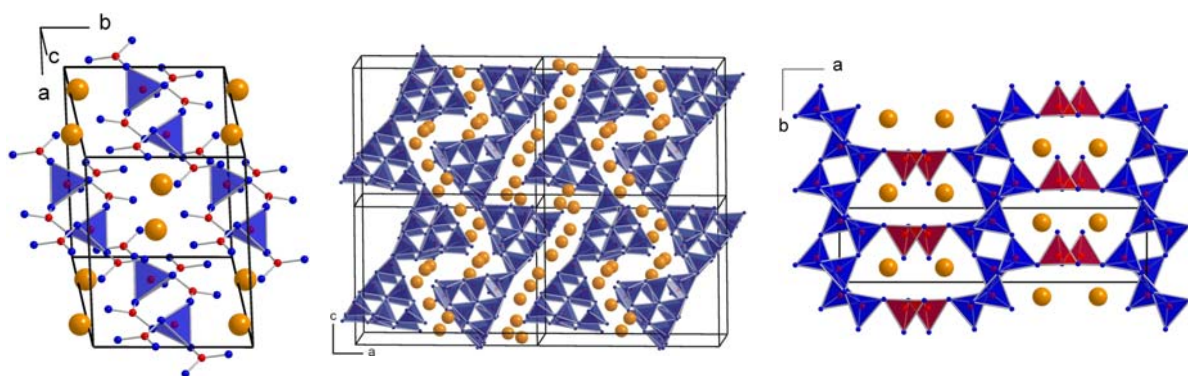


Figure 4.1-4: Crystal structures of the rare-earth *meta*-borates α - (left), β - (middle), and γ - $RE(BO_2)_3$ (right).

Due to the fact that the monoclinic phases α - $RE(BO_2)_3$ are built up from trigonal $[BO_3]^{3-}$ and tetrahedral $[BO_4]^{5-}$ groups, a possible transformation into a new

modification applying high-pressure conditions was assumed. This assumption was fulfilled by the synthesis of the orthorhombic phases $\gamma RE(BO_2)_3$ ($RE = La-Nd$) at conditions of 7.5 GPa and 1000 °C [191, 210]. As expected for a high-pressure phase in oxoborate chemistry, the structure consists of corner-sharing $[BO_4]^{5-}$ tetrahedra exclusively, forming a three-dimensional network (Figure 4.1-4, right). A more detailed look at the connectivity between the $[BO_4]^{5-}$ tetrahedra shows topologically identical layers of $[BO_4]^{5-}$ tetrahedra as found in oxoborates like SrB_4O_7 [200-202], PbB_4O_7 [200, 203], EuB_4O_7 [204], β - CaB_4O_7 [206], and β - HgB_4O_7 [207]. However, in $\gamma RE(BO_2)_3$ ($RE = La-Nd$) the layers are separated or interconnected by chains of $[BO_4]^{5-}$ tetrahedra. Also here, threefold coordinated oxygen atoms $O^{[3]}$ are part of the layers.

Naturally, the difference between normal-pressure and a pressure of 7.5 GPa is remarkable. For example, CaB_2O_4 -I [132, 133] exhibits three pressure-induced transformations up to a pressure of 4 GPa [206]: CaB_2O_4 -II can be obtained in the pressure range of 1.2–1.5 GPa [134], CaB_2O_4 -III in the area of 1.5–2.5 GPa [135], and CaB_2O_4 -IV is synthesized in the range of 2.5–4 GPa [136].

For the large rare-earth cations from lanthanum to neodymium we analyzed the pressure range below 7.5 GPa and discovered a new phase at 5.5 GPa and a formation temperature of 1050 °C. Due to the chronological designation of the former rare-earth metal(III) *meta*-oxoborates α , β , and $\gamma RE(BO_2)_3$, we denoted this new phase $\delta RE(BO_2)_3$. In Chapter 4.1.5, we report about the high-pressure / high-temperature synthesis, the crystal structure, and some properties of this δ modification within the scope of rare-earth metal(III) *meta*-oxoborates.

Chapter 4.1.6 of this thesis presents the synthesis, single crystal structure, and properties of the new compound $Pr_4B_{10}O_{21}$ established at 3.5 GPa and 1050 °C revealing a new composition in rare-earth oxoborate chemistry.

Some results of the work on the rare-earth borates are due to the excellent work of Almut Haberer who carried out her Bachelor work under my supervision.

4.1.2 Starting Materials

For the preparation of new rare-earth borates in this work, various commercially acquirable chemical substances were used. Table 4.1-1 lists up the different substances, state, purity, and source of supply.

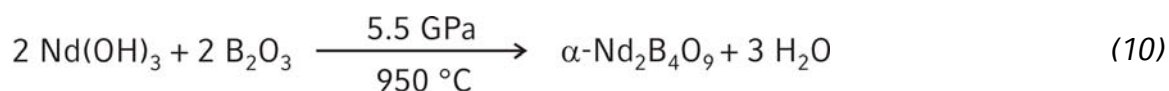
Table 4.1-1: Purity and source of supply of commercially available substances

Substance	State	Purity	Source of Supply
La ₂ O ₃	Powder	> 99.99%	Dr. Theodor Schuchardt, München, Germany
CeO ₂	Powder	> 99.9%	Auer Remy, Hamburg, Germany
Pr ₆ O ₁₁	Powder	>99.9%	Auer Remy, Hamburg, Germany
Nd ₂ O ₃	Powder	>99%	unknown, ICDD-PDF [21-579]
B ₂ O ₃	Grains	> 99.9%	Strem Chemicals, Newburyport, U.S.A.

4.1.3 The Borate α -Nd₂B₄O₉

4.1.3.1 Synthesis

The borate α -Nd₂B₄O₉ was synthesized according to equation (10) *via* a multianvil high-pressure / high-temperature route. The starting material for the synthesis was a thoroughly mixed 1 : 2 molar mixture of Nd(OH)₃, obtained by hydrolysis of Nd₂O₃ with B₂O₃.



An 18/11-assembly was used to compress the sample within 2 h to 5.5 GPa and heated to 950 °C in the following 25 min. After holding this temperature for 5 min, the sample was cooled down to 450 °C within 25 min. Subsequent quenching of the sample to room temperature finished the temperature program. After decompression, the recovered experimental octahedron was broken apart and the sample carefully separated from the surrounding BN. The compound α -Nd₂B₄O₉ is air- and water-resistant, crystallizing as large, pale-pink crystals (see Figure 4.1-5). EDX investigations of single



Figure 4.1-5: α -Nd₂B₄O₉ crystal on a glass fiber.

crystals confirmed the theoretical Nd/B ratio of 0.5 with a measured ratio of 0.55 in a good way. Unfortunately, the compound α -Nd₂B₄O₉ always appeared in combination with the already known *meta*-oxoborate γ -Nd(BO₂)₃ [191], which remained as only phase at higher pressures.

4.1.3.2 Crystal Structure Analysis

Small single-crystals of α -Nd₂B₄O₉ were isolated by mechanical fragmentation and first investigated by Laue photographs in a Buerger camera. Single-crystal intensity data were collected at room temperature from a regularly shaped pink crystal (block) by use of a STOE IPDS detector diffractometer [MoK_α radiation (71.073 pm)]. An empirical absorption correction (XPREP [78]) was applied to the intensity data. All relevant information concerning the data collection is listed in Table 4.1-2. According to the systematic extinctions hkl with $h + k \neq 2n$, $h0l$ with $h, l \neq 2n$, and $0kl$ with $k \neq 2n$, the space groups Cc (No. 9) and $C2/c$ (No. 15) were derived. During the structure refinement the centrosymmetric group was found to be correct. The starting positional parameters were deduced from an automatic interpretation of *Direct methods* with SHELXS-97 [79]. The structure of α -Nd₂B₄O₉ was refined with anisotropic displacement parameters for all atoms with SHELXL-97 [80] (full-matrix least-squares on F^2). The final difference Fourier synthesis did not reveal any significant residual peaks in the refinement (see Table 4.1-2). Details of the single crystal structure measurement are shown in Table 4.1-2. Additionally, the positional parameters (Table 4.1-3), anisotropic displacement parameters (Table 4.1-4), interatomic distances (Table 4.1-5), and angles (Table 4.1-6) are listed. Calculations of Cycle-Class Spectra confirmed the isotopy to the other representatives α -RE₂B₄O₉ (RE = Sm–Ho).

Table 4.1-2: Crystal data and structure refinement for α -Nd₂B₄O₉

Empirical formula	α -Nd ₂ B ₄ O ₉
Molar mass (g·mol ⁻¹)	475.72
Crystal system	monoclinic
Space group	C2/c (No. 15)
Single crystal diffractometer	STOE-IPDS
Radiation	MoK α ($\lambda = 71.073$ pm)
Single crystal data	
<i>a</i> (pm)	2570.8(5)
<i>b</i> (pm)	447.30(9)
<i>c</i> (pm)	2504.1(5)
β (°)	99.82(3)
Volume (Å ³)	2837(1)
Formula units per cell	<i>Z</i> = 20
Temperature (K)	293(2)
Calculated density (g·cm ⁻³)	5.57
Crystal size (mm ³)	0.12 x 0.06 x 0.03
Detector distance (mm)	50
Irradiation / exposure (min)	3.50
Number of exposures	225
Absorption coefficient (mm ⁻¹)	18.1
F(000)	4240
θ Range (°)	3.22 to 30.33
Range in <i>hkl</i>	$\pm 36, \pm 6, \pm 33$
Total no. reflections	14419
Independent reflections	3930 (<i>R</i> _{int} = 0.0308)
Reflections with <i>I</i> > 2 σ (<i>I</i>)	3508 (<i>R</i> _{σ} = 0.0229)
Data / parameters	3930 / 340
Absorption correction	empirical (XPREP [78])
Transm. ratio (max / min)	0.259 / 0.183
Goodness-of-fit (<i>F</i> ²)	1.071
Final <i>R</i> indices (<i>I</i> > 2 σ (<i>I</i>))	<i>R</i> 1 = 0.0206 <i>wR</i> 2 = 0.0526
<i>R</i> Indices (all data)	<i>R</i> 1 = 0.0255 <i>wR</i> 2 = 0.0550
Extinction coefficient	0.00041(2)
Larg. diff. peak and hole (e·Å ⁻³)	1.47 / -1.38

Table 4.1-3: Atomic coordinates and isotropic equivalent displacement parameters ($U_{\text{eq}} / \text{\AA}^2$) for $\alpha\text{-Nd}_2\text{B}_4\text{O}_9$ (space group: $C2/c$). U_{eq} is defined as one third of the trace of the orthogonalized U_{ij} tensor.

Atom	Wyckoff Site	x	y	z	U_{eq}
Nd1	8f	0.063660(8)	0.19800(5)	0.06964(1)	0.00465(6)
Nd2	8f	0.215482(9)	0.20577(5)	0.13097(1)	0.00537(6)
Nd3	8f	0.012785(8)	0.66879(5)	0.17868(1)	0.00425(6)
Nd4	8f	0.358568(9)	0.17464(5)	0.20827(1)	0.00632(6)
Nd5	8f	0.155921(9)	0.22572(5)	0.95995(1)	0.00750(6)
B1	8f	0.2417(2)	0.726(1)	0.0386(2)	0.0043(8)
B2	8f	0.2511(2)	0.181(1)	0.2816(2)	0.0064(9)
B3	8f	0.9258(2)	0.302(1)	0.0310(2)	0.0038(8)
B4	8f	0.1479(2)	0.713(1)	0.0583(2)	0.0038(8)
B5	8f	0.0985(2)	0.1734(9)	0.1915(2)	0.0043(8)
B6	8f	0.3550(2)	0.19(1)	0.3376(2)	0.0044(8)
B7	8f	0.9478(2)	0.1712(9)	0.2250(2)	0.0036(8)
B8	8f	0.3049(2)	0.669(1)	0.1326(2)	0.0072(9)
B9	8f	0.9680(2)	0.817(1)	0.0655(2)	0.0047(8)
B10	8f	0.9082(2)	0.132(1)	0.1241(2)	0.0043(8)
O1	8f	0.2714(2)	0.5349(6)	0.0820(2)	0.0055(5)
O2	8f	0.1986(2)	0.8776(7)	0.0552(2)	0.0052(6)
O3	8f	0.2251(2)	0.5597(7)	0.9865(2)	0.0059(6)
O4	8f	0.0637(2)	0.3807(6)	0.9775(2)	0.0047(5)
O5	8f	0.4055(2)	0.7891(7)	0.2546(2)	0.0051(6)
O6	4e	0	0.3070(9)	1/4	0.0026(7)
O7	8f	0.0637(2)	0.1424(6)	0.8889(2)	0.0050(6)
O8	8f	0.0191(2)	0.6943(6)	0.0844(2)	0.0047(6)
O9	8f	0.3809(2)	0.3584(6)	0.3002(2)	0.0059(6)
O10	8f	0.3698(2)	0.3198(6)	0.3914(2)	0.0052(6)
O11	8f	0.9723(2)	0.1169(6)	0.0424(2)	0.0052(6)
O12	8f	0.935(2)	0.3055(6)	0.1695(2)	0.0053(6)
O13	8f	0.1078(2)	0.8406(6)	0.0153(2)	0.0046(6)
O14	8f	0.1533(2)	0.3997(6)	0.0556(2)	0.0054(6)
O15	8f	0.1078(2)	0.7006(6)	0.926(2)	0.0048(6)
O16	8f	0.0469(2)	0.1739(7)	0.1586(2)	0.0057(6)
O17	8f	0.2963(2)	0.2273(7)	0.3266(2)	0.0074(6)
O18	8f	0.3032(2)	0.9805(7)	0.1311(2)	0.0070(6)
O19	8f	0.9480(2)	0.8566(6)	0.2264(2)	0.0047(6)
O20	8f	0.2120(2)	0.0436(7)	0.313(2)	0.0079(6)
O21	8f	0.2331(2)	0.4802(7)	0.2599(2)	0.0112(6)
O22	8f	0.3647(2)	0.8638(7)	0.3346(2)	0.0070(6)
O23	8f	0.3566(2)	0.5157(7)	0.1364(2)	0.0051(5)

Table 4.1-4: Anisotropic displacement parameters ($U_{ij} / \text{\AA}^2$) for $\alpha\text{-Nd}_2\text{B}_4\text{O}_9$ (space group: $C2/c$)

Atom	U_{11}	U_{22}	U_{33}	U_{23}	U_{13}	U_{12}
Nd1	0.0039(1)	0.0056(1)	0.0046(2)	0.00066(7)	0.00132(8)	0.00099(7)
Nd2	0.0048(1)	0.0045(1)	0.0070(2)	0.00017(7)	0.00131(8)	-0.00050(7)
Nd3	0.005(1)	0.0039(1)	0.0041(2)	0.00006(7)	0.00134(8)	0.00012(7)
Nd4	0.0057(1)	0.0062(1)	0.0065(2)	0.00055(7)	-0.00040(8)	0.00084(7)
Nd5	0.0051(1)	0.0068(2)	0.0107(2)	-0.00104(7)	0.00146(8)	-0.00321(8)
B1	0.005(2)	0.003(2)	0.005(3)	-0.003(2)	0.000(2)	-0.002(2)
B2	0.008(2)	0.006(2)	0.005(3)	-0.003(2)	0.001(2)	-0.001(2)
B3	0.003(2)	0.005(2)	0.003(2)	-0.000(2)	-0.001(2)	0.001(2)
B4	0.004(2)	0.005(2)	0.003(2)	0.001(2)	0.001(2)	-0.001(2)
B5	0.005(2)	0.002(2)	0.006(3)	-0.001(2)	0.001(2)	-0.001(2)
B6	0.005(2)	0.003(2)	0.004(3)	0.003(2)	0.001(2)	0.001(2)
B7	0.006(2)	0.003(2)	0.001(2)	-0.001(2)	-0.001(2)	-0.001(2)
B8	0.009(2)	0.001(2)	0.011(3)	0.003(2)	0.000(2)	-0.002(2)
B9	0.005(2)	0.005(2)	0.004(3)	-0.001(2)	0.000(2)	-0.000(2)
B10	0.003(2)	0.004(2)	0.006(2)	0.001(2)	0.001(2)	0.001(2)
O1	0.005(2)	0.004(2)	0.006(2)	0.000(1)	-0.002(1)	-0.000(1)
O2	0.003(2)	0.004(2)	0.009(2)	-0.001(1)	0.002(2)	-0.002(1)
O3	0.006(2)	0.006(2)	0.005(2)	-0.005(1)	0.001(2)	-0.002(2)
O4	0.006(2)	0.003(2)	0.005(2)	-0.002(1)	0.000(2)	0.000(1)
O5	0.004(2)	0.007(2)	0.006(2)	0.002(1)	0.003(2)	0.002(1)
O6	0.001(2)	0.004(2)	0.003(2)	0	-0.001(2)	0
O7	0.006(2)	0.005(2)	0.005(2)	0.002(1)	0.002(2)	0.001(1)
O8	0.004(2)	0.005(2)	0.005(2)	0.0015(9)	0.000(2)	0.000(1)
O9	0.011(2)	0.004(2)	0.005(2)	-0.002(1)	0.005(2)	-0.001(1)
O10	0.007(2)	0.005(2)	0.004(2)	-0.003(1)	0.002(2)	0.001(1)
O11	0.006(2)	0.003(2)	0.007(2)	-0.000(1)	0.001(2)	0.001(1)
O12	0.005(2)	0.004(2)	0.006(2)	-0.002(1)	-0.001(2)	0.001(1)
O13	0.006(2)	0.003(2)	0.004(2)	-0.000(1)	-0.000(2)	0.000(1)
O14	0.007(2)	0.002(2)	0.007(2)	0.001(1)	-0.000(2)	-0.000(1)
O15	0.005(2)	0.006(2)	0.003(2)	0.000(1)	-0.001(2)	0.001(1)
O16	0.004(2)	0.008(2)	0.005(2)	-0.001(1)	0.001(2)	-0.001(1)
O17	0.006(2)	0.007(2)	0.009(2)	0.002(1)	0.002(2)	-0.002(2)
O18	0.008(2)	0.005(2)	0.008(2)	0.000(1)	-0.001(2)	-0.001(1)
O19	0.003(2)	0.004(2)	0.007(2)	-0.001(1)	0.000(2)	0.001(1)
O20	0.006(2)	0.009(2)	0.011(2)	-0.002(1)	0.004(2)	0.000(1)
O21	0.014(2)	0.01(2)	0.011(2)	0.003(2)	0.003(2)	0.005(2)
O22	0.011(2)	0.002(2)	0.011(2)	0.001(1)	0.008(2)	0.000(2)
O23	0.002(2)	0.007(2)	0.006(2)	0.000(1)	0.001(1)	0.002(1)

4.1.3.3 Crystal Structure Description

Figure 4.1-6 gives a view of the crystal structure of α -Nd₂B₄O₉ along [010]. The structure exhibits a complex network of linked [BO₄]⁵⁻ tetrahedra and is isotopic to the formerly investigated α -RE₂B₄O₉ (RE = Sm–Ho) [137, 138] compounds. The structure of α -RE₂B₄O₉ (RE = Nd, Sm–Ho) is the second example after RE₄B₆O₁₅ (RE = Dy, Ho) [113, 114] of an oxoborate, in which the [BO₄]⁵⁻ tetrahedra are linked by common corners as well as by common edges. For a clearer representation the edge-sharing tetrahedra are drawn as red polyhedra in Figure 4.1-6. The centrosymmetric fundamental building block (FBB) consisting of 18 corner-sharing and two edge-sharing [BO₄]⁵⁻ tetrahedra is shown in Figure 4.1-7. They are linked together by the single outer tetrahedron and the one tetrahedron of the five-membered rings, which is neither linked to the single outer tetrahedron nor is part of one of the six-membered rings. The linkage of the fundamental building blocks gives rise to further rings.

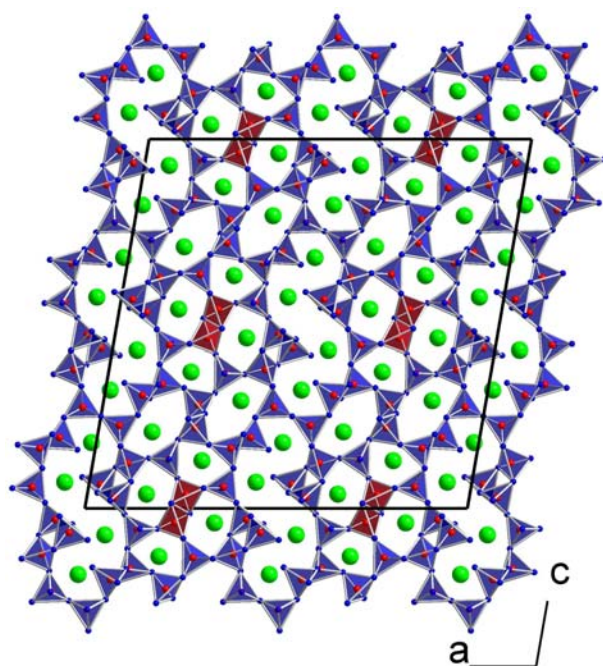


Figure 4.1-6: Crystal structure of α -Nd₂B₄O₉ along [010]. The Nd cations are shown as green spheres; [BO₄]⁵⁻ tetrahedra are given in the polyhedral representation.

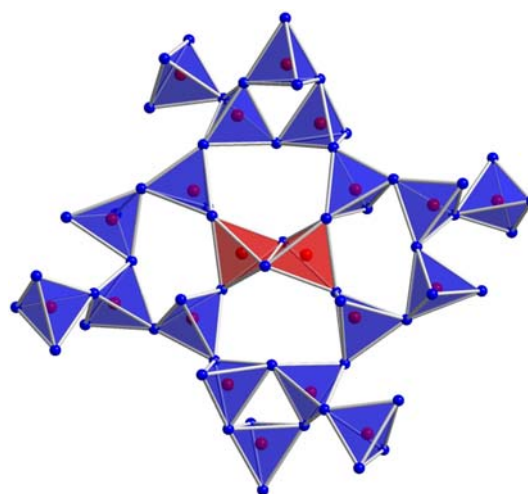


Figure 4.1-7: Fundamental building block of α -Nd₂B₄O₉.

Inside the channels, formed by the ring system, the rare-earth cations are positioned. There exist five crystallographically different neodymium cations, which are coordinated by 8, 9, 10, or 11 oxygen atoms in a distance of 230–300 pm. Further-

more, the Nd–O bond distances are in the same range like for the other isotypic compounds α -RE₂B₄O₉ (RE = Sm–Ho) [137, 138].

The B–O bond lengths vary between 139 and 160 pm. The highest and the lowest bond lengths slightly exceed the typical B–O bond lengths in [BO₄]⁵⁻ tetrahedra [196], and both can be attributed to the tetrahedron B8, which is directly linked to the edge-sharing tetrahedra. But the average B–O bond length with a value of 148.0 pm corresponds well to the known average value of 147.6 pm for oxoborates [196]. The O–B–O angles in the corner-sharing [BO₄]⁵⁻ tetrahedra vary between 98 and 120°. As a rare feature in oxoborate chemistry, the edge-sharing tetrahedra are of special interest. Figure 4.1-8 displays the B–O bond lengths and O–B–O angles inside the building unit of edge-sharing tetrahedra.

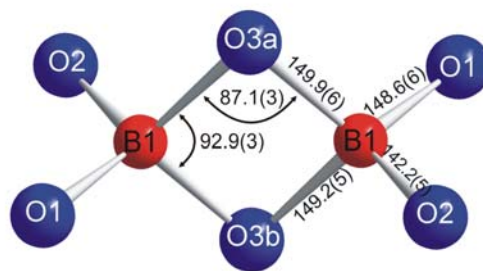


Figure 4.1-8: Interatomic bond lengths /pm and angles /° inside the edge-sharing [BO₄]⁵⁻ tetrahedra of α -Nd₂B₄O₉.

Table 4.1-5: Interatomic distances (pm) calculated with the single crystal lattice parameters of α -Nd₂B₄O₉ (standard deviations in parentheses).

Nd1–O16	234.2(3)	Nd2–O2	237.6(3)	Nd3–O19a	236.4(3)		
Nd1–O11	235.8(3)	Nd2–O14	241.8(3)	Nd3–O8	239.7(3)		
Nd1–O4	244.8(3)	Nd2–O17a	243.1(3)	Nd3–O16a	246.5(3)		
Nd1–O10	248.4(3)	Nd2–O22	247.0(3)	Nd3–O6	247.3(3)		
Nd1–O13	249.4(3)	Nd2–O18	247.0(3)	Nd3–O16b	250.6(3)		
Nd1–O14	255.3(3)	Nd2–O1	251.7(3)	Nd3–O7	251.1(3)		
Nd1–O8a	255.4(3)	Nd2–O17b	260.2(3)	Nd3–O12	255.6(3)		
Nd1–O8b	258.3(3)	Nd2–O20	261.4(3)	Nd3–O19b	256.1(3)		
Nd1–O22	286.1(4)	Nd2–O10	277.2(3)	Nd3–O9	282.3(3)		
		Nd2–O21	300.0(4)	Nd3–O5	298.2(3)		
	Ø 252.0		Ø 256.7		Ø 256.4		
Nd4–O5	230.2(3)	Nd5–O3	233.1(3)				
Nd4–O23	235.4(3)	Nd5–O14	253.0(3)				
Nd4–O18	236.2(3)	Nd5–O15a	253.1(3)				
Nd4–O19	240.7(3)	Nd5–O1	257.5(3)				
Nd4–O9	241.8(3)	Nd5–O4	258.0(3)				
Nd4–O20	244.3(3)	Nd5–O23	261.2(3)				
Nd4–O21	275.4(3)	Nd5–O13	264.7(3)				
Nd4–O12	286.1(3)	Nd5–O15b	272.2(3)				
		Nd5–O7	273.6(3)				
		Nd5–O2	290.6(3)				
		Nd5–O18	297.3(3)				
	Ø 248.8		Ø 264.9				
B1–O2	142.2(5)	B2–O21a	148.9(6)	B3–O11	144.2(5)	B4–O14	141.0(5)
B1–O1	148.6(6)	B2–O17	148.9(6)	B3–O13	146.7(6)	B4–O13	147.5(6)
B1–O3a	149.9(6)	B2–O21b	148.2(6)	B3–O4	146.8(5)	B4–O10	148.9(6)
B1–O3b	149.2(5)	B2–O20	150.8(6)	B3–O15	149.1(6)	B4–O2	151.0(5)
	Ø 147.5		Ø 149.2		Ø 146.7		Ø 147.1
B5–O16	143.5(6)	B6–O9	145.2(5)	B7–O19	140.7(5)	B8–O18	139.4(5)
B5–O5	146.6(6)	B6–O10	145.7(6)	B7–O12	149.9(6)	B8–O23	148.2(5)
B5–O22	150.3(5)	B6–O22	148.4(5)	B7–O6	150.7(5)	B8–O1	152.9(6)
B5–O9	150.7(5)	B6–O17	149.5(5)	B7–O5	151.3(5)	B8–O20	160.2(6)
	Ø 147.8		Ø 147.2		Ø 148.2		Ø 150.2
B9–O8	142.8(5)	B10–O12	145.0(6)				
B9–O11	147.2(5)	B10–O15	145.9(6)				
B9–O4	151.7(6)	B10–O7	148.9(5)				
B9–O7	152.1(6)	B10–O23	150.5(5)				
	Ø 148.5		Ø 147.6				

Table 4.1-6: Interatomic angles (°), calculated with the single crystal lattice parameters of α -Nd₂B₄O₉ (standard deviations in parentheses).

O2- B1-01	112.7(4)	O21b-B2-017	110.1(4)	O11- B3-013	105.3(3)
O2- B1-03b	110.3(3)	O21a-B2-021b	113.2(4)	O11- B3-04	114.6(3)
O1- B1-03b	114.7(3)	O17- B2-021a	107.8(3)	O13- B3-04	113.8(4)
O2- B1-03a	111.9(4)	O21b-B2-020	113.9(3)	O11- B3-015	114.6(4)
O1- B1-03a	112.7(3)	O17- B2-020	99.6(4)	O13- B3-015	103.4(3)
O3a- B1-03b	92.9(3)	O21a-B2-020	111.2(4)	O4- B3-015	104.8(3)
	∅ 109.2		∅ 109.3		∅ 109.4
O14- B4-013	114.2(4)	O16- B5-05	109.0(3)	O9- B6-010	108.3(3)
O14- B4-010	114.0(4)	O16- B5-022	109.8(4)	O9- B6-022	112.2(3)
O13- B4-010	102.5(3)	O5- B5-022	110.3(3)	O10- B6-022	114.8(4)
O14- B4-02	113.0(3)	O16- B5-09	110.5(3)	O9- B6-017	112.5(4)
O13- B4-02	106.1(3)	O5- B5-09	106.3(4)	O10- B6-017	102.8(3)
O10- B4-02	106.0(3)	O22- B5-09	111.0(3)	O22- B6-017	105.9(3)
	∅ 109.3		∅ 109.5		∅ 109.4
O19- B7-012	115.0(4)	O18- B8-023	119.2(4)	O8- B9-011	110.6(3)
O19- B7-06	113.2(4)	O18- B8-01	111.1(4)	O8- B9-04	111.2(3)
O12- B7-06	105.2(3)	O23- B8-01	104.1(3)	O11- B9-04	108.7(4)
O19- B7-05	109.6(3)	O18- B8-020	111.2(4)	O8- B9-07	112.1(4)
O12- B7-05	104.6(3)	O23- B8-020	98.8(3)	O11- B9-07	105.8(3)
O6 - B7-05	108.6(3)	O1- B8-020	111.7(3)	O4- B9-07	108.1(3)
	∅ 109.4		∅ 109.4		∅ 109.4
O12- B10-015	115.2(3)				
O12- B10-07	115.4(3)				
O15- B10-07	108.1(4)				
O12- B10-023	110.1(4)				
O15- B10-023	103.0(3)				
O7 - B10-023	103.8(3)				
	∅ 109.3				

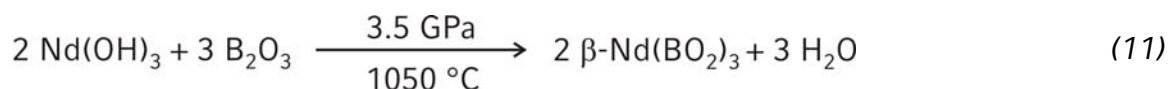
4.1.3.4 Theoretical Calculations

Lattice energy calculations for a finishing verification of the crystal structure were performed with the MAPLE program suite [87-89]. A comparison of the calculated value of α -Nd₂B₄O₉ (58596.59 kJ/mol) with the value derived from the binary oxides (58453.45 kJ/mol) merely revealed a deviation of 0.2%. [1 · Nd₂O₃ [150] (14576.75 kJ/mol) + 2 · B₂O₃-II [198] (21938.35 kJ/mol)]

4.1.4 The *meta*-Borate β -Nd(BO₂)₃

4.1.4.1 Synthesis

For the synthesis of β -Nd(BO₂)₃, an 18/11-assembly with a 3 : 1 molar mixture of B₂O₃ and Nd(OH)₃, obtained by hydrolysis of Nd₂O₃, (equation (11)) was compressed within 80 min to 3.5 GPa and heated to 1050 °C in the following 25 min. Having maintained this temperature for 5 min, the sample was cooled to about 400 °C in further 25 min. Afterwards, the sample was quenched to room temperature. After the decompression of the assembly the recovered octahedral pressure media was broken apart. The sample was carefully separated from the surrounding boron nitride crucible. The compound β -Nd(BO₂)₃ was gained as single-phase crystalline product (yield: ca. 75 mg (18/11) per run). The substance is air- and water-resistant, crystallizing as thin, pale-pink platelets.



4.1.4.2 Crystal Structure Analysis

Small, irregularly shaped single crystals of the compound β -Nd(BO₂)₃ were first investigated by Laue photographs in a Buerger camera. The single crystal intensity data were collected at -73 °C by a STOE IPDS-I diffractometer with graphite monochromatized MoK_α (71.073 pm) radiation. For β -Nd(BO₂)₃, an empirical absorption correction was applied on the basis of psi-scan data. All relevant details of the data collection and evaluation are listed in Table 4.1-7. The atomic parameters of β -Dy(BO₂)₃ [208] were taken as starting values, and the structure was refined by using SHELXL-97 [80] (full-matrix least-squares on F^2) with anisotropic atomic displacement parameters for all atoms except the boron atoms of β -Nd(BO₂)₃, which were refined isotropically. The final difference Fourier syntheses revealed no significant residual peaks. The positional parameters of the refinement are listed in Table 4.1-8. Anisotropic displacement parameters, interatomic distances, and interatomic angles are listed in Table 4.1-9, Table 4.1-10, and Table 4.1-11, respectively.

Table 4.1-7: Crystal data and structure refinement for β -Nd(BO₂)₃

Empirical formula	β -Nd(BO ₂) ₃
Molar mass (g·mol ⁻¹)	272.67
Crystal system	orthorhombic
Space group	<i>Pnma</i> (No. 62)
Powder diffractometer	STOE Stadi P
Radiation	CuK _{α1} ($\lambda = 154.06$ pm)
Powder-diffraction data	
<i>a</i> (pm)	1618.2(4)
<i>b</i> (pm)	748.71(9)
<i>c</i> (pm)	1247.0(3)
Volume (nm ³)	1.5108(7)
Single crystal diffractometer	STOE-IPDS
Radiation	MoK _α ($\lambda = 71.073$ pm)
Single crystal data	
<i>a</i> (pm)	1616.2(3)
<i>b</i> (pm)	747.4(2)
<i>c</i> (pm)	1244.2(3)
Volume (nm ³)	1.5028(5)
Formula units per cell	<i>Z</i> = 16
Temperature (K)	200(2)
Calculated density (g·cm ⁻³)	4.82
Crystal size (mm ³)	0.050 x 0.035 x 0.030
Detector distance (mm)	40
Irradiation / exposure (min)	14
Number of exposures	150
Absorption coefficient (mm ⁻¹)	13.8
F(000)	1968
θ Range (°)	3.2 to 31.0
Range in <i>hkl</i>	±23, ±10, ±18
Total no. reflections	16464
Independent reflections	2550 (<i>R</i> _{int} = 0.0802)
Reflections with <i>I</i> > 2σ(<i>I</i>)	1897 (<i>R</i> _σ = 0.0603)
Data / parameters	2550 / 167
Absorption correction	psi-scan
Transm. ratio (max / min)	0.663 / 0.469
Goodness-of-fit (<i>F</i> ²)	0.927
Final <i>R</i> indices (<i>I</i> > 2σ(<i>I</i>))	<i>R</i> 1 = 0.0420 <i>wR</i> 2 = 0.0965
<i>R</i> Indices (all data)	<i>R</i> 1 = 0.0629 <i>wR</i> 2 = 0.1023
Larg. diff. peak and hole (e·Å ⁻³)	2.86 / -2.93

Table 4.1-8: Atomic coordinates and isotropic equivalent displacement parameters ($U_{\text{eq}} / \text{\AA}^2$) for $\beta\text{-Nd}(\text{BO}_2)_3$ (space group: $Pnma$). U_{eq} is defined as one third of the trace of the orthogonalized U_{ij} tensor.

Atom	Wyckoff Site	x	y	z	U_{eq}
Nd1	4c	0.17059(4)	1/4	0.92991(5)	0.0061(2)
Nd2	4c	0.12034(4)	3/4	0.00416(5)	0.0071(2)
Nd3	4c	0.04745(4)	1/4	0.58560(5)	0.0064(2)
Nd4	4c	0.12564(4)	3/4	0.72233(5)	0.0070(2)
B1	8d	0.2831(6)	0.931(2)	0.8123(7)	0.008(2)
B2	8d	0.9403(5)	0.928(2)	0.6558(7)	0.005(2)
B3	8d	0.0273(6)	0.061(2)	0.8199(8)	0.008(2)
B4	8d	0.1554(5)	0.928(2)	0.4817(7)	0.005(2)
B5	8d	0.1105(5)	0.079(2)	0.1458(7)	0.007(2)
B6	8d	0.2568(5)	0.932(2)	0.1297(7)	0.005(2)
O1	4c	0.1616(6)	3/4	0.5321(7)	0.009(2)
O2	8d	0.2816(4)	0.0558(8)	0.8997(5)	0.006(2)
O3	8d	0.9270(4)	0.0496(8)	0.5665(5)	0.008(2)
O4	8d	0.0500(4)	0.9386(7)	0.1254(5)	0.005(2)
O5	8d	0.3701(4)	0.9274(7)	0.7665(5)	0.007(2)
O6	8d	0.1852(3)	0.0352(7)	0.0813(4)	0.005(2)
O7	4c	0.0596(5)	1/4	0.8012(7)	0.007(2)
O8	4c	0.2256(5)	3/4	0.1363(7)	0.009(2)
O9	8d	0.0930(4)	0.9636(7)	0.8723(5)	0.007(2)
O10	8d	0.1666(4)	0.0584(8)	0.5675(5)	0.007(2)
O11	4c	0.0796(5)	1/4	0.1105(6)	0.004(2)
O12	4c	0.2556(5)	3/4	0.8503(7)	0.006(2)
O13	4c	0.0471(6)	1/4	0.3911(8)	0.009(2)
O14	8d	0.0171(4)	0.9846(8)	0.7087(5)	0.007(2)
O15	8d	0.2249(4)	0.9861(9)	0.7323(5)	0.008(2)

Table 4.1-9: Anisotropic displacement parameters ($U_{ij} / \text{\AA}^2$) for $\beta\text{-Nd}(\text{BO}_2)_3$ (space group: $Pnma$)

Atom	U_{11}	U_{22}	U_{33}	U_{23}	U_{13}	U_{12}
Nd1	0.0059(3)	0.0051(2)	0.0071(3)	0	-0.0002(2)	0
Nd2	0.0085(3)	0.0061(2)	0.0066(3)	0	0.0000(2)	0
Nd3	0.0059(3)	0.0064(3)	0.0070(3)	0	-0.0003(2)	0
Nd4	0.0075(3)	0.0070(2)	0.0066(3)	0	0.0002(2)	0
O1	0.018(5)	0.004(3)	0.005(3)	0	-0.002(3)	0
O2	0.004(2)	0.008(2)	0.005(2)	0.001(2)	-0.002(2)	-0.002(2)
O3	0.009(3)	0.008(2)	0.006(2)	-0.001(2)	-0.002(2)	0.005(2)
O4	0.005(2)	0.003(2)	0.007(2)	0.001(2)	0.001(2)	0.001(2)
O5	0.010(3)	0.004(2)	0.006(2)	0.001(2)	0.002(2)	0.000(2)
O6	0.007(3)	0.001(2)	0.005(2)	0.001(2)	0.003(2)	0.001(2)
O7	0.009(4)	0.001(3)	0.011(4)	0	0.007(3)	0
O8	0.010(4)	0.006(3)	0.011(4)	0	0.006(3)	0
O9	0.010(3)	0.004(2)	0.008(3)	-0.000(2)	0.000(2)	0.001(2)
O10	0.006(2)	0.008(2)	0.007(2)	0.002(2)	-0.002(2)	-0.006(2)
O11	0.002(3)	0.007(3)	0.004(3)	0	0.001(3)	0
O12	0.007(3)	0.004(3)	0.006(3)	0	0.004(3)	0
O13	0.011(4)	0.002(3)	0.014(4)	0	0.002(3)	0
O14	0.008(3)	0.007(2)	0.006(2)	0.001(2)	0.001(2)	0.002(2)
O15	0.009(3)	0.013(3)	0.003(3)	0.001(2)	0.000(2)	0.004(2)

4.1.4.3 Crystal Structure Description

Figure 4.1-9 gives a view of the crystal structure of $\beta\text{-Nd}(\text{BO}_2)_3$, which is composed of strongly corrugated layers of corner sharing $[\text{BO}_4]^{5-}$ tetrahedra. The Fundamental Building Block (FBB) of the B-O structure is built up around two three-coordinate oxygen atoms $\text{O}^{[3]}$, which represent a rare feature for bridging $[\text{BO}_4]^{5-}$ tetrahedra in oxoborate chemistry. Figure 4.1-10 (top) gives a view of the FBB along $[010]$, and Figure 4.1-10 (down) along $[100]$. The FBB-piles are linked to corrugated layers *via* the O(10) atoms. Between the layers, the Nd^{3+} cations are positioned. Each of the four crystallographically different Nd^{3+} cations is coordinated by eight oxygen atoms in distances of 233–296 pm (see Table 4.1-10). The B–O bond lengths in $\beta\text{-Nd}(\text{BO}_2)_3$ are in the range of 142–154 pm (Table 4.1-10), similar to the B–O bond lengths found in the isotypic compounds with $RE = \text{Sm}, \text{Gd-Lu}$. The B–O bond lengths in the $[\text{OB}_3]^{7+}$ groups around the three-coordinate O(5) atoms of the compounds vary in between 149–153 pm. A more detailed description of this structure type can be found in the references [208, 209].

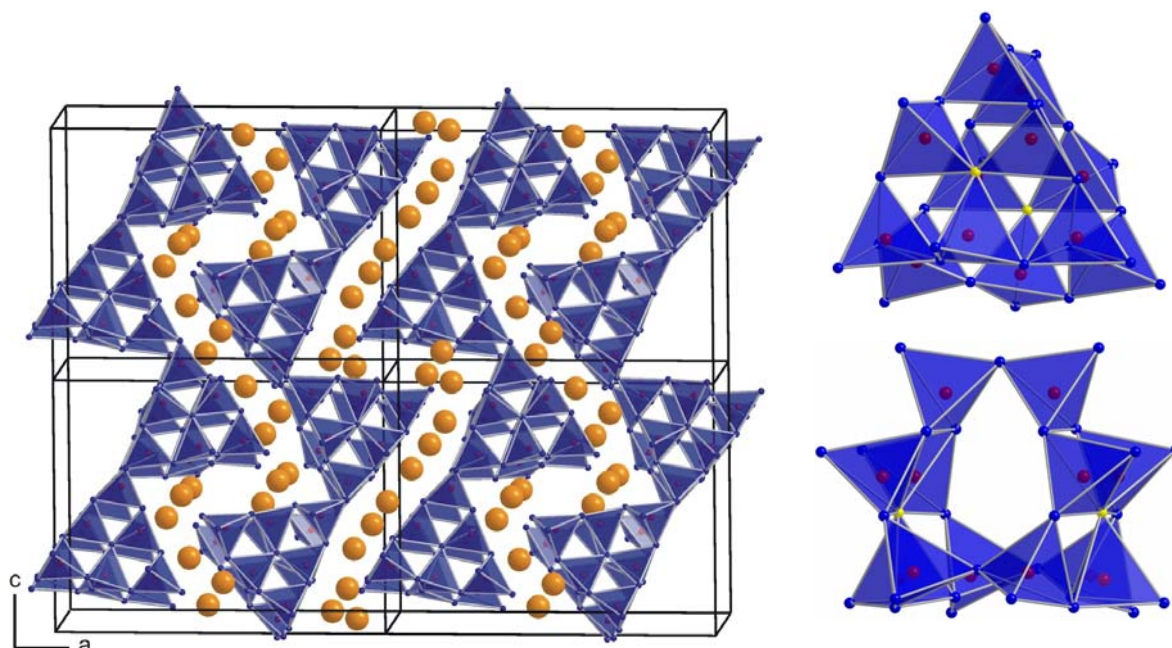


Figure 4.1-9: Crystal structure of the orthorhombic compound β -Nd(BO₂)₃; the rare-earth cations are shown as orange spheres. The [BO₄]⁵⁻ tetrahedra are given in the polyhedral representation.

Figure 4.1-10: FBB of β -Nd(BO₂)₃; top: view along [010], down: view along [100]; O^[3]: yellow spheres

Table 4.1-10: Interatomic distances (pm) calculated with the single crystal lattice parameters of β -Nd(BO₂)₃ (standard deviations in parentheses).

Nd1–O2a	233.8(6)	Nd2–O9a	233.1(6)	Nd3–O10a	241.0(6)	Nd4–O15a	238.8(6)
Nd1–O2b	233.8(6)	Nd2–O9b	233.1(6)	Nd3–O10b	241.0(6)	Nd4–O15b	238.8(6)
Nd1–O7	240.6(9)	Nd2–O4a	235.7(6)	Nd3–O13	242.0(9)	Nd4–O1	243.7(9)
Nd1–O6a	248.6(6)	Nd2–O4b	235.7(6)	Nd3–O3a	246.8(6)	Nd4–O14a	248.6(6)
Nd1–O6b	248.6(6)	Nd2–O8	236.6(9)	Nd3–O3b	246.8(6)	Nd4–O14b	248.6(6)
Nd1–O9a	258.2(6)	Nd2–O6a	256.2(6)	Nd3–O14a	255.4(6)	Nd4–O9a	251.2(6)
Nd1–O9b	258.2(6)	Nd2–O6b	256.2(6)	Nd3–O14b	255.4(6)	Nd4–O9b	251.2(6)
Nd1–O11	268.5(8)	Nd2–O12	290.6(8)	Nd3–O7	268.9(9)	Nd4–O12	263.5(9)
	Ø 248.8		Ø 247.2		Ø 249.7		Ø 248.1
B1–O15	143(2)	B2–O3	145(1)	B3–O4	142(2)		
B1–O2	144(2)	B2–O13	146.5(9)	B3–O9	144(2)		
B1–O12	149.8(9)	B2–O14	147(1)	B3–O14	151(2)		
B1–O5	152(2)	B2–O5	149(1)	B3–O7	153(1)		
	Ø 147.2		Ø 146.9		Ø 147.5		
B4–O2	145(1)	B5–O11	144.4(9)	B6–O15	144(1)		
B4–O10	146(1)	B5–O4	146(1)	B6–O8	145.6(9)		
B4–O3	147(1)	B5–O6	149(1)	B6–O10	146(1)		
B4–O1	147.2(9)	B5–O5	153(1)	B6–O6	152(1)		
	Ø 146.3		Ø 148.1		Ø 146.9		

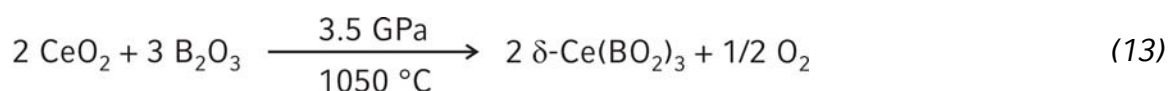
Table 4.1-11: Interatomic angles ($^{\circ}$), calculated with the single crystal lattice parameters of β -Nd(BO₂)₃ (standard deviations in parentheses).

O2– B1–O15	109.1(7)	O3– B2–O13	106.5(7)	O4– B3–O9	115.6(7)
O15– B1–O12	106.6(7)	O3– B2–O14	106.6(6)	O4– B3–O14	110.2(7)
O2– B1–O12	110.1(7)	O13– B2–O14	108.9(7)	O9– B3–O14	107.9(7)
O15– B1–O5	110.6(7)	O3– B2–O5	112.6(6)	O4– B3–O7	111.7(7)
O2– B1–O5	108.1(7)	O13– B2–O5	111.3(7)	O9– B3–O7	106.5(7)
O12– B1–O5	112.3(7)	O14– B2–O5	110.7(6)	O14– B3–O7	104.3(7)
	∅ 109.5		∅ 109.4		∅ 109.4
O2– B4–O10	111.8(6)	O11– B5–O4	110.6(7)	O15– B6–O8	114.6(7)
O3– B4–O2	109.9(7)	O11– B5–O6	108.1(7)	O15– B6–O10	106.0(6)
O3– B4–O10	109.5(6)	O4– B5–O6	107.2(6)	O8– B6–O10	111.5(7)
O2– B4–O1	109.2(7)	O11– B5–O5	113.2(7)	O15– B6–O6	107.1(6)
O10– B4–O1	106.5(7)	O5– B5–O4	106.7(6)	O8– B6–O6	103.4(6)
O3– B4–O1	109.8(7)	O6– B5–O5	110.9(6)	O10– B6–O6	114.4(6)
	∅ 109.5		∅ 109.5		∅ 109.5

4.1.5 The *meta*-Borates δ -RE(BO₂)₃ (RE = La, Ce)

4.1.5.1 Synthesis

The two new rare-earth *meta*-oxoborates δ -RE(BO₂)₃ (RE = La, Ce) were synthesized *via* a high-pressure / high-temperature route. According to equation (12) and (13), the starting materials La(OH)₃ (obtained by hydrolysis of La₂O₃), CeO₂, and B₂O₃ were carefully mixed and filled in a boron nitride crucible of an 18/11-assembly.



In order to synthesize δ -La(BO₂)₃, the reactants were compressed within 2 h to 5.5 GPa and heated up to 1050 °C in the following 10 min. After a period of 15 min at constant temperature, the sample was cooled down to 700 °C within 20 min, followed by quenching to room temperature.

For the synthesis of δ -Ce(BO₂)₃, the crucible was compressed up to 3.5 GPa in 90 min. At constant pressure, the sample was heated up to 1050 °C in 20 min, kept at this temperature for 5 min, and cooled down to 450 °C in another 30 min. Afterwards, the sample was quenched to room temperature by switching off the heating. A decompression period of five hours followed.

δ -RE(BO₂)₃ (RE = La, Ce) could be easily separated from the boron nitride crucible as colourless, air- and water-resistant, crystalline solids.

In order to define the pressure range, in which this δ modification of cerium *meta*-oxoborate can be synthesized, additional experiments under varying pressure conditions and identical temperature were performed. Pressure conditions of 2 GPa led to the synthesis of the cerium *ortho*-oxoborate π -CeBO₃ [139, 140, 193] and a hitherto unknown by-product. Slightly higher pressure of 3 GPa resulted in the formation of a glass. At 5.5 GPa, the synthesis formed the densest modification of the rare-earth *meta*-oxoborates: γ -Ce(BO₂)₃ [191, 210]. Obviously, there exists only a small pressure range (3.5–4.5 GPa), in which δ -Ce(BO₂)₃ can be synthesized successfully.

4.1.5.2 Crystal Structure Analysis

The powder diffraction data of monoclinic δ - $RE(\text{BO}_2)_3$ ($RE = \text{La}, \text{Ce}$) were collected with a STOE Stadi P diffractometer, using monochromatized $\text{CuK}\alpha_1$ radiation. The diffraction patterns of δ - $\text{La}(\text{BO}_2)_3$ and δ - $\text{Ce}(\text{BO}_2)_3$ were indexed with the program ITO [70] on the basis of a monoclinic unit cell. The lattice parameters $a = 424.27(2)$, $b = 1172.17(5)$, $c = 730.40(3)$ pm, and $\beta = 91.15(1)^\circ$ for δ - $\text{La}(\text{BO}_2)_3$ and $a = 423.29(2)$, $b = 1170.97(6)$, $c = 725.87(4)$ pm, and $\beta = 91.30(1)^\circ$ for δ - $\text{Ce}(\text{BO}_2)_3$ (Table 4.1-12) were obtained from least-squares fits of the powder data. Figure 4.1-11 shows the two *meta*-oxoborate powder patterns in comparison with the simulations obtained from single crystal data. The correct indexing of the patterns was confirmed by intensity calculations [66], taking the atomic positions from the structure refinements of δ - $\text{La}(\text{BO}_2)_3$ and δ - $\text{Ce}(\text{BO}_2)_3$, respectively (Table 4.1-13). The lattice parameters determined from the powder and the single crystal data (δ - $\text{La}(\text{BO}_2)_3$: $a = 424.1(1)$, $b = 1171.2(2)$, $c = 731.1(2)$ pm, and $\beta = 91.2(1)^\circ$; δ - $\text{Ce}(\text{BO}_2)_3$: $a = 422.52(8)$, $b = 1169.7(2)$, $c = 725.2(2)$ pm, and $\beta = 91.33(3)^\circ$) do agree well.

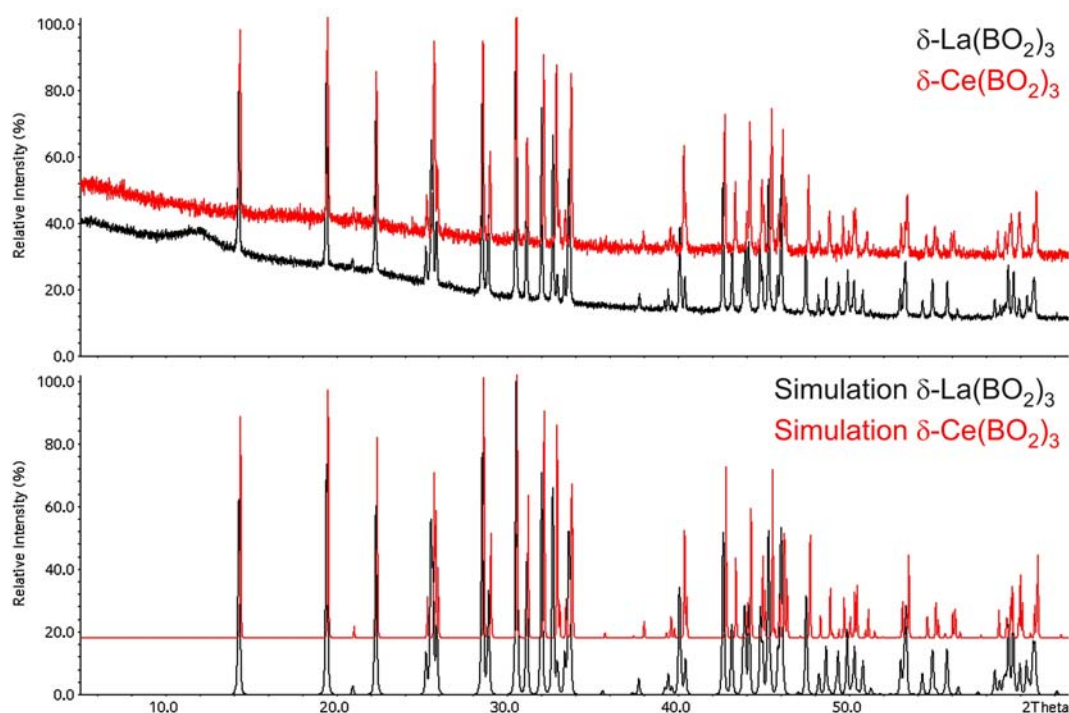


Figure 4.1-11: Recorded powder patterns of δ - $RE(\text{BO}_2)_3$ ($RE = \text{La}, \text{Ce}$) in comparison to the simulation derived from single crystal data.

Small single crystals of the two compounds were isolated by mechanical fragmentation and first investigated by Laue photographs in a Buerger camera. Single crystal intensity data were collected at room temperature from a regularly brick-shaped colorless crystal by use of a STOE IPDS-I detector diffractometer ($\text{MoK}\alpha$ ra-

diation: 71.073 pm). A numerical absorption correction (Habitus [77]) was applied to the intensity data. All relevant information concerning the data collection is listed in Table 4.1-12. According to the systematic extinctions $h0l$ with $l \neq 2n$, $0k0$ with $k \neq 2n$, and $00l$ with $l \neq 2n$, the space group $P2_1/c$ (No. 14) was derived. The starting positional parameters were deduced from an automatic interpretation of *Direct methods* with SHELXS-97 [79]. The final difference Fourier synthesis did not reveal any significant residual peaks in the refinement (see Table 4.1-12). The details of the single crystal structure measurement are shown in Table 4.1-12. Additionally, the positional parameters (Table 4.1-13), anisotropic displacement parameters (Table 4.1-14), interatomic distances, and angles (Table 4.1-15) are listed.

Table 4.1-12: Crystal data and structure refinement for $\delta RE(BO_2)_3$ ($RE = La, Ce$).

Empirical formula	$\delta La(BO_2)_3$	$\delta Ce(BO_2)_3$
Molar mass ($g \cdot mol^{-1}$)	267.34	268.55
Crystal system		monoclinic
Space group		$P2_1/c$ (No. 14)
Powder diffractometer		STOE Stadi P
Radiation		$CuK_{\alpha 1}$ ($\lambda = 154.06$ pm)
Powder-diffraction data		
a (pm)	424.27(2)	423.29(2)
b (pm)	1172.17(5)	1170.97(6)
c (pm)	730.40(3)	725.87(4)
β ($^\circ$)	91.15(1)	91.30(1)
Volume (\AA^3)	363.17(2)	359.69(2)
Single crystal diffractometer		STOE-IPDS
Radiation		MoK_{α} ($\lambda = 71.073$ pm)
Single crystal data		
a (pm)	424.1(1)	422.52(8)
b (pm)	1171.2(2)	1169.7(2)
c (pm)	731.1(2)	725.2(2)
β ($^\circ$)	91.2(1)	91.33(3)
Volume (\AA^3)	363.0(2)	358.3(2)
Formula units per cell		$Z = 4$
Temperature (K)		293(2)
Calculated density ($g \cdot cm^{-3}$)	4.89	4.98
Crystal size (mm^3)	$0.076 \times 0.044 \times 0.024$	$0.12 \times 0.06 \times 0.03$
Detector distance (mm)	45	45
Irradiation / exposure (min)	22	14
Number of exposures	263	200
Absorption coefficient (mm^{-1})	11.7	12.6
$F(000)$	480	484
θ Range ($^\circ$)	3.29 to 31.67	3.31 to 31.57
Range in hkl	$\pm 6, \pm 17, \pm 10$	$\pm 6, -16/17, \pm 10$
Total no. reflections	4960	4583
Independent reflections	1224 ($R_{int} = 0.0555$)	1153 ($R_{int} = 0.0276$)
Reflections with $I > 2\sigma(I)$	959 ($R_{\sigma} = 0.0331$)	946 ($R = 0.0199$)
Data / parameters	1224 / 92	1153 / 92
Absorption correction		numerical (HABITUS [77])
Transm. ratio (max / min)	0.767 / 0.684	0.677 / 0.516
Goodness-of-fit (F^2)	0.955	0.974
Final R indices ($I > 2\sigma(I)$)	$R1 = 0.0157$	$R1 = 0.0176$
	$wR2 = 0.0361$	$wR2 = 0.0430$
R Indices (all data)	$R1 = 0.0248$	$R1 = 0.0237$
	$wR2 = 0.0376$	$wR2 = 0.0445$
Extinction coefficient	0.0028(5)	0.006(1)
Larg. diff. peak and hole ($e \cdot \text{\AA}^{-3}$)	1.4 / -0.75	0.76 / -0.86

Table 4.1-13: Atomic coordinates (*Wyckoff* site 4e for all atoms) and isotropic equivalent displacement parameters ($U_{\text{eq}} / \text{\AA}^2$) for $\delta RE(\text{BO}_2)_3$ ($RE = \text{La, Ce}$) (space group: $P2_1/c$). U_{eq} is defined as one third of the trace of the orthogonalized U_{ij} tensor.

Atom	x	y	z	U_{eq}
La	0.22003(3)	0.37551(2)	0.88153(2)	0.00561(6)
B1	0.6895(7)	0.3780(3)	0.5719(4)	0.0040(4)
B2	0.8045(7)	0.5937(3)	0.6265(4)	0.0052(5)
B3	0.6772(7)	0.3341(3)	0.2111(4)	0.0041(5)
O1	0.8471(4)	0.3731(2)	0.3890(2)	0.0046(3)
O2	0.7925(5)	0.4758(2)	0.6816(3)	0.0055(3)
O3	0.3496(4)	0.3786(2)	0.5461(2)	0.0063(3)
O4	0.7480(5)	0.4100(2)	0.0618(3)	0.0061(3)
O5	0.7812(5)	0.2839(2)	0.6919(3)	0.0063(3)
O6	0.6674(5)	0.6683(2)	0.7645(3)	0.0048(3)
Ce	0.21780(4)	0.37691(2)	0.88148(2)	0.00572(8)
B1	0.6875(8)	0.3785(3)	0.5727(5)	0.0047(5)
B2	0.8060(8)	0.5936(3)	0.6262(4)	0.0046(6)
B3	0.6762(9)	0.3339(3)	0.2115(5)	0.0049(5)
O1	0.8449(5)	0.3737(2)	0.3898(3)	0.0047(4)
O2	0.7928(6)	0.4763(2)	0.6839(3)	0.0059(4)
O3	0.3473(5)	0.3796(2)	0.5481(3)	0.0057(4)
O4	0.7461(6)	0.4096(2)	0.0603(3)	0.0065(4)
O5	0.7817(6)	0.2843(2)	0.6940(3)	0.0071(4)
O6	0.6702(6)	0.6691(2)	0.7643(3)	0.0051(4)

Table 4.1-14: Anisotropic displacement parameters (U_{ij} / \AA^2) for $\delta\text{-RE}(\text{BO}_2)_3$ ($\text{RE} = \text{La}, \text{Ce}$) (space group: $P2_1/c$).

Atom	U_{11}	U_{22}	U_{33}	U_{23}	U_{13}	U_{12}
La	0.00517(8)	0.00673(8)	0.00493(8)	-0.00064(6)	0.00014(5)	0.00067(6)
B1	0.004(2)	0.004(2)	0.004(2)	-0.001(2)	0.0005(8)	-0.000(2)
B2	0.006(2)	0.006(2)	0.004(2)	0.0005(9)	-0.0002(9)	-0.0010(9)
B3	0.005(2)	0.004(2)	0.004(2)	-0.0019(9)	0.0013(9)	-0.0009(9)
O1	0.0034(8)	0.0081(7)	0.0023(7)	-0.0023(7)	0.0009(6)	-0.0007(7)
O2	0.0091(9)	0.0031(8)	0.0044(8)	-0.0004(6)	-0.0006(6)	-0.0003(6)
O3	0.0046(8)	0.0102(7)	0.0041(7)	0.0019(7)	0.0011(6)	-0.0001(7)
O4	0.0080(9)	0.0067(8)	0.0037(8)	0.0008(7)	0.0001(6)	-0.0004(7)
O5	0.0074(9)	0.0036(8)	0.0080(9)	0.0027(7)	-0.0007(7)	-0.0004(6)
O6	0.0031(8)	0.0051(7)	0.0063(8)	-0.0020(7)	0.0010(6)	0.0005(6)
Ce	0.0048(2)	0.0075(1)	0.0048(1)	-0.00061(6)	-0.00014(6)	-0.00059(6)
B1	0.002(2)	0.006(2)	0.006(2)	-0.001(2)	0.000(2)	-0.000(1)
B2	0.005(2)	0.005(2)	0.004(2)	-0.0014(9)	0.000(2)	-0.003(1)
B3	0.004(2)	0.007(2)	0.004(2)	-0.001(1)	0.002(2)	0.001(1)
O1	0.0023(9)	0.0089(9)	0.0029(9)	-0.0017(7)	0.0003(7)	-0.0002(7)
O2	0.01(2)	0.0028(9)	0.0052(9)	0.0009(7)	-0.0009(8)	-0.0001(7)
O3	0.003(1)	0.0087(9)	0.0052(8)	0.0015(7)	0.0009(7)	-0.0006(7)
O4	0.006(2)	0.0059(8)	0.008(1)	0.0029(7)	0.0019(8)	-0.0006(7)
O5	0.006(2)	0.0064(9)	0.009(1)	-0.0001(7)	-0.0024(8)	-0.0017(7)
O6	0.004(1)	0.0065(8)	0.0053(9)	-0.0008(7)	-0.0006(8)	0.0001(7)

4.1.5.3 Crystal Structure Description

The crystal structure of the fourth modification of a rare-earth metal(III) *meta*-oxoborate is exclusively built up from corner-sharing $[\text{BO}_4]^{5-}$ tetrahedra. The linkage of these tetrahedra *via* common corners leads to a network with large ten-membered rings, in which the rare-earth cations are positioned (Figure 4.1-12). In the centre of the unit cell, small four-membered rings are formed by the linkage of four ten-membered rings. Formally, the structure can be divided in corrugated layers of linked $[\text{BO}_4]^{5-}$ tetrahedra, which extend over the *ac* plane. Figure 4.1-13 (centre) gives a view of such a layer, representing the arrangement of the blue tetrahedra of Figure 4.1-12. A closer look into the layer exhibits the main building block $[\text{O}^{[3]}(\text{B}^{[4]}\text{O}_3^{[2]})_3]^{11-}$, consisting of three $[\text{BO}_4]^{5-}$ tetrahedra connected *via* one common oxygen atom $\text{O}^{[3]}$ (yellow spheres in Figure 4.1-13). Along $[100]$, two

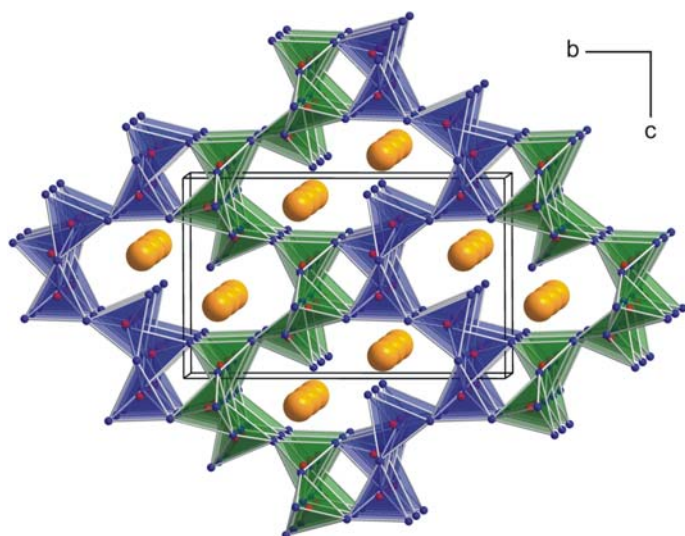


Figure 4.1-12 (top): Crystal structure of δ - $RE(BO_2)_3$ ($RE = La, Ce$) as viewed along [100]; the rare-earth cations are shown as orange spheres. The $[BO_4]^{5-}$ tetrahedra are given in the polyhedral representation.

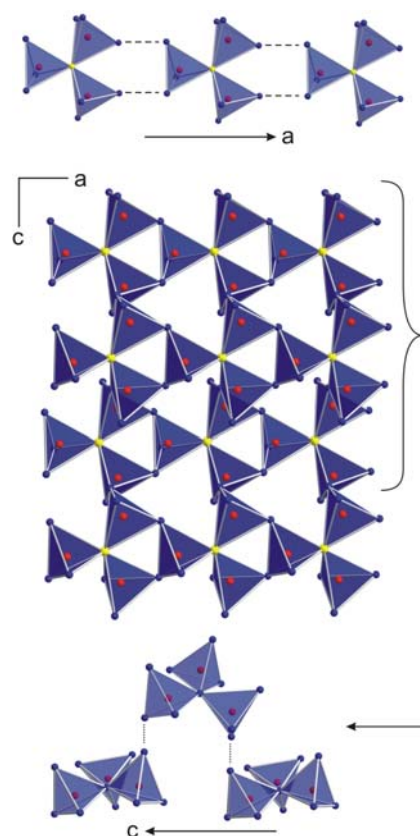


Figure 4.1-13 (right): Corrugated layer in δ - $RE(BO_2)_3$ as viewed along [010] (centre). At the top and the bottom, the linkage of the building blocks is shown along a and c , respectively.

$[BO_4]^{5-}$ tetrahedra of the building block are linked by vertices to one $[BO_4]^{5-}$ tetrahedra of the next building block, forming a three-membered ring (Figure 4.1-13, top). In the bottom part of Figure 4.1-13 one can see the linkage of the building blocks in the c direction, where two building blocks are connected by a third one on top. This leads to the strong corrugation of the layer of interconnected $[O^{[3]}(B^{[4]}O_3^{[2]})_3]^{11-}$ units in the ac plane. Additionally, six-membered rings of $[BO_4]^{5-}$ tetrahedra are formed inside the layer. For a better understanding of the structure, the different corrugated layers in Figure 4.1-12 are shown in different colours of the polyhedra. The linkage of these layers leads to the formation of the four- and ten-membered rings. Figure 4.1-14 gives another view of the structure of δ - $RE(BO_2)_3$ ($RE = La, Ce$) along [001]. From this point of view it is evident that the orientation of the $[BO_4]^{5-}$ tetrahedra changes from layer to layer. Inside the green coloured parts, the tetrahedra point to the top and inside the blue ones, they are pointing top down. The bottom part of Figure 4.1-14 shows an enlargement of the linkage between the two oppositely oriented layers. A separate illustration of the main building block is shown in Figure 4.1-15. Two of the three $[BO_4]^{5-}$ tetrahedra (tetrahedra around B1 and B2) are Q^4 tetrahedra, which share all vertices with other tetrahedra, whereas the remaining one surrounding B3 represents a Q^3 tetrahedron with one terminal oxygen atom.

These unshared oxygen atoms inside the ten-membered rings are oriented and coordinate to the La^{3+} ions.

Due to the smaller size of Ce^{3+} (radius = 148 pm for a 12 fold coordination [141]), in comparison to La^{3+} (radius = 150 pm for coordination number 12 [141]) only short variations of the bond-length occur. Inside of the framework of $[\text{BO}_4]^{5-}$ tetrahedra, the B–O distances of the three crystallographically different $[\text{BO}_4]^{5-}$ groups vary between 144 and 155 pm (Ce: 143–154 pm (Table 4.1-15)). With the exception of the three largest values (La: 150.8, 153.4, and 154.3 pm; Ce: 149.9, 153.1, and 153.4 pm), these B–O separations correspond well with the known average value of 147.6 pm for oxoborates [195, 196]. The three long B–O distances reflect the situation around the threefold coordinated oxygen atom O1 (Fig. 5), possessing significantly longer bonds to boron than two-fold coordinated oxygen atoms. The O–B–O angles within the $[\text{BO}_4]^{5-}$ tetrahedra range from 100 to 117° (Ce: 100–117°) with an average value of 109.4° for both compounds. The B–O–B angles around the threefold coordinated oxygen atom O1 show a perfectly planar arrangement with an angle sum of 360°. Corresponding bond angles for the $\delta\text{-La}(\text{BO}_2)_3$ example are quoted in Figure 4.1-15.

Small differences are found in the coordination distances of the rare-earth ions. For $\delta\text{-La}(\text{BO}_2)_3$, we suggest a 10+2 coordination in the range 245–310 pm (ten atoms) plus two oxygen atoms in a distance of 325 and 331 pm. In the case of δ

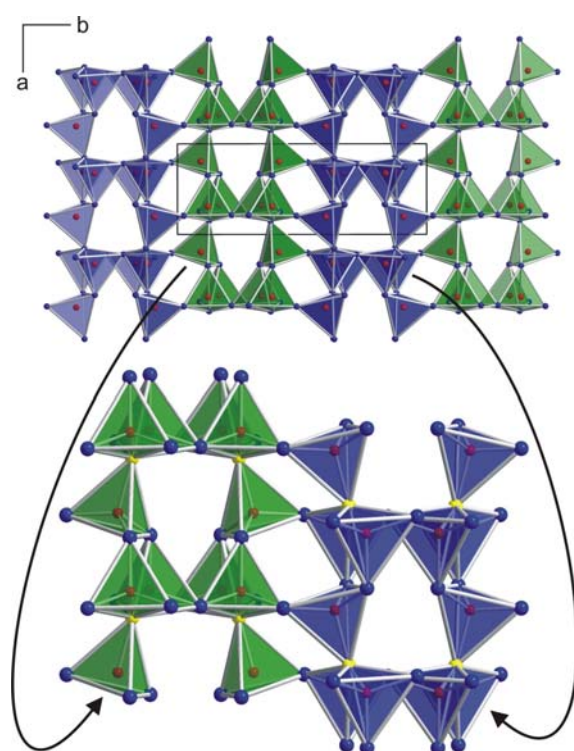


Figure 4.1-14: Top: Crystal structure of $\delta\text{-La}(\text{BO}_2)_3$ as viewed along [001]. Alternating orientation of layers perpendicular to the b axis with $[\text{BO}_4]^{5-}$ tetrahedra tops up and down. Bottom: Enlargement of two different oriented layers with $\text{O}^{[3]}$ atoms marked as yellow spheres in the centre of the building blocks.

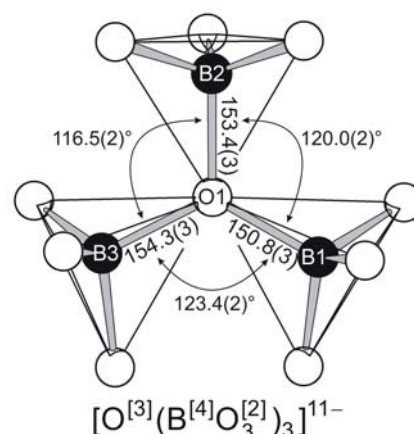


Figure 4.1-15: Illustration of the main building block including distances and angles at the threefold coordinated oxygen atom $\text{O}^{[3]}$ of $\delta\text{-La}(\text{BO}_2)_3$.

Ce(BO₂)₃, we find ten oxygen atoms in the range 243–308 pm plus two oxygen atoms in a distance of 328 and 333 pm, displaying slightly shorter values due to the smaller size of Ce³⁺ in contrast to La³⁺. A detailed discussion concerning the coordination numbers of the rare-earth atoms of the *meta*-borates will be given in Chapter 4.1.7.

Table 4.1-15: Interatomic distances (pm) and angles (°), calculated with the single crystal lattice parameters of δ -RE(BO₂)₃ (RE = La, Ce) (standard deviations in parentheses).

La-04a	245.2(2)	B1-03	145.0(3)	B2-02	144.1(3)	B3-04	144.4(4)
La-03a	252.5(2)	B1-05	145.7(3)	B2-03	144.6(3)	B3-05	145.8(4)
La-05a	253.6(2)	B1-02	145.9(3)	B2-06	146.3(4)	B3-06	147.6(4)
La-04b	255.0(2)	B1-01	150.8(3)	B2-01	153.4(4)	B3-01	154.3(3)
La-02a	258.8(2)						
La-04c	260.6(2)		∅ 146.9		∅ 147.1		∅ 148.0
La-06a	267.2(2)						
La-06b	269.8(2)	05-B1-02	100.9(2)	03-B2-06	106.8(2)	05-B3-01	103.0(2)
La-05b	297.8(2)	03-B1-05	109.6(2)	06-B2-01	107.2(2)	05-B3-06	107.2(2)
La-02b	309.1(2)	03-B1-01	110.0(2)	03-B2-01	107.3(2)	04-B3-06	108.9(2)
La-03b	325.3(2)	03-B1-02	110.7(2)	02-B2-01	107.7(2)	06-B3-01	110.5(2)
La-01	331.4(2)	02-B1-01	112.6(2)	02-B2-06	111.3(2)	04-B3-01	110.8(2)
		05-B1-01	112.8(2)	02-B2-03	116.2(2)	04-B3-05	116.2(2)
	∅ 277.2						
			∅ 109.4		∅ 109.4		∅ 109.4
Ce-04a	243.3(3)	B1-03	144.4(4)	B2-02	143.6(4)	B3-04	144.6(4)
Ce-03a	249.1(2)	B1-05	145.9(4)	B2-03	144.2(4)	B3-05	145.9(4)
Ce-05a	251.0(2)	B1-02	146.3(4)	B2-06	146.3(4)	B3-06	147.8(5)
Ce-04b	253.6(2)	B1-01	149.9(4)	B2-01	153.1(4)	B3-01	153.4(4)
Ce-02a	255.1(2)						
Ce-04c	258.4(2)		∅ 146.6		∅ 146.8		∅ 147.9
Ce-06a	265.6(2)						
Ce-06b	269.7(2)	05-B1-02	100.5(2)	03-B2-06	107.1(3)	05-B3-01	102.9(2)
Ce-05b	297.5(3)	03-B1-05	109.7(3)	06-B2-01	107.1(2)	05-B3-06	107.1(2)
Ce-02b	307.7(2)	03-B1-01	110.6(2)	03-B2-01	107.0(2)	04-B3-06	108.9(2)
Ce-03b	327.6(3)	03-B1-02	110.5(3)	02-B2-01	107.8(3)	06-B3-01	110.4(2)
Ce-01	332.9(3)	02-B1-01	112.4(2)	02-B2-06	111.0(3)	04-B3-01	110.7(2)
		05-B1-01	112.6(2)	02-B2-03	116.4(2)	04-B3-05	116.5(3)
	∅ 276.0						
			∅ 109.4		∅ 109.4		∅ 109.4

4.1.5.4 IR Spectroscopy

Infrared (IR) spectra of δ - $RE(\text{BO}_2)_3$ ($RE = \text{La}, \text{Ce}$) were recorded, scanning a range from 400 to 4000 cm^{-1} . Figure 4.1-16 shows the section 400–2000 cm^{-1} of the infrared spectrum of δ - $\text{Ce}(\text{BO}_2)_3$ in direct comparison to the spectrum of the isotopic *meta*-oxoborate δ - $\text{La}(\text{BO}_2)_3$. The spectrum of δ - $\text{Ce}(\text{BO}_2)_3$ is nearly identical to the spectrum of δ - $\text{La}(\text{BO}_2)_3$ with a slight shift to higher wave numbers. The absorption peaks between 790 and 1150 cm^{-1} are those typical for the tetrahedral borate group $[\text{BO}_4]^{5-}$ as in π - GdBO_3 , π - YBO_3 , or TaBO_4 [142-144]. Between 1300 and 1400 cm^{-1} , around 1200 cm^{-1} , and below 790 cm^{-1} , we observe absorptions, which are normally typical for triangular $[\text{BO}_3]^{3-}$ groups as in λ - LaBO_3 [145], H-LaBO_3 [140], or EuB_2O_4 [146]. Since $[\text{BO}_3]^{3-}$ groups are missing in the investigated compound, the absorptions could be assigned to the corresponding $[\text{OB}_3]^{7+}$ vibrations. Analogous geometric and similar force parameters in the $[\text{OB}_3]^{7+}$ triangle recommend this assignment, as it is valid also for β - ZnB_4O_7 [205], β - CaB_4O_7 [206], $\text{Na}_3[\text{B}_6\text{O}_9(\text{VO}_4)]$ [147], β - $RE(\text{BO}_2)_3$ ($RE = \text{Tb-Lu}$) [208, 209], and γ - $RE(\text{BO}_2)_3$ ($RE = \text{La-Nd}$) [191, 210]. Additionally, the absorption spectra of SrB_4O_7 [200-202] and PbB_4O_7 [203] reported by Weir *et al.* [148], which also exhibit $[\text{OB}_3]^{7+}$ groups next to $[\text{BO}_4]^{5-}$ tetrahedra, show quite similar absorption bands. The existence of three crystallographically independent $[\text{BO}_4]^{5-}$ groups in the structures of δ - $RE(\text{BO}_2)_3$ ($RE = \text{La}, \text{Ce}$), in combination with a single $[\text{OB}_3]^{7+}$ group, makes a detailed assignment of the broad bands more difficult, however.

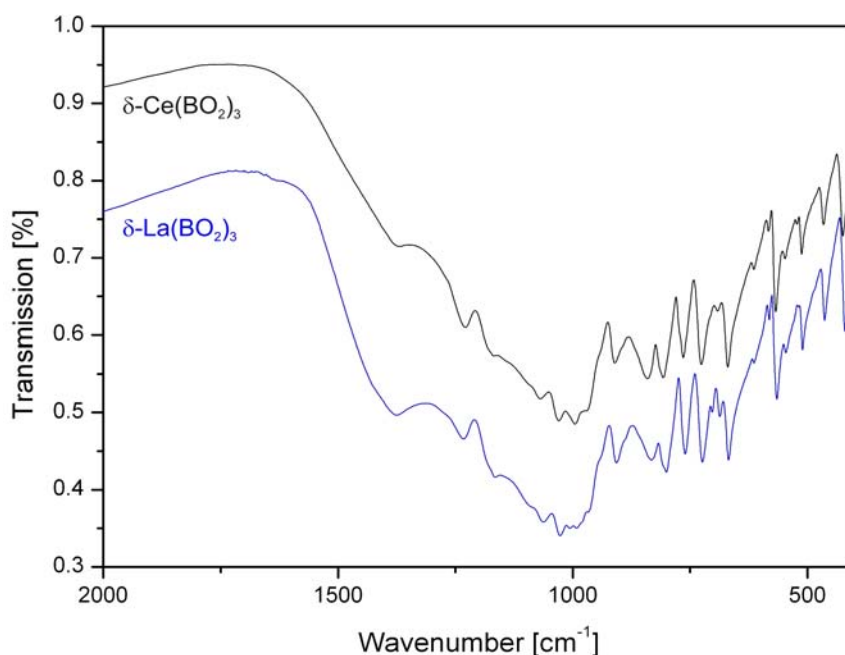


Figure 4.1-16: IR-spectrum of δ - $\text{Ce}(\text{BO}_2)_3$ in comparison to the IR-spectrum of the isotopic compound δ - $\text{La}(\text{BO}_2)_3$.

4.1.5.5 Thermal Behaviour

The *in-situ* temperature-programmed X-ray powder diffraction experiments were performed on a STOE Stadi P powder diffractometer (MoK α radiation) with a computer controlled STOE furnace. The samples were enclosed into a quartz capillary and heated from room temperature up to 500 °C in steps of 100 °C, from 500 to 1100 °C and back to 500 °C in steps of 50 °C. From 500 °C down to room temperature, the temperature shift per range was again 100 °C. At each temperature, a diffraction pattern was recorded over the angular range $5^\circ \leq 2\theta \leq 21^\circ$ (La: $5^\circ \leq 2\theta \leq 22^\circ$). Figure 4.1-18 shows that the reflections of the *meta*-oxoborate δ -Ce(BO $_2$) $_3$ can be detected up to a temperature of 850 °C. Afterwards, a transformation of the high-pressure phase δ -Ce(BO $_2$) $_3$ into the monoclinic normal-pressure *meta*-oxoborate α -Ce(BO $_2$) $_3$ occurs. Additionally, reflections of CeO $_2$ appear in the powder patterns, which result from a partial decomposition of the *meta*-oxoborates into CeO $_2$ and B $_2$ O $_3$.

In the case of δ -La(BO $_2$) $_3$ (Figure 4.1-17) we observed the same transformation into the monoclinic normal-pressure *meta*-oxoborate α -La(BO $_2$) $_3$ at 850 °C. At the maximum temperature of 1100 °C, an additional phase appeared and stayed present down to room temperature. This phase can be attributed to a side reaction of La(BO $_2$) $_3$ with the quartz capillary, resulting in the formation of the *stillwellite* type compound La(BSiO $_5$) [149].

This back-transformation from a high-pressure phase to the monoclinic normal-pressure phase has been already observed in the field of *meta*-oxoborates for the compounds γ -RE(BO $_2$) $_3$ (RE = La–Nd) [210]. In contrast, the orthorhombic β -type *meta*-oxoborates β -RE(BO $_2$) $_3$ of Dy to Lu [208] decompose into the *ortho*-oxoborates μ - and π -REBO $_3$. From these observations, we can infer the metastable character of the high-pressure phases δ -RE(BO $_2$) $_3$ (RE = La, Ce).

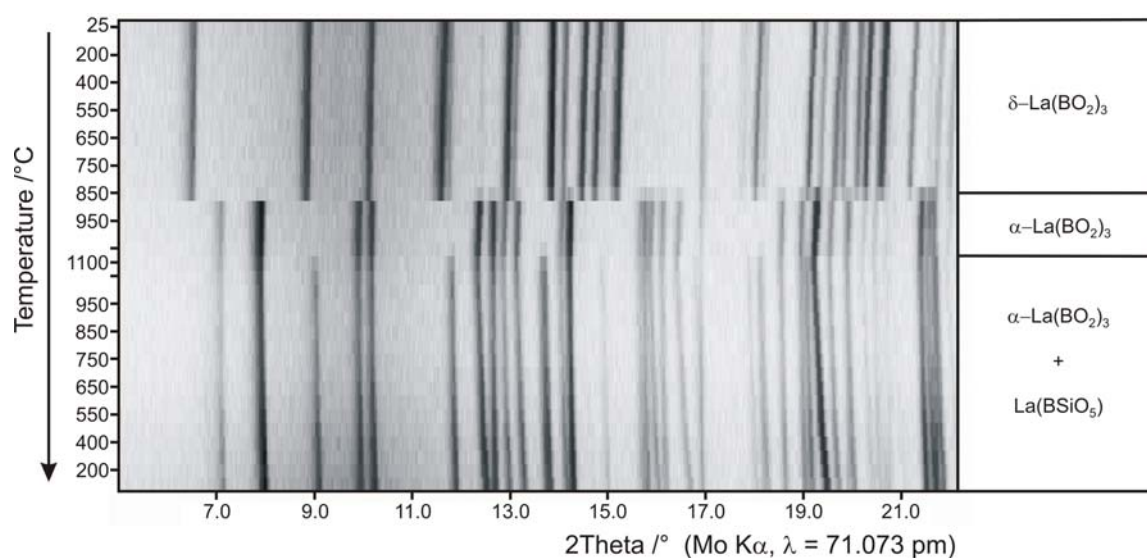


Figure 4.1-17: Temperature-programmed X-ray powder diffraction patterns, following the back-transformation of the metastable high-pressure phase δ -La(BO₂)₃ into the normal-pressure form α -La(BO₂)₃.

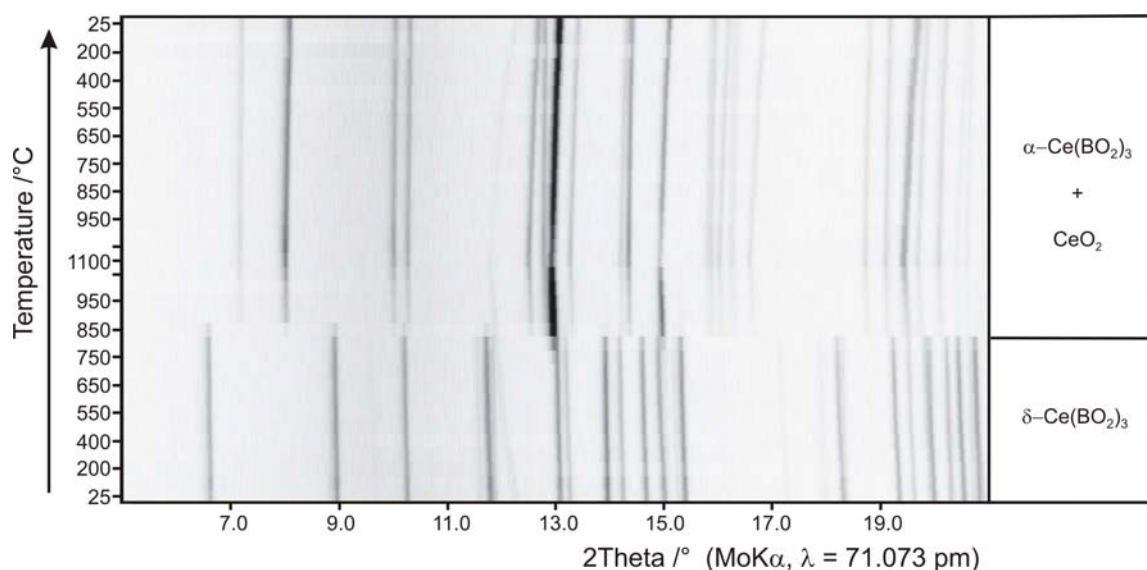


Figure 4.1-18: *In-situ* temperature-programmed X-ray powder diffraction patterns of the transformation of δ -Ce(BO₂)₃ into the normal pressure modification α -Ce(BO₂)₃ at a temperature of 850–900 °C.

4.1.5.6 Theoretical Calculations

For better evidence, bond-valence sums for δ -La(BO₂)₃ and δ -Ce(BO₂)₃ with the bond-length / bond-strength [91-93] and the CHARDI (Charge Distribution in Solids [94, 95]) concept were calculated. Table 4.1-16 displays the results of the formal ionic charges of the atoms, which are in agreement within the limits of both concepts. The only exception concerns the threefold coordinated oxygen atom O1, which shows a reduced value (La: -1.75 (ΣQ), Ce: -1.79 (ΣQ)) in the CHARDI-picture. Similar deviating values are obtained for the threefold coordinated oxygen atoms in

β -Er(BO₂)₃ [208] (O^[3]: -1.96 (ΣV); -1.76 (ΣQ)), β -Tm(BO₂)₃ [208] (O^[3]: -1.98 (ΣV); -1.76 (ΣQ)), γ -Ce(BO₂)₃ [191] (O^[3]: -1.91 (ΣV); -1.62 (ΣQ)), β -CaB₄O₇ [206] (O^[3]: -1.92 (ΣV); -1.77 (ΣQ)), β -HgB₄O₇ [207] (O^[3]: -2.06 (ΣV); -1.83 (ΣQ)), and β -ZnB₄O₇ [205] (O^[3]: -1.83 (ΣV); -1.67 (ΣQ)). It is remarkable that in all these cases deviations are observed only in the CHARDI calculations, whereas the bond-length / bond-strength values correspond well to the expected ones.

Additionally, we have calculated the MAPLE values (Madelung Part of Lattice Energy [87-89]) of δ -La(BO₂)₃ and δ -Ce(BO₂)₃ to compare them with the sum of the MAPLE values for the underlying binary components A-type La₂O₃ [150] and the high-pressure modification B₂O₃-II [198] (0.5 · La₂O₃ (14234 kJ·mol⁻¹) + 1.5 · B₂O₃-II (21938 kJ·mol⁻¹)). The deviation of the calculated value (40158 kJ·mol⁻¹) for δ -La(BO₂)₃ amounts to +0.3% in comparison to the MAPLE value obtained from the sum of the binary sesqui-oxides (40024 kJ·mol⁻¹). In the case of δ -Ce(BO₂)₃ the deviation of the calculated MAPLE value (40252 kJ·mol⁻¹) amounts to +0.7% (0.5 · Ce₂O₃ (14150 kJ·mol⁻¹) [52] + 1.5 · B₂O₃-II (21938 kJ·mol⁻¹) [53] → δ -Ce(BO₂)₃ (39982 kJ·mol⁻¹)).

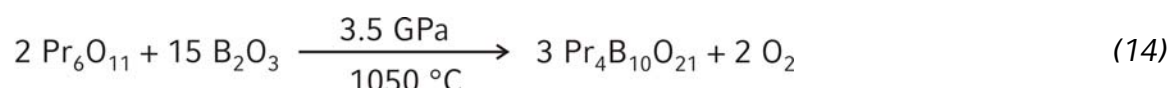
Table 4.1-16: Charge distribution in δ -La(BO₂)₃ and δ -Ce(BO₂)₃, calculated with the bond-length / bond-strength (ΣV) and the CHARDI concept (ΣQ).

δ -La(BO ₂) ₃		La	B1	B2	B3	
ΣQ		+2.93	+3.04	+3.03	+3.00	
ΣV		+2.72	+3.08	+3.07	+2.99	
	O1	O2	O3	O4	O5	O6
ΣQ	-1.75	-2.02	-2.04	-2.04	-2.09	-2.07
ΣV	-2.01	-2.02	-1.98	-1.88	-2.04	-2.00
δ -Ce(BO ₂) ₃		Ce	B1	B2	B3	
ΣQ		+2.94	+3.02	+3.02	+3.02	
ΣV		+2.89	+3.10	+3.09	+3.00	
	O1	O2	O3	O4	O5	O6
ΣQ	-1.79	-2.03	-2.06	-2.03	-2.07	-2.02
ΣV	-2.04	-2.02	-2.03	-1.90	-2.04	-1.99

4.1.6 The Oxoborate $\text{Pr}_4\text{B}_{10}\text{O}_{21}$

4.1.6.1 Synthesis

According to equation (14), $\text{Pr}_4\text{B}_{10}\text{O}_{21}$ was prepared *via* a high-pressure / high-temperature synthesis from Pr_6O_{11} and B_2O_3 .



A stoichiometric mixture of the oxides (ca. 50 mg) was ground and placed into a boron nitride crucible of an 18/11-assembly, which was compressed up to 3.5 GPa during 90 min. The sample was heated to 1050 °C in 20 min. After 5 min at 1050 °C, the sample was cooled down to 450 °C in 30 min, followed by quenching to room temperature. The decompression of the assembly required five hours. The recovered experimental octahedron was opened and the sample carefully separated from the surrounding boron nitride crucible, yielding the light-green, crystalline, nearly phase pure compound $\text{Pr}_4\text{B}_{10}\text{O}_{21}$.

4.1.6.2 Crystal Structure Analysis

The powder diffraction pattern was obtained in transmission geometry from a flat sample of $\text{Pr}_4\text{B}_{10}\text{O}_{21}$, using a STOE Stadi P powder diffractometer with monochromatized CuK_α radiation. The diffraction pattern was indexed with the program ITO [70] on the basis of a monoclinic unit cell. The calculation of the lattice parameters (Table 4.1-17) was founded on least-squares fits of the powder data. The correct indexing of the patterns of $\text{Pr}_4\text{B}_{10}\text{O}_{21}$ was confirmed by intensity calculations, employing the atomic positions of the structure refinement [66]. The lattice parameters, deduced from the powder data and the single crystal data, matched well. Figure 4.1-19 shows the powder pattern of $\text{Pr}_4\text{B}_{10}\text{O}_{21}$ in comparison to the simulation.

Small single crystals of $\text{Pr}_4\text{B}_{10}\text{O}_{21}$ were isolated by mechanical fragmentation and examined by Laue photographs on a Buerger precession camera. Single crystal intensity data of $\text{Pr}_4\text{B}_{10}\text{O}_{21}$ were measured with a STOE-IPDS [MoK_α radiation (71.073 pm)]. The data were subjected to a numerical absorption correction (HABITUS [77]). According to the systematic extinctions $h0l$ with $h + l \neq 2n$, $0k0$ with $k \neq 2n$, $h00$ with $h \neq 2n$, and $00l$ with $l \neq 2n$, the monoclinic space group $P2_1/n$

(Nr. 14) was derived. The structure solution and the parameter refinement (full-matrix least squares against F^2) were carried out *via Direct methods*, making use of the SHELX-97 software suite [79, 80]. The final difference Fourier syntheses revealed no significant residual peaks. All relevant crystallographic data and details of the data collection are given in Table 4.1-17. The positional parameters, anisotropic displacement parameters, and interatomic distances are listed in Table 4.1-18, Table 4.1-19, and Table 4.1-20.

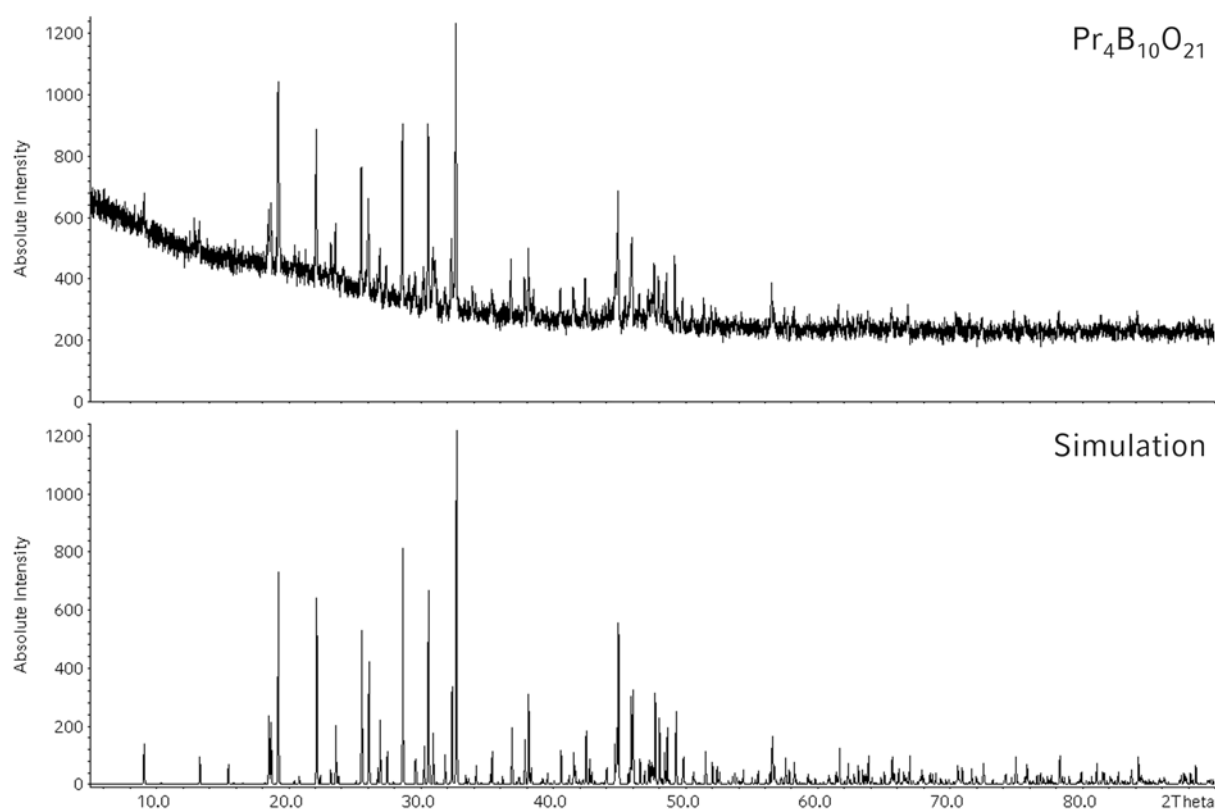


Figure 4.1-19: Recorded powder patterns of $\text{Pr}_4\text{B}_{10}\text{O}_{21}$ in comparison to the simulation derived from single crystal data.

Table 4.1-17: Crystal data and structure refinement for Pr₄B₁₀O₂₁

Empirical formula	Pr ₄ B ₁₀ O ₂₁
Molar mass (g·mol ⁻¹)	1007.74
Crystal system	monoclinic
Space group	<i>P</i> 2 ₁ / <i>c</i> (No. 14)
Powder diffractometer	STOE Stadi P
Radiation	CuK _{α1} (λ = 154.06 pm)
Powder-diffraction data	
<i>a</i> (pm)	711.2(2)
<i>b</i> (pm)	1951.9(3)
<i>c</i> (pm)	952.1(2)
β (°)	93.20(2)
Volume (Å ³)	1319.7(3)
Single crystal diffractometer	STOE-IPDS
Radiation	MoK _α (λ = 71.073 pm)
Single crystal data	
<i>a</i> (pm)	710.2(2)
<i>b</i> (pm)	1948.8(4)
<i>c</i> (pm)	951.6(2)
β (°)	93.27(3)
Volume (Å ³)	1314.9(5)
Formula units per cell	<i>Z</i> = 4
Temperature (K)	293(2)
Calculated density (g·cm ⁻³)	5.09
Crystal size (mm ³)	0.082 x 0.072 x 0.045
Detector distance (mm)	40
Irradiation / exposure (min)	10
Number of exposures	180
Absorption coefficient (mm ⁻¹)	14.7
F(000)	1816
θ Range (°)	3.49 to 30.00
Range in <i>hkl</i>	±9, ±27, ±13
Total no. reflections	13476
Independent reflections	3808 (<i>R</i> _{int} = 0.0326)
Reflections with <i>I</i> > 2σ(<i>I</i>)	3143 (<i>R</i> _σ = 0.0249)
Data / parameters	3808 / 317
Absorption correction	numerical (HABITUS [77])
Transm. ratio (max / min)	0.528 / 0.380
Goodness-of-fit (<i>F</i> ²)	0.981
Final <i>R</i> indices (<i>I</i> > 2σ(<i>I</i>))	<i>R</i> 1 = 0.0219 <i>wR</i> 2 = 0.0540
<i>R</i> Indices (all data)	<i>R</i> 1 = 0.0302 <i>wR</i> 2 = 0.0558
Extinction coefficient	0.00130(8)
Larg. diff. peak and hole (e·Å ⁻³)	1.52 / -1.33

Table 4.1-18: Atomic coordinates (Wyckoff site 4e for all atoms) and isotropic equivalent displacement parameters ($U_{\text{eq}} / \text{\AA}^2$) for $\text{Pr}_4\text{B}_{10}\text{O}_{21}$ (space group: $P2_1/n$). U_{eq} is defined as one third of the trace of the orthogonalized U_{ij} tensor.

Atom	x	y	z	U_{eq}
Pr1	0.37346(3)	0.19987(2)	0.83901(2)	0.00979(6)
Pr2	0.89592(3)	0.29474(2)	0.82460(2)	0.00943(7)
Pr3	0.35865(3)	0.41705(1)	0.83722(2)	0.00849(6)
Pr4	0.84521(3)	0.08081(1)	0.84440(2)	0.00927(7)
O1	0.2975(4)	0.5180(2)	0.9721(3)	0.0083(5)
O2	0.6293(4)	0.1588(2)	0.0183(3)	0.0093(5)
O3	0.3520(4)	0.1187(2)	0.6331(3)	0.0080(5)
O4	0.1273(4)	0.3429(2)	0.0180(3)	0.0088(5)
O5	0.8732(4)	0.3857(2)	0.6440(3)	0.0084(5)
O6	0.0520(4)	0.1778(2)	0.8969(3)	0.0099(5)
O7	0.1641(4)	0.0417(2)	0.7727(3)	0.0078(5)
O8	0.4543(4)	0.0718(2)	0.9146(3)	0.0091(5)
O9	0.5734(4)	0.3129(2)	0.9052(3)	0.0109(5)
O10	0.9560(4)	0.4288(2)	0.9141(3)	0.0090(5)
O11	0.6933(4)	0.1880(2)	0.7579(3)	0.0085(5)
O12	0.2156(4)	0.3159(2)	0.7641(3)	0.0091(5)
O13	0.1349(4)	0.4519(2)	0.1397(3)	0.0094(5)
O14	0.8911(4)	0.2346(2)	0.0785(3)	0.0102(5)
O15	0.3298(4)	0.5398(2)	0.2247(3)	0.0082(5)
O16	0.5373(4)	0.3749(2)	0.6262(3)	0.0104(5)
O17	0.0141(4)	0.1134(2)	0.5991(3)	0.0102(5)
O18	0.6868(4)	0.4740(2)	0.5260(3)	0.0093(5)
O19	0.7262(4)	0.2697(2)	0.5814(3)	0.0115(5)
O20	0.0886(4)	0.2296(2)	0.6396(3)	0.0119(5)
O21	0.1583(4)	0.4521(2)	0.6277(3)	0.0110(5)
B1	0.0155(6)	0.4058(2)	0.0557(4)	0.0077(7)
B2	0.8060(6)	0.4786(2)	0.8967(4)	0.0081(7)
B3	0.0251(6)	0.4055(2)	0.5560(4)	0.0076(7)
B4	0.2968(6)	0.0239(2)	0.8986(4)	0.0068(7)
B5	0.6982(6)	0.4230(2)	0.6386(4)	0.0079(7)
B6	0.5454(6)	0.3126(2)	0.5460(5)	0.0096(8)
B7	0.7089(6)	0.2070(2)	0.1204(5)	0.0092(7)
B8	0.1941(6)	0.0715(2)	0.6332(4)	0.0069(7)
B9	0.5637(6)	0.3224(2)	0.0456(5)	0.0099(7)
B10	0.6814(6)	0.2028(2)	0.6201(5)	0.0103(7)

Table 4.1-19: Anisotropic displacement parameters (U_{ij} / Å²) for Pr₄B₁₀O₂₁ (space group: $P2_1/n$).

Atom	U_{11}	U_{22}	U_{33}	U_{23}	U_{13}	U_{12}
Pr1	0.0092(1)	0.0104(1)	0.0099(2)	-0.00077(8)	0.00110(7)	0.00051(7)
Pr2	0.0090(1)	0.0105(2)	0.0088(1)	0.00052(7)	0.00060(7)	-0.00046(7)
Pr3	0.0102(1)	0.0072(1)	0.0081(1)	-0.00064(7)	0.00046(7)	-0.00012(6)
Pr4	0.0102(1)	0.0074(1)	0.0101(1)	0.00003(7)	0.00039(7)	0.00012(7)
O1	0.011(2)	0.008(2)	0.006 (2)	0.0026(9)	0.0002(9)	0.0025(9)
O2	0.013(2)	0.007(2)	0.008(2)	0.000(2)	0.001(1)	-0.000(2)
O3	0.007(2)	0.007(2)	0.010(2)	-0.001(2)	0.0023(9)	-0.001(2)
O4	0.011(2)	0.007(2)	0.008(2)	-0.000(2)	0.001(1)	0.000(2)
O5	0.01(2)	0.009(2)	0.007(2)	0.003(1)	0.0010(9)	0.0018(9)
O6	0.011(2)	0.01(2)	0.009(2)	0.001(1)	0.003(1)	0.000(1)
O7	0.007(2)	0.009(2)	0.008(2)	0.0025(9)	-0.0016(9)	-0.0019(9)
O8	0.010(2)	0.01(2)	0.007(2)	-0.000(2)	0.001(1)	-0.002(1)
O9	0.010(2)	0.012(2)	0.010(2)	0.000(2)	0.001(1)	0.0013(9)
O10	0.01(2)	0.009(2)	0.008(2)	0.001(1)	0.001(1)	0.0021(9)
O11	0.009(2)	0.008(2)	0.008(2)	-0.0003(9)	-0.001(1)	0.0005(9)
O12	0.01(2)	0.009(2)	0.008(2)	0.0000(9)	0.001(1)	-0.0002(9)
O13	0.009(2)	0.008(2)	0.011(2)	0.001(1)	-0.003(1)	-0.0032(9)
O14	0.01(2)	0.009(2)	0.012(2)	0.001(1)	0.000(2)	0.0008(9)
O15	0.008(2)	0.008(2)	0.008(2)	-0.0013(9)	-0.0005(9)	0.0010(9)
O16	0.007(2)	0.01(2)	0.014(2)	-0.005(1)	0.003(1)	-0.0024(9)
O17	0.009(2)	0.008(2)	0.013(2)	0.003(1)	0.002(1)	0.0000(9)
O18	0.011(2)	0.010(2)	0.006(2)	0.003(1)	0.0026(9)	0.004(1)
O19	0.010(2)	0.010(2)	0.014(2)	0.002(1)	0.002(1)	-0.000(2)
O20	0.010(2)	0.013(2)	0.013(2)	-0.001(2)	0.003(1)	-0.002(1)
O21	0.012(2)	0.007(2)	0.014(2)	0.002(1)	-0.005(1)	-0.001(1)
B1	0.007(2)	0.009(2)	0.007(2)	-0.002(2)	0.003(2)	-0.000(2)
B2	0.011(2)	0.006(2)	0.007(2)	-0.001(2)	0.001(2)	-0.003(2)
B3	0.008(2)	0.007(2)	0.007(2)	-0.001(2)	0.000(2)	-0.000(2)
B4	0.008(2)	0.008(2)	0.004(2)	-0.002(2)	-0.001 (2)	0.003(2)
B5	0.007(2)	0.011(2)	0.006(2)	0.001(2)	-0.000(2)	-0.003(2)
B6	0.012(2)	0.008(2)	0.009(2)	0.001(2)	-0.000(2)	-0.001(2)
B7	0.008(2)	0.013(2)	0.007(2)	0.002(2)	0.002(2)	0.000(2)
B8	0.006(2)	0.011(2)	0.004(2)	-0.001(2)	-0.001(2)	-0.002(2)
B9	0.007(2)	0.011(2)	0.012(2)	-0.002(2)	-0.003(2)	0.001(2)
B10	0.01(2)	0.009(2)	0.012(2)	-0.000(2)	-0.000(2)	0.001(2)

4.1.6.3 Crystal Structure Description

Figure 4.1-20 shows the crystal structure of $\text{Pr}_4\text{B}_{10}\text{O}_{21}$ along [100]. The structure is composed of trigonal $[\text{BO}_3]^{3-}$ and tetrahedral $[\text{BO}_4]^{5-}$ groups, which are linked to a highly condensed network. For a better understanding of the structure, the $[\text{BO}_4]^{5-}$ tetrahedra in Figure 4.1-20 are partitioned in corrugated layers of blue tetrahedra and orange tetrahedra. These layers are connected *via* corner sharing $[\text{BO}_4]^{5-}$ tetrahedra. Figure 4.1-21 clearly reveals the linkage of $[\text{BO}_3]^{3-}$ and $[\text{BO}_4]^{5-}$ groups inside the layer. In the bottom of Figure 4.1-21 the two building blocks of this layer appear. The first building block (Figure 4.1-21, bottom left) consists of 10 tetrahedra, forming a central four membered ring and two three-membered rings. Additionally, four $[\text{BO}_4]^{5-}$ tetrahedra are added to the outer rings (two on each side). The second building block (Figure 4.1-21, bottom right) is built up from six $[\text{BO}_4]^{5-}$ tetrahedra and four $[\text{BO}_3]^{3-}$ groups. Similar to the first building block, the $[\text{BO}_4]^{5-}$ tetrahedra form a central four-membered ring with two three-membered rings on either side. In contrast, the four $[\text{BO}_4]^{5-}$ tetrahedra added to the outer rings in the first building block are substituted by four trigonal $[\text{BO}_3]^{3-}$ groups. The linkage of these two building blocks *via* the outer $[\text{BO}_4]^{5-}$ tetrahedra and $[\text{BO}_3]^{3-}$ groups constructs the entire layer.

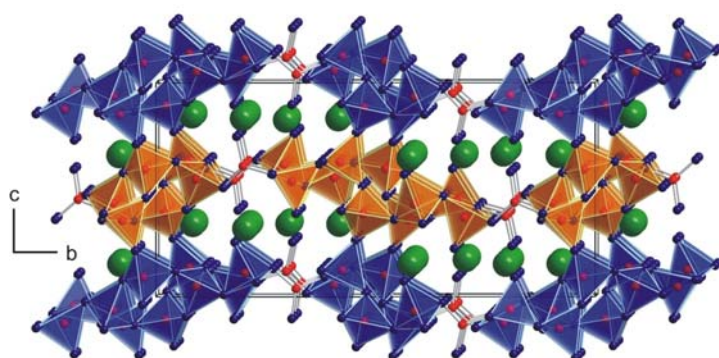


Figure 4.1-20: Crystal structure of $\text{Pr}_4\text{B}_{10}\text{O}_{21}$, view along [100]. The Pr cations are shown as green spheres, B as red spheres, and O as blue spheres.

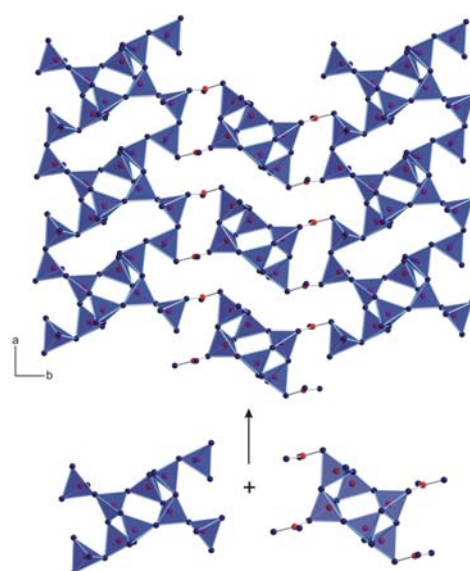


Figure 4.1-21 (right): Crystal structure of $\text{Pr}_4\text{B}_{10}\text{O}_{21}$, showing a layer of $[\text{BO}_3]^{3-}$ groups and $[\text{BO}_4]^{5-}$ tetrahedra along [001].

$\text{Pr}_4\text{B}_{10}\text{O}_{21}$ contains ten crystallographically distinguishable boron atoms. Eight of them possess a tetrahedral and two a trigonal oxygen coordination sphere. Inside the tetrahedra, the B–O distances vary between 143–156 pm (Table 4.1-20) with a

mean value of 147.5 pm, which corresponds well with the known average value of 147.6 pm for boron-oxygen bond lengths in $[\text{BO}_4]^{5-}$ tetrahedra [195, 196]. The trigonal groups show boron-oxygen distances of 134 to 140 pm with a mean value of 136.8 pm, which agrees with the known value of 137.0 pm for oxoborates within $[\text{BO}_3]^{3-}$ groups [151, 196]. The angles O-B-O inside the $[\text{BO}_4]^{5-}$ groups range between 97.3 and 117.2°, at a mean value of 109.4°. The angles inside the trigonal $[\text{BO}_3]^{3-}$ groups exhibit values of 116.9 to 124.0° at a mean value of 120°.

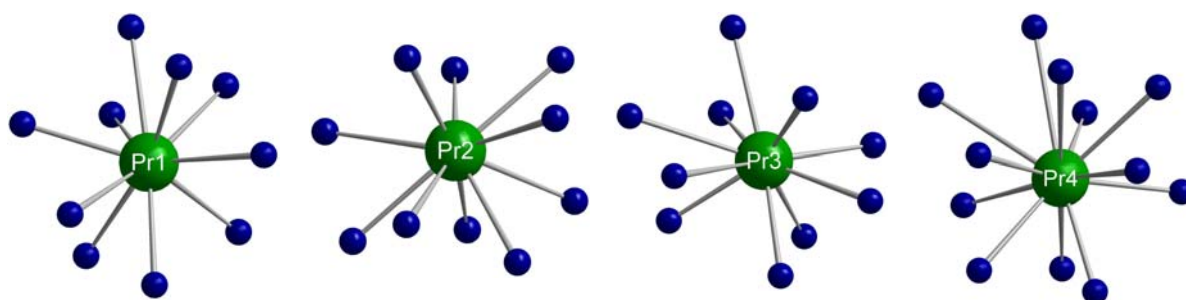


Figure 4.1-22: Coordination spheres of the praseodymium ions in $\text{Pr}_4\text{B}_{10}\text{O}_{21}$.

The Pr^{3+} ions are positioned in channels between the layers (Figure 4.1-20). Figure 4.1-22 provides a view of the coordination spheres of the four Pr^{3+} ions in $\text{Pr}_4\text{B}_{10}\text{O}_{21}$. The ions Pr1, Pr2, and Pr3 are coordinated by ten oxygen atoms in the ranges 242–280 pm, 241–278 pm, and 231–301 pm, respectively (Table 4.1-20). These values fit well to the coordination polyhedra of the Pr^{3+} ion in the praseodymium *meta*-borate $\text{Pr}(\text{BO}_2)_3$, where the Pr^{3+} ions are also coordinated by ten oxygen atoms with Pr–O distances ranging from 239 to 281 pm [152]. The fourth praseodymium ion (Pr4) in $\text{Pr}_4\text{B}_{10}\text{O}_{21}$ exhibits a larger coordination number of 12 with Pr–O distances of 243–314 pm. A calculation of the bond-valence sums [91, 92] for the praseodymium ions in $\text{Pr}_4\text{B}_{10}\text{O}_{21}$ revealed values of +2.96 (Pr1), +3.14 (Pr2), +3.23 (Pr3), and +3.07 (Pr4), which fit well to the formal ionic charges of the atoms.

Table 4.1-20: Interatomic distances (pm) calculated with the single crystal lattice parameters of Pr₄B₁₀O₂₁ (standard deviations in parentheses).

Pr1-O6	241.7(3)	Pr2-O12	241.0(3)	Pr3-O12	230.6(3)	Pr4-O6	242.8(3)
Pr1-O11	245.1(3)	Pr2-O5	246.7(3)	Pr3-O1	240.2(3)	Pr4-O18a	243.7(3)
Pr1-O3	251.6(3)	Pr2-O9	248.2(3)	Pr3-O15	247.0(3)	Pr4-O13	247.0(3)
Pr1-O2	254.9(3)	Pr2-O4	257.3(3)	Pr3-O21	247.8(3)	Pr4-O11	247.1(3)
Pr1-O12	260.6(3)	Pr2-O11	258.7(3)	Pr3-O16	257.0(3)	Pr4-O7	252.0(3)
Pr1-O8	265.2(3)	Pr2-O19	259.4(3)	Pr3-O9	259.9(3)	Pr4-O15	261.2(3)
Pr1-O19	265.4(3)	Pr2-O6	261.0(3)	Pr3-O7	264.7(3)	Pr4-O17	275.9(3)
Pr1-O9	267.6(3)	Pr2-O20	261.9(3)	Pr3-O17	273.3(3)	Pr4-O2	277.3(3)
Pr1-O20	275.6(3)	Pr2-O14	268.8(3)	Pr3-O4	284.0(3)	Pr4-O8	289.8(3)
Pr1-O14	279.8(3)	Pr2-O10	277.4(3)	Pr3-O10	300.1(3)	Pr4-O16	306.3(3)
						Pr4-O18b	308.8(3)
						Pr4-O21	313.8(3)
	Ø260.7		Ø258.0		Ø260.5		Ø272.1
B1-O13	144.6(5)	B2-O10	144.3(5)	B3-O21	145.3(5)	B4-O8	145.8(5)
B1-O10	145.9(5)	B2-O13	146.4(5)	B3-O5	145.6(5)	B4-O21	146.1(5)
B1-O3	148.9(5)	B2-O1	148.7(5)	B3-O8	147.7(5)	B4-O18	147.9(5)
B1-O4	151.4(5)	B2-O15	150.6(5)	B3-O2	150.8(5)	B4-O7	152.1(4)
	Ø 147.1		Ø 147.5		Ø 147.4		Ø 148.0
B5-O5	143.8(5)	B6-O6	143.5(5)	B7-O12	143.7(5)	B8-O1	144.9(5)
B5-O18	146.1(5)	B6-O16	143.7(5)	B7-O2	144.3(5)	B8-O3	145.0(5)
B5-O16	147.9(5)	B6-O14	147.6(5)	B7-O14	147.7(5)	B8-O7	147.5(5)
B5-O15	151.1(5)	B6-O19	155.3(5)	B7-O20	152.0(5)	B8-O17	153.5(5)
	Ø 147.2		Ø 147.5		Ø 146.9		Ø 147.7
		B9-O9	135.4(5)	B10-O11	134.0(5)		
		B9-O20	135.7(3)	B10-O4	135.7(5)		
		B9-O17	140.2(5)	B10-O19	139.7(5)		
			Ø 137.1		Ø 136.5		

4.1.6.4 IR Spectroscopy

The infrared spectrum of Pr₄B₁₀O₂₁ was recorded on a Bruker IFS66/v spectrometer, scanning a range from 400 to 4000 cm⁻¹. The samples were thoroughly mixed with dried KBr (5 mg sample, 500 mg KBr) in a glove box under dried argon atmosphere. Figure 4.1-23 shows the spectral region between 400 and 2000 cm⁻¹. The presence of [BO₄]⁵⁻ groups next to [BO₃]³⁻ groups could be confirmed by this

investigation. The absorption peaks between 790 and 1200 cm^{-1} are typical of the tetrahedral borate group $[\text{BO}_4]^{5-}$ as in $\pi\text{-GdBO}_3$, $\pi\text{-YBO}_3$, or TaBO_4 [143, 144, 142]. The absorptions between 1300 and 1450 cm^{-1} , around 1200 cm^{-1} and below 790 cm^{-1} , are characteristic of triangular $[\text{BO}_3]^{3-}$ groups as in $\lambda\text{-LaBO}_3$ [143], H-LaBO_3 [140], or EuB_2O_4 [146]. Due to the fact that eight different tetrahedra and two trigonal groups occur in the structure of $\text{Pr}_4\text{B}_{10}\text{O}_{21}$, a more detailed assignment of the bands is not possible.

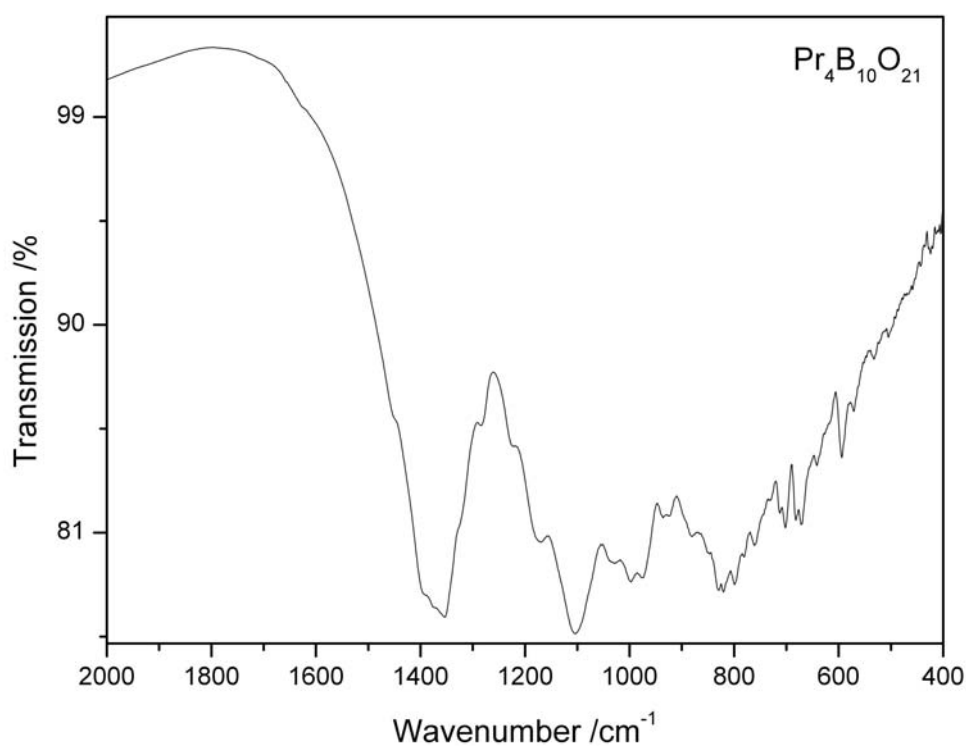


Figure 4.1-23: IR spectrum of $\text{Pr}_4\text{B}_{10}\text{O}_{21}$ representing absorption bands of $[\text{BO}_3]^{3-}$ and $[\text{BO}_4]^{5-}$ groups.

4.1.6.5 Thermal Behaviour

Temperature-programmed X-ray powder diffraction experiments were performed on a STOE Stadi P powder diffractometer [MoK α radiation (71.073 pm)] with a computer controlled STOE furnace: The sample was enclosed in a quartz capillary and heated from room temperature to 500 °C in 100 °C steps, and from 500 °C to 1100 °C in 50 °C steps. Afterwards, the sample was cooled down to 500 °C in 50 °C steps, and from 500 °C to room temperature in 100 °C steps. After each heating step, a diffraction pattern was recorded over the angular range $9^\circ \leq 2\theta \leq 18^\circ$. Figure 4.1-24 illustrates the temperature-programmed X-ray powder diffraction patterns of Pr₄B₁₀O₂₁, showing a decomposition of the high-pressure phase into α -Pr(BO₂)₃ and supposable B₂O₃ at a temperature of 900 °C. At 1100 °C, a side reaction of α -Pr(BO₂)₃ with the quartz capillary occurs, leading to Pr(BSiO₅) [153]. Despite of the metastable character of Pr₄B₁₀O₂₁, it is stable up to a temperature of 850 °C.

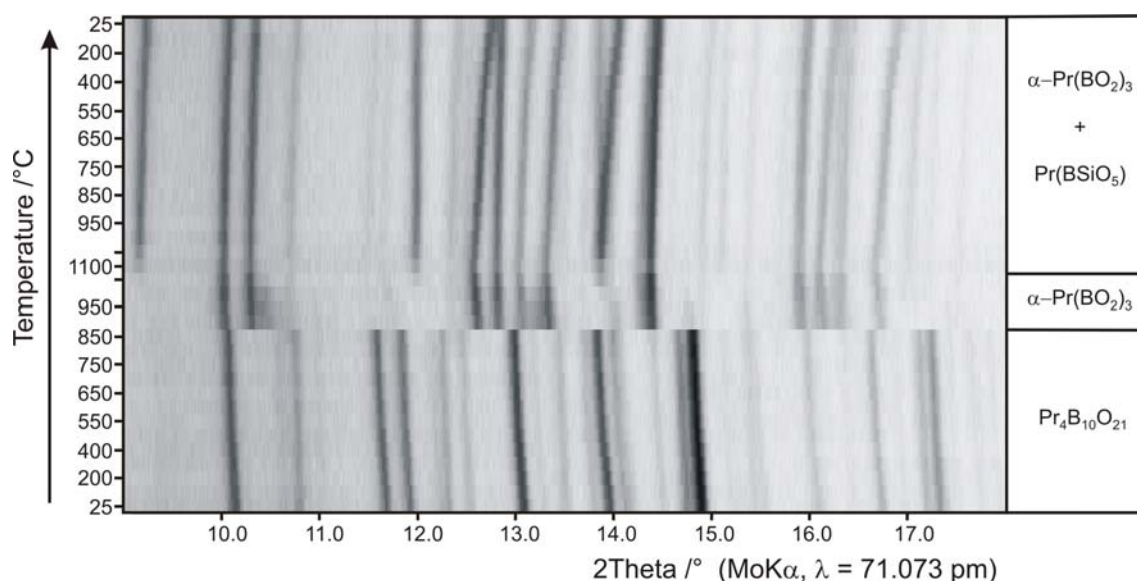


Figure 4.1-24: Temperature-programmed X-ray powder diffraction patterns, following the decomposition of the metastable high-pressure phase Pr₄B₁₀O₂₁ into the normal-pressure form α -Pr(BO₂)₃.

4.1.7 Discussion

The following discussion tries to implement the new results of the high-pressure / high-temperature experiments performed at the lower pressure range into already existing facts. The synthesis of new materials through the densification effect [5], as already mentioned in the introduction, is a well known and often utilized way in high-pressure chemistry. Especially the borates are good research compounds due to the fact that compounds with planar $[\text{BO}_3]^{3-}$ groups tend to transform into high-pressure polymorphs consisting of higher linked networks with mainly $[\text{BO}_4]^{5-}$ tetrahedra.

Polymorphism is a frequently observed phenomenon, especially among the rare-earth metal(III) *meta*-oxoborates. In this family, the three modifications α -, β -, and γ - $\text{RE}(\text{BO}_2)_3$ are hitherto known as depending on the size of the rare-earth metal(III) cations and the synthetic conditions of pressure and temperature. Now the supplementary new δ modification has to be integrated. A synopsis of the different crystal structures of these polymorphs is shown in Figure 4.1-25. Additionally Figure 4.1-26 illustrates the modifications of all rare-earth *meta*-oxoborates synthesized up to now.

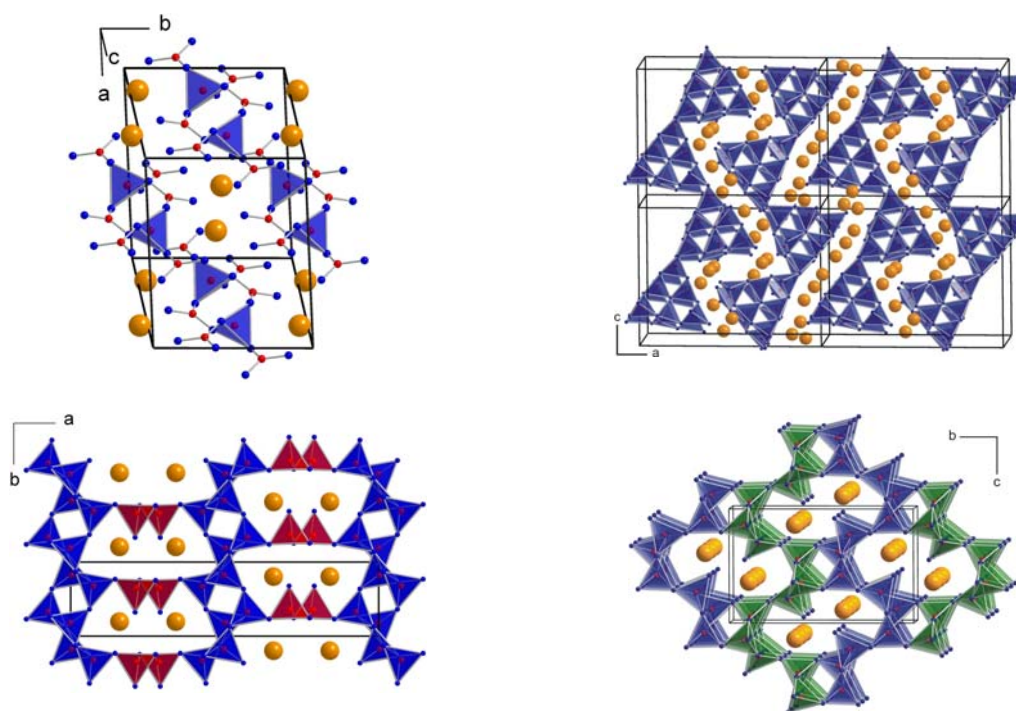


Figure 4.1-25: Crystal structures of the rare-earth *meta*-oxoborates α (top left), β (top right), γ (down left), and δ - $\text{RE}(\text{BO}_2)_3$ (down right).

	La	Ce	Pr	Nd	Pm	Sm	Eu	Gd	Tb	Dy	Ho	Er	Tm	Yb	Lu
α -RE(BO ₂) ₃	X	X	X	X		X	X	X	X						
β -RE(BO ₂) ₃				∅		∅		∅	X	X	∅	∅	∅	∅	∅
γ -RE(BO ₂) ₃	∅	∅	∅	∅											
δ -RE(BO ₂) ₃	∅	∅													

X Ambient-pressure conditions; ∅ High-pressure conditions.

Figure 4.1-26: Schematic view of the existing modifications in the rare-earth *meta*-oxoborates RE(BO₂)₃.

ECoN calculations (Effective Coordination Numbers [94, 95]) for the La³⁺ compounds indicate a coordination number of 10 in α , γ , and δ -La(BO₂)₃, if values of δ -ECoN smaller than 0.05 are neglected. The “ambient” pressure modification α -La(BO₂)₃ [154, 155] builds up from [BO₃]³⁻ as well as [BO₄]⁵⁻ groups. According to the pressure-coordination rule [192], an increase of pressure favours the fourfold coordination of boron, as observed in the γ and δ modifications, exclusively built up from corner-sharing [BO₄]⁵⁻ tetrahedra. Interestingly, both modifications reveal the identical number of Q³ and Q⁴ tetrahedra. Due to the fact, that the γ modification does not exhibit the rare structural feature of edge-sharing tetrahedra [113], we have to find the structural reason for the difference between the γ and δ modification in the coordination of the lanthanum cations. Therefore, we had a closer look at the following nearest oxygen atoms in the coordination sphere of the La³⁺ ions in δ -La(BO₂)₃ (δ -ECoN < 0.05). Next to the 10 oxygen atoms with δ -ECoN > 0.05 (245–310 pm), there are two more oxygen atoms at a distance of 325 and 331 pm (see Table 4.1-15). The following oxygen atom appears in a distance of 350 pm. In this way, the lanthanum cations in δ -La(BO₂)₃ are surrounded by 12 oxygen atoms (10+2) in a distance of 245–331 pm with an average value of 277 pm (see Table 4.1-15). Because of the lack of single crystal data for γ -La(BO₂)₃, we calculated the La–O distances on the basis of the positional parameters of γ -Ce(BO₂)₃ and the known lattice parameters of γ -La(BO₂)₃ [191, 210]. Next to the ten oxygen atoms with δ -ECoN > 0.05 (240–304 pm), there exist five oxygen atoms with distances of 322, 324, 330, 333, and 334 pm, leading to a 10+5 coordinated lanthanum cation in γ -La(BO₂)₃. Beyond 335 pm, the nearest oxygen atom is located at a distance of 358 pm. Taking into account a distance criterion of 335 pm for the coordination sphere of the La³⁺ ions, α , δ , and γ -La(BO₂)₃ possess 10, 10+2, and 10+5 coordinated lanthanum cations, respectively (see Figure 4.1-27).

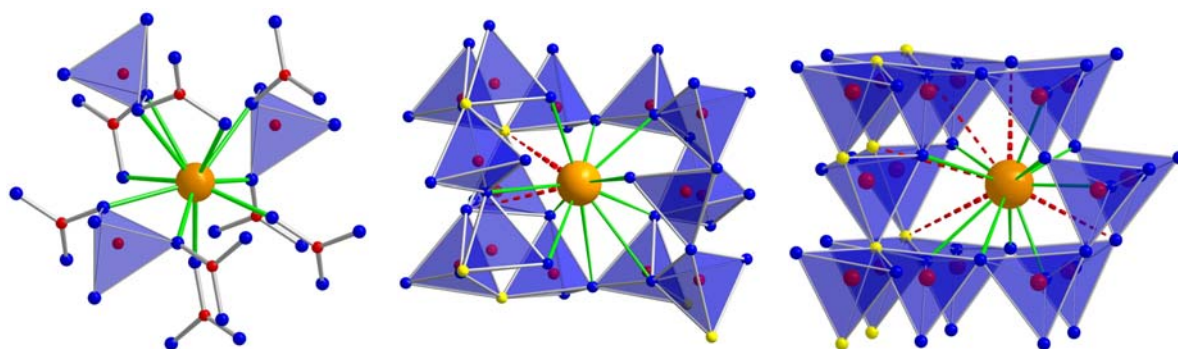


Figure 4.1-27: Coordination of the RE^{3+} atom in α - (left), δ - (middle), and γ - $RE(\text{BO}_2)_3$ (right).

This interpretation confirms the middle-ranking position of δ - $\text{La}(\text{BO}_2)_3$ (synthesized at 5.5 GPa) compared to the “ambient” pressure modification α - $\text{La}(\text{BO}_2)_3$ and the high-pressure modification γ - $\text{La}(\text{BO}_2)_3$ (synthesized at 7.5 GPa). Analogously to the series of lanthanum *meta*-oxoborates α -, δ -, and γ - $\text{La}(\text{BO}_2)_3$, in which the La^{3+} ions possess a 10-, 10+2-, and 10+5-fold coordination, δ - $\text{Ce}(\text{BO}_2)_3$ takes also the middle position between α - and γ - $\text{Ce}(\text{BO}_2)_3$. Appropriately to that, the calculated densities of α - $\text{Ce}(\text{BO}_2)_3$ (4.30 g/cm³) [193], δ - $\text{Ce}(\text{BO}_2)_3$ (4.98 g/cm³), and γ - $\text{Ce}(\text{BO}_2)_3$ (5.04 g/cm³) [191] increase with the applied pressure from “ambient” *via* 3.5 GPa (La: 5.5 GPa) up to 7.5 GPa, respectively.

The successful syntheses of δ - $\text{La}(\text{BO}_2)_3$ (5.5 GPa) and the isotypic cerium *meta*-oxoborate δ - $\text{Ce}(\text{BO}_2)_3$ at a pressure of 3.5 GPa suggest that identical synthetic conditions applied to the next smaller rare-earth ion Pr^{3+} could lead to an isotypic praseodymium *meta*-oxoborate. Interestingly, the experiments with Pr_6O_{11} as rare-earth oxide did not lead to the expected δ - $\text{Pr}(\text{BO}_2)_3$. Instead, the synthesis resulted in a new composition $\text{Pr}_4\text{B}_{10}\text{O}_{21}$, in which nine boron atoms possess a tetrahedral coordination and one boron atom a trigonal coordination. Higher pressures would prefer higher coordination numbers and we expect a structure with all boron atoms exhibiting fourfold coordination. This assumption is fulfilled with the γ - $\text{Pr}(\text{BO}_2)_3$ modification synthesized at 7.5 GPa and 1000 °C. Surprisingly, the density of γ - $\text{Pr}(\text{BO}_2)_3$ with 5.11 g/cm³ is not significantly higher than the density of the new compound $\text{Pr}_4\text{B}_{10}\text{O}_{21}$ (5.09 g/cm³) obtained at much lower pressures. Hints of the existence of the hypothetical β - or δ - $\text{Pr}(\text{BO}_2)_3$ *meta*-oxoborates were not obvious in spite of the broad pressure range from 3.5 to 7.5 GPa.

Next to $\text{La}(\text{BO}_2)_3$, which can be synthesized in three different modifications (α -, γ -, δ -), $\text{Nd}(\text{BO}_2)_3$ is the second example, that can be synthesized in three different structures (α -, β -, γ -), depending on the applied pressure. Up to now, it is not clear if the phases β - $RE(\text{BO}_2)_3$ ($RE = \text{Nd}, \text{Sm}, \text{Gd}$) can also be synthesized under ambient

pressure conditions, as it is possible for $RE = \text{Tb, Dy}$. However, high-pressure conditions favour the formation of the β modifications due to the densification effect [5]. At pressures of 3.5 GPa (Nd) the compound crystallize into the orthorhombic β - $RE(\text{BO}_2)_3$ structure, possessing a higher density than the corresponding α -phase. *E.g.*, α - $\text{Nd}(\text{BO}_2)_3$ has a density of 4.50 g/cm^3 and the denser modification β - $\text{Nd}(\text{BO}_2)_3$ presented here exhibits a value of 4.82 g/cm^3 . A δ modification for neodymium is conceivable because of a large step in density from the β (4.82 g/cm^3) to the γ modification (5.20 g/cm^3) but was not achievable during our experiments.

Figure 4.1-28 presents a survey of the lattice parameters of all known β - $RE(\text{BO}_2)_3$ phases ($RE = \text{Nd-Lu}$ except Pm and Eu). The new *meta*-borate fits well into the scheme of the earlier known compounds. Nd^{3+} represents the largest rare-earth ion in this series, and here we also observe the trend towards a smaller decrease of the lattice parameter b in contrast to a and c , as we already noted for the compounds β - $RE(\text{BO}_2)_3$ ($RE = \text{Sm, Gd-Lu}$). This is caused by the ability to contract more strongly along the a and c direction in the crystal structure (Figure 4.1-25), in contrast to b (layers of $[\text{BO}_4]^{5-}$ tetrahedra), in accordance with the shrinking radius of the RE^{3+} ions (lanthanoide contraction).

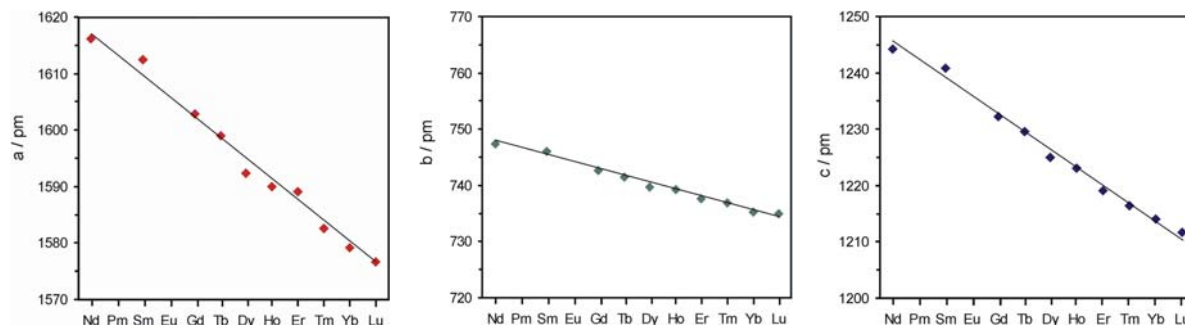


Figure 4.1-28: Plot of the lattice parameters of the rare-earth *meta*-oxoborates β - $RE(\text{BO}_2)_3$ ($RE = \text{Nd-Lu}$, except Pm and Eu).

The here introduced results clearly reveal the effect of high-pressure, its influence on the formation of various compounds and polymorphs by increasing the coordination numbers on the one hand, but on the other hand the results indicate how small the fields of existence are and how much phases remain undiscovered if the experimental pressures are varied in too wide steps.

Beside the borates, we wanted to extend our syntheses under high-pressure conditions into the field of rare-earth germanates. The following Chapter gives an introduction of existing compounds in the systems rare-earth germanates and rare-earth borate germanates and describes first synthetic approaches and results.

4.2 Rare-Earth Borate Germanates

4.2.1 Introduction

The use of high-pressure / high-temperature conditions in the synthesis of borates can lead to new metastable but tangible borates with new compositions and special structural motifs as seen in the Chapters before. Recently, we extended our syntheses under high-pressure conditions into the field of rare-earth germanates, which is a promising class of substances, especially considering the variable coordination numbers of germanium from four, five, or six possible oxygen atoms [212].

Screening the literature, we found that the system RE_2O_3 and GeO_2 beside the solid solutions only exhibits three phases: RE_4GeO_8 , RE_2GeO_5 , and $RE_2Ge_2O_7$. The oxyorthogermanates ($2RE_2O_3 \cdot GeO_2$) and diorthogermanates ($RE_2O_3 \cdot 2GeO_2$) [156–159] were found, when studying the phase diagrams of Er_2O_3 - GeO_2 [160] and Y_2O_3 - GeO_2 [161]. Most of the above mentioned compounds can be synthesized by a solid-state high-temperature approach (1200–1600 °C) directly from the corresponding binary oxides. High quality single crystals of $RE_2O_3 \cdot GeO_2$ and $RE_2O_3 \cdot 2GeO_2$ ($RE = Tb$ – Lu) were obtained by the flux method from a molten mixture of PbO - GeO_2 [162]. The use of PbO as a flux resulted in single crystals of lutetium germanate $3Lu_2O_3 \cdot 4GeO_2$, a composition, that is so far unknown for other lanthanoides [163].

The analysis of all available data on $RE_2O_3 \cdot GeO_2$ systems for all rare-earth cations showed the following trends. In varying the rare-earth atoms from La to Lu, the number of formed compounds and their composition change. In binary systems $RE_2O_3 \cdot GeO_2$, there are three complete morphotropic series ($RE_2O_3 \cdot 2GeO_2$, $RE_2O_3 \cdot GeO_2$, $2RE_2O_3 \cdot GeO_2$) and two incomplete isostructural series ($7RE_2O_3 \cdot 9GeO_2$ ($RE = La$ – Dy), $3RE_2O_3 \cdot 4GeO_2$ ($RE = Lu$)).

First high-pressure experiments up to pressures of 6.5 GPa and temperatures of 1100 °C were carried out for the compounds $RE_2O_3 \cdot 2GeO_2$ ($RE = Er$ – Lu) [23]. In contrast to these compounds, erbium and yttrium diorthogermanates were prepared under hydrothermal conditions [158].

Our introductory high-pressure / high-temperature experiments rapidly led to the conclusion that the experimental setup, in particular the h-BN used as crucible material, was unsuitable for the synthesis of rare-earth germanates. At temperatures above 1000 °C the reductive influence of the boron crucible was too strong and the experiments always resulted in elemental germanium and corresponding rare-earth borates. Lower temperatures led to no significant reactions. Therefore, we tested a flux strategy to synthesize rare-earth germanates in molten lead, derived from

thermal decomposition of PbO. This reaction put down the reactivity of the BN crucible and it was possible to isolate rare-earth germanate compounds in good quality as flux grown crystals. Unfortunately all isolated phases of these first experiments were well known and structurally sufficiently characterized compounds. It was not possible to prevent any participation of the BN crucible during the flux experiments. So we were able to isolate a new quaternary compound consisting of cerium, boron, germanium, and oxygen. This new possible access to high-pressure phases with interesting structural features in the substance class of borogermanates is described in the following. But first a short introduction into this new system is given.

Interestingly, three-component systems from rare-earth oxides and two acid oxides like boron oxide and germanium oxide never form many ternary systems. Screening the literature, we found that the system $RE_2O_3 / B_2O_3 / GeO_2$ shows only two families of compounds: $RE_{14}(GeO_4)_2(BO_3)_6O_8$ ($RE = Pr, Nd, Sm-Gd$) [184-190] (earlier designated as $RE_{14}(GeO_4)_2(BO_3)_8O_5$ [184, 185]) and $REBGeO_5$. Single crystals of the first family were obtained by spontaneous crystallization from a flux, e.g. 6 Gd_2O_3 , 3 B_2O_3 , 6 GeO_2 , and 85 PbO in the case of $Gd_{14}(GeO_4)_2(BO_3)_6O_8$ [189]. Inside the isotypic compounds $RE_{14}(GeO_4)_2(BO_3)_6O_8$, the rare-earth cations exhibit coordination numbers ranging from 6 to 10, which restricts the composition to the rare-earth cations Pr, Nd, and Sm-Gd. The attempts to synthesize analogous compounds with larger and smaller rare-earth cations were unsuccessful. Experiments with terbium oxide resulted in binary borates and germanates [188]. Furthermore, rare-earth ions of different sizes were added to the composition, and in some cases solid solutions were obtained, which melt congruently. Following that way, the region of existence of this structure type was extended to mixtures of two, three, or four rare-earth's, e.g. $La_7RE_7(GeO_4)_2(BO_3)_6O_8$ ($RE = Tb, Dy, Ho, Er$) [164, 165], $Nd_xSm_yEu_{4-x-y}(GeO_4)_2(BO_3)_6O_8$ [166], and $Nd_xSm_yEu_zGd_{4-x-y-z}(GeO_4)_2(BO_3)_6O_8$ [167]. The solid solution with lanthanum and terbium ($La_xTb_{14-x}(GeO_4)_2(BO_3)_6O_8$) is of special interest, whereas the individual compounds $RE_{14}(GeO_4)_2(BO_3)_6O_8$ with $RE = La$ and Tb are still unknown.

The second family, represented by the formula $REBGeO_5$ [168-173], exhibits two types of structures. For the larger rare-earth ions ($RE = La, Pr, and Nd$ (low-temperature phase)) a trigonal cell symmetry was realized (space group $P3_1$), crystallizing with the $REBSiO_5$ *stillwellite* structure type ($CeBSiO_5$) [153, 174-176]. Both atoms, germanium and boron are coordinated tetrahedrally forming helical chains along the c axes. The smaller rare-earth's ($RE = Nd$ (high-temperature) -Er) were described in a monoclinic cell ($P2_1/a$), isotypic with the *datolite* type structure ($CaBSiO_4OH$) [177]. This structure is layered, and the cations are separated by $[BO_4]^{5-}$ and $[GeO_4]^{4-}$ tetrahedra. For the smallest ions ($RE = Tm, Yb, Lu$), the compound

does not exist until now. Additionally, solid solutions in the system $\text{La}_{1-x}\text{Nd}_x\text{BGeO}_5$ have been investigated. For $0 \leq x \leq 0.6$ the *stillwellite* structure was stabilized, and for $x \geq 0.8$ the monoclinic modification is observed [172].

Recently, it was shown that boron can be incorporated into germanate frameworks [178-183]. In this context, the combination of borate and germanate groups in the same crystalline material generated a new class of materials with novel framework topologies.

Concerning the structures, all former mentioned borate germanates are characterized by the combination of trigonal $[\text{BO}_3]^{3-}$ groups with $[\text{GeO}_4]^{4-}$ tetrahedra and the combination of $[\text{BO}_4]^{5-}$ tetrahedra with $[\text{GeO}_4]^{4-}$ tetrahedra. A third variety of building blocks can be found in the class of transition-metal borate germanates, namely $\text{Ni}_5\text{GeB}_2\text{O}_{10}$ (space group *Pbam*), where the combination of $[\text{BO}_3]^{3-}$ groups with $[\text{GeO}_6]^{8-}$ octahedra exists [214]. A synopsis of the few crystal structures is given in Figure 4.2-1 to Figure 4.2-4.

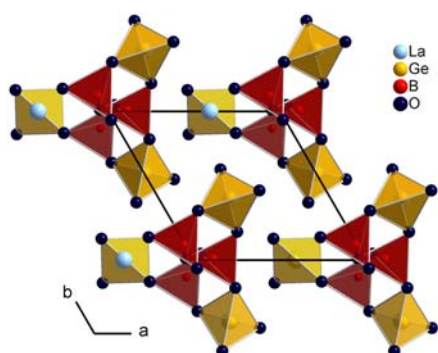


Figure 4.2-1: Crystal structure of trigonal LaBGeO_5 .

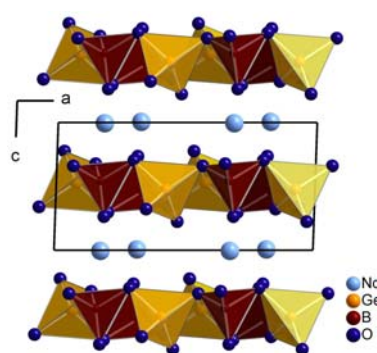


Figure 4.2-2: Crystal structure of monoclinic NdBGeO_5 .

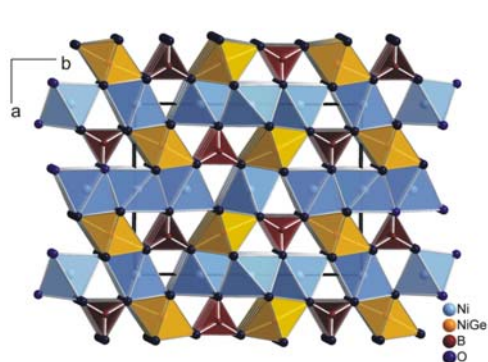


Figure 4.2-3: Crystal structure of $\text{Ni}_5\text{GeB}_2\text{O}_{10}$.

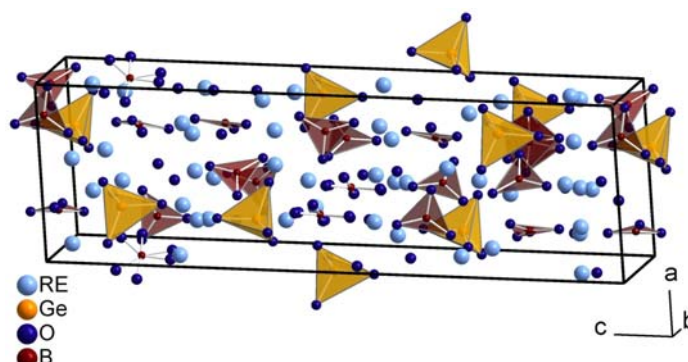


Figure 4.2-4: Crystal structure of $\text{RE}_{14}(\text{GeO}_4)_2(\text{BO}_3)_6\text{O}_8$.

Missing motives in this series are the combination of $[\text{BO}_4]^{5-}$ tetrahedra with $[\text{GeO}_5]^{6-}$ polyhedra or $[\text{GeO}_6]^{8-}$ octahedra, because germanium may adopt three different coordinations, e.g. four, five, and six [212]. High-pressure conditions should

prefer combinations, in which boron and germanium exhibit their highest coordination numbers four and six, respectively. This assumption was confirmed by the borogermanate $Ce_6(BO_4)_2Ge_9O_{22}$, described in the following.

4.2.2 Starting Materials

For the preparation of new rare-earth borate germanates in this work, various commercially acquirable chemical substances were used. Table 4.2-1 lists up the different substances, state, purity, and source of supply.

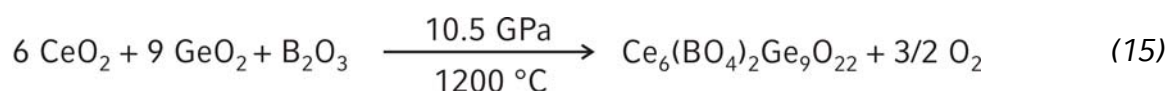
Table 4.2-1: Purity and source of supply of commercially available substances.

Substance	State	Purity	Source of Supply
CeO ₂	Powder	> 99.9%	Auer Remy, Hamburg, Germany
GeO ₂	Powder	> 99.999%	Chempur, Karlsruhe, Germany
B ₂ O ₃	Grains	> 99.9%	Strem Chemicals, Newburyport, U.S.A.
PbO	Powder	> 99.7%	Acros, Geel, Belgium
PbO ₂	Powder	> 99.9%	Merck, Darmstadt, Germany

4.2.3 The Rare-Earth Borate Germanate $Ce_6(BO_4)_2Ge_9O_{22}$

4.2.3.1 Synthesis

According to the experiment (equation (15)), the compound $Ce_6(BO_4)_2Ge_9O_{22}$ was synthesized *via* a high-temperature / high-pressure route, using molar mixtures of CeO₂, GeO₂ (trigonal, α -quartz type), and B₂O₃.



A boron nitride crucible of a 14/8-assembly was loaded with a carefully milled mixture of the compounds, compressed within 3 h to 10.5 GPa, using a multianvil apparatus, and heated up to 1200 °C in the following 10 minutes. After a period of 10 minutes with a constant temperature of 1200 °C, the assembly was slowly cooled down to 700 °C followed by quenching to room temperature. Decompression past, the recovered experimental octahedron was broken apart, and the sample carefully

separated from the surrounding hexagonal boron nitride. This procedure led to a slightly yellow to colorless, crystalline composite, consisting of the new borate germanate $\text{Ce}_6(\text{BO}_4)_2\text{Ge}_9\text{O}_{22}$, the orthorhombic *meta*-borate $\gamma\text{-Ce}(\text{BO}_2)_3$ [191], and rests of GeO_2 (*argutite*, *rutile* type), which were identified by X-ray powder diffraction.

For an optimization of the synthetic parameters, the synthesis pressure was decreased to 8.5 GPa resulting in a nearly complete prevention of the byproduct $\gamma\text{-Ce}(\text{BO}_2)_3$ [191]. But, we detected a new phase next to the main phase $\text{Ce}_6(\text{BO}_4)_2\text{Ge}_9\text{O}_{22}$ in the powder pattern of this system, unknown until now. Hitherto, it was not possible to obtain a single phase product by varying the temperature and pressure conditions. An examination of the crystallinity of the sample for the selection of single crystals revealed inadequate quality. Therefore, the experiments were repeated with the addition of a PbO/PbO_2 -flux ($\text{CeO}_2 : \text{GeO}_2 : \text{B}_2\text{O}_3 : \text{PbO} : \text{PbO}_2 = 6 : 9 : 1 : 12 : 0.3$) at 10.5 GPa and 1200 °C to improve the growth and quality of the crystals to an acceptable size similar to the crystallization of $\text{RE}_{14}(\text{GeO}_4)_2(\text{BO}_3)_6\text{O}_8$ ($\text{RE} = \text{Pr}, \text{Nd}, \text{Sm-Gd}$) [184-190]. Single crystals of $\text{Ce}_6(\text{BO}_4)_2\text{Ge}_9\text{O}_{22}$ were isolated from the mentioned flux-synthesis. The composition and the absence of lead inside the single crystals were examined by EDX-analysis. The analysis of the cerium and germanium content in $\text{Ce}_6(\text{BO}_4)_2\text{Ge}_9\text{O}_{22}$ via EDX was determined to 12 and 17 atom%, respectively (theoretical: / atom%: 12.8% Ce, 19.1% Ge).

4.2.3.2 Crystal Structure Analysis

Small single crystals of $\text{Ce}_6(\text{BO}_4)_2\text{Ge}_9\text{O}_{22}$ were isolated by mechanical fragmentation, and examined by Buerger precession photographs. Single crystal intensity data were collected at room temperature from a regularly shaped colorless crystal (block) by use of a STOE IPDS detector diffractometer [MoK_α radiation (71.073 pm)]. A numerical absorption correction (HABITUS [77]) was applied to the intensity data. All relevant information concerning the data collection is listed in Table 4.2-2. According to the systematic extinctions $h0l$ with $h+l \neq 2n$, $0k0$ with $k \neq 2n$, $h00$ with $h \neq 2n$, and $00l$ with $l \neq 2n$, the space group $P2_1/n$ (No. 14) was derived. The starting positional parameters were deduced from an automatic interpretation of *Direct methods* with SHELXS-97 [79]. The structure of $\text{Ce}_6(\text{BO}_4)_2\text{Ge}_9\text{O}_{22}$ was refined with anisotropic displacement parameters for all atoms with SHELXL-97 [80] (full-matrix least-squares on F^2). The final difference Fourier synthesis did not reveal any significant residual peaks in the refinement (see Table 4.2-2). Details of the single crystal structure measurement are shown in Table 4.2-2. Additionally, the positional parameters (Table 4.2-3), anisotropic displacement parameters (Table 4.2-4), and interatomic distances (Table 4.2-5) are listed.

Table 4.2-2: Crystal data and structure refinement for $\text{Ce}_6(\text{BO}_4)_2\text{Ge}_9\text{O}_{22}$.

Empirical formula	$\text{Ce}_6(\text{BO}_4)_2\text{Ge}_9\text{O}_{22}$
Molar mass ($\text{g}\cdot\text{mol}^{-1}$)	1995.65
Crystal system	monoclinic
Space group	$P2_1/n$ (No. 14)
Single crystal diffractometer	STOE-IPDS
Radiation	MoK_α ($\lambda = 71.073$ pm)
Single crystal data	
a (pm)	877.0(2)
b (pm)	1079.4(2)
c (pm)	1079.1(2)
β ($^\circ$)	95.94(3)
Volume (\AA^3)	1016.0(4)
Formula units per cell	$Z = 2$
Temperature (K)	293(2)
Calculated density ($\text{g}\cdot\text{cm}^{-3}$)	6.52
Crystal size (mm^3)	$0.03 \times 0.03 \times 0.03$
Detector distance (mm)	50
Irradiation / exposure (min)	10
Number of exposures	113
Measurement duration (h)	24
Absorption coefficient (mm^{-1})	26.4
$F(000)$	1772
θ Range ($^\circ$)	2.68 to 30.42
Range in hkl	$\pm 12, -15/+13, \pm 15$
Total no. reflections	10704
Independent reflections	2899 ($R_{\text{int}} = 0.0633$)
Reflections with $I > 2\sigma(I)$	2053 ($R_\sigma = 0.0591$)
Data / parameters	2899 / 215
Absorption correction	numerical (HABITUS [77])
Transm. ratio (max / min)	0.658 / 0.444
Goodness-of-fit (F^2)	0.889
Final R indices ($I > 2\sigma(I)$)	$R1 = 0.0401$ $wR2 = 0.0913$
R Indices (all data)	$R1 = 0.0584$ $wR2 = 0.0967$
Extinction coefficient	0.0006(2)
Larg. diff. peak and hole ($\text{e}\cdot\text{\AA}^{-3}$)	2.3 / -2.2

Table 4.2-3: Atomic coordinates and isotropic equivalent displacement parameters U_{eq} (\AA^2) for $\text{Ce}_6(\text{BO}_4)_2\text{Ge}_9\text{O}_{22}$ (space group: $P2_1/n$). U_{eq} is defined as one third of the trace of the orthogonalized U_{ij} tensor.

Atom	Wyckoff Site	x	y	z	U_{eq}
Ce1	4e	0.04490(6)	0.66854(5)	0.05792(5)	0.0084(2)
Ce2	4e	0.65196(6)	0.83259(5)	0.94610(5)	0.0093(2)
Ce3	4e	0.99656(6)	0.82240(5)	0.73165(5)	0.0077(2)
B1	4e	0.779(2)	0.663(2)	0.475(2)	0.010(2)
Ge1	4e	0.8644(2)	0.8279(1)	0.2372(1)	0.0076(2)
Ge2	4e	0.7492(2)	0.5822(1)	0.7511(1)	0.0073(2)
Ge3	2a	0	0	0	0.0077(3)
Ge4	4e	0.8751(2)	0.5146(1)	0.2603(1)	0.0073(2)
Ge5	4e	0.3452(2)	0.5381(1)	0.9685(1)	0.0080(2)
O1	4e	0.8543(8)	0.6864(6)	0.8639(7)	0.011(2)
O2	4e	0.1387(7)	0.0258(6)	0.1386(6)	0.007(2)
O3	4e	0.1333(8)	0.5174(7)	0.9171(6)	0.009(2)
O4	4e	0.8263(8)	0.6707(6)	0.1958(7)	0.010(2)
O5	4e	0.2972(8)	0.5466(6)	0.1280(7)	0.011(2)
O6	4e	0.0763(8)	0.8061(6)	0.2657(6)	0.009(2)
O7	4e	0.8560(8)	0.3567(6)	0.3130(7)	0.009(2)
O8	4e	0.8037(8)	0.6843(6)	0.6118(6)	0.009(2)
O9	4e	0.8556(8)	0.9849(6)	0.2908(7)	0.010(2)
O10	4e	0.0808(7)	0.5314(6)	0.2666(7)	0.008(2)
O11	4e	0.1169(8)	0.8660(6)	0.9395(7)	0.010(2)
O12	4e	0.1090(8)	0.1292(7)	0.9284(7)	0.011(2)
O13	4e	0.4499(8)	0.3910(6)	0.9853(7)	0.011(2)
O14	4e	0.8789(8)	0.5686(6)	0.4284(7)	0.008(2)
O15	4e	0.3109(9)	0.7110(7)	0.9140(7)	0.012(2)

Table 4.2-4: Anisotropic displacement parameters (\AA^2) for $\text{Ce}_6(\text{BO}_4)_2\text{Ge}_9\text{O}_{22}$ (space group: $P2_1/n$).

Atom	U_{11}	U_{22}	U_{33}	U_{23}	U_{13}	U_{12}
Ce1	0.0091(2)	0.0075(2)	0.0088(3)	0.0000(2)	0.0023(2)	0.0006(2)
Ce2	0.0083(2)	0.0109(3)	0.0086(3)	0.0006(2)	0.0008(2)	-0.0001(2)
Ce3	0.0084(2)	0.0066(2)	0.0082(3)	-0.0001(2)	0.0015(2)	-0.0002(2)
B1	0.004(4)	0.017(5)	0.009(5)	-0.002(4)	0.003(4)	-0.002(4)
Ge1	0.0082(4)	0.0055(4)	0.0092(5)	-0.0008(4)	0.0016(4)	-0.0003(4)
Ge2	0.0078(4)	0.0064(4)	0.0078(5)	-0.0004(3)	0.0009(4)	0.0000(3)
Ge3	0.0088(6)	0.0060(6)	0.0085(7)	-0.0009(5)	0.0018(6)	-0.0002(5)
Ge4	0.0075(4)	0.0061(4)	0.0084(5)	-0.0001(3)	0.0012(4)	-0.0001(3)
Ge5	0.0083(5)	0.0085(5)	0.0072(5)	0.0001(4)	0.0009(4)	0.0004(4)
O1	0.009(3)	0.009(3)	0.013(4)	-0.002(3)	-0.002(3)	0.002(2)
O2	0.004(3)	0.009(3)	0.010(3)	0.005(2)	0.003(3)	0.004(2)
O3	0.007(3)	0.014(3)	0.007(3)	0.001(3)	0.002(3)	-0.002(3)
O4	0.0012(3)	0.004(3)	0.014(3)	0.002(3)	-0.003(3)	-0.001(2)
O5	0.014(3)	0.008(3)	0.010(3)	0.004(3)	0.004(3)	0.000(3)
O6	0.007(3)	0.011(3)	0.007(3)	0.001(2)	0.001(3)	0.001(2)
O7	0.009(3)	0.009(3)	0.010(3)	0.001(3)	0.002(3)	-0.002(2)
O8	0.013(3)	0.008(3)	0.007(3)	0.007(2)	0.001(3)	0.000(3)
O9	0.011(3)	0.008(3)	0.012(4)	-0.005(3)	0.002(3)	0.001(3)
O10	0.004(3)	0.005(3)	0.017(4)	0.002(2)	0.002(3)	-0.003(2)
O11	0.008(3)	0.010(3)	0.011(3)	0.000(3)	-0.002(3)	0.000(2)
O12	0.013(3)	0.009(3)	0.011(3)	0.001(3)	0.006(3)	0.002(3)
O13	0.018(4)	0.010(3)	0.006(3)	-0.002(2)	0.008(3)	-0.001(3)
O14	0.005(3)	0.007(3)	0.011(4)	0.001(2)	0.000(3)	0.002(2)
O15	0.019(4)	0.007(3)	0.009(3)	0.006(3)	-0.002(3)	0.004(3)

4.2.3.3 Crystal Structure Description

The crystal structure of the new borogermanate $\text{Ce}_6(\text{BO}_4)_2\text{Ge}_9\text{O}_{22}$ is built up from corner- and edge-sharing $[\text{GeO}_6]^{8-}$ octahedra, which are furthermore connected *via* corner-sharing $[\text{BO}_4]^{5-}$ tetrahedra. Figure 4.2-5 gives a view of the structure of $\text{Ce}_6(\text{BO}_4)_2\text{Ge}_9\text{O}_{22}$, where the $[\text{GeO}_6]^{8-}$ octahedra and $[\text{BO}_4]^{5-}$ tetrahedra are represented as orange and red polyhedra, respectively. The remaining voids inside the polyhedral arrangement are filled with cerium ions. Figure 4.2-6 offers a more detailed view of the linkage between octahedra and tetrahedra in the *ac*-plane. In detail, six octahedra are edge-linked to form a Ge_6O_{24} -group, and three octahedra are connected *via* common corners to generate a Ge_3O_{16} -group. These groups are connected among each other and additionally interconnected by $[\text{BO}_4]^{5-}$ tetrahedra

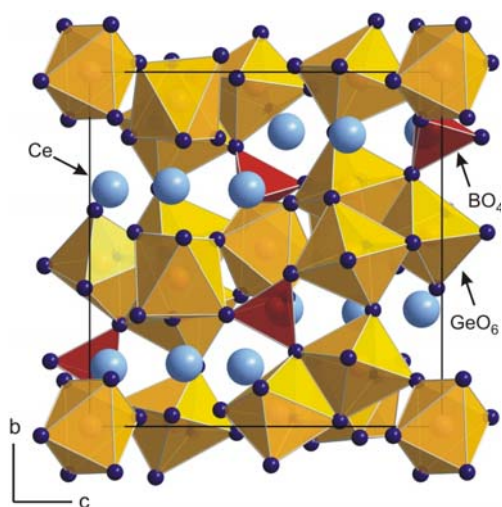


Figure 4.2-5: Crystal structure of $\text{Ce}_6(\text{BO}_4)_2\text{Ge}_9\text{O}_{22}$, view along $[100]$. The cerium cations are shown as light blue spheres and the oxygen atoms as dark blue spheres. The $[\text{GeO}_6]^{8-}$ octahedra and $[\text{BO}_4]^{5-}$ tetrahedra are given in the polyhedral representation.

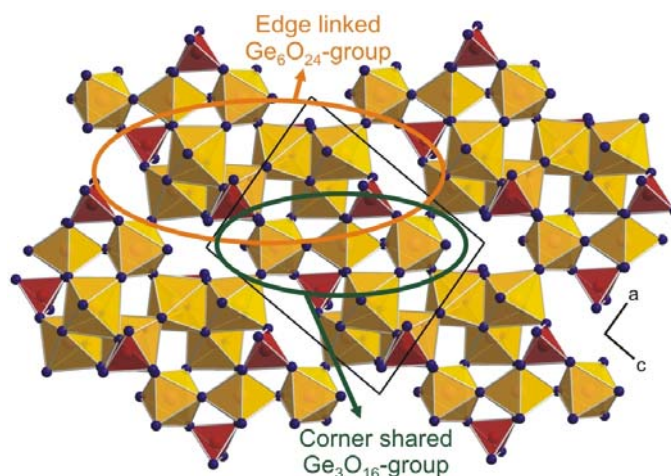


Figure 4.2-6: Crystal structure of $\text{Ce}_6(\text{BO}_4)_2\text{Ge}_9\text{O}_{22}$, view along $[010]$.

to result in a network structure from $[\text{GeO}_6]^{8-}$ octahedra and $[\text{BO}_4]^{5-}$ tetrahedra. Figure 4.2-7 shows the coordination of the three crystallographically distinguishable cerium ions. They are coordinated by 11 (Ce1) and 9 (Ce2 and Ce3) oxygen atoms in a distance of 240–297 pm (see Table 4.2-5). These values correspond to the distance-range in the recently published high-pressure *meta*-borate $\gamma\text{-Ce}(\text{BO}_2)_3$, where the cerium cations are coordinated by 10 oxygen atoms in a distance between 239 and 303 pm with an average value of 265.8 pm [191]. Due to the pressure-coordination rule [192], the high-pressure phases $\text{Ce}_6(\text{BO}_4)_2\text{Ge}_9\text{O}_{22}$ and $\gamma\text{-Ce}(\text{BO}_2)_3$

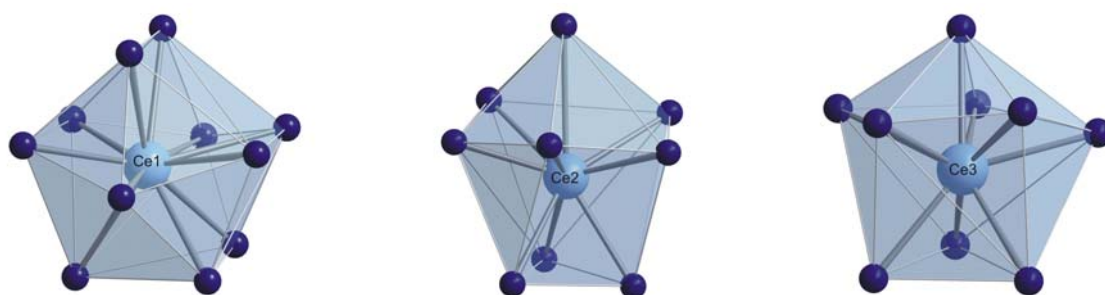


Figure 4.2-7: Coordination spheres of the Ce^{3+} ions in the crystal structure of $\text{Ce}_6(\text{BO}_4)_2\text{Ge}_9\text{O}_{22}$.

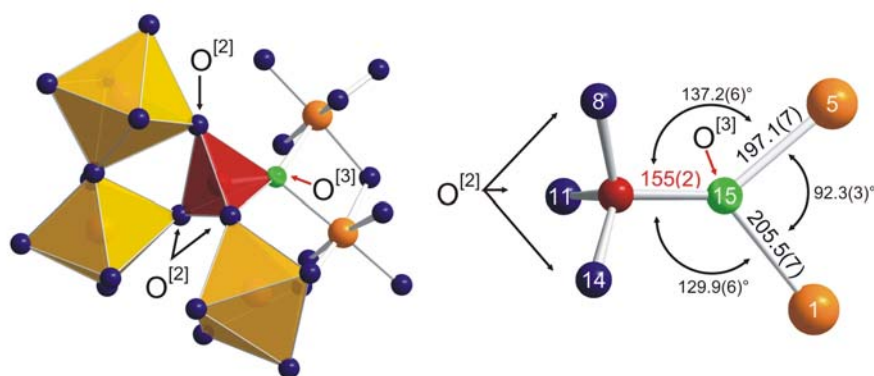


Figure 4.2-8: Environment of the three-fold coordinated oxygen atom in $\text{Ce}_6(\text{BO}_4)_2\text{Ge}_9\text{O}_{22}$. Left: Representation of the polyhedral environment of the three-fold coordinated oxygen $\text{O}^{[3]}$. Right: Distances and angles around oxygen fifteen ($\text{O}^{[3]}$). (Boron: red sphere; germanium: orange sphere; oxygen: blue sphere).

possess high coordination numbers and large Ce–O distances in contrast to known cerium borates like α - $\text{Ce}(\text{BO}_2)_3$ [193] (CN: 10) with Ce–O distances of 236–276 pm, λ - CeBO_3 [193] (CN: 9) with 239–272 pm, H- CeBO_3 [193] (CN: 9) with 244–275 pm, and an oxide like Ce_2O_3 [194] (CN: 7) with 234–269 pm. A closer view of the coordination sphere of Ce1 in $\text{Ce}_6(\text{BO}_4)_2\text{Ge}_9\text{O}_{22}$ shows a gap between the 10 nearest oxygen atoms ranging from 241–279 pm and the 11th oxygen atom in a distance of 297 pm. A theoretical point of view on the coordination sphere of Ce is given in Chapter 4.2.3.5.

In the tetrahedral $[\text{BO}_4]^{5-}$ group, the B–O distances vary between 147 and 155 pm (see Table 4.2-5). With the exception of the largest value (155 pm), the B–O distances correspond well with the known average value of 147.6 pm for borates [195, 196]. Figure 4.2-8 gives a view of the coordination sphere of O15, featuring the large distance of 155 pm to the boron atom. In fact, O15 is a three-coordinated oxygen atom $\text{O}^{[3]}$, possessing a significantly longer distance to boron than two-fold coordinated oxygen atoms. Three coordinated oxygen atoms can be found in a few minerals like *tunnelite* ($\text{SrB}_6\text{O}_9(\text{OH})_2 \cdot 3 \text{H}_2\text{O}$) [197], *strontioginorite* ($(\text{Sr},\text{Ca})_2\text{B}_{14}\text{O}_{20}(\text{OH})_6 \cdot 5 \text{H}_2\text{O}$) [198], *aristarainite* ($\text{Na}_2\text{Mg}[\text{B}_6\text{O}_8(\text{OH})_4]_2 \cdot 4 \text{H}_2\text{O}$) [199], and synthetic borates like SrB_4O_7 [200–202], PbB_4O_7 [201, 203], and EuB_4O_7 [204]. More often, $\text{O}^{[3]}$ was observed in high-pressure phases like β - ZnB_4O_7 [205], β - CaB_4O_7 [206], β - HgB_4O_7 [207], β - $\text{RE}(\text{BO}_2)_3$ [208, 209], γ - $\text{RE}(\text{BO}_2)_3$ [210, 211], and the high-pressure modification of B_2O_3 [211] (see Figure 4.1-2) itself. The corresponding average B– $\text{O}^{[3]}$ distances in these compounds range around 155 pm.

The O–B–O angles inside of the $[\text{BO}_4]^{5-}$ tetrahedra range from 105° to 115° with an average value of 109.4°. The two B–O–Ge angles and the Ge–O–Ge one at $\text{O}^{[3]}$ are 137.2(6)°, 129.9(6)°, and 92.3(3)°, respectively (see Figure 4.2-8). As far as we know,

$\text{Ce}_6(\text{BO}_4)_2\text{Ge}_9\text{O}_{22}$ is the first structure, in which a three-fold coordinated oxygen atom, bonded to one boron and two germanium atoms, was observed.

The Ge–O distances inside the $[\text{GeO}_6]^{8-}$ octahedra range from 178–207 pm with an average value of 190.3 pm, which corresponds well with known average values of Ge–O distances in $[\text{GeO}_6]^{8-}$ octahedra, e.g. 189.9 pm in $\text{La}_2\text{Ge}_3\text{O}_9$ [212], 189.4 pm in $\text{Ce}_2\text{Ge}_3\text{O}_9$ [212], 188.5 pm in *rutile* type GeO_2 [213], and 199.7 pm in $\text{Ni}_5\text{GeB}_2\text{O}_{10}$ [214].

Table 4.2-5: Interatomic distances (pm) calculated with the single crystal lattice parameters in $\text{Ce}_6(\text{BO}_4)_2\text{Ge}_9\text{O}_{22}$ (standard deviations in parentheses).

Ce1–O3a	241.1(7)	Ce2–O12	241.1(8)	Ce3–O7	240.2(7)	Ge1–O4	177.8(7)
Ce1–O4	254.6(7)	Ce2–O10	245.9(7)	Ce3–O11	242.4(7)	Ge1–O9	179.5(7)
Ce1–O1	254.8(8)	Ce2–O6	249.1(7)	Ce3–O5	243.0(8)	Ge1–O6	186.7(7)
Ce1–O3b	257.5(7)	Ce2–O1	259.9(7)	Ce3–O1	247.3(7)	Ge1–O12	188.4(7)
Ce1–O12	257.9(7)	Ce2–O14	261.0(7)	Ce3–O9	247.6(7)	Ge1–O7	197.8(7)
Ce1–O11	259.6(7)	Ce2–O7	262.0(7)	Ce3–O8	251.0(7)	Ge1–O15	205.5(7)
Ce1–O5	261.8(7)	Ce2–O2	262.5(6)	Ce3–O2	252.9(6)		
Ce1–O6	268.0(7)	Ce2–O13	270.3(7)	Ce3–O13	254.5(7)		∅ 189.3
Ce1–O10	268.6(7)	Ce2–O14	291.1(7)	Ce3–O4	295.8(7)		
Ce1–O8	278.3(7)					B1–O11	147(2)
Ce1–O15	296.9(7)					B1–O8	149(2)
	∅ 263.6		∅ 260.3		∅ 252.7	B1–O15	155(2)
						B1–O14	146(2)
							∅ 149
Ge2–O1	183.4(7)	Ge3–O2a	184.9(7)	Ge4–O10	180.8(6)	Ge5–O5	181.6(7)
Ge2–O2	187.8(7)	Ge3–O2b	184.9(7)	Ge4–O7	181.0(7)	Ge5–O13a	183.4(7)
Ge2–O10	195.4(7)	Ge3–O12a	189.9(7)	Ge4–O4	185.6(7)	Ge5–O3	189.8(7)
Ge2–O6	195.7(7)	Ge3–O12b	189.9(7)	Ge4–O14	190.3(7)	Ge5–O9	194.5(7)
Ge2–O8	196.2(6)	Ge3–O11a	192.5(7)	Ge4–O3	193.9(7)	Ge5–O13b	196.9(8)
Ge2–O5	197.7(7)	Ge3–O11b	192.5(7)	Ge4–O9	206.6(7)	Ge5–O15	197.1(7)
	∅ 192.7		∅ 189.1		∅ 189.7		∅ 190.6

4.2.3.4 Thermal Behaviour

Temperature-programmed X-ray powder diffraction experiments were performed on a STOE Stadi P powder diffractometer (MoK α) with a computer controlled STOE furnace. The sample was enclosed in a quartz capillary and heated from room temperature to 500 °C in steps of 100 °C, from 500 to 1100 °C in steps of 50 °C, and back to 550 °C in steps of 50 °C. At each temperature, a diffraction pattern was recorded over the angular range $4^\circ \leq 2\theta \leq 20^\circ$. In the temperature range 500 °C to room temperature, no diffraction data were received due to a Mark capillary breakage. Figure 4.2-9 gives a view of the powder patterns, in which the reflections of the borate germanate Ce₆(BO₄)₂Ge₉O₂₂ can be detected up to a temperature of 750 °C. Further heating (750–1000 °C) led to a decomposition of Ce₆(BO₄)₂Ge₉O₂₂ into the rare-earth germanate CeGeO₄ [215], GeO₂ (*argutite*), B₂O₃ in its probably molten state, and a phase, which is still unknown. Subsequent cooling to 550 °C showed that all three phases endured. The reflections near 9 and 17° are artifacts from the furnace. From these results, we presume that the high-pressure phase Ce₆(BO₄)₂Ge₉O₂₂ has a metastable character under ambient pressure conditions.

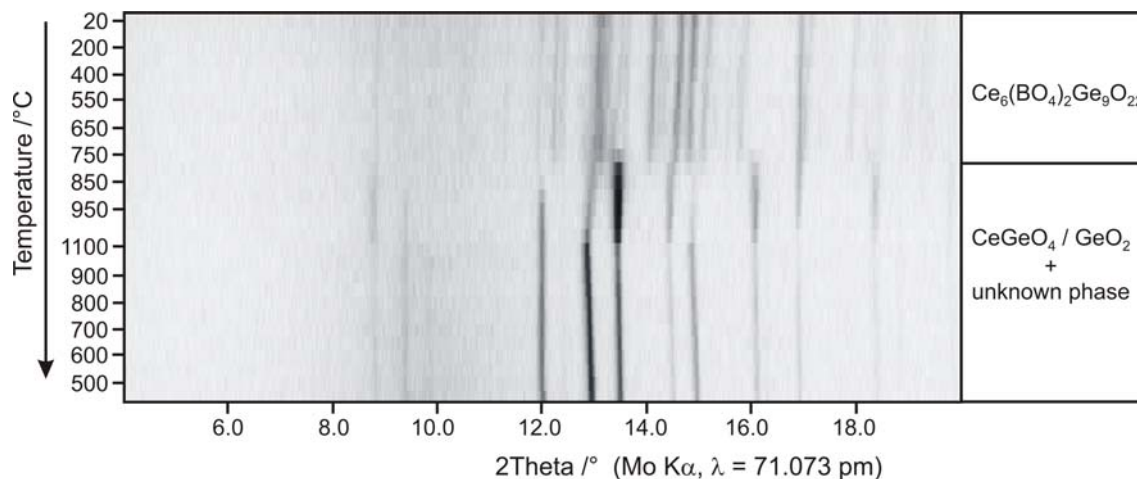


Figure 4.2-9: Temperature-programmed X-ray powder patterns, following the decomposition reaction of the metastable high-pressure phase Ce₆(BO₄)₂Ge₉O₂₂.

4.2.3.5 Theoretical Calculations

The coordination sphere around the cerium atoms was verified with the help of MAPLE-calculations (Madelung Part of Lattice Energy) [87-89]. These calculations confirmed the coordinative contribution of the oxygen O15 (Ce1–O15 = 297 pm) atom followed by the next oxygen atom in a distance of 400 pm, without any coordinative contribution. In the case of Ce3, the gap is much more pronounced (be-

tween 255 and 296 pm), but the coordinative contribution of this oxygen is also not negligible as the calculations prove.

Additionally, we calculated the MAPLE value for $\text{Ce}_6(\text{BO}_4)_2\text{Ge}_9\text{O}_{22}$ to compare it with the MAPLE value from the binary components Ce_2O_3 , GeO_2 , and the high-pressure modification $\text{B}_2\text{O}_3\text{-II}$ [$3 \cdot \text{Ce}_2\text{O}_3$ ($14150 \text{ kJ}\cdot\text{mol}^{-1}$) [216] + $9 \cdot \text{GeO}_2$ (*rutile* type; *argutite*) ($14207 \text{ kJ}\cdot\text{mol}^{-1}$) [217] + $1 \cdot \text{B}_2\text{O}_3\text{-II}$ ($21938 \text{ kJ}\cdot\text{mol}^{-1}$) [211]]. The deviation of the calculated value of $191881 \text{ kJ}\cdot\text{mol}^{-1}$ for $\text{Ce}_6(\text{BO}_4)_2\text{Ge}_9\text{O}_{22}$ differs only by 0.2% compared with the MAPLE value obtained from the binary oxides ($192251 \text{ kJ}\cdot\text{mol}^{-1}$).

For better evidence, we calculated bond-valence sums for $\text{Ce}_6(\text{BO}_4)_2\text{Ge}_9\text{O}_{22}$ with the bond-length/bond-strength [91-93] and CHARDI (Charge Distribution in Solids) concept (Table 4.2-6) [94, 95]. The formal ionic charges of the atoms, acquired by the X-ray structure analysis, are in agreement within the limits of the concepts, except oxygen fifteen, which shows values of -1.77 (ΣV) and -1.49 (ΣQ). As shown in Figure 4.2-8 this oxygen atom (O15) is coordinated to one boron and two germanium atoms with relatively long distances. This situation leads to lower values than expected and can be compared to calculated values of three-coordinated oxygen atoms $\text{O}^{[3]}$ in former mentioned borates like $\beta\text{-ZnB}_4\text{O}_7$ [205] ($\text{O}^{[3]}$: -1.83 (ΣV); -1.67 (ΣQ)), $\beta\text{-CaB}_4\text{O}_7$ [206] ($\text{O}^{[3]}$: -1.77 (ΣV); -1.92 (ΣQ)), $\beta\text{-HgB}_4\text{O}_7$ [207] ($\text{O}^{[3]}$: -2.06 (ΣV); -1.83 (ΣQ)), $\beta\text{-Er}(\text{BO}_2)_3$ [208] ($\text{O}^{[3]}$: -1.96 (ΣV); -1.76 (ΣQ)), and $\gamma\text{-Ce}(\text{BO}_2)_3$ [210] ($\text{O}^{[3]}$: -1.91 (ΣV); -1.62 (ΣQ)). These examples represent $\text{O}^{[3]}$ atoms exclusively coordinated by boron, whereas the $\text{O}^{[3]}$ atoms in $\text{Ce}_6(\text{BO}_4)_2\text{Ge}_9\text{O}_{22}$ are linked to one boron and two germanium atoms. Due to the higher distances between germanium and oxygen (197.1(7) and 205.5(7) pm), compared to the distance between boron and oxygen (155(2) pm), the deviation from the expected value -2 is larger than in the corresponding borates.

Table 4.2-6: Charge distribution in $\text{Ce}_6(\text{BO}_4)_2\text{Ge}_9\text{O}_{22}$, calculated with the bond-length/bond-strength concept (ΣV) and the CHARDI concept (ΣQ).

	Ce1	Ce2	Ce3	Ge1	Ge2	Ge3	Ge4	Ge5
ΣQ	+2.99	+2.96	+2.95	+3.96	+3.97	+3.74	+3.89	+4.17
ΣV	+3.11	+2.53	+3.11	+4.20	+3.74	+4.09	+4.12	+3.98
	01	02	03	04	05	06	07	08
ΣQ	-1.90	-2.16	-1.98	-2.07	-2.11	-1.98	-2.07	-1.86
ΣV	-1.76	-2.05	-2.00	-2.09	-2.06	-1.88	-2.10	-1.80
	09	010	011	012	013	014	015	B1
ΣQ	-2.15	-2.16	-2.13	-2.13	-1.90	-1.91	-1.49	+3.24
ΣV	-2.27	-2.03	-2.10	-2.09	-1.86	-1.82	-1.77	+2.89

4.2.3.6 Conclusion

Following the pressure-coordination rule [192], the coordination numbers of boron and germanium exhibit the highest known values 4 and 6, respectively. In contrast to all known borogermanates, the compound $\text{Ce}_6(\text{BO}_4)_2\text{Ge}_9\text{O}_{22}$ is the first one with a simultaneous realization of $[\text{BO}_4]^{5-}$ tetrahedra in combination with $[\text{GeO}_6]^{8-}$ octahedra. Additionally, a three-fold coordinated oxygen atom $\text{O}^{[3]}$, linked to one boron and two germanium atoms, was observed for the first time. From these results, we think it is possible to have access to new high-pressure phases with interesting structural features in the substance class of borate germanates.

As mentioned in the introduction (Chapter 1), the stabilisation of high coordination numbers and high oxidation states is possible through applying high pressures. In the next Chapter a new access into gallium oxonitrides is given, in which the parameter pressure was used for pressure induced crystallisation. It will also be shown that the success depends extremely on a clever chosen precursor material.

4.3 Gallium Oxonitrides

4.3.1 Introduction

Ceramics and single crystalline phases in the solid solution system GaN-Ga₂O₃ are scarcely investigated, even though the system promises a high potential for industrial relevant properties stressed by the analogous phases in the well-investigated system AlN-Al₂O₃ designated as alon phases. Recently, *Kinski et al.* reported on a new approach to the formation of bulk gallium oxonitride *via* a pyrolysis process [224]. The reported new synthesis pathway, using molecular precursors with defined bonding of gallium simultaneously to nitrogen and oxygen, led to nanocrystalline GaON ceramics at low temperatures of 350 °C with variable N/O ratios of 0.86 to 2.1 controlled by the chemical composition of the molecular precursor. Because of their composition and nanocrystallinity, these ceramics provide an ideal starting material for high-pressure / high-temperature experiments to form highly crystalline gallium oxonitride phases.

For a theoretical ideal phase composition of Ga₃O₃N with a spinel structure, *Lowther et al.* calculated a lattice constant of $a_0 = 8.20 \pm 0.07 \text{ \AA}$ [218]. Considering other theoretical simulations, the end member phases *wurtzite* type GaN and monoclinic β -Ga₂O₃ tend to form from solid solutions resulting in a phase separation [219]. This situation and the fact that networks build up from Ga-O-Ga and Ga-N-Ga units are seldomly reported in literature and never found with a high degree of crystallinity, make the synthesis of new crystalline phases in the system GaN-Ga₂O₃ challenging. Therefore, the most promising starting materials are not the already existing crystalline end member phases GaN and Ga₂O₃, using a solid-state reaction, but new nanocrystalline GaON ceramics. This approach provides a method that bypasses the formation of the stable end members GaN with *wurtzite* type structure and monoclinic β -Ga₂O₃. Another ambient-pressure approach for the synthesis of GaN, which uses Ga(NO₃)₃ · x H₂O as starting material, was developed by *Jung et al.* [220] and modified in the *Riedel* group providing a *spinel* type structure gallium oxonitride with a low degree of crystallinity displayed in the powder X-ray diffraction pattern in Figure 4.3-1. From elemental analysis, the chemical formula was calculated to Ga_{2.7}N_{3.66}O_{0.34}, but the degree of crystallinity could not be improved by optimization of the pyrolysis- or tempering-parameters. This emphasizes the necessity of a high-pressure / high-temperature approach with appropriate starting materials to reach phases with high crystallinity in the system GaN-Ga₂O₃.

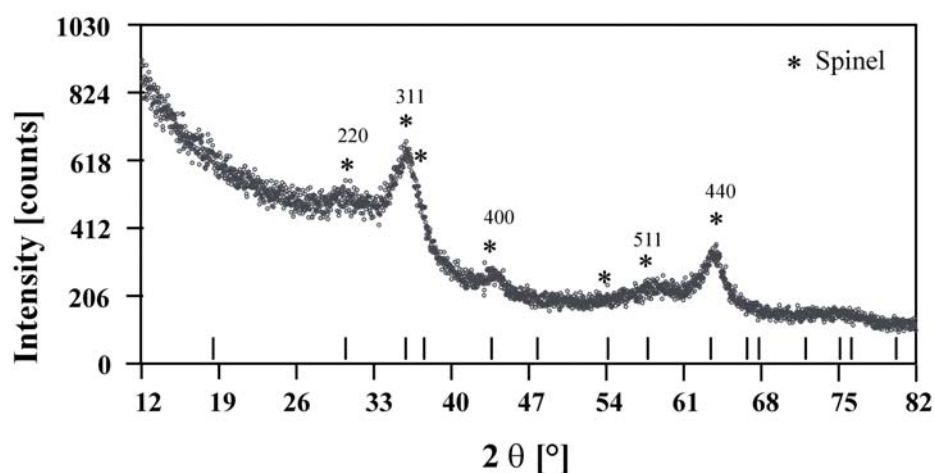


Figure 4.3-1: Observed powder X-ray diffraction pattern ($\text{CuK}\alpha_1$) of a *spinel* type structure gallium oxonitride with a low degree of crystallinity synthesized *via* a pyrolysis process using $\text{Ga}(\text{NO}_3)_3 \cdot x \text{H}_2\text{O}$ as starting material.

The subsequent experiments are results of the preliminary works for a research grant within the Deutsche Forschungs Gemeinschaft (DFG). All experiments were carried out in cooperation with *I. Kinski et al.*, Institute of Materials Science, Dispersive Solids, Darmstadt University of Technology, who was involved in the precursor preparation and the following characterisation of the Ga-O-N species. The high-pressure experiments and their optimization were performed within the context of this thesis and reveal a further example of the wide fields of application taking advantage of the parameter pressure.

4.3.2 The Spinel Type Structure of $\text{Ga}_{2.81}\text{O}_{3.57}\text{N}_{0.43}$

4.3.2.1 Synthesis

General: All reactions and operations were carried out under inert conditions with rigorous exclusion of oxygen and moisture. All solvents were dried and distilled from a Na/K alloy prior using.

Syntheses of the educts and the precursor: Lithiumdimethylamide (LiNMe_2) and bis(trisdimethylamino)gallane ($[\text{Ga}(\text{NMe}_2)_3]_2$) were synthesized following the literature procedures [221, 222]. The molecular precursor $[\text{Ga}(\text{O}^t\text{Bu})_2\text{NMe}_2]_2$, with gallium simultaneously bonded to nitrogen and oxygen, was synthesized by a modified reaction procedure according to equation (16) [223].



Synthesis of the GaON ceramic: The novel nanocrystalline ceramic was derived from the molecular precursor in ammonia atmosphere at elevated temperatures in quartz glass Schlenk tubes via a pyrolysis process reported in reference [224]. Therefore, the precursor $[\text{Ga}(\text{O}^t\text{Bu})_2\text{NMe}_2]_2$ was homogeneously distributed in an Al_2O_3 boat deposited in the hottest zone of a furnace within a quartz glass Schlenk tube. The pyrolysis was performed in dry ammonia with a heating rate of $100 \text{ }^\circ\text{C}/\text{h}$ up to the holding temperature of $350 \text{ }^\circ\text{C}$. The maximum temperature was kept constant for two hours with subsequent cooling to ambient temperatures.

Experiments under HP/HT conditions: For the high-pressure / high-temperature treatment of the new material, the GaON ceramic was filled into a molybdenum capsule (outside diameter: 2.35 mm; wall thickness: 0.25 mm), which was inserted the other way round in a second molybdenum capsule (inner diameter: 2.45 mm) under argon in a glove box. To prevent a reaction between the molybdenum capsules and the graphite furnace, the sample capsule was loaded into a 3.66 mm outside diameter, 0.33 mm wall thickness, and 6.0 mm length hexagonal boron nitride cylinder, that was sealed by a BN plate. This arrangement was placed as described in Chapter 2.2.3 into the center of a cylindrical resistance heater (graphite) with variable wall thickness. The other steps of mounting the assembly were equal.

For the reaction, the assembly was compressed in 3 hours to 7.0 GPa and heated up to $1000 \text{ }^\circ\text{C}$ in the following 10 min. After holding this temperature for 10 min, the sample was quenched to room temperature. After decompression, the recovered experimental octahedron was broken apart in a glove box and the sample carefully separated from the surrounding Mo and revealed as transparent greenish crystals.

4.3.2.2 Analytical Methods

Transmission electron microscopy and electron energy loss spectroscopy were performed on a Jeol JEM 3010 microscope operated at 300 kV with LaB_6 filament and post column energy filter (Gatan imaging filter (GIF)). The spatial resolution for the elemental analysis is about 2 nm. In order to determine the structure of the crystalline high-pressure phase a Philips CM20 microscope with LaB_6 cathode operated at 200 kV and equipped with an energy-dispersive X-ray (EDX) system (Voyager,

HPGe-detector) was used. For selected-area electron diffraction (SAED) the camera length was calibrated through an external Au-standard.

X-ray powder diffraction data were collected with a STOE Stadi/P diffractometer equipped with a linear position sensitive detector (6°) using transmission geometry ($\text{CuK}\alpha_1$ and $\text{MoK}\alpha_1$ radiation). X-ray powder data were measured from 5° to 50° 2θ with a step size of 0.02° 2θ and a counting time of 120 sec per step. For phase analysis and structure refinement the program Winplotr package was used [225]. The morphology of the crystals (see Figure 4.3-2) was visualized using a scanning electron microscope (SEM) (Jeol 6300F). Table 4.3-1 gives all information derived from the structure refinement.

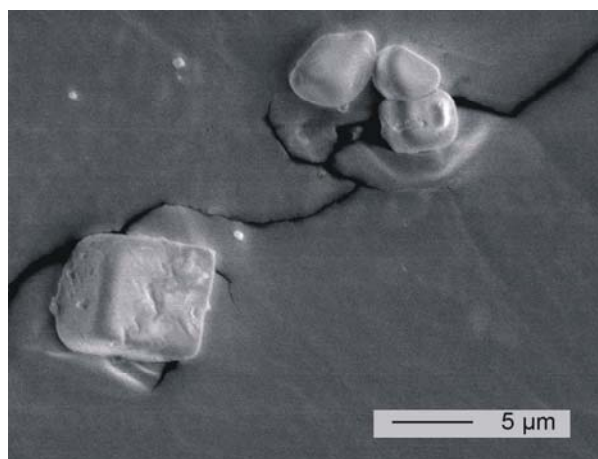


Figure 4.3-2: In the SEM picture the morphology of the crystals point to a cubic habitus though faces and edges are not clearly grown.

Table 4.3-1: Crystal data of $\text{Ga}_{2.81}\text{O}_{3.57}\text{N}_{0.43}$

Empirical formula	$\text{Ga}_{2.81}\text{O}_{3.57}\text{N}_{0.43}$			
Space group	$Fd3m$ (Nr. 227)			
Lattice constant a_0 (Å)	8.264 ± 0.1			
Unit cell volume (Å ³)	564			
Z	8			
x parameter	0.250(5)			
Atom	Wyckoff site	x/a	y/b	z/c
Ga	8a	1/8	1/8	1/8
Ga	16d	1/2	1/2	1/2
(O, N)	32e	0.250(5)	0.250(5)	0.250(5)

4.3.2.3 Results and Discussion

For the high-pressure / high-temperature treatment, the starting material was a nanocrystalline GaON ceramic with a mean N/O ratio of 0.86 that was derived from $[\text{Ga}(\text{O}^t\text{Bu})_2\text{NMe}_2]_2$ as precursor at 350 °C in ammonia atmosphere. After the high-pressure / high-temperature experiment, the retrieved transparent crystals displayed a light greenish color in a microscope with polarized-light. In order to get an overview about the homogeneity of the sample and the structural characteristics, EDX spectroscopy was used to distinguish between residual molybdenum particles from the capsule, side products, and newly formed crystallites.

All the crystallites of the new phase exhibited the same high degree of crystallinity and stability in the electron beam during TEM analysis. Figure 4.3-3 shows the selected-area electron diffraction (SAED) pattern indicating a cubic face centered cell. Extinctions owing to a d -glide plane perpendicular to the 4-fold axis ($hk0$ present only for $h + k = 4n$) indicate space group $Fd3m$ (Nr. 227) leading to a *spinel* type structure. Extinctions and pseudo-extinctions within the zone $[120]$ (Figure 4.3-3) prove this suggestion.

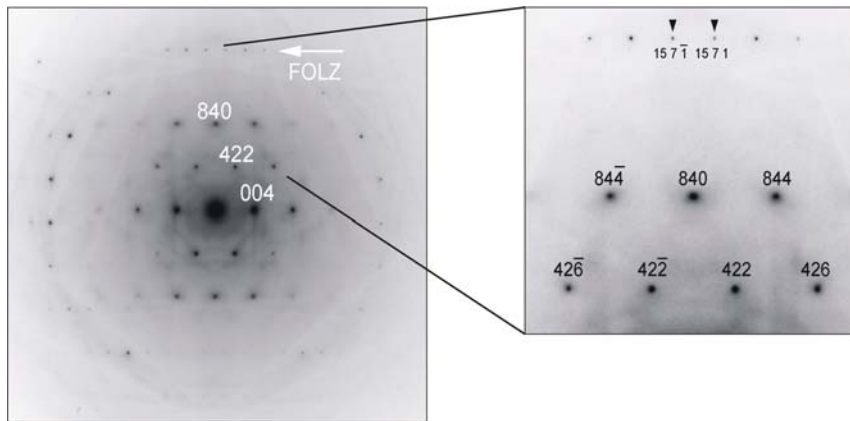


Figure 4.3-3: Electron diffraction pattern of zone [120]. The zero order Laue zone (ZOLZ) displays only reflections with all indices even. Because of the anion position at x, x, x with the special value $x = \frac{1}{4}$, only reflections with $h + k + l = 4n$ are present (see magnified area on the right side). The row of reflections marked by an arrow in the 1st order Laue zone (FOLZ) indicates where the missing ZOLZ-reflections should be.

In the following, the general conditions limiting possible reflections due to F -centering (h, k, l all even or all odd) are always presupposed. Zone [120] is spanned by the reflections 002 and 420. These two reflections are extinct because of the d -glide plane ($hk0$ present only for $h + k = 4n$). However, in the central part of Figure 4.3-3 - which represents the zero order Laue zone - reflections with $h + k + l \neq 4n$ are generally absent - also if none of the indices is 0 (002 and 002 are present as very weak spots owing to multiple diffraction by interaction with FOLZ-reflections). This extinction cannot be described by a crystallographic glide plane. It allows an estimation of the positional parameters of the anion and is interpreted as follows:

In a spinel structure the atomic positions depend on the choice of setting for the origin in the space group $Fd3m$. The equipoint with point symmetry $3m$ as unit cell origin was chosen. The cations occupy Wyckoff positions $8a$ ($1/8, 1/8, 1/8$) and $16d$ ($1/2, 1/2, 1/2$) with the special conditions limiting possible reflections, respectively:

- for positions $8a$ ($1/8, 1/8, 1/8$) hkl present only for $h + k + l = 2n + 1$ or $4n$
- for positions $16d$ ($1/2, 1/2, 1/2$) hkl present only for h, k, l all $2n + 1$ or all $4n$ or all $4n + 2$.

If both positions are occupied the parity group of *forbidden* reflections may be expressed as follows:

- $h + k + l = 4n + 2$ (negation of $8a$) and *not* all indices of type $4n + 2$ (negation of $16d$).

The anion occupies Wyckoff position 32e (x, x, x). No limiting condition is associated with this position. Therefore, any special limiting condition should be overruled if this position is occupied. There is, however, a very special case: If $x = 1/4$, the atoms occupying site 32e form a Cu type *fcc* structure with $a_0' = 1/2 a_0$. Therefore, an "accidental" special condition for possible reflections is generated: $h k l$ present only if:

- all h, k, l are of type $4n + 2$ (corresponding to "all odd" for $a_0' = 1/2 a_0$)
- or all h, k, l are of type $4n$ (corresponding to "all even" for $a_0' = 1/2 a_0$).

This means that reflections of the above mentioned parity group $h + k + l = 4n + 2$ and *not* all indices of type $4n + 2$ are extinct as well if position 32e (x, x, x) is occupied with $x = 1/4$. However, these reflections gain intensity as soon as x deviates from $1/4$. (Note that there is no special position $1/4, 1/4, 1/4$ in space group *Fd3m*). From the absence of those reflections in the zero order Laue zone in the diffraction pattern shown in Figure 4.3-3 and from the degree of overexposure of the photographic negative, one can therefore conclude that x is very close to $1/4$. As estimated from model calculations, reflections of this parity group should be visible in Figure 4.3-3 if x deviates by more than ≈ 0.005 from $1/4$.

For an accurate determination of the lattice constant a_0 an XRD pattern was recorded displayed in Figure 4.3-4. Residuals of the molybdenum capsule can be distinguished next to the main spinel phase in the powder XRD pattern caused by the sample preparation. Additionally, the XRD diagram exhibits the diffraction patterns of cubic $\gamma\text{Mo}_2\text{N}$ and hexagonal *wurtzite* GaN as by-products indicating a loss of nitrogen and formation of GaN from the GaON ceramic during transformation to the crystalline spinel structure under high-pressure. From the refined pattern the lattice constant a_0 of the spinel phase was determined to be $8.264(1) \text{ \AA}$. This lattice constant is slightly larger than the value of 8.22 \AA found for the lattice constant of the metastable *spinel* type structure of $\gamma\text{Ga}_2\text{O}_3$ first reported by *Pohl* [226]. In order to distinguish the new spinel phase from the known $\gamma\text{Ga}_2\text{O}_3$, the nitrogen to oxygen content of the crystallites were recorded using EEL spectra in the TEM analysis (see Figure 4.3-5). The results, which are listed in Table 4.3-2, exhibit a nearly similar atomic N/O ratio of $0.12(2)$ on all crystallites. Obviously, most of the nitrogen (starting ratio $\text{N/O} = 0.86$) has reacted to the former mentioned metal nitrides. Nevertheless, a significant part of nitrogen is built-in the spinel structure. Therefore, we propose rather a gallium oxonitride than a pure $\gamma\text{Ga}_2\text{O}_3$ phase. Using the assumption of a filled anion substructure without any vacancies for the new GaON spinel, the theo-

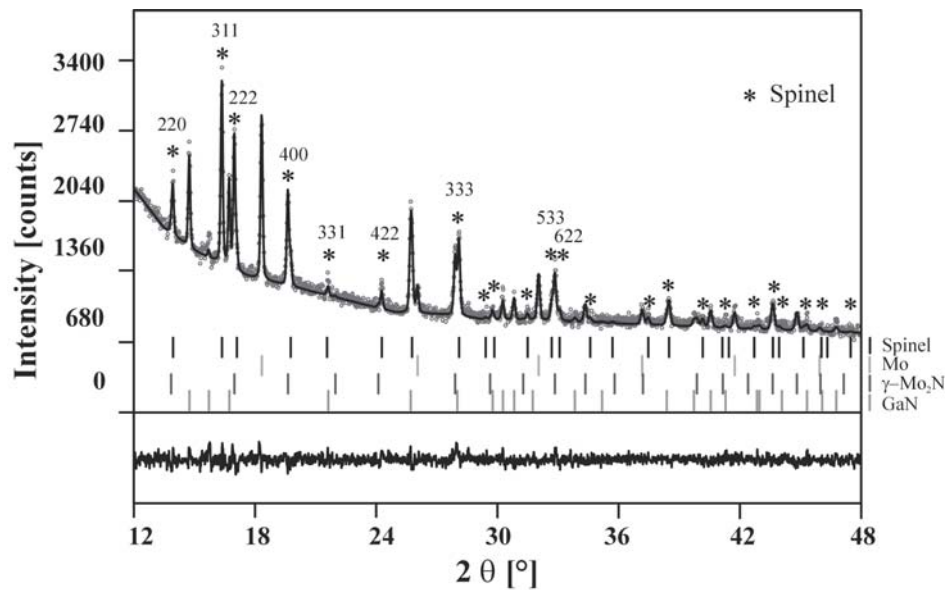


Figure 4.3-4: The structure refinement was performed on a powder X-ray diffraction pattern. Next to the main spinel phase, residual particles of the Mo capsule and by-products of $\gamma\text{-Mo}_2\text{N}$ and hexagonal GaN contribute to the observed and calculated X-ray powder diffraction pattern. The Bragg positions of all four phases are displayed underneath the observed and calculated intensities, respectively, as well as the difference curve.

retical chemical formula $\text{Ga}_{2.81}\text{O}_{3.57}\text{N}_{0.43}$ can be calculated from the N/O ratio if charge neutrality is maintained.

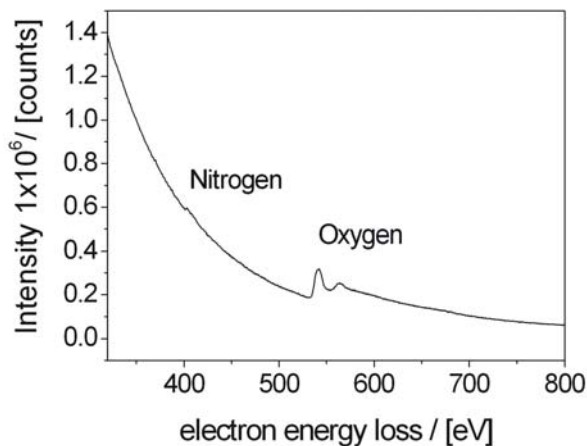


Table 4.3-2: TEM analysis of the atomic ratio N/O on several different crystals and different positions determined with EEL spectroscopy.

N/O
0.09 ± 0.01
0.12 ± 0.02
0.11 ± 0.019
0.15 ± 0.015
N/O = 0.12(2)

Figure 4.3-5: Electron energy loss spectroscopy performed on a spinel GaON crystal during TEM analysis with a beam resolution of 2 nm. The quantitative analysis of the two characteristic edges for nitrogen and oxygen results in a mean atomic ratio of 0.12(2).

Considering the model developed by *McCauley* for the alon phases, the ideal spinel structure demands 32 anion sites and 24 cation sites for maintaining charge balance. This takes into account that there might be vacancies occurring in the cation sites while the occupation of the anion sites are kept constant [227]. This is

the designated constant anion model, in which the general formula for the GaON-spinel results in:



Inside this formula, the symbol “ \oplus ” stands for a cation vacancy. The ideal spinel is represented by the value $x = 8$.

Screening the literature, *Puchinger et al.* reported on a similar gallium oxonitride with *spinel* type structure proposing a composition of $\text{Ga}_{2.8}\text{O}_{3.5}\text{N}_{0.5}$ [228]. This phase formed in small areas as an impurity on a thin GaN film and was determined using HRTEM-SAED coupled with EEL and Auger spectroscopy.

Interestingly, an analogous phase to the here presented new $\text{Ga}_{2.81}\text{O}_{3.57}\text{N}_{0.43}$ spinel phase can be found in the system AlN-Al₂O₃. With a given composition of $\text{Al}_{2.81}\text{O}_{3.56}\text{N}_{0.44}$ (ICDD-JCPDS No. 80-2172, lattice constant $a_0 = 7.95 \text{ \AA}$ [229]), the compound fits nearly exactly the theoretical value of the here presented gallium oxonitride. Due to the substitution of Al \rightarrow Ga, a comparison of the lattice parameters seems worthwhile. Therefore, we consider the changes between the phase γ -Al_{2.14}O_{3.2} (commonly referred to as γ -Al₂O₃) and the analogous γ -Ga₂O₃ phase, in which the substitution of Al³⁺ against Ga³⁺ leads to an increase of the lattice constant from $a_0 = 7.911 \text{ \AA}$ (γ -Al_{2.14}O_{3.2} [230]) to $a_0 = 8.22 \text{ \AA}$ (γ -Ga₂O₃ [226]) corresponding to an increase of 3.9%. Enhancing the value of the former mentioned phase Al_{2.81}O_{3.56}N_{0.44} ($a_0 = 7.95 \text{ \AA}$) by 3.9% leads to an expected lattice constant of about 8.26 \AA for the analogous Ga-compound, which fits well to the measured value of $8.264(1) \text{ \AA}$ for $\text{Ga}_{2.81}\text{O}_{3.57}\text{N}_{0.43}$.

4.3.2.4 Conclusion

Though there are some reports on gallium oxonitrides in the literature, the structural features of these compounds could only be proposed. Former investigations suffered on the low degree of crystallinity. With the synthesis of $\text{Ga}_{2.81}\text{O}_{3.57}\text{N}_{0.43}$, it was possible to realize a characterizable, highly crystalline phase of the solid solution between the binary compounds GaN and Ga₂O₃ for the first time. The novel phase crystallizes under high-pressure / high-temperature conditions in a *spinel* type structure with the space group *Fd3m* (No. 227) exhibiting a lattice constant of $a_0 = 8.264(1) \text{ \AA}$ and an x parameter of 0.250(5) causing extinctions in the TEM diffraction pattern. The high degree of crystallinity was not only revealed by TEM diffraction but also by powder X-ray diffraction.

Shortly after the publication of these results, *Soignard et al.* reported about the multianvil high-pressure synthesis of another spinel-structured gallium oxonitride $\text{Ga}_3\text{O}_3\text{N}$ [231]. Due to vacancies on the octahedrally coordinated Ga sites, the experimental stoichiometry was given as $\text{Ga}_{2.8}\text{O}_{3.24}\text{N}_{0.64}$. The structure was refined based on X-ray powder data by *Rietveld* methods in the space group *Fd3m* with a lattice parameter of $a = 8.281(2) \text{ \AA}$, slightly larger than in the here presented compound. Furthermore, Raman and photoluminescence spectra as well as electronic band structure calculations were presented in this paper.

The here presented results give strong evidence for realizing further compounds in the system $\text{GaN}/\text{Ga}_2\text{O}_3$ using different GaON ceramics in combination with extreme conditions of pressure and temperature. These experiments will be carried out in the context of the new DFG Priority Program SPP1236 "Synthesis, *in-situ* characterization, and quantum mechanical modeling of earth materials, oxides, carbides, and nitrides at extremely high-pressures and temperatures". The here presented results laid the foundations of this new DFG project.

Dipl.-Chem. S. Hering, who followed up this project during her diploma works, was presumably able to synthesize a gallium oxonitride spinel compound with the up to now highest nitrogen concentration of 25% [232]. Therefore, the ideal spinel stoichiometry $\text{Ga}_3\text{O}_3\text{N}$ could be assumed, but one Ga site was not fully occupied which resulted in a defect *spinel* type structure of the composition $\text{Ga}_{2.79}\text{O}_{2.80}\text{N}_{0.93}$. The structure was refined on the basis of single crystal data and the corresponding cubic lattice parameter $a = 8.289(3) \text{ \AA}$ (powder data) is in the range of the other spinel compounds.

Further experiments revealed that high crystalline $\gamma\text{-Ga}_2\text{O}_3$ can be formed under high-pressure / high-temperature conditions as well, and a completely detailed characterization accounts to our future goals.

In contrast to borates, silicates, or nitrides, high-pressure investigations of alloys or intermetallic phases are rare. The following part of this thesis concerns with the examination of selected ternary intermetallic phases and their structural transitions under high-pressure / high-temperature conditions as well as their physical properties.

4.4 Ternary Intermetallic Phases Synthesized at HP/HT-Conditions

4.4.1 Introduction

Going back in history, alloys and intermetallic compounds are among the oldest and most important man-made materials. Even two ages in human civilization, the Bronze and the Iron Age demonstrate with their names the importance of metals for the development of culture and progress. The properties of metals and alloys were useful for mankind right from the start of the first civilizations and grew to a steady companion. As means of payment, tools, weapons, or as materials for medical prostheses metals conquered an important key role in first advanced cultures. The knowledge of better alloys could not only decide in ancient world or in the Middle Age about the end of wars or the welfare of a whole nation.

Today, alloys or intermetallic phases and their various properties and utilization cause constant interest for inorganic chemists, physicists, and material scientists. The largest deductive potential lays among the metallic elements, which are numerical by the largest group of the Periodic Table. But about the structures and the chemical bonding situation in alloys and intermetallic phases we do know less than for a lot of other chemical systems. The basic difference between the two groups of phases is that alloys in general exhibit homogeneity ranges, whereas intermetallic compounds are defined by a - at least in principle - definite composition.

The development of an understanding of systematic trends concerning phase stability is one of the central points in the chemistry of intermetallic compounds. In this context, the following Chapters of high-pressure / high-temperature investigations of ternary intermetallic phases can be seen. High-pressure is one of the fundamental state variables, which can be varied in order to uncover factors governing stability fields of structure and bonding types as well as to separate electronic effects from packing aspects. In quantum chemical calculations, compressions can be easily simulated by a corresponding reduction of the unit cell parameters and therefore it is a useful tool to predict new compounds or structure types [233].

In the period of the last two years, only a few new papers in the field of preparative high-pressure investigations of intermetallic phases were published. A short summary about this progress is given in the following.

Concerning the binary compounds, the new high-pressure phase MgCu with CsCl type structure was described [234]. MgCu is formed at pressures of 6 GPa and temperatures of 800 °C, but the metastable phase decomposes at temperatures higher than 520 K into the phases Mg₂Cu and MgCu₂.

Investigations of binary silicides in diamond anvil cells up to pressures of 30 GPa showed for Fe_5Si_3 (Mn_5Si_3 type) an isotropic contraction of the lattice parameter, but no structural phase transformation [235]. Similar experiments were performed also at binary iron stannides [236]. Up to pressures of 25 GPa the phases FeSn , FeSn_2 , Fe_5Sn_3 , and Fe_3Sn revealed no structural changes, whereas Fe_3Sn_2 passed through two structural transformations. The crystal structures are not clarified up till now.

Very interesting are also the investigations of potassium-copper-samples in a Mao-Bell-diamond anvil cell [25]. These *in-situ* high-pressure experiments with X-ray diffraction detection gave hints of the existence of three compounds with the approximate composition K_2Cu , KCu , and KCu_2 . Recently, a good review article published by *Demchyna et al.* summarized the whole structure chemistry of binary intermetallic high-pressure phases [233]. Beside structural data, also details about bonding situations were discussed. The different high-pressure modifications of the metallic elements were summarized by *McMahon* and *Nelmes* in a review article [237] published in a special high-pressure edition [238].

During the research of ternary intermetallic phases, the new filled *skutterudite* $\text{TbFe}_4\text{P}_{12}$ was discovered, synthesized at 4 GPa and 1050 °C [239]. Many of these phosphides with filled *skutterudite* structure were formed only under high-pressure / high-temperature conditions. The metallic compound $\text{TbFe}_4\text{P}_{12}$ orders ferromagnetically at a temperature of 10 K. Another new phosphide also synthesized under high-pressure conditions of 2 GPa and 1873 K is the compound MoIrP with TiNiSi type structure [240]. In contrast to MoRuP and MoNiP , no transition into a superconducting state was observable down to 2 K.

At 3 GPa and 800 °C a very interesting solid solution of $\text{Ba}_{8-\delta}\text{Si}_{46-x}\text{Ge}_x$ ($0 \leq x \leq 23$) with clathrate-I structure was synthesized [241]. These silicide germanides show superconductivity with falling critical temperature T_c from 8.0 to 2.0 K. The silicides EuSi_6 and $\text{EuSi}_{6-x}\text{Ge}_x$ ($x = 0-0.60$) with EuGa_2Ge_4 type structure were formed at 8 GPa and 1520 K [242]. EuSi_6 is built up from a three dimensional network of four bonded silicon atoms in which the divalent europium ions are embedded. Hence, the following Zintl analogue ionic formula can be assumed: $\text{Eu}[\text{Si}^0]_6 \cdot 2e^-$. The same structure type was also found for SrSi_6 [243] and BaSi_6 [244].

Beside the single preparative approach, a series of publications concerning structural characteristics or physical properties at high-pressure conditions, which are not mentioned here, can be found in the literature. At the present state, two countries, Japan and China, develop a strong effort in materials chemistry under high-pressure conditions. For that reason the COST Commission (European Cooperation in the Field of Scientific and Technical Research) financially supported of

the European Commission, founded a network to provide “Materials Chemistry under High-Pressures” in Europe. Six groups (2 Spanish, 1 French, 1 Scottish, and 2 German) were selected, all featured with different competences required for developing such research activities: a team involved in the synthesis of specific precursors, three research groups specialized in different high-pressure techniques in materials chemistry, and research groups developing specific physico-chemical characterization methods well adapted to the small quantities of materials prepared under high-pressure conditions. The groups of Prof. Dr. R. Pöttgen (Institut für Anorganische und Analytische Chemie, Universität Münster) and PD Dr. H. Huppertz have been embedded as the two German groups into this network, which had in a first approach three main scientific objectives: *(i)*, the stabilization of oxides with mixed valences; *(ii)*, the stabilization of unusual oxidation states of transition metals; and *(iii)*, the structural transformation under high-pressure conditions.

The following part of this thesis deals with the last of the three objectives and was performed in cooperation with Dipl.-Chem. J. F. Riecken (Institut für Anorganische und Analytische Chemie, Universität Münster) during his PhD work. Thereby, the work was split into the synthesis of the precursor compounds, which was performed by Dipl.-Chem. J. F. Riecken in Münster and the subsequent high-pressure / high-temperature experiments performed in Munich. The following characterization of the normal-pressure and high-pressure phases happened in Münster as well as in Munich, depending on the characterization method and the available equipment. Published results in cooperation with the other members of the COST group are summarized in Chapter 4.5.

At the beginning of the project, the choice of appropriate precursor compounds was an important point. For the first orienting experiments, already known and well characterized compounds of the *Pöttgen* group were used. The following ternary intermetallic compounds were tested in a first run: NbIrSi, TaIrSi, CeNiSn, CeRhGe, CeIrGe, CeCuSn, CePtSn, CePtIn, EuPdSn, EuPtSn, YbPtSn, and YbAuIn.

The first experiments quickly revealed that the orthorhombic stannide CePtSn went through a structural transformation. Systematic investigations of the corresponding other rare-earth platinum stannides led to the development of trends (see Chapter 4.4.3). In a first step, the transition metal component was changed from Pt to Pd and Ni (see Chapter 4.4.4 and 4.4.5) in order to observe the behaviour of the system. In the second step, the structure type of the precursor compound was changed and the supposed structural transformation took place (see Chapter 4.4.8). Without varying the structure type again, in a third step, the main group component tin was replaced through germanium and surprising results were obtained (see Chapter 4.4.8).

4.4.2 Starting Materials

For the preparation of the intermetallic precursors, various commercially available metals were used. Table 4.4-1 lists up the different elements, state, purity, and source of supply.

Table 4.4-1: Purity and source of supply of commercially available substances

Substance	State	Purity	Source of Supply
Lanthanum	Ingots	>99.9%	Chempur, Karlsruhe, Germany
Cerium	Ingots	> 99%	Johnson Matthey, London, England
Praseodymium	Ingots	>99.9%	Chempur, Karlsruhe, Germany
Neodymium	Ingots	>99.9%	Johnson Matthey, London, England
Samarium	Ingots	>99.9%	Chempur, Karlsruhe, Germany
Erbium	Ingots	>99.9%	Johnson Matthey, London, England
Nickel	Powder (200 mesh)	>99.9%	Degussa-Hüls, Düsseldorf, Germany
Palladium	Powder (200 mesh)	>99.9%	Degussa-Hüls, Düsseldorf, Germany
Platinum	Powder (200 mesh)	>99.9%	Degussa-Hüls, Düsseldorf, Germany
Silver	Wire (Ø 1mm)	>99.9%	Degussa-Hüls, Düsseldorf, Germany
Gold	Wire (Ø 1mm)	>99.9%	Degussa-Hüls, Düsseldorf, Germany
Germanium	Bar	>99.9%	Wacker, Burghausen, Germany
Tin	Granules/bar	> 99.999%	Heraeus / Merck, Germany

4.4.3 The Stannides $REPtSn$ ($RE = La-Nd, Sm$)

4.4.3.1 Introduction

The equiatomic $REPtSn$ ($RE =$ rare-earth element) stannides have first been synthesized by Dwight and coworkers some thirty years ago [272] and preliminary magnetic studies were performed in the *Yakinthos* group [268]. Later, these stannides have intensively been studied with respect to their interesting magnetic and electronic properties. A good literature overview on the manifold work is given in [245, 246 and ref. therein]. Especially the equiatomic cerium intermetallics $CeTX$ ($T =$ transition metal; $X =$ element of the 3rd, 4th, or 5th main group) have attracted considerable interest by solid-state chemists and physicists in the last 15 years, due

to their largely varying magnetic and electrical properties, such as mixed valency, Kondo behaviour, ferro- or antiferromagnetic ordering, metamagnetism, or heavy Fermion behaviour. An overview on the many compounds is given in [245, 247, 248, 305].

A peculiar compound in the series of these $CeTX$ intermetallics is the stannide $CePtSn$, which was synthesized for the first time by *Sakurai et al.* [249]. The orthorhombic $TiNiSi$ type structure was evident from the X-ray powder data. In a subsequent single crystal study *Higashi et al.* [257] assigned a non-centrosymmetric variant of the $TiNiSi$ type in the space group $Pna2_1$. Subsequent X-ray and neutron diffraction studies [250, 258, 259] again confirmed the centrosymmetric $TiNiSi$ type structure.

$CePtSn$ has intensively been studied with respect to the outstanding magnetic and electrical properties. This stannide is a metallic Kondo lattice material, that orders antiferromagnetically around 8 K and shows an additional magnetic phase transition at 5.5 K. Neutron powder and single crystal data showed incommensurate magnetic ordering of the cerium magnetic moments [250-252, 259]. The magnetic structure seems to depend on the nature of the sample [259]. Inelastic neutron scattering showed well defined crystal field excitations at 24.0 and 34.9 meV [253]. In the magnetically ordered state, a transferred hyperfine field of 12 T at the tin nuclei can be detected at 1.5 K in the ^{119}Sn Mössbauer spectra [254].

With La, Ce, Pr, Nd, Sm, and Eu as rare-earth metal component, these stannides crystallize with the orthorhombic $TiNiSi$ type structure [263], while those with the smaller rare-earth elements adopt the hexagonal $ZrNiAl$ type [264, 322, 265]. This change in the crystal structure seems to be driven by the size of the rare-earth elements (lanthanoide contraction).

All these investigations were carried out under ambient pressure conditions. We have now studied $CePtSn$ under high-pressure / high-temperature conditions. Interestingly, NP- $CePtSn$ with $TiNiSi$ type structure transforms to HP- $CePtSn$ with $ZrNiAl$ type structure at 9.2 GPa and 1325 K. Since this is a reconstructive phase transition, the high-pressure samples can be quenched and characterized under ambient pressure conditions. Afterwards, the investigations were extended with respect to the $REPtSn$ stannides with $RE = La, Pr, Nd, Sm$, in order to complete the series. So far, only X-ray powder data of $LaPtSn$ [271, 255] and $PrPtSn$ [268, 277] have been reported, while no lattice parameters can be found in the literature for $SmPtSn$ [270]. The focus was set in the characterization of the new high-pressure phases but we did not miss the chance to fully characterize the normal-pressure modification as well.

4.4.3.2 Syntheses

Precursor

The arc-melting procedure took place in a furnace described in Chapter 2.1. Starting materials for the preparation of the intermetallic precursor are listed in Table 4.4-1. The larger rare-earth ingots were first cut into smaller pieces under paraffin oil and subsequently washed with *n*-hexane. The paraffin oil and *n*-hexane were dried over sodium wire. The small metal pieces were then arc-melted [27] to small buttons (ca. 500 mg) under an argon atmosphere of ca. 800 mbar and then kept under argon in Schlenk tubes prior to the reactions. The argon was purified over silica gel, molecular sieves, and titanium sponge (900 K). The pre-melting procedure for cerium strongly reduces shattering effects during the exothermic reaction with platinum and tin.

A cerium button was then mixed with a cold-pressed pellet of platinum and pieces of the tin granules in the ideal 1:1:1 atomic ratio and arc-melted under an argon pressure of about 800 mbar. The product button was remelted three times in order to ensure homogeneity. The total weight-loss after the melting procedures was smaller than 0.5 weight-%. The purity of the NP-REPtSn ($RE = \text{La-Nd, Sm}$) samples were studied *via* powder X-ray diffraction. NP-REPtSn ($RE = \text{La-Nd, Sm}$) melts congruently.

High-pressure / high-temperature treatment

The high-pressure/high-temperature treatment took place *via* a multianvil assembly. Boron nitride crucibles were loaded with carefully milled NP-REPtSn ($RE = \text{La-Nd, Sm}$), compressed within several hours to the synthesis pressure (9.2–13.5 GPa) and heated to temperatures between 1000 and 1400 °C in the following. After holding the corresponding temperature for some minutes, the samples were quenched or cooled down to temperatures between 500 and 850 °C within a minute. Subsequent annealing under pressure at elevated temperatures for several hours enhanced the crystallinity of the samples followed by quenching to room temperature. Table 4.4-2 gives a compilation of the exact synthesis conditions and temperature programs of the various high-pressure experiments. After decompression, the samples were carefully separated from the surrounding assembly parts and obtained as single phase products, except HP-LaPtSn, which always resulted in a mixture of HP- and NP-LaPtSn.

NP-REPtSn and HP-REPtSn are stable in moist air over weeks. The polycrystalline samples are silvery with metallic lustre. Powdered samples of both modifica-

tions are dark gray. The crystals investigated on the single crystal diffractometer were analysed using a Leica 420i scanning electron microscope equipped with an EDX detector. No impurities of elements heavier than sodium (the detection limit of the microscope) were observed. The compositions determined by EDX, exemplary for the neodymium compounds, (34 ± 2 at.-% Nd; 33 ± 2 at.-% Pt; 33 ± 2 at.-% Sn for NP-NdPtSn and 34 ± 2 at.-% Nd; 32 ± 2 at.-% Pt; 34 ± 2 at.-% Sn for HP-NdPtSn) were in good agreement with the ideal 1:1:1 composition. Additionally, a phase analysis on a flat grinded sample of HP-CePtSn was performed using a Leica 420i scanning electron microscope with CeO_2 , platinum, and tin as standards. Small variations in composition are displayed in Figure 4.4-1 as different shaded areas.

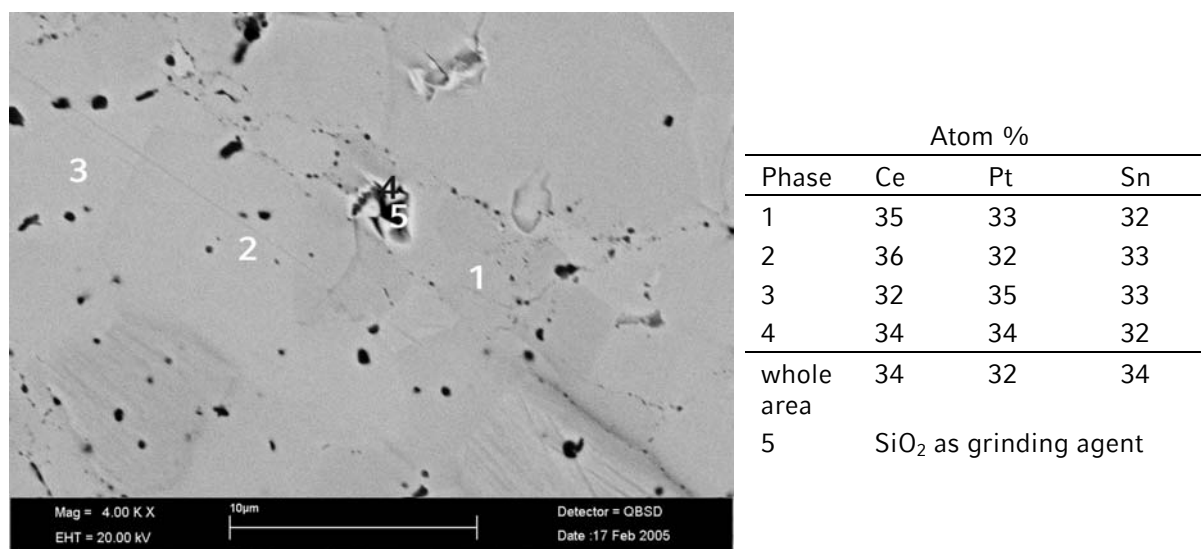


Figure 4.4-1: Phase analysis of a polished HP-CePtSn sample. Different compositions are displayed as different shaded areas. The exact atomic ratio is given in the table on the right side.

Table 4.4-2: Experimental details of the high-pressure / high-temperature experiments

Sample	Assembly	Max. pressure	Temperature program
HP-LaPtSn	14/8	11.5 GPa	↗ 1100 °C/20 min, → 1100 °C/3 min ↓ 900 °C/1 min, ↘ 900 to 500 °C/180 min, ↓ RT
HP-CePtSn	18/11	9.2 GPa	↗ 1000 °C/20 min, → 1000 °C/3 min ↓ 500 °C/1 min, → 500 °C/50 min, ↓ RT
HP-PrPtSn	14/8	10.5 GPa	↗ 1100 °C/20 min, → 1100 °C/3 min ↓ 700 °C/1 min, → 700 °C/140 min, ↓ RT
HP-NdPtSn	14/8	10.5 GPa	↗ 1150 °C/20 min, → 1150 °C/3 min ↓ 800 °C/1 min, ↘ 800 to 700 °C/240 min, ↓ RT
HP-SmPtSn	10/5	13.5 GPa	↗ 1400 °C/10 min, → 1400 °C/10 min, ↘ RT/10 min

↗ : increase of temperature in x min, → : constant temperature for x min, ↘ : decrease of temperature in x min, ↓ : quenching of the sample

4.4.3.3 Crystal Structure Analysis

The samples, high-pressure as well as normal-pressure phases were characterized through Guinier powder patterns using $\text{CuK}\alpha_1$ radiation and α -quartz ($a = 491.30$, $c = 540.46$ pm) as an internal standard. The orthorhombic and hexagonal lattice parameters (Table 4.4-4 to Table 4.4-7) were obtained from least-squares fits of the powder data. The correct indexing of the patterns was ensured through intensity calculations [256] taking the atomic positions from the structure refinements. The lattice parameters determined from the powders and the single crystals agreed well and they were also in good agreement with the literature data [257-260].

For the HP-CePtSn sample a *Rietveld* refinement was exemplary performed. The data are presented in Figure 4.4-2. The measurement was performed in transmission geometry with a flat sample using $\text{CuK}\alpha_1$ radiation ($\lambda = 154.0598$ pm, Ge monochromator). All experimental details are listed in Table 4.4-3.

The *Rietveld* calculations were performed with the FULLPROF [261] software. The background was set manually and the profiles were modeled using the pseudo-Voigt function. An arbitrary absorption value of $\mu R = 0.7$ was used. The experimen-

tal data of the refinement are summarized in Table 4.4-3. The standard deviations of the refined parameters were multiplied with the *Bérar-Lelann* factor [262]. The resulting positional parameters are listed in Table 4.4-8. The standard deviations of the x parameters for the rare-earth metal and the tin position are similar to the single crystal data. The powder data fully confirm the HP structure and show that the sample is very pure on the level of X-ray powder diffraction.

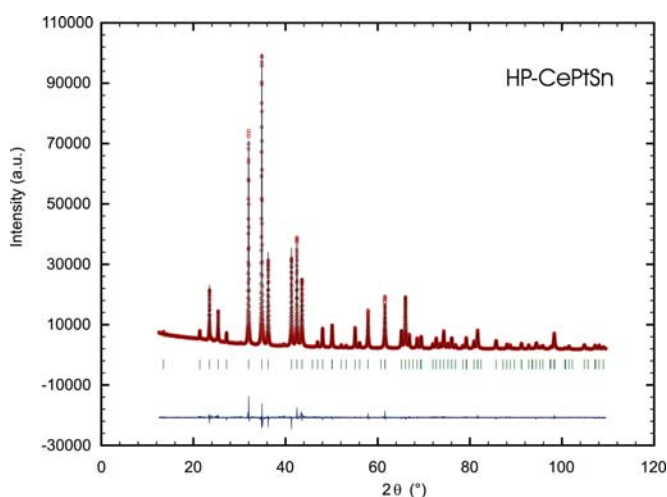


Figure 4.4-2: *Rietveld* refinement plot for HP-CePtSn in which the observed intensities are indicated with open circles and the calculated pattern with a line on top of the circles. The vertical lines indicate the Bragg positions. The difference $I(\text{obs})-I(\text{calc})$ is drawn below the Bragg indicators.

Table 4.4-3: X-ray powder data ($\text{CuK}\alpha_1$, $\lambda = 1.54051 \text{ \AA}$) and structure refinement for HP-CePtSn ($P6_2m$, $Z = 3$).

Empirical formula	CePtSn
Formula weight (g/mol)	453.91
Latt. param. (pm)	$a = 756.919(5)$
(diff. data)	$c = 415.166(4)$
Volume (nm^3)	0.2060
Cal. density (g/cm^3)	10.98
Abs. correction (μR)	0.70
$F(000)$	558
Range in 2θ ($^\circ$)	10–110
Scan mode, step width	$\omega/2\theta$, 0.01
No. data points	10000
Tot. no. Bragg reflect.	72
No. structure param.	8
No. total parameters	14
R_F , R_{wp}	0.037, 0.044
$R_{\text{Bragg}(I)}$	0.053
<i>Bérar-Lelann</i> Factor	5.66

Small single crystals of NP- and HP-REPtSn ($RE = \text{La-Nd, Sm}$) were isolated from the crushed samples. The crystals were first examined on a Buerger precession camera (equipped with an image plate system, Fujifilm, BAS-1800) in order to establish their suitability for intensity data collection. Single crystal intensity data were collected at room temperature by use of a four-circle diffractometer (CAD4) with graphite monochromatized $\text{MoK}\alpha$ (71.073 pm) radiation and a scintillation counter with pulse height discrimination. Scans were taken in the $\omega/2\theta$ mode. Empirical absorption corrections were applied on the basis of Ψ -scan data, followed by spherical absorption corrections. Some other crystals were measured on a STOE IPDS-I or II image plate system in oscillation mode. Numerical absorption corrections were applied to these data sets. All relevant details concerning the data collections and evaluations are listed in Table 4.4-4 to Table 4.4-7.

Analysis of the data sets was consistent with the space groups $Pnma$ and $P6_2m$ for NP- and HP-REPtSn ($RE = \text{La-Nd, Sm}$), respectively. The isotropy with the ortho-

rhombic TiNiSi [263] and the hexagonal ZrNiAl [264, 265] type structures was evident from the powder data. The starting atomic positions were deduced from automatic interpretations of *Directs methods* with SHELXS-97 [79] and all structures were refined using SHELXL-97 (full-matrix least-squares on F_o^2) [80] with anisotropic atomic displacement parameters for all sites. Refinement of the correct absolute structure of HP-REPtSn was ensured through refinement of the *Flack* parameter [266, 267]. The occupancy parameters of all crystals were refined in a separate series of least-squares cycles in order to check for the correct composition. In the case of CePtSn, they varied between 99.7(3)% for Pt and 100.3(4)% for Sn for NP-CePtSn and from 99.2(16)% for Sn and 101.5(15)% for Pt₂ for HP-CePtSn. Thus, all sites were fully occupied within one standard deviation. In the last cycles, the ideal occupancies were assumed again. Final difference Fourier synthesis revealed no significant residual peaks (see Table 4.4-6). The positional parameters and interatomic distances are listed in Table 4.4-4 to Table 4.4-10.

Table 4.4-4: Crystal data and structure refinement for NP-LaPtSn, NP-CePtSn, and NP-PrPtSn.

Empirical formula	NP-LaPtSn	NP-CePtSn	NP-PrPtSn
Molar mass (g·mol ⁻¹)	452.69	453.90	454.69
Crystal system		orthorhombic	
Space group		<i>Pnma</i>	
Radiation		CuK α_1 ($\lambda = 154.06$ pm)	
Powder-diffraction data			
<i>a</i> (pm)	755.8(1)	746.89(9)	742.81(6)
<i>b</i> (pm)	465.7(1)	462.88(4)	461.77(4)
<i>c</i> (pm)	805.3(1)	801.93(7)	802.30(5)
Volume (nm ³)	0.2835	0.2772	0.2752
Single crystal diffractometer	STOE IPDS II	CAD4	STOE IPDS II
Radiation		MoK α ($\lambda = 71.073$ pm)	
Formula units per cell		<i>Z</i> = 4	
Temperature (K)		293	
Calculated density (g·cm ⁻³)	10.61	10.87	10.97
Crystal size (μm^3)	20 x 30 x 60	10 x 10 x 20	20 x 30 x 30
Detector distance (mm)	60	-	60
Irradiation / exposure (min)	5	-	6
ω range, increment	0-180°, 1.0°	-	0-180°, 1.0°
Absorption coefficient (mm ⁻¹)	72.4	75.0	76.8
F(000)	740	744	748
θ Range	3° to 35°	3° to 30°	3° to 35°
Range in <i>hkl</i>	-12/+11, -7/+6, ± 12	$\pm 10, \pm 6, \pm 11$	$\pm 11, \pm 7, -12/+11$
Total no. reflections	3869	3014	3870
Independent reflections	683 ($R_{\text{int}} = 0.0367$)	452 ($R_{\text{int}} = 0.0644$)	653 ($R_{\text{int}} = 0.0594$)
Reflections with $I > 2\sigma(I)$	552 ($R_{\sigma} = 0.0405$)	415 ($R_{\sigma} = 0.0340$)	511 ($R_{\sigma} = 0.0480$)
Data / parameters	683 / 20	452 / 20	653 / 20
Absorption correction	numerical	psi-scan	numerical
Transm. ratio (max / min)	0.490 / 0.138	0.795 / 0.495	0.335 / 0.193
Goodness-of-fit (F^2)	0.897	1.065	0.867
Final <i>R</i> indices ($I > 2\sigma(I)$)	<i>R</i> 1 = 0.0252 <i>wR</i> 2 = 0.0541	<i>R</i> 1 = 0.0215 <i>wR</i> 2 = 0.0474	<i>R</i> 1 = 0.0286 <i>wR</i> 2 = 0.0470
<i>R</i> Indices (all data)	<i>R</i> 1 = 0.0368 <i>wR</i> 2 = 0.0558	<i>R</i> 1 = 0.0249 <i>wR</i> 2 = 0.0487	<i>R</i> 1 = 0.0457 <i>wR</i> 2 = 0.0500
Extinction coefficient	0.0067(3)	0.0023(3)	0.0026(2)
Larg. diff. peak and hole (e·Å ⁻³)	2.76 / -3.86	1.91 / -2.05	3.24 / -3.44

Table 4.4-5: Crystal data and structure refinement for NP-NdPtSn and NP-SmPtSn.

Empirical formula	NP-NdPtSn	NP-SmPtSn
Molar mass (g·mol ⁻¹)	458.02	464.13
Crystal system		orthorhombic
Space group		<i>Pnma</i>
Radiation		CuK α_1 ($\lambda = 154.06$ pm)
Powder-diffraction data		
<i>a</i> (pm)	737.2(1)	731.6(2)
<i>b</i> (pm)	460.0(1)	459.1(2)
<i>c</i> (pm)	799.6(2)	801.1(3)
Volume (nm ³)	0.2712	0.2691
Single crystal diffractometer		CAD4
Radiation		MoK α ($\lambda = 71.073$ pm)
Formula units per cell		<i>Z</i> = 4
Temperature (K)		293
Calculated density (g·cm ⁻³)	11.22	11.46
Crystal size (μm^3)	3 x 7 x 12	20 x 20 x 30
Absorption coefficient (mm ⁻¹)	79.1	82.2
F(000)	752	760
θ Range	3° to 30°	3° to 35°
Range in <i>hkl</i>	$\pm 10, \pm 6, \pm 11$	$\pm 11, -7/0, \pm 12$
Total no. reflections	2934	2413
Independent reflections	441 ($R_{\text{int}} = 0.1486$)	641 ($R_{\text{int}} = 0.1021$)
Reflections with $I > 2\sigma(I)$	313 ($R_{\sigma} = 0.0727$)	611 ($R_{\sigma} = 0.0653$)
Data / parameters	441 / 20	641 / 20
Absorption correction		psi-scan
Transm. ratio (max / min)	2.03	0.923 / 0.178
Goodness-of-fit (F^2)	1.086	1.046
Final <i>R</i> indices ($I > 2\sigma(I)$)	$R1 = 0.0331$ $wR2 = 0.0568$	$R1 = 0.0234$ $wR2 = 0.0453$
<i>R</i> Indices (all data)	$R1 = 0.0678$ $wR2 = 0.0662$	$R1 = 0.0251$ $wR2 = 0.0459$
Extinction coefficient	0.0025(2)	0.0034(2)
Larg. diff. peak and hole (e·Å ⁻³)	3.06 / -3.09	3.48 / -3.30

Table 4.4-6: Crystal data and structure refinement for HP-LaPtSn, HP-CePtSn, and HP-PrPtSn.

Empirical formula	HP-LaPtSn	HP-CePtSn	HP-PrPtSn
Molar mass (g·mol ⁻¹)	452.69	453.90	454.69
Crystal system		hexagonal	
Space group		<i>P62m</i>	
Radiation		CuK α_1 ($\lambda = 154.06$ pm)	
Powder-diffraction data			
<i>a</i> (pm)	762.6(2)	756.919(5)	754.97(7)
<i>c</i> (pm)	418.55(7)	415.166(4)	412.64(3)
Volume (nm ³)	0.2108	0.2060	0.2037
Single crystal diffractometer	CAD4	STOE IPDS II	CAD4
Radiation		MoK α ($\lambda = 71.073$ pm)	
Formula units per cell		<i>Z</i> = 3	
Temperature (K)		293	
Calculated density (g·cm ⁻³)	10.70	10.98	11.12
Crystal size (μm^3)	20 x 20 x 40	20 x 20 x 35	20 x 20 x 60
Detector distance (mm)	-	60	-
Irradiation / exposure (min)	-	5	-
ω range, increment	-	0-180°; 1.0°	-
Absorption coefficient (mm ⁻¹)	73.0	75.7	77.8
F(000)	555	558	561
θ Range	3° to 30°	3° to 30°	3° to 30°
Range in <i>hkl</i>	$\pm 10, \pm 10, \pm 5$	$\pm 10, \pm 10, \pm 5$	$\pm 10, \pm 10, \pm 5$
Total no. reflections	2279	1745	3233
Independent reflections	256 ($R_{\text{int}} = 0.1939$)	252 ($R_{\text{int}} = 0.1111$)	252 ($R_{\text{int}} = 0.2026$)
Reflections with $I > 2\sigma(I)$	221 ($R_{\sigma} = 0.0757$)	228 ($R_{\sigma} = 0.0756$)	225 ($R_{\sigma} = 0.0600$)
Data / parameters	256 / 14	252 / 14	252 / 14
Absorption correction	numerical	numerical	numerical
Transm. ratio (max / min)	0.705 / 0.453	0.502 / 0.262	0.315 / 0.297
Goodness-of-fit (F^2)	1.218	0.956	1.171
Final <i>R</i> indices ($I > 2\sigma(I)$)	$R1 = 0.0495$ $wR2 = 0.0978$	$R1 = 0.0363$ $wR2 = 0.0536$	$R1 = 0.0345$ $wR2 = 0.0708$
<i>R</i> Indices (all data)	$R1 = 0.0693$ $wR2 = 0.1147$	$R1 = 0.0423$ $wR2 = 0.0546$	$R1 = 0.0471$ $wR2 = 0.0782$
<i>Flack</i> parameter <i>x</i>	-0.04(5)	0.00(3)	-0.04(5)
Extinction coefficient	0.0001(7)	0.0031(4)	0.0012(4)
Larg. diff. peak and hole (e·Å ⁻³)	4.27 / -4.86	2.83 / -3.00	3.09 / -3.02

Table 4.4-7: Crystal data and structure refinement for HP-NdPtSn and HP-SmPtSn

Empirical formula	HP-NdPtSn	HP-SmPtSn
Molar mass (g·mol ⁻¹)	458.02	464.13
Crystal system		hexagonal
Space group		<i>P62m</i>
Radiation		CuK α_1 ($\lambda = 154.06$ pm)
Powder-diffraction data		
<i>a</i> (pm)	753.55(5)	750.1(2)
<i>c</i> (pm)	410.55(4)	407.6(1)
Volume (nm ³)	0.2019	0.1986
Single crystal diffractometer		CAD4
Radiation		MoK α ($\lambda = 71.073$ pm)
Formula units per cell		<i>Z</i> = 3
Temperature (K)		293
Calculated density (g·cm ⁻³)	11.30	11.64
Crystal size (μm^3)	11 x 13 x 16	20 x 20 x 20
Absorption coefficient (mm ⁻¹)	79.7	83.5
<i>F</i> (000)	564	570
θ Range	3° to 30°	3° to 29°
Range in <i>hkl</i>	$\pm 10, \pm 10, \pm 5$	$\pm 10, \pm 10, \pm 5$
Total no. reflections	2124	2140
Independent reflections	248 ($R_{\text{int}} = 0.1670$)	229 ($R_{\text{int}} = 0.3491$)
Reflections with $I > 2\sigma(I)$	219 ($R_{\sigma} = 0.0661$)	204 ($R_{\sigma} = 0.1421$)
Data / parameters	248 / 14	229 / 14
Absorption correction		psi-scan
Transm. ratio (max / min)	2.40	0.252 / 0.069
Goodness-of-fit (F^2)	1.244	1.031
Final <i>R</i> indices ($I > 2\sigma(I)$)	$R1 = 0.0344$ $wR2 = 0.0567$	$R1 = 0.0457$ $wR2 = 0.0985$
<i>R</i> Indices (all data)	$R1 = 0.0500$ $wR2 = 0.0709$	$R1 = 0.0583$ $wR2 = 0.1060$
<i>Flack</i> parameter <i>x</i>	0.01(3)	-0.01(5)
Extinction coefficient	0.0005(3)	0.002(1)
Larg. diff. peak and hole (e·Å ⁻³)	3.29 / -4.01	4.89 / -6.80

Table 4.4-8: Atomic coordinates and anisotropic displacement parameters (pm^2) for NP- and HP-REPtSn (RE = La–Nd, Sm). U_{eq} is defined as one third of the trace of the orthogonalized U_{ij} tensor. The anisotropic displacement factor exponent takes the form $-2\pi^2[(ha)^2U_{11}+\dots+2kha^*b^*U_{12}]$. $U_{23} = 0$. The positional parameters of HP-CePtSn determined from the *Rietveld* refinement are given in italics.

Atom	Wyckoff position	x	y	z	U_{11}	U_{22}	U_{33}	U_{12}	U_{13}	U_{eq}
NP-LaPtSn (normal-pressure phase)										
La	4c	0.01293(8)	¼	0.69532(7)	49(3)	59(2)	48(2)	0	3(2)	52(1)
Pt	4c	0.29273(6)	¼	0.40883(5)	73(2)	44(2)	46(2)	0	-1(1)	54(1)
Sn	4c	0.17590(9)	¼	0.08304(9)	63(3)	36(3)	36(3)	0	-2(2)	45(1)
NP-CePtSn										
Ce	4c	0.01216(7)	¼	0.69585(7)	58(3)	80(3)	70(2)	0	4(2)	69(2)
Pt	4c	0.29042(5)	¼	0.40901(4)	82(2)	67(2)	67(2)	0	-1(1)	72(1)
Sn	4c	0.17657(9)	¼	0.08318(7)	75(3)	57(3)	59(3)	0	-1(2)	64(2)
NP-PrPtSn										
Pr	4c	0.01117(9)	¼	0.69785(8)	94(3)	96(2)	117(3)	0	3(2)	102(1)
Pt	4c	0.28722(6)	¼	0.40766(6)	109(2)	80(2)	85(2)	0	1(2)	91(1)
Sn	4c	0.17551(10)	¼	0.08176(11)	122(3)	80(3)	85(4)	0	4(3)	96(2)
NP-NdPtSn										
Nd	4c	0.0112(2)	¼	0.6965(2)	79(5)	90(5)	88(5)	0	0(5)	86(3)
Pt	4c	0.2889(1)	¼	0.4094(1)	101(4)	70(4)	73(4)	0	2(4)	81(2)
Sn	4c	0.1779(2)	¼	0.0832(2)	99(6)	60(5)	57(8)	0	8(6)	72(3)
NP-SmPtSn										
Sm	4c	0.01070(4)	¼	0.69735(6)	71(1)	75(1)	33(2)	0	2(1)	60(1)
Pt	4c	0.28729(3)	¼	0.40942(4)	90(1)	60(1)	27(2)	0	-2(1)	59(1)
Sn	4c	0.17866(6)	¼	0.08367(7)	88(2)	52(2)	12(3)	0	-2(2)	51(1)
<hr/>										
Atom	Wyckoff position	x	y	z	U_{11}	U_{22}	U_{33}	U_{12}	U_{13}	U_{eq}
HP-LaPtSn (high-pressure phase)										
La	3f	0.5859(5)	0	0	24(11)	45(16)	37(13)	23(8)	0	33(7)
Pt1	1a	0	0	0	36(10)	U_{11}	51(16)	18(5)	0	41(7)
Pt2	2d	⅓	⅓	½	49(7)	U_{11}	58(12)	24(4)	0	52(6)
Sn	3g	0.2490(5)	0	½	22(12)	13(17)	37(17)	7(8)	0	25(7)
HP-CePtSn										
Ce	3f	0.5870(3) <i>0.5846(6)</i>	0	0	76(6)	82(8)	78(10)	41(4)	0	78(4)
Pt1	1a	0	0	0	90(6)	U_{11}	43(11)	45(3)	0	74(4)
Pt2	2d	⅓	⅓	½	91(4)	U_{11}	80(9)	45(2)	0	87(4)
Sn	3g	0.2513(3) <i>0.2526(7)</i>	0	½	70(7)	66(10)	56(12)	33(5)	0	65(5)

Atom	Wyckoff position	x	y	z	U_{11}	U_{22}	U_{33}	U_{12}	U_{13}	U_{eq}
HP-PrPtSn										
Pr	3f	0.4110(3)	0	0	44(7)	56(10)	68(10)	28(5)	0	55(5)
Pt1	1a	0	0	0	46(6)	U_{11}	54(12)	23(3)	0	49(5)
Pt2	2d	$\frac{1}{3}$	$\frac{2}{3}$	$\frac{1}{2}$	46(5)	U_{11}	101(10)	23(2)	0	64(4)
Sn	3g	0.7473(3)	0	$\frac{1}{2}$	35(8)	31(11)	63(14)	16(6)	0	44(5)
HP-NdPtSn										
Nd	3f	0.4101(3)	0	0	44(7)	29(9)	50(9)	15(5)	0	43(5)
Pt1	2d	$\frac{1}{3}$	$\frac{2}{3}$	$\frac{1}{2}$	35(5)	U_{11}	78(10)	17(2)	0	49(4)
Pt2	1a	0	0	0	45(7)	U_{11}	24(12)	23(3)	0	38(5)
Sn	3g	0.7472(3)	0	$\frac{1}{2}$	28(8)	37(12)	22(12)	18(6)	0	28(5)
HP-SmPtSn										
Sm	3f	0.5919(4)	0	0	114(11)	136(13)	29(13)	68(6)	0	91(7)
Pt1	1a	0	0	0	107(9)	U_{11}	5(17)	53(5)	0	73(7)
Pt2	2d	$\frac{2}{3}$	$\frac{1}{3}$	$\frac{1}{2}$	104(7)	U_{11}	62(14)	52(4)	0	90(6)
Sn	3g	0.2558(4)	0	$\frac{1}{2}$	72(11)	119(16)	29(19)	60(8)	0	68(8)

4.4.3.4 Crystal Structure Description

The equiatomic $REPtSn$ stannides with the light rare-earth metals La, Ce, Pr, Nd, Sm, and Eu [268-271] crystallize with the orthorhombic $TiNiSi$ type structure with four formula units per cell, while those with the smaller Sc, Y, and Gd–Lu atoms [272] adopt the hexagonal $ZrNiAl$ type with $Z = 3$. At this point a comment on the structural work on NP-CePtSn listed in the literature should be given. The first structure refinement based on single crystal data was performed by *Higashi et al.* [257]. These authors described the NP-CePtSn structure in the non-centrosymmetric space group $Pn2_1a$, since they obtained slightly better residuals as compared to a refinement in the centrosymmetric supergroup $Pnma$. Later on, the NP-CePtSn structure was also refined on the basis of a neutron diffraction study using a Czochralski grown single crystal. The latter data confirmed the centrosymmetric space group $Pnma$ in good agreement with the present investigation. The U_{22} parameters of all three sites give absolutely no hint for a violation of the mirror plane perpendicular to the b axis.

Projections of the NP- $REPtSn$ and HP- $REPtSn$ ($RE = La-Nd, Sm$) structures along the short unit cell axis are presented in Figure 4.4-3. From a geometrical point of view, both modifications are built up from platinum centered trigonal prisms that are formed by four rare-earth and two tin atoms for NP- $REPtSn$, while two RE_6 and Sn_6 prisms occur for the Pt2 and Pt1 atoms of HP- $REPtSn$. The prisms show different patterns of condensation.

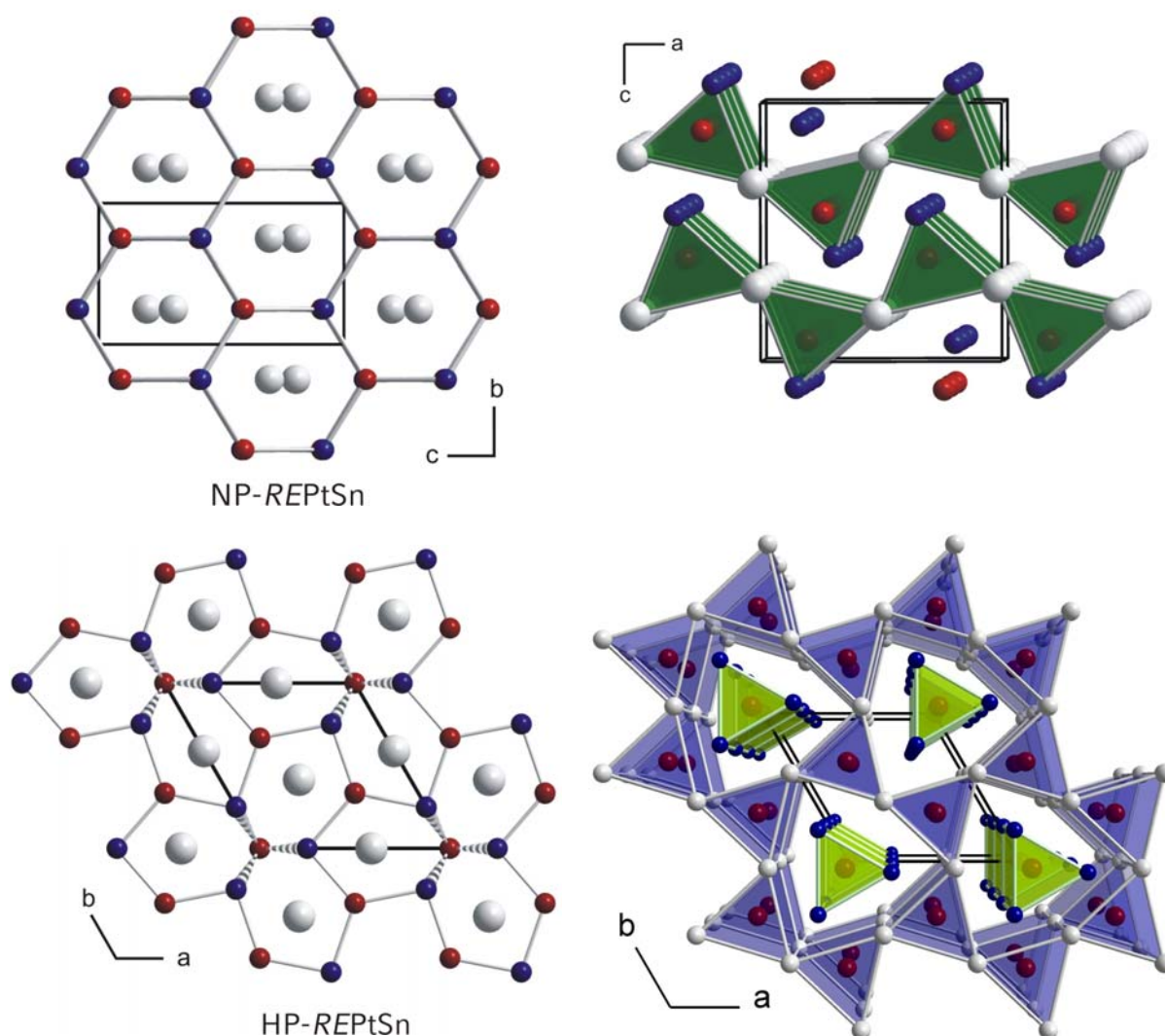


Figure 4.4-3: Projections of the NP- and HP-REPtSn structures. In the right-hand part of the drawing the platinum-centered trigonal prisms are emphasized. The structural relationship of both structures is shown at the left-hand part of the drawing. For clarity, only half of the unit cell is drawn for the NP-REPtSn structure in the projection direction. The rare-earth, platinum, and tin atoms are drawn as grey, red, and blue spheres, respectively.

The shortest interatomic distances in both modifications occur between the platinum and tin atoms: 269–290 pm in NP-REPtSn and 279–292 pm in HP-REPtSn ($RE = \text{La-Nd, Sm}$), close to or slightly longer than the sum of the covalent radii of 269 pm (for CePtSn) [273]. Together, the platinum and tin atoms build up three-dimensional networks of puckered hexagons as emphasized at the right-hand part of Figure 4.4-3. The rare-earth atoms are located in slightly distorted hexagonal channels formed by these networks. They are bonded through relatively short $RE\text{-Pt}$ contacts, which vary between 313–325 pm (NP-LaPtSn), 310–316 pm (HP-LaPtSn), 306–322 pm (NP-SmPtSn), and 305–307 pm (HP-SmPtSn) inside the networks.

The most accented difference in both modifications concerns the rare-earth coordination as emphasized in Figure 4.4-4. Both rare-earth atom sites have six nearest rare-earth neighbors with an average Ce–Ce distance of 412 pm (range of 383–463 pm) in NP-CePtSn and 402 pm (range of 395–415 pm) in HP-CePtSn. The high-pressure phase shows clearly the smaller range and also the smaller average distance. Even more drastic is the situation for the Ce–Pt contacts with an average distance of 330 pm for the six platinum neighbors in NP-CePtSn and of 309 pm for the five platinum neighbors in HP-CePtSn. In contrast, the average Ce–Sn distance of 338 pm in HP-CePtSn is slightly longer than in NP-CePtSn (333 pm). Comparable situations can be found at the other representatives of these intermetallic phases. The corresponding distances can be found in Table 4.4-9 and Table 4.4-10.

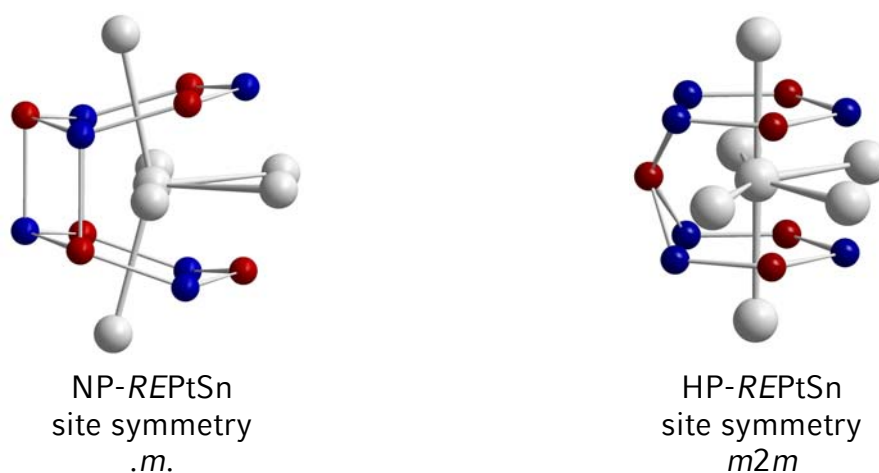


Figure 4.4-4: Coordination polyhedra of the cerium atoms in NP-REPtSn and HP-REPtSn. The site symmetries are indicated. The rare-earth, platinum, and tin atoms are drawn as grey, red, and blue spheres, respectively.

A striking difference occurs for the platinum-tin coordination. In NP-REPtSn, each platinum atom has four nearest tin neighbors in a strongly distorted tetrahedral coordination with an average Pt–Sn distance of 278 pm (NP-LaPtSn) and 275 pm (NP-SmPtSn), while there occur two crystallographically independent platinum sites in HP-REPtSn, both with significantly longer Pt1–Sn and Pt2–Sn distances of 282 pm (6×) and 292 pm (3×) in HP-LaPtSn and 279 pm (6×) and 284 pm (3×) in HP-SmPtSn, respectively. The longer Pt1–Sn contact is comprehensible with the increased coordination number through the pressure-distance paradoxon, but the longer Pt2–Sn distance with only three contacts is remarkable.

Table 4.4-9: Interatomic distances (pm), calculated with the powder lattice parameters in NP- and HP-REPtSn ($RE = \text{La-Nd}$). All distances of the first coordination sphere are listed.

normal-pressure															
LaPtSn				CePtSn				PrPtSn				NdPtSn			
La:	1	Pt	313.0(1)	Ce:	1	Pt	310.0(1)	Pr:	1	Pt	310.2(1)	Nd:	1	Pt	307.6(2)
	2	Pt	324.6(1)		2	Pt	323.3(1)		2	Sn	322.2(1)		2	Sn	321.5(2)
	2	Sn	326.3(1)		2	Sn	323.8(1)		2	Pt	322.6(1)		2	Pt	321.9(2)
	1	Sn	335.7(1)		1	Sn	334.0(1)		2	Pt	331.1(1)		2	Pt	330.1(2)
	2	Pt	338.6(1)		2	Pt	334.2(1)		1	Sn	331.3(2)		1	Sn	332.3(2)
	1	Sn	339.3(1)		1	Sn	336.0(1)		1	Sn	335.4(1)		1	Sn	332.7(2)
	2	Sn	343.1(1)		2	Sn	340.3(1)		2	Sn	340.8(1)		2	Sn	337.1(2)
	1	Pt	359.6(1)		1	Pt	357.5(1)		1	Pt	357.6(1)		1	Pt	355.2(2)
	2	La	388.0(1)		2	Ce	383.4(1)		2	Pr	380.7(1)		2	Nd	378.4(1)
	2	La	391.9(1)		2	Ce	390.6(1)		2	Pr	392.9(2)		2	Nd	389.8(2)
Pt:	2	Sn	272.9(1)	Pt:	2	Sn	271.4(1)	Pt:	2	Sn	271.3(1)	Pt:	2	Sn	269.9(1)
	1	Sn	276.8(1)		1	Sn	274.8(1)		1	Sn	274.3(1)		1	Sn	273.4(2)
	1	Sn	289.7(1)		1	Sn	288.5(1)		1	Sn	288.6(1)		1	Sn	286.8(2)
	1	La	313.0(1)		1	Ce	310.0(1)		1	Pr	310.2(1)		1	Nd	307.6(2)
	2	La	324.6(1)		2	Ce	323.3(1)		2	Pr	322.6(1)		2	Nd	321.9(2)
	2	La	338.6(1)		2	Ce	334.2(1)		2	Pr	331.1(1)		2	Nd	330.1(2)
	1	La	359.6(1)		1	Ce	357.5(1)		1	Pr	357.6(1)		1	Nd	355.2(2)
Sn:	2	Pt	272.9(1)	Sn:	2	Pt	271.4(1)	Sn:	2	Pt	271.3(1)	Sn:	2	Pt	269.9(1)
	1	Pt	276.8(1)		1	Pt	274.8(1)		1	Pt	274.3(1)		1	Pt	273.4(2)
	1	Pt	289.7(1)		1	Pt	288.5(1)		1	Pt	288.6(1)		1	Pt	286.8(2)
	2	La	326.3(1)		2	Ce	323.8(1)		2	Pr	322.2(1)		2	Nd	321.5(2)
	1	La	335.7(1)		1	Ce	334.0(1)		1	Pr	331.3(2)		1	Nd	332.3(2)
	1	La	339.3(1)		1	Ce	336.0(1)		1	Pr	335.4(1)		1	Nd	332.7(2)
	2	La	343.1(1)		2	Ce	340.3(1)		2	Pr	340.8(1)		2	Nd	337.1(2)
high-pressure															
LaPtSn				CePtSn				PrPtSn				NdPtSn			
La:	4	Pt2	310.1(1)	Ce:	4	Pt2	308.5(1)	Pr:	4	Pt2	307.6(1)	Nd:	4	Pt1	306.7(1)
	1	Pt1	315.8(4)		1	Pt1	312.6(2)		1	Pt1	310.3(2)		1	Pt2	309.1(3)
	2	Sn	331.4(4)		2	Sn	328.1(2)		2	Sn	327.2(3)		2	Sn	326.6(3)
	4	Sn	345.9(3)		4	Sn	342.9(1)		4	Sn	340.7(2)		4	Sn	339.2(2)
	4	La	397.8(2)		4	Ce	395.3(1)		4	Pr	395.0(1)		4	Nd	394.6(2)
	2	La	418.6(1)		2	Ce	415.2(1)		2	Pr	412.6(1)		2	Nd	410.6(1)
Pt1:	6	Sn	282.6(2)	Pt1:	6	Sn	281.6(1)	Pt1:	6	Sn	281.0(2)	Pt1:	3	Sn	286.4(2)
	3	La	315.8(4)		3	Ce	312.6(2)		3	Pr	310.3(2)		6	Nd	306.7(1)
Pt2:	3	Sn	291.8(2)	Pt2:	3	Sn	288.4(1)	Pt2:	3	Sn	287.0(2)	Pt2:	6	Sn	280.1(2)
	6	La	310.7(1)		6	Ce	308.5(1)		6	Pr	307.5(1)		3	Nd	309.1(3)
Sn:	2	Pt1	282.6(2)	Sn:	2	Pt1	281.6(1)	Sn:	2	Pt1	281.0(2)	Sn:	2	Pt2	280.1(2)
	2	Pt2	291.8(2)		2	Pt2	288.4(1)		2	Pt2	287.0(2)		2	Pt1	286.4(2)
	2	Sn	328.8(6)		2	Sn	329.5(3)		2	Sn	330.5(4)		2	Nd	326.6(3)
	2	La	331.4(4)		2	Ce	328.1(2)		2	Pr	327.2(3)		2	Sn	330.0(4)
	4	La	345.9(3)		4	Ce	342.9(1)		4	Pr	340.7(2)		4	Nd	339.2(2)

Table 4.4-10: Interatomic distances (pm), calculated with the powder lattice parameters in NP- and HP-SmPtSn. All distances of the first coordination sphere are listed.

normal-pressure				high-pressure			
SmPtSn				SmPtSn			
Sm:	1	Pt	306.8(1)	Sm:	4	Pt2	305.3(1)
	2	Sn	320.4(1)		1	Pt1	306.1(3)
	2	Pt	321.6(1)		2	Sn	324.4(4)
	2	Pt	327.9(1)		4	Sn	336.6(2)
	1	Sn	331.2(1)		4	Sm	393.7(2)
	1	Sn	333.0(2)		2	Sm	407.6(1)
	2	Sn	335.6(1)				
	1	Pt	354.9(2)				
	2	Sm	375.4(2)				
	2	Sm	391.0(2)				
Pt:	2	Sn	269.8(1)	Pt1:	6	Sn	279.8(2)
	1	Sn	272.8(2)		3	Sm	306.1(3)
	1	Sn	286.4(1)	Pt2:	3	Sn	283.7(2)
	1	Sm	306.8(1)		6	Sm	305.3(1)
	2	Sm	321.6(1)				
	2	Sm	327.9(1)				
	1	Sm	354.9(2)				
Sn:	2	Pt	269.8(1)	Sn:	2	Pt1	279.8(2)
	1	Pt	272.8(2)		2	Pt2	283.7(2)
	1	Pt	286.4(1)		2	Sn	332.1(4)
	2	Sm	320.4(1)		2	Sm	324.4(4)
	1	Sm	331.2(1)		4	Sm	336.6(2)
	1	Sm	333.0(2)				
	2	Sm	335.6(1)				

4.4.3.5 Thermal Behaviour

To investigate the high-temperature behaviour of the intermetallic high-pressure phases $REPtSn$ ($RE = La-Nd, Sm$), temperature-programmed *in-situ* X-ray diffractometry was performed on a STOE Stadi P powder diffractometer (MoK_{α} ; $\lambda = 71.073$ pm) with a computer-controlled STOE furnace as described in Chapter 3.1.3.

HP-CePtSn

Successive heating of HP-CePtSn filled in a 0.1 mm outside diameter Mark capillary showed that the high-pressure modification is stable up to 500 °C in an argon atmosphere (Figure 4.4-5). The complete transformation into the normal-pressure modification takes place at about 850 °C. No further transformations could be detected, when heating up the sample to 1100 °C followed by lowering the temperature to ambient conditions. The consistent low intensity reflection near 17° is an artifact of the oven setup. The same experiment with a capillary under air led to the analogous transformation of the metastable high-pressure phase into the normal-pressure modification, followed by oxidation reactions leading to CeO_2 , SnO_2 , and platinum metal at about 850 °C.

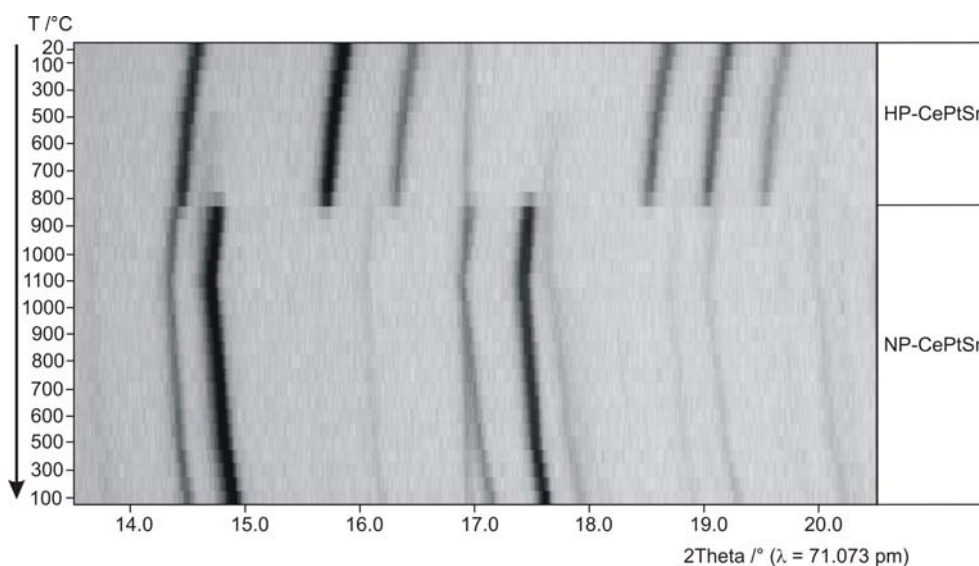


Figure 4.4-5: Temperature-programmed X-ray powder patterns of HP-CePtSn. The continuous line at $2\theta \approx 17^\circ$ resulted from the oven setup.

HP-SmPtSn

Successive heating of HP-SmPtSn filled in a 0.1 mm outside diameter Mark capillary showed that the high-pressure modification is stable up to 850 °C under argon atmosphere (Figure 4.4-6). The complete transformation into the normal-pressure modification takes place at about 1000 °C. Interestingly, HP-SmPtSn transforms back to the normal-pressure modification at temperatures about 150 °C higher than isotopic HP-CePtSn. In contrast to HP-CePtSn, where the transformation into the normal-pressure phase started at 500 °C and ended up at 850 °C, the samarium compound retransformed in a smaller range between 850–1000 °C. At the maximum temperature of 1100 °C, another phase transformation into an unknown phase takes place. Under these conditions, a reaction with the Mark capillary can not be excluded. No further transformation of the unknown phase was detectable by lowering the temperature to ambient conditions.

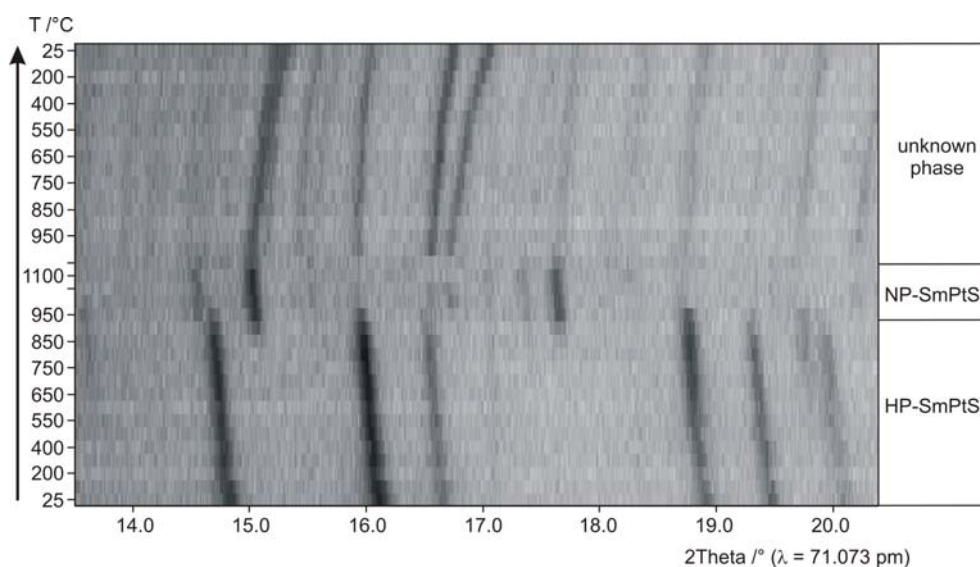


Figure 4.4-6: Temperature-programmed X-ray powder patterns of HP-SmPtSn. The continuous line at $2\theta \approx 17^\circ$ resulted from the oven setup.

4.4.3.6 Magnetic Properties and Heat Capacity Measurements

The magnetic and heat capacity measurements were carried out on a Quantum Design Physical Property Measurement System (PPMS) in cooperation with Dr. R.-D. Hoffmann and Dr. S. Rayaprol, Universität Münster, using AC-, DC-MS, and heat capacity options, respectively.

HP-CePtSn

10.6 mg of the sample were enclosed in a small gelatin capsule and fixed at the sample holder rod. The sample was then cooled to 2 K in zero magnetic field and slowly heated to room temperature in the applied external field.

The temperature dependence of the reciprocal magnetic susceptibility is presented in Figure 4.4-7. HP-CePtSn shows Curie-Weiss behavior above 40 K with an experimental magnetic moment of $2.55(1) \mu_B/\text{Ce}$ atom, close to the free ion value [274] of $2.54 \mu_B$ for Ce^{3+} . The paramagnetic Curie temperature (Weiss constant) of $-35(1)$ K, determined by linear extrapolation of the $1/\chi$ vs. T plot to $1/\chi = 0$, is indicative for antiferromagnetic interactions. The inverse susceptibility significantly deviates from Curie-Weiss behavior below 40 K, indicating crystal field splitting of the

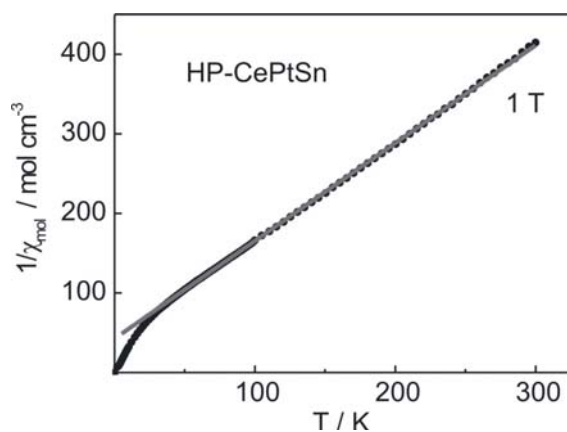


Figure 4.4-7: Temperature dependence of the reciprocal magnetic susceptibility of HP-CePtSn measured in an external field of 1 T. The straight line corresponds to the Curie-Weiss fit.

$J = 5/2$ ground state, but also the beginning of short range magnetic fluctuations. No magnetic ordering is evident down to 2 K. Additional specific heat measurements at very low temperatures of 50 mK to 2.5 K were performed in cooperation with Dr. E.-W. Scheidt (Institut für Chemische Physik und Materialwissenschaften, Universität Augsburg). Here a magnetic ordering transition with an ordering temperature $T_0 = 2.11$ K was observed, but the C_P curve characteristics below the ordering temperature gave no clear indication of a ferromagnetic or antiferromagnetic transition (see Figure 4.4-8). The entropy of the transition with a value of 3.6 J/molK is in the range of an antiferromagnetic transition, which could be for example slightly reduced through Kondo effects. The reduced C_P at the maximum, which lies at 6 J/molK and not at 12 J/molK suggests similar conclusions. Further investigations to clarify the kind of the transition are in progress.

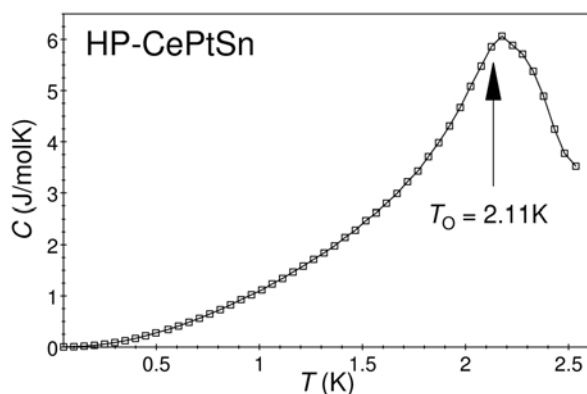


Figure 4.4-8: Specific heat (C_p) of HP-CePtSn plotted as C_p vs. T in the temperature range of 50 mK to 2.5 K indicating a magnetic ordering transition at 2.11 K.

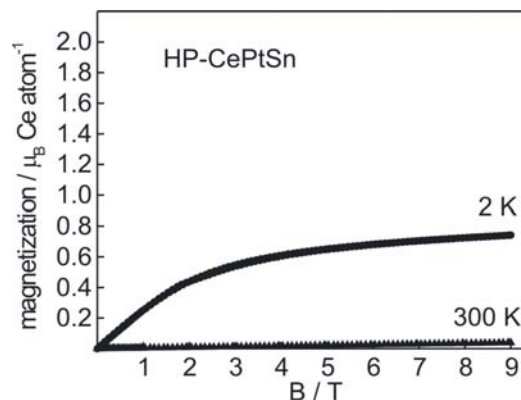


Figure 4.4-9: Magnetization vs. external flux density for HP-CePtSn at 2 and 300 K.

The magnetization vs. field behaviour is presented in Figure 4.4-9. At 300 K, the magnetization increases linearly with a very small value at 9 T, as expected for a paramagnetic material. At 2 K, the magnetization shows a steeper increase, however, we do not observe saturation at the highest obtainable field of 9 T. The magnetization at 2 K and 9 T is only $0.74(1) \mu_B/\text{Ce atom}$, significantly reduced from the theoretical value for Ce^{3+} of $2.14 \mu_B$. This magnetic behavior is similar to CeRhSn_2 [275, 276]. The value of the magnetic moment is small due to crystal field splitting of the $J = 5/2$ ground state.

HP-PrPtSn

The magnetic behavior of NP-PrPtSn was studied on polycrystalline samples [268] and a Czochralski grown single crystal [277]. The detailed studies by *Janušova et al.* [277] gave no hint for magnetic ordering down to 0.4 K.

In Figure 4.4-10 the *dc* susceptibility (χ) of HP-PrPtSn measured in an applied *dc* field of 5 kOe is presented. The susceptibility $\chi(T)$ increases monotonously with decreasing temperature, as seen for a paramagnet. Below 10 K a broad step like anomaly appears, however without any clear signature of magnetic ordering. From the linear region of the inverse susceptibility at temperatures above 100 K, the paramagnetic Curie temperature observed is about -4.5 K. The negative sign indicates antiferromagnetic interactions. The effective Bohr magneton number (μ_B) per Pr^{3+} calculated from the inverse susceptibility is $3.31(2) \mu_B$ close to the expected theoretical value of $3.58 \mu_B$. In contrast, the investigations on NP-PrPtSn data [268, 277] revealed an experimental moment slightly higher than the theoretical one.

The anomaly below 10 K is more clearly visible in the $\chi(T)$ curve measured at a low field of 100 Oe (Figure 4.4-11). The susceptibility $\chi(T)$ measured in ZFC and FC states of the sample do not bifurcate and are the same within the experimental errors. The peak in the 100 Oe measurements appears near 10 K, as compared to the 5 kOe measurement. To probe response of this anomaly to the *dc* field, the susceptibility $\chi(T)$ of HP-PrPtSn at different applied fields was measured and plotted as presented in Figure 4.4-12. The figure clearly shows the field dependence of the susceptibility. The moment values (in emu/mol) also decrease with increasing field. Also the step in $\chi(T)$ observed for $H \leq 10$ kOe vanished with increasing field. The overlap of the ZFC-FC curves $\chi(T)$ in low field rules out any spin-glass anomalies. Therefore, the origin of the broad feature below 10 K can be due to short range magnetic ordering arising from inhomogeneous magnetism.

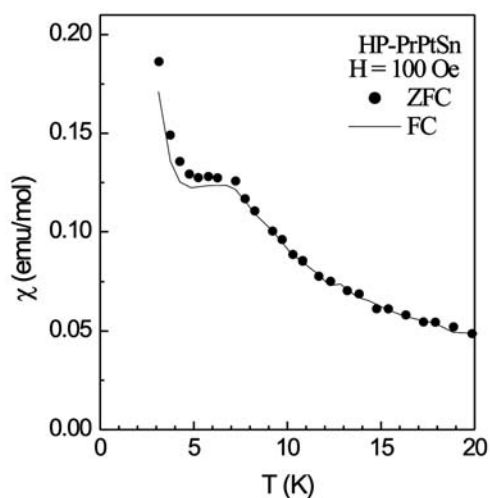


Figure 4.4-11: The *dc* susceptibility ($\chi = M/H$) of HP-PrPtSn measured in ZFC-FC state of the sample at a *dc* field of 100 Oe.

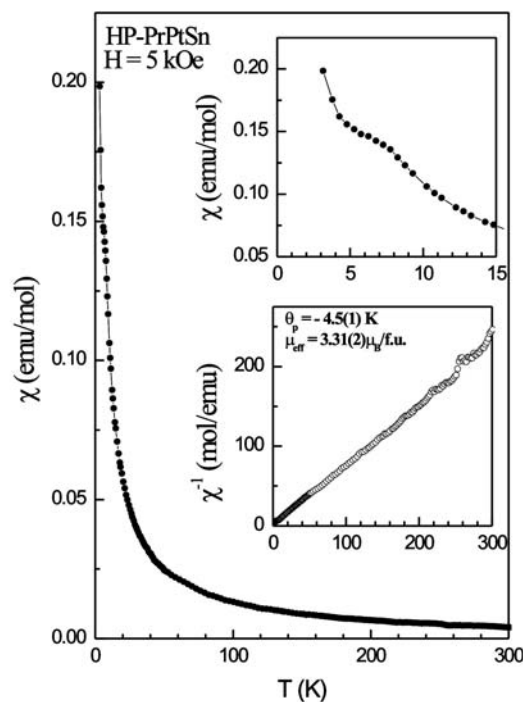


Figure 4.4-10: The *dc* susceptibility ($\chi = M/H$) as a function of temperature (T) for HP-PrPtSn measured in a steady field of 5 kOe. The top inset shows the anomaly in $\chi(T)$ at low temperatures. The bottom inset shows the inverse susceptibility in the measured temperature range.

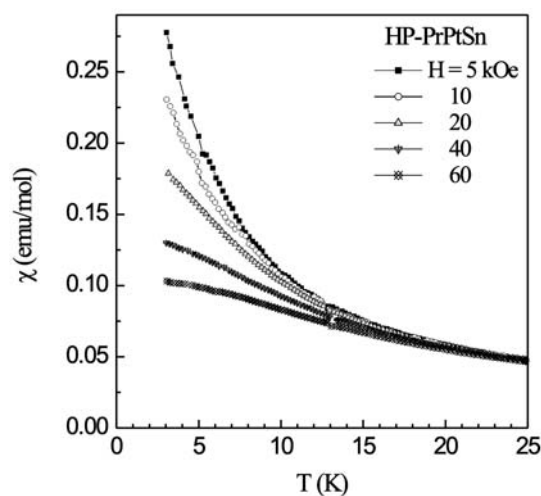


Figure 4.4-12: The *dc* susceptibility ($\chi = M/H$) of HP-PrPtSn measured in ZFC state of the sample at several applied fields.

The *ac* susceptibility (χ' and χ'') data of HP-PrPtSn measured at different frequencies and an *ac* field (amplitude, H_{ac}) of 1 Oe is presented in Figure 4.4-13. Here, the real and imaginary parts of the linear susceptibility (χ' and χ'') are plotted. The broad peak around 6 K is consistent with the step like feature in *dc* susceptibility. The two main observations from this measurement are (i) no frequency dependence in χ' and (ii) featureless χ'' . Conclusively this rules out any type of spin-glass like anomaly in HP-PrPtSn.

Furthermore, isothermal magnetizations of HP-PrPtSn at several temperatures were measured. In Figure 4.4-14, the $M(H)$ data measured after reaching the measurement temperature in ZFC state is shown. For $T \leq 10$ K, isotherms increase in a non-linear manner with increasing H behaving as an antiferromagnet and without saturating up to 80 kOe. The moment value at 80 kOe and 3 K is about $1.1 \mu_B$, about 30% of the expected saturation moment for Pr^{3+} (given by $g \times J = 3.20 \mu_B$). The features of $M(H)$ are similar up to $T = 10$ K, which indicates the persistence of inhomogeneous magnetism up to 10 K. At 50 K, the $M(H)$ is linear indicative of the paramagnetic state.

Now we focus on the $C_p(T)$ of HP-PrPtSn in Figure 4.4-15. The anomalies observed in the magnetic measurements can also be seen in C_p in the form of a broad peak around 5 K. In the same figure the plot of C_p/T vs. T is also shown. The absence of any clear peak is indicative for inhomogeneous magnetism in HP-PrPtSn. *Stewart et al.* [278] have shown that one of the signatures for non-Fermi liquid behavior in an intermetallic compound with

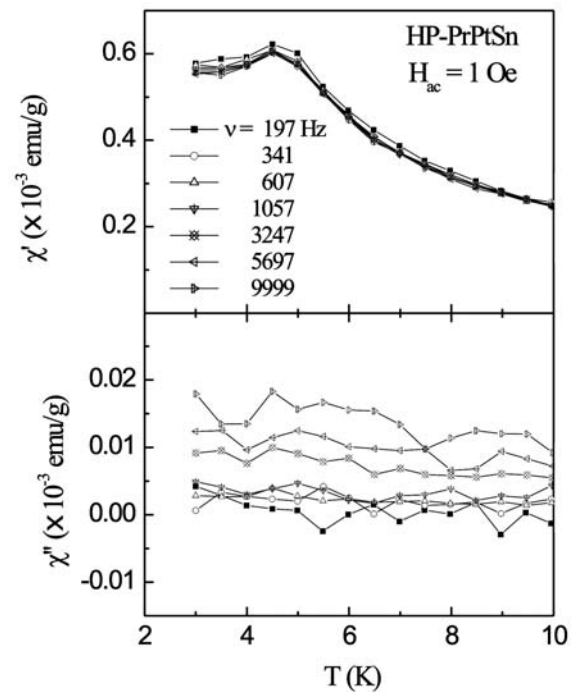


Figure 4.4-13: The *ac* susceptibility of HP-PrPtSn measured in an *ac* field (H_{ac}) of 1 Oe and at different driving frequencies (ν).

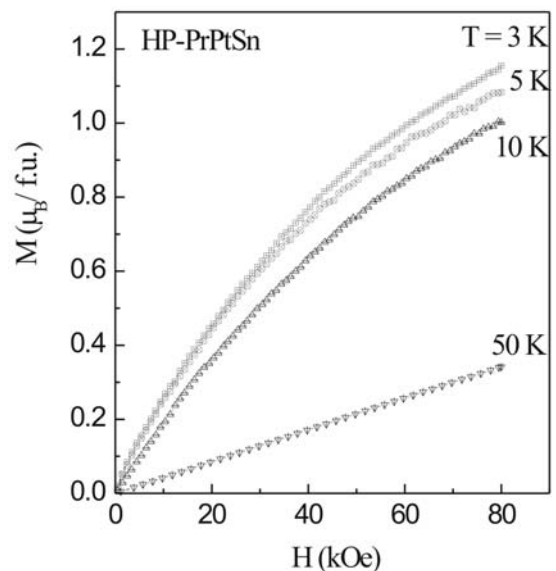
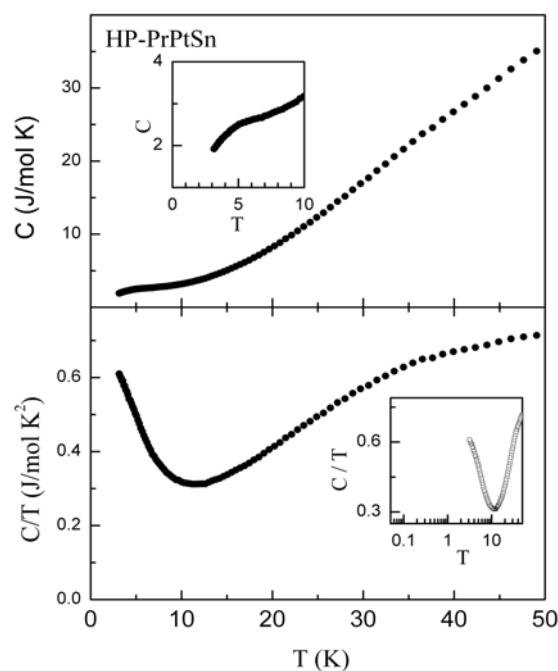


Figure 4.4-14: Magnetization (M) as a function of varying field (H) for HP-PrPtSn, measured at various temperatures.

d - f electrons is a $-\log T$ temperature dependence of C_p (*i.e.*, upturn in the plot of C_p/T vs. $\log T$). The inset of the bottom panel illustrates the C_p/T vs. T , with T plotted on a log scale to highlight $C_p/T \sim -\log T$ at low temperatures. Thus, the C_p data are in line with the susceptibility data.

Figure 4.4-15: Specific heat (C_p) of HP-PrPtSn plotted as C_p vs. T and C_p/T vs. T in the top and bottom panels. The inset in the top panel highlights the features below 10 K. The inset in the bottom panel is shown to highlight the logarithmic increase in C_p/T at low temperatures (below 10 K).



HP-NdPtSn

The dc susceptibility (χ) for HP-NdPtSn, measured at 10 kOe is shown in Figure 4.4-16. The sample was cooled to the lowest available temperature (3 K) in zero field (ZFC). The susceptibility $\chi(T)$ was measured while warming the sample in a steady field of 10 kOe. χ exhibits an upturn below 50 K, with no peak at lower temperatures. The inverse susceptibility (χ^{-1}) deviates from Curie-Weiss (CW) law below 100 K. The CW fit at higher temperatures yields a paramagnetic Curie temperature (θ_p) of -5 K where the negative sign indicates antiferromagnetic correlations. The effective Bohr magneton number (μ_{eff}) given by $g\sqrt{J(J+1)}$ is $3.62 \mu_B$ for Nd^{3+} . Experimentally μ_{eff} was calculated from the CW-fit in the linear region of χ^{-1} at high-temperatures (100–300 K). The observed value for NdPtSn is $3.73(2) \mu_B$, which is close to the expected value for free Nd^{3+} .

The ZFC–FC curves for $\chi(T)$ measured in $H = 40, 100$ Oe, and 1 kOe are shown in Figure 4.4-17. The sample was zero field cooled (ZFC) and then field cooled (FC) for measuring the low field susceptibility. For $\chi(T)$ measured in low fields of 40 and 100 Oe, one can see a prominent peak around 4.5 K in the ZFC measurement. The FC curve bifurcates from ZFC at this point, and increases at lower temperatures. This is a typical feature of spin-glasses. We refer to this temperature as T_f or freezing temperature as referred for spin-glasses [279]. However, freezing temperature is not seen in the ZFC–FC curves for the $\chi(T)$ measured in 1 kOe field, as this field strength is large enough to smear out the peak.

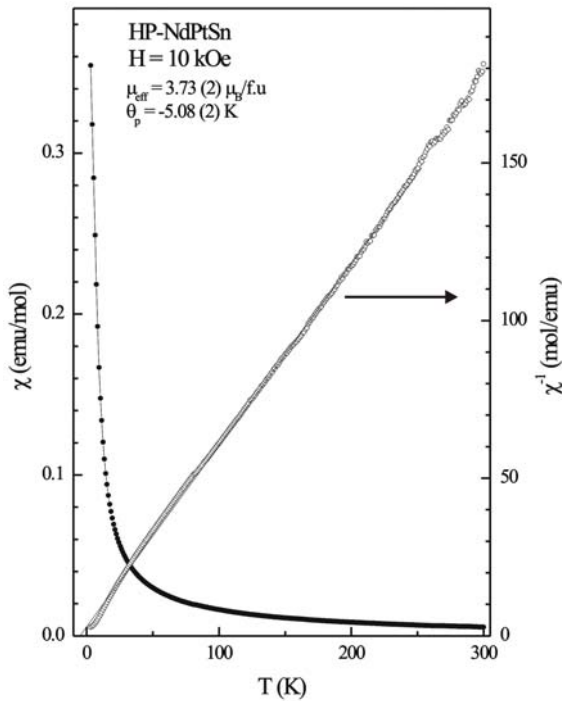


Figure 4.4-16: χ vs. T measured in a field of 10 kOe for NdPtSn. χ^{-1} vs. T is also shown by open circles. The continuous line passing through χ^{-1} is a Curie-Weiss fit at high temperatures extrapolated to show the small deviation below 100 K.

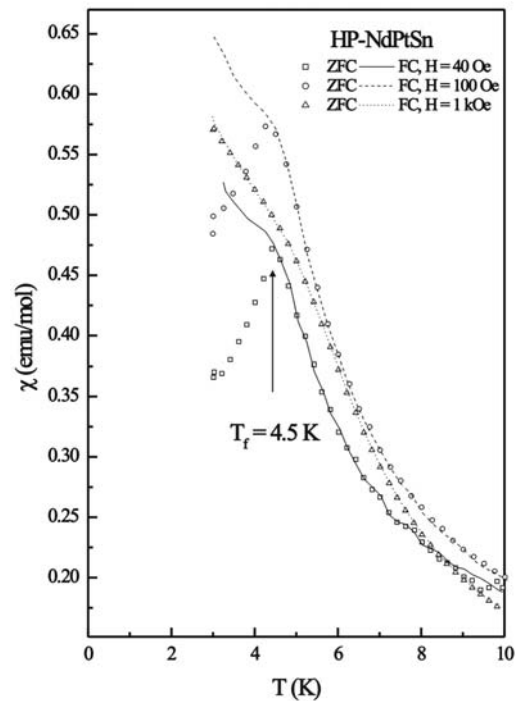


Figure 4.4-17: χ vs. T measured in ZFC and FC conditions in fields of 40, 100 Oe, and 1 kOe for HP-NdPtSn. The vertical arrow shows the freezing temperature observed for the 40 and 100 Oe measurements.

Figure 4.4-18(a) shows the magnetization as a function of the field, $M(H)$ for HP-NdPtSn at temperatures below and above T_f . The magnetization $M(H)$ at 3 K increases with increasing field with a tendency to saturate at the higher fields. The value of the magnetization at 80 kOe and 3 K is $\sim 1.6 \mu_B$, corresponding to 50% of the moment for the free Nd^{3+} ion. Measurements at temperatures $\gg T_f$, *i.e.*, at 50 and 300 K, show linear variation of the moment with increasing field. No traces of any ferromagnetic impurity or interactions could be observed. In Figure 4.4-18(b), the low-temperature low field M - H curves are plotted. The sample was cooled to $T < T_f$ in zero field state and then field was swept slowly. A small hysteresis could be seen at low fields (< 500 Oe) while sweeping the field in positive and negative directions. The small initial slope near the origin is comparable to the values obtained from *ac*-susceptibility measurement, confirming the frozen state of spins at this temperature [279, 280]. At 8 K (*i.e.*, $T > T_f$) there is no such effect. These signatures of a spin-glass are an interesting observation considering the fact that the title compound is stoichiometric and the spin-glass anomalies arises presumably due to geometrical frustration (triangular arrangement of the neodymium atoms) as frequently observed in ZrNiAl type intermetallics [281].

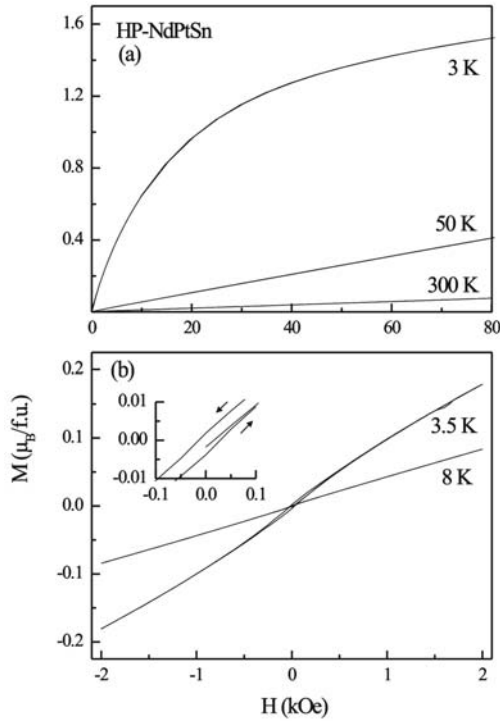


Figure 4.4-18: (a) M vs. H measured at 3, 50, and 300 K and (b) M vs. H measured in a sweeping field of ± 2 kOe at 3.5 and 8 K for HP-NdPtSn. The low field hysteresis observed for $T = 3.5$ K is shown in an expanded scale in the insert.

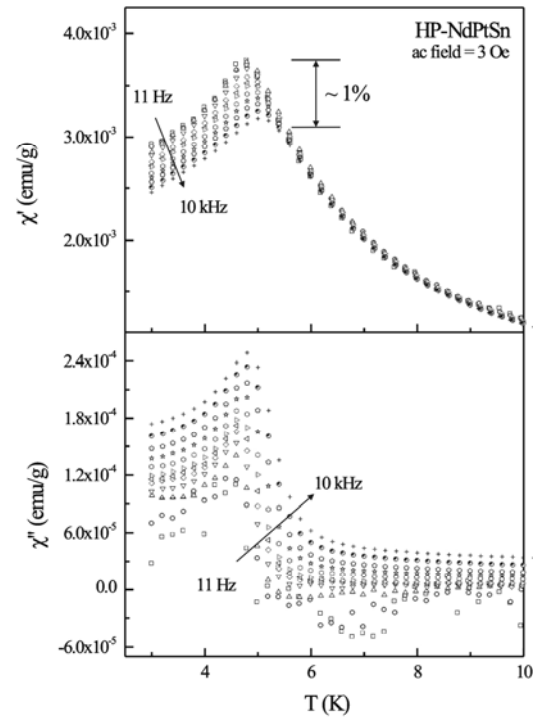


Figure 4.4-19: Real (χ') and imaginary (χ'') part of ac susceptibility for HP-NdPtSn measured in an ac field of 3 Oe, as a function of temperature for $\nu = 11, 21, 61, 111, 197, 341, 607, 1057, 1847, 3247, 5697$ Hz, and 10 kHz.

The frequency dependence of the ac susceptibility χ for HP-NdPtSn is shown in Figure 4.4-19. For $\nu = 11$ Hz, a broad peak around 4.5 K is seen, which moves to higher temperatures with increasing frequency. The shift in peak temperature, though broadened, can be clearly seen when moving from $\nu = 11$ Hz to 10 kHz. As observed in metallic spin-glasses, the peak shifts down while moving to higher temperatures with increasing frequency. The maximum observed for $\nu = 11$ Hz shifts down by about 1% for $\nu = 10$ kHz. Spin-glasses exhibit a sudden onset in χ'' near T_f . HP-NdPtSn also exhibits a peak in χ'' around T_f . The appearance of a peak in χ'' (absorption) means that the relaxation processes are affecting the measurement and by decoupling the spins from the lattice they cause the absorption [279]. Also the ratio of change in peak temperature in χ' to change of the frequency given by $\Delta T_f / T_f \Delta(\ln \nu)$ is observed to be of the order of 0.01, comparable to ideal spin-glasses [280, 282].

The magnetization of a spin-glass in a frozen state reacts to the externally applied field over a period of time. Therefore, in order to verify the spin-glass behaviour for HP-NdPtSn exhibited in the ac susceptibility χ and magnetization measurements, the isothermal relaxation magnetization (M_{IRM}) at 3 K was measured.

After zero field cooling of the sample, a field of 5 kOe was applied for five minutes and then reduced to zero. For a period of 2400 seconds the M_{IRM} was measured as soon as the field reached zero (Figure 4.4-20). The M_{IRM} decays logarithmically over the entire duration of the measurement and can be fitted to a function of the type

$$M_{IRM} = P1 - P2 \log(t) \quad (17)$$

where $P1 = 0.05969$ and $P2 = 0.01314$ are two fitting parameters, which depend on the temperature, waiting, and relaxation rate in 'dynamical equilibrium'.

The spin-glass behaviour of HP-NdPtSn can be better understood by analyzing the *ac* susceptibility χ more carefully. The shift of T_f with frequency can be better understood by the *Volgel-Fulcher* (V-F) law given by

$$\nu = \nu_0^{-E_a/k_B(T_f - T_a)} \quad (18)$$

where ν is the driving frequency, ν_0 is the characteristic spin-glass frequency ($\sim 10^8$ Hz for ideal spin-glasses), E_a is the activation energy, and T_a is called the ideal spin-glass temperature, which gives the strength of interaction among clusters [279, 280]. Therefore, for a spin-glass system the plot of T_f vs. $1/\ln(\nu/\nu_0)$ should be a straight line. Figure 4.4-21 shows the V-F law fitting to the observed data, which establishes that NdPtSn is indeed a spin-glass system. From the linear fit, we can deduce the values of T_a and E_a/k_B , where k_B is the Boltzmann constant.

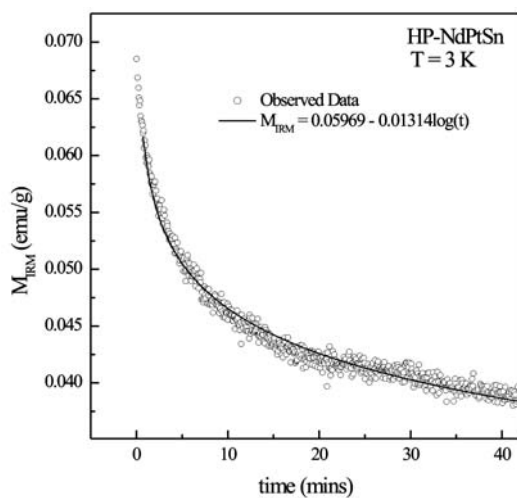


Figure 4.4-20: Isothermal relaxation of magnetization measured as a function of time (in minutes) for HP-NdPtSn measured at $T = 3$ K after subjecting the sample to a steady field of 5 kOe for five minutes.

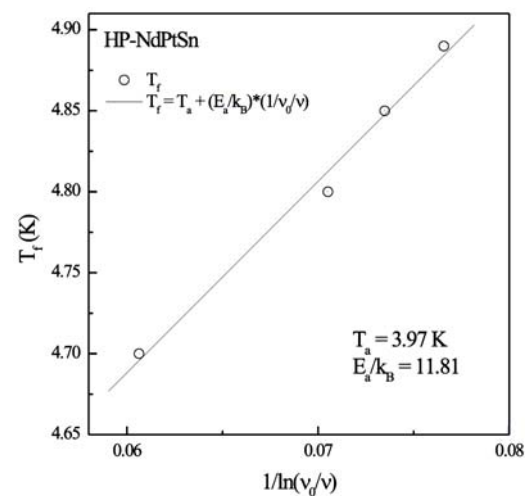


Figure 4.4-21: V-F law fit for HP-NdPtSn. The values of the fitting parameters are shown. For details see text.

The real part (χ') and imaginary part (χ'') of the ac susceptibility χ are usually related through a relaxation time by *Casimir du Pré* equations. According to these equations the real and imaginary part of the ac susceptibility are given by

$$\chi' = \chi_s + \frac{\chi_T - \chi_s}{1 + \nu^2 \tau^2} \quad (19)$$

and

$$\chi'' = \omega \tau \left(\frac{\chi_T - \chi_s}{1 + \nu^2 \tau^2} \right) \quad (20)$$

where τ is a single relaxation time, χ_T is the isothermal susceptibility in the limit $\nu \rightarrow 0$, and χ_s is the adiabatic susceptibility in the limit $\nu \rightarrow \infty$. At $\nu = 1/\tau$, the real part of susceptibility χ' (dispersion) will have an inflection point, whereas the imaginary part, χ'' (absorption) will show a maximum. Thus, this maximum provides a method of determining an average relaxation time τ_{av} for each temperature. Also according to equation (20), χ'' should follow a $\text{sech}(\ln \nu \tau)$ functional dependence for single τ and should be considerable broadened if a distribution of relaxation times $g(\tau)$ is present [279, 283].

In Figure 4.4-22 a plot of χ'' vs. frequency (in Hz) is shown. For $T < T_f$, absorption increases gradually with increasing frequency and remains at a higher value. However, for $T > T_f$, though there is a rapid increase with increasing frequency, the overall absorption drops with increasing T across T_f . These broad features in the absorption, also seen for canonical (RKKY) spin-glasses, indicate the presence of distribution relaxation times in the range of 10^{-14} s to ∞ [283].

Due to the frustration effects, the entropy in a spin-glass system is lost much above T_f , resulting in a very broad feature around T_f . This broadness smears out with the application of magnetic field, while moving to higher temperatures with increasing

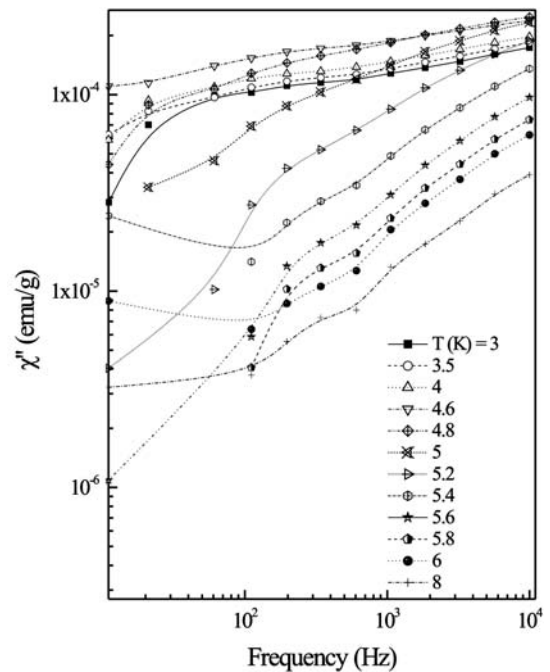


Figure 4.4-22: χ'' (absorption) vs. ν of HP-NdPtSn for different temperatures spanning T_f . The lines passing through the data points are guides for the eyes only.

field [279, 284, 285]. Figure 4.4-23 shows the specific heat of NdPtSn measured under various applied fields. For the measurement in $H = 0$, there is a broad peak in C around 5.4 K which is about 1.2 times T_f (shown in expanded form in the insert). With increasing temperature, the broad maximum above T_f is followed by a slow decrease up to 2.2 times T_f . The broad features observed in zero field become less pronounced with the application of external fields. For $H = 50$ kOe, the broad feature is completely smeared out around the vicinity of T_f . Figure 4.4-23(b) shows a plot of C/T vs. T . Once again, one can see a broad peak in C/T vs. T at around 1.2 times of T_f followed by a drop at higher T . Increasing field shifts this broad feature to higher temperatures.

In Figure 4.4-24 the total entropy measured for various fields is plotted. The sluggish variation of S with T , without any signs of saturation suggests that a great deal of magnetic entropy is lost or frozen-out far above T_f . The total entropy also smears out with the application of field, thus shifting entropy from low-temperature to high-temperatures.

Figure 4.4-24: Total entropy (S_{tot}) of HP-NdPtSn vs. T for various applied fields.

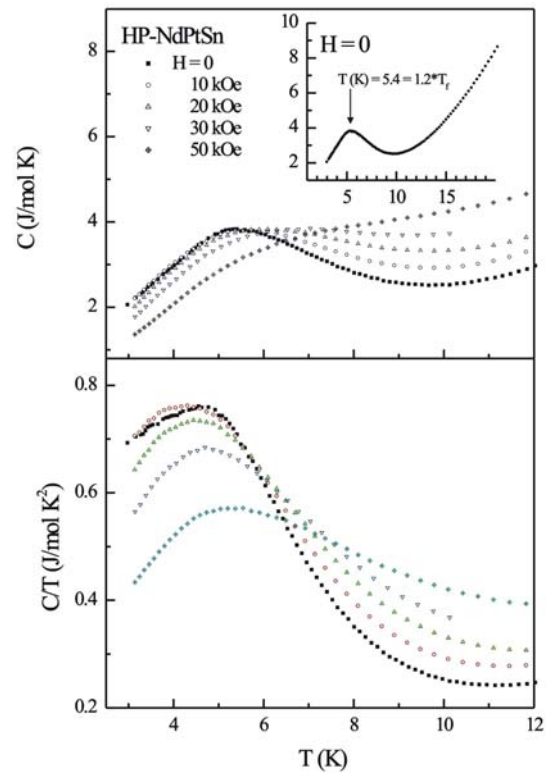
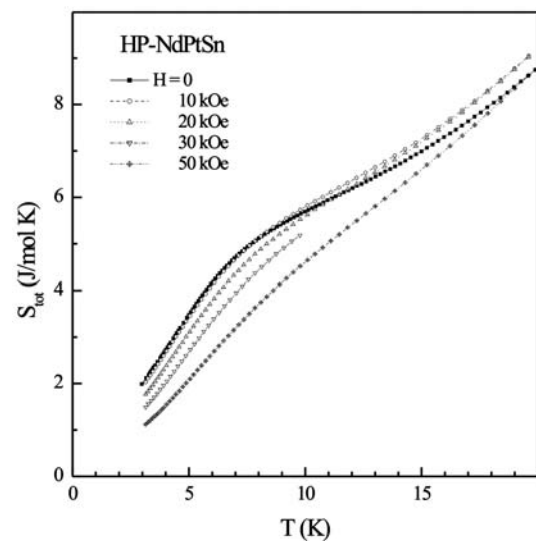


Figure 4.4-23: Change in heat capacity with temperature for HP-NdPtSn plotted in different ways. The top panel shows C vs. T measured at various applied fields and the bottom panel shows C/T vs. T at the same fields. The broad feature in $C(T)$ observed in $H = 0$ has been highlighted in the insert of the top panel.



4.4.3.7 Electronic Structure Calculation

CePtSn, as the first example where the pressure induced structural transformation from TiNiSi type to ZrNiAl type structure was observed, was the object of interest for electronic structure calculations. Self-consistent DFT band structure calculations were performed in cooperation with Prof. Dr. D. Johrendt (LMU-München) using the LMTO-method in its scalar-relativistic version (program TB-LMTO-ASA) [286]. Detailed descriptions are given elsewhere [287, 288]. Reciprocal space integrations were performed with the tetrahedron method [289] using 490 (NP-CePtSn) or 700 (HP-CePtSn) k -points within the irreducible wedges of the tetragonal Brillouin zones. The basis sets consisted of Ce: $6s\{6p\}/5d/4f$, Pt: $6s/6p/5d\{4f\}$ and Sn: $5s/5p\{5d/4f\}$. Orbitals given in parenthesis were downfolded [290]. In order to achieve space filling within the atomic sphere approximation, interstitial spheres were introduced to avoid too large overlap of the atom-centered spheres. The empty spheres positions and radii were calculated automatically. We did not allow overlaps of more than 15% for any two atom centered spheres. The COHP method was used for the bond analysis [291]. COHP gives the energy contributions of all electronic states for a selected bond. The values are negative for bonding and positive for antibonding interactions. With respect to the COOP diagrams, we plot $-COHP(E)$ to get positive values for bonding states.

The self consistent field (SCF) calculations of HP-CePtSn converge to a metallic ground state as expected. The resulting theoretical magnetic moment is compatible to one unpaired spin localized at the Ce atom, which is in agreement with the experimental magnetic moment of $2.53(1) \mu_B$ and confirms again the trivalent state of cerium. Figure 4.4-25 shows the COHP diagrams of the Pt–Sn, Ce–Pt, and Ce–Sn interactions, which surely amount the main part of the bonding energy of these structures. For clarity, we do not distinguish between crystallographically different bonds. Each of the COHP curves and integration values represent a weighted average of multiple (similar) bonds and thereby allows comparing their strengths directly. In both cases, we find the Pt–Sn bonds to be the by far strongest, which agrees with the idea of a covalent $[PtSn]^{3-}$ substructure. The distorted tetrahedral tin coordination in NP-CePtSn splits into one sixfold and one threefold coordinated Pt. But the latter one occurs twice in the unit cell, thus we count the same number of four Pt–Sn bonds per formula unit. Using the different bond frequencies, the COHP diagram reveals, that the Pt–Sn bonds get considerably (-25%) weaker in the high-pressure phase, whereas the Ce–Pt bonds get only slightly weaker (-6%) and finally the Ce–Sn bonds get stronger (+12%). If we multiply the ICOHP energies/bond by their frequency of occurrence per formula unit, we get a total covalent ICOHP

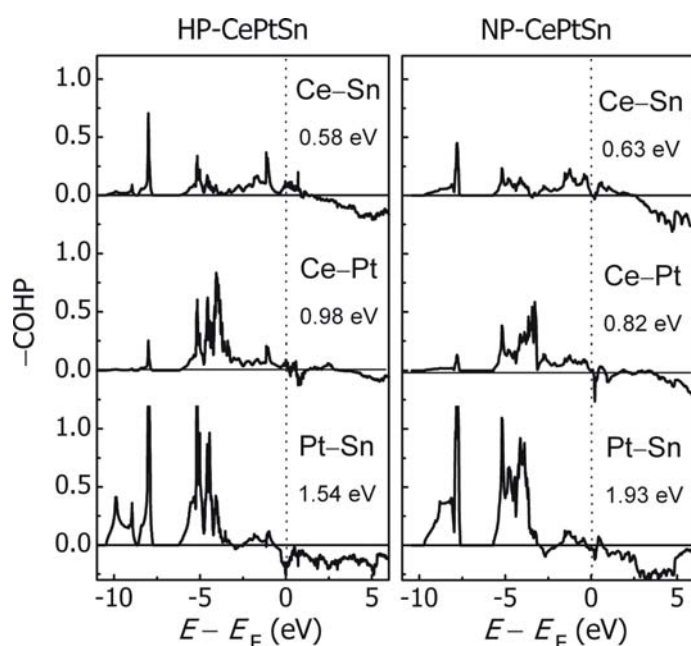


Figure 4.4-25: Crystal Orbital Hamilton Population (COHP) diagrams of the major bonds in HP- and NP-CePtSn. The mean integrated (ICOHP) energies per bond are given in eV; the energy zero is taken at the Fermi level.

bonding energy of 16.4 eV for NP-CePtSn and 15.5 eV for HP-CePtSn. This is attributed to the weaker Pt–Sn bonds and to the loss of one Ce–Pt contact in HP-CePtSn. Such a decrease of covalent bonding energy is typical for high-pressure phases and corresponds to a further metallization of all bonds due to the volume reduction. But altogether the total bonding energies of NP- and HP-CePtSn are remarkably similar despite the drastic changes in the coordination geometries. Also the total energy of the normal pressure structure is almost identical to that of the high-pressure variant and differs only by 0.78 eV/cell. Volume dependent calculations predict no phase transition from NP- to HP-CePtSn, *i.e.* NP-CePtSn remains more stable at pressures up to 20 GPa, but strictly only at $T = 0$ K. However, from this we expect that no structural transition under pressure will occur at room temperature. We approximate the volume reduction for NP-CePtSn from the calculated bulk module to be about -9% at 10 GPa. Thus the unit cell volume at ambient conditions of 68.66 \AA^3 will be compressed to 62.5 \AA^3 at 10 GPa. This is smaller than the volume of GdPtSn with 64.84 \AA^3 , which already adopts the hexagonal structure of HP-CePtSn. Although NP- and HP-CePtSn form different structures, both have nearly the same stabilities. In our opinion, the activation energy to transform one to the other is very high and can only be overcome by applying high-temperature and high-pressure conditions simultaneously. This is also supported by the remarkable stability of HP-CePtSn upon heating up to 850 °C, before it transforms back to the more stable NP-CePtSn.

In the following Chapters, the high-pressure / high-temperature investigations were extended with respect to other transition metals.

4.4.4 The Stannides $REPdSn$ ($RE = La, Ce$)

4.4.4.1 Introduction

Although $CePdSn$ has intensively been investigated with respect to its chemical bonding and Kondo lattice peculiarities [249, 292, 300, 301], only one high-pressure study can be found in the literature. Resistivity measurements with a standard *dc* four-probe method in a cubic-anvil device up to 8 GPa [303] revealed disappearance of the magnetic transition above 6 GPa and transformation to a non-magnetic Kondo lattice. This behavior was a strong hint for a structural phase transition, similar to $CePtSn$. For $LaPdSn$ no high-pressure / high-temperature investigations were known.

Both compounds crystallize with the orthorhombic $TiNiSi$ type structure. The change in structure type of the normal-pressure modification takes place for the rare-earth cations smaller than holmium. But holmium can adopt at normal-pressure conditions both structure types, the $TiNiSi$ type [263] and the $ZrNiAl$ type [264, 265, 322]. For ytterbium, besides the $ZrNiAl$ type modification an orthorhombic $TiNiSi$ type high-temperature modification is known [293].

Besides the structural characterization, especially the $CeTSn$ ($T = Ni, Rh, Pd, Ag, Ir, Pt, Au$) stannides have intensively been studied with respect to their interesting magnetic properties. $CeNiSn$ [294], $CeRhSn$ [295], and $CeIrSn$ [296] are intermediate valence systems, while $CePdSn$ ($T_N = 7.5$ K) [292] and $CePtSn$ ($T_N = 8$ K) [297, and ref. therein] are antiferromagnetic Kondo lattices. $CeAgSn$ orders antiferromagnetically at 6.5 K [319] and $CeAuSn$ ($T_C = 4.1$ K) [298] is the only ferromagnet within this series.

There are two possibilities to influence the magnetic behaviour of such intermetallic compounds. One is the hydrogenation of the materials. To give some examples, intermediate-valent $CeNiSn$ transforms to the 7.0 K ferromagnet $CeNiSnH_{1.8}$ [299] and the Néel temperature is reduced from 7.5 to 5.0 K ingoing from $CePdSn$ to $CePdSnH$ [302].

The second possibility is a high-pressure treatment. As Chapter 4.4.3 revealed, the orthorhombic $TiNiSi$ type normal-pressure (NP/ $CePtSn$) modification transforms at 9.2 GPa and 1325 K to a hexagonal $ZrNiAl$ type high-pressure (HP) modification. The cerium atoms remain trivalent in HP- $CePtSn$, and both compounds show magnetic ordering at low temperatures, whereas the kind of transition in HP- $CePtSn$ is unclear up till now.

In the following the high-pressure / high-temperature synthesis and the magnetic properties of HP-REPdSn ($RE = \text{La, Ce}$) with ZrNiAl type structure are presented.

4.4.4.2 Syntheses

For the precursor preparation of NP-REPdSn ($RE = \text{La, Ce}$) see Chapter 4.4.3.2. Similar to the REPtSn ($RE = \text{La, Ce, Pr, Nd, Sm}$) stannides, the high-pressure / high-temperature treatment took place *via* a multianvil assembly. A boron nitride crucible of an 14/8-assembly was loaded with carefully milled NP-REPdSn ($RE = \text{La, Ce}$), compressed within 4 h to 10.5 GPa and heated to 1100 °C for 20 min. Holding this temperature for 3 min, the sample was cooled down rapidly to 850 °C and annealed for 180 min to enhance the crystallinity. Afterwards the sample was cooled down to room temperature. After decompression, the sample was obtained as a nearly single phase product after carefully separating it from the surrounding assembly parts. Both NP- and HP-CePdSn are stable in moist air over months in powdered as well as in polycrystalline form. Single crystals exhibit metallic lustre while ground powders are dark grey.

The single crystals investigated on the diffractometer and the bulk samples of NP- and HP-CePdSn were studied by energy dispersive analyses of X-rays (EDX). The experimentally observed compositions were close to the ideal one and no impurity elements were observed.

4.4.4.3 Crystal Structure Analysis

The samples were characterized by powder patterns on a STOE Stadi P powder diffractometer with $\text{CuK}\alpha_1$ radiation ($\lambda = 154.06$ pm, Ge monochromator). To ensure correct indexing, the observed patterns were compared with calculated ones [57], taking the atomic positions obtained from the structure refinements. The lattice parameters were then refined through least-squares fits. The single crystal and powder lattice parameters were in good agreement. Figure 4.4-26 shows the powder patterns of the HP-phases in comparison with the simulation derived from the single crystal data. Small additional reflexes are belonging to an unidentified byproduct. Lowering the synthesis temperatures and pressures to 1000 °C and only 9 GPa with a simultaneous shortening of the heating period resulted in purer samples but at the expense of the crystal quality.

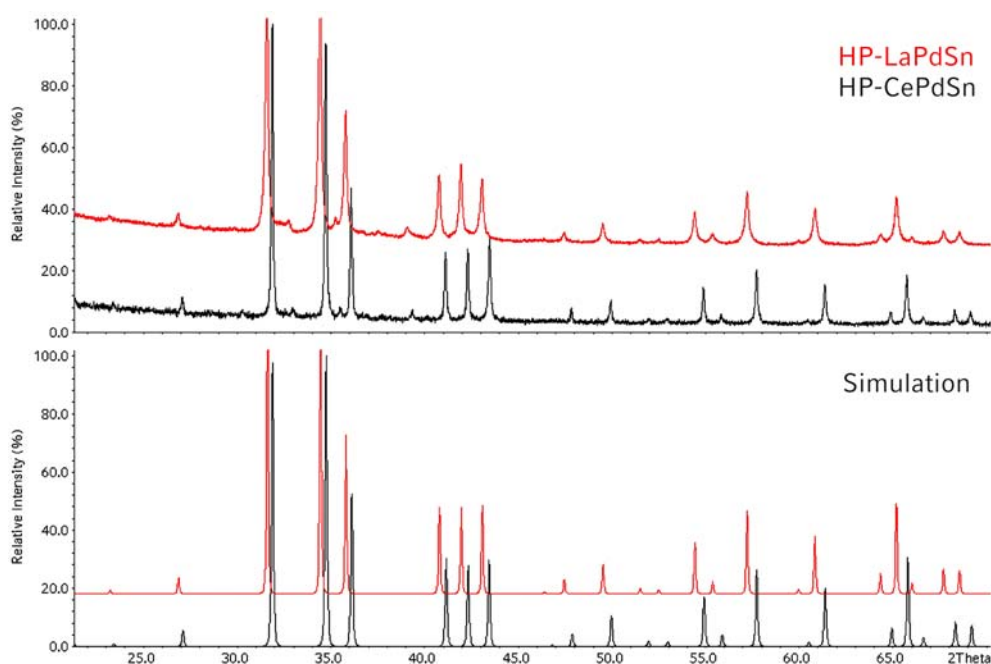


Figure 4.4-26: Recorded powder patterns of HP-REPdSn ($RE = La, Ce$) in comparison to the simulation derived from single crystal data.

Small, irregularly shaped single crystals of NP- and HP-REPdSn ($RE = La, Ce$) were selected by mechanical fragmentation from the arc-melted and the high-pressure treated samples, respectively. The crystals were first investigated by Laue photographs in a Buerger camera (white molybdenum radiation; imaging plate technique, Fujifilm, BAS-1800) in order to check the quality for intensity data collection. Intensity data of a suitable crystal of NP-CePdSn were collected at room temperature by use of a four-circle diffractometer (CAD4) with graphite monochromatized MoK_{α} ($\lambda = 71.073$ pm) radiation and a scintillation counter with pulse height discrimination. The scans were taken in the $\omega/2\theta$ mode and an empirical absorption correction was applied on the basis of psi-scan data, accompanied by a spherical absorption correction.

Data of the HP-CePdSn crystal were collected in oscillation mode on a STOE IPDS-I image plate diffractometer using monochromatized MoK_{α} radiation ($\lambda = 71.073$ pm). A numerical absorption correction was applied to this data set.

The HP-LaPdSn crystal was investigated on a Kappa CCD diffractometer (Bruker AXS / Nonius, Karlsruhe) equipped with a rotating anode. For NP-LaPdSn, no single crystal data are available up to now. All relevant crystallographic data and details of the data collections are listed in Table 4.4-11.

Similar to the recent results obtained for NP- and HP-REPtSn ($RE = La-Nd, Sm$), the data sets of NP- and HP-REPdSn ($RE = La, Ce$) were compatible with space

groups *Pnma* (TiNiSi type) and *P62m* (ZrNiAl type), respectively. The atomic parameters of NP- and HP-CePtSn were taken as starting values and both structure were then successfully refined using SHELXL-97 [80] (full-matrix least-squares on F^2) with anisotropic atomic displacement parameters for all atoms.

As a check for the correct composition, the occupancy parameters were refined in separate series of least-squares cycles. All sites were fully occupied within two standard uncertainties and in the final cycles the ideal occupancy parameters were assumed again. Refinement of the correct absolute structure for HP-LaPdSn or HP-CePdSn was ensured through refinement of the *Flack* parameter [266, 267]. Final difference Fourier syntheses revealed no significant residual peaks. The positional parameters and interatomic distances of the refinements are listed in Table 4.4-12 and Table 4.4-13.

Table 4.4-11: Crystal data and structure refinement for HP-LaPdSn, NP-CePdSn, and HP-CePdSn

Empirical formula	HP-LaPdSn	NP-CePdSn	HP-CePdSn
Molar mass (g·mol ⁻¹)	364.00	365.21	365.21
Crystal system	hexagonal	orthorhombic	hexagonal
Space group	<i>P62m</i>	<i>Pnma</i>	<i>P62m</i>
Radiation		CuK α_1 ($\lambda = 154.06$ pm)	
Powder-diffraction data			
<i>a</i> (pm)	765.1(3)	754.1(2)	760.03(5)
<i>b</i> (pm)	<i>b = a</i>	470.6(1)	<i>b = a</i>
<i>c</i> (pm)	419.4(2)	798.4(3)	416.06(3)
Volume (nm ³)	0.2126	0.2833	0.2081
Single crystal diffractometer	KappaCCD	CAD4	STOE IPDS I
Radiation		MoK α ($\lambda = 71.073$ pm)	
Formula units per cell	<i>Z</i> = 3	<i>Z</i> = 4	<i>Z</i> = 3
Temperature (K)		293	
Calculated density (g·cm ⁻³)	8.51	8.56	8.74
Crystal size (μm^3)	10 x 10 x 10	20 x 20 x 20	15 x 20 x 25
Detector distance (mm)	50	-	45
Irradiation / exposure (min)	-	-	14
ω range, increment	0-180°, 2.0°	-	0-180°, 0.9°
Scan time per degree (sec)	70		
Absorption coefficient (mm ⁻¹)	29.4	30.5	31.0
F(000)	459	616	462
θ Range	4° to 38°	3° to 40°	3° to 30°
Range in <i>hkl</i>	$\pm 13, \pm 10, \pm 7$	$\pm 13, \pm 8, \pm 14$	$\pm 10, \pm 10, \pm 5$
Total no. reflections	1482	6568	2042
Independent reflections	455 ($R_{\text{int}} = 0.0290$)	945 ($R_{\text{int}} = 0.0769$)	248 ($R_{\text{int}} = 0.0391$)
Reflections with $I > 2\sigma(I)$	416 ($R_{\sigma} = 0.0309$)	651 ($R_{\sigma} = 0.0366$)	240 ($R_{\sigma} = 0.0169$)
Data / parameters	455 / 14	945 / 20	248 / 13
Absorption correction	multi-scan [339]	psi-scan	numerical
Transm. ratio (max / min)	-	1.15 (0.953/0.830)	1.64 (0.720 / 0.440)
Goodness-of-fit (F^2)	0.974	1.021	1.134
Final <i>R</i> indices ($I > 2\sigma(I)$)	$R1 = 0.0168$ $wR2 = 0.0236$	$R1 = 0.0268$ $wR2 = 0.0290$	$R1 = 0.0181$ $wR2 = 0.0442$
<i>R</i> Indices (all data)	$R1 = 0.0230$ $wR2 = 0.0244$	$R1 = 0.0575$ $wR2 = 0.0336$	$R1 = 0.0189$ $wR2 = 0.0443$
<i>Flack</i> parameter	0.02(2)	-	-0.01(5)
Extinction coefficient	0.0015(3)	0.00119(9)	-
Larg. diff. peak and hole (e·Å ⁻³)	1.42 / -1.55	2.39 / -2.25	0.91 / -1.60

Table 4.4-12: Atomic coordinates and anisotropic displacement parameters (pm^2) for NP- and HP-*REPtSn* ($RE = \text{La}, \text{Ce}$). U_{eq} is defined as one third of the trace of the orthogonalized U_{ij} tensor. The anisotropic displacement factor exponent takes the form: $-2\pi^2[(ha^*)^2U_{11} + \dots + 2kha^*b^*U_{12}]$. $U_{23} = 0$.

Atom	Wyckoff position	x	y	z	U_{11}	U_{22}	U_{33}	U_{12}	U_{13}	U_{eq}
HP-LaPdSn										
Pr	3f	0.58610(5)	0	0	90(2)	99(2)	86(2)	49(1)	0	91(1)
Pt1	1a	0	0	0	108(2)	U_{11}	78(3)	54(1)	0	98(2)
Pt2	2d	$\frac{2}{3}$	$\frac{1}{3}$	$\frac{1}{2}$	115(2)	U_{11}	118(2)	57(1)	0	116(2)
Sn	3g	0.24682(5)	0	$\frac{1}{2}$	88(2)	92(2)	88(2)	46(1)	0	89(1)
NP-CePdSn										
Ce	4c	0.01218(5)	$\frac{1}{4}$	0.70118(4)	78(1)	90(1)	87(1)	0	3(1)	85(1)
Pd	4c	0.29942(7)	$\frac{1}{4}$	0.41500(8)	137(2)	81(3)	80(2)	0	-1(2)	99(1)
Sn	4c	0.18673(6)	$\frac{1}{4}$	0.0869(7)	107(2)	71(2)	72(2)	0	2(1)	83(1)
HP-CePdSn										
Ce	3f	0.5871(1)	0	0	110(2)	117(3)	107(3)	58(2)	0	111(2)
Pd1	1a	0	0	0	125(4)	U_{11}	88(7)	63(2)	0	113(3)
Pd2	2d	$\frac{2}{3}$	$\frac{1}{3}$	$\frac{1}{2}$	130(3)	U_{11}	143(6)	65(2)	0	134(2)
Sn	3g	0.2491(1)	0	$\frac{1}{2}$	104(3)	106(4)	106(4)	53(2)	0	106(2)

4.4.4.4 Crystal Structure Description

Parallel to isotypic *REPtSn* ($RE = \text{La-Nd}, \text{Sm}$) (see Chapter 4.4.3), also the orthorhombic *TiNiSi* type modification of *CePdSn* [300, 301] transforms to a high-pressure modification with hexagonal *ZrNiAl* type. The cell volume per formula unit of 69.4 \AA^3 of the high-pressure form of *CePdSn* is slightly smaller than that for the normal-pressure modification (70.8 \AA^3). The crystal chemical peculiarities and chemical bonding have been discussed in detail for NP- and HP-*REPtSn* ($RE = \text{La-Nd}, \text{Sm}$) (see Chapter 4.4.3 and the general discussion part in Chapter 4.4.7). The corresponding interatomic distances are listed in Table 4.4-13.

The cerium near-neighbour coordinations in NP- and HP-*CePdSn* are shown in Figure 4.4-4. It is clearly evident that besides the change in the cerium site symmetry (*m* in NP-*CePdSn* and *m2m* in HP-*CePdSn*), drastic changes in the cerium substructure occur. The latter plays an important role for the magnetic behaviour (see Chapter 4.4.4.6), which is mainly determined by the Ce–Ce distances and the Ce (4*f*)–Pd (4*d*) hybridisation.

Table 4.4-13: Interatomic distances (pm), calculated with the powder lattice parameters in NP- and HP-REPtSn ($RE = La, Ce$). All distances of the first coordination spheres are listed.

high-pressure				normal-pressure				high-pressure			
LaPdSn				CePdSn				CePdSn			
La:	4	Pd2	311.8(1)	Ce:	1	Pd	314.9(1)	Ce:	4	Pd2	309.5(1)
	1	Pd1	316.9(1)		2	Pd	323.6(1)		1	Pd1	313.9(1)
	2	Sn	333.9(1)		2	Sn	326.3(1)		2	Sn	330.5(1)
	4	Sn	346.8(1)		1	Sn	334.9(1)		4	Sn	343.8(1)
	4	La	399.5(1)		1	Sn	336.4(1)		4	Ce	396.9(1)
	2	La	419.6(1)		2	Sn	339.5(1)		2	Ce	416.1(1)
					2	Pd	345.2(1)				
					1	Pd	345.9(1)				
					2	Ce	385.0(1)				
					2	Ce	398.6(1)				
Pd1:	6	Sn	282.4(1)	Pd:	2	Sn	272.6(1)	Pd1:	6	Sn	281.3(1)
	3	La	316.9(1)		1	Sn	275.4(1)		3	Ce	313.9(1)
Pd2:	3	Sn	294.0(1)		1	Sn	292.1(1)	Pd2:	3	Sn	290.7(1)
	6	La	311.8(1)		1	Ce	314.9(1)		6	Ce	309.5(1)
					2	Ce	323.6(1)				
					2	Ce	345.2(1)				
					1	Ce	345.9(1)				
Sn:	2	Pd1	282.4(1)	Sn:	2	Pd	272.6(1)	Sn:	2	Pd1	281.3(1)
	2	Pd2	294.0(1)		1	Pd	275.4(1)		2	Pd2	290.7(1)
	2	Sn	327.3(1)		1	Pd	292.1(1)		2	Sn	328.0(1)
	2	La	333.9(1)		2	Ce	326.3(1)		2	Ce	330.5(1)
	4	La	346.8(1)		1	Ce	334.9(1)		4	Ce	343.8(1)
					1	Ce	336.4(1)				
					2	Ce	339.5(1)				

4.4.4.5 Thermal Behaviour

To investigate the high-temperature behaviour of the intermetallic high-pressure phases $REPdSn$ ($RE = La, Ce$), temperature-programmed *in-situ* X-ray diffractometry was performed on a STOE Stadi P powder diffractometer ($MoK\alpha_1$; $\lambda = 71.073$ pm) with a computer-controlled STOE furnace as described in Chapter 3.1.3.

HP-LaPdSn

Successive heating of HP-LaPdSn filled in a 0.1 mm outside diameter Mark capillary showed that the high-pressure modification is only stable up to 400 °C in an argon atmosphere (Figure 4.4-27). The complete transformation into a hitherto unknown phase takes place at about 700 °C. No further transformations could be detected, when heating the sample up to 1100 °C followed by lowering the temperature to ambient conditions. A decomposition of HP-LaPdSn into the corresponding oxides or metals can be excluded and was checked through comparison with the “SEARCH-MATCH” powder database [73].

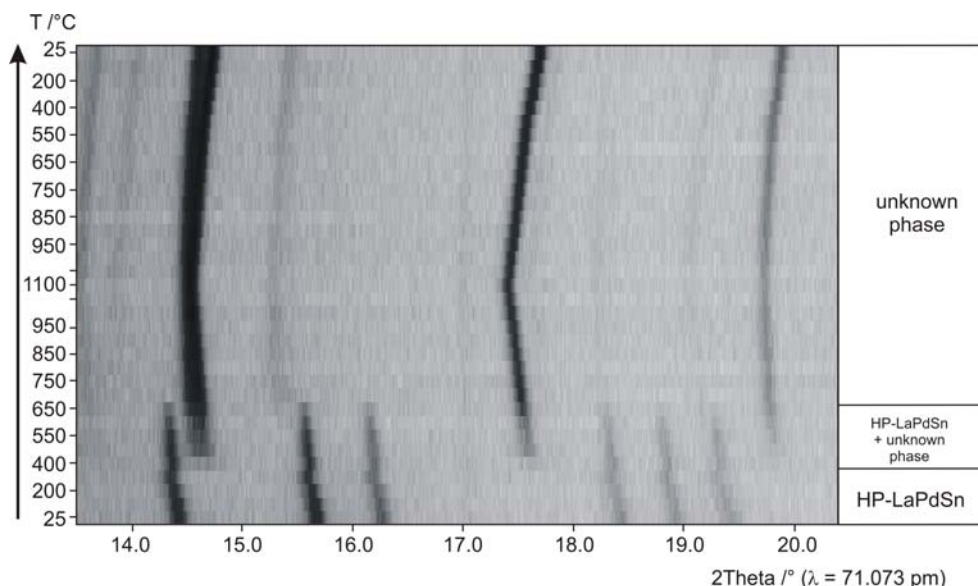


Figure 4.4-27: Temperature-programmed X-ray powder patterns of HP-LaPdSn.

HP-CePdSn

Successive heating of HP-CePdSn also filled in a 0.1 mm outside diameter Mark capillary showed deviating behaviour. The high-pressure modification is stable up to 300 to 350 °C under argon atmosphere (Figure 4.4-28). Then a transformation comparable to HP-LaPdSn into an unknown product occurs. But the high-pressure

phase remains present in the powder diffractograms up to a temperature of 1000 °C. Already at a temperature of 750 °C first peaks of the normal-pressure modification NP-CePdSn appear in the diffraction pattern. The complete transformation into the normal-pressure modification and the unknown phase is finished above 1000 °C. Both phases remain stable up to the maximum temperature of 1100 °C and also during the subsequent temperature decrease. A reaction with the Mark capillary as described for HP-SmPtSn can be excluded at these low temperature conditions. But interestingly, the reflections belonging to the small amount of byproduct at the high-pressure / high-temperature experiment show the same diffraction angles as the unknown phase detected at the temperature-programmed X-ray diffraction as far as it is possible to decide from the temperature-programmed diffraction pattern. This indicates that a further thermodynamically more stable phase than the HP-CePdSn seems to be present in this system. The differing HP-LaPdSn results and the missing back transformation indicate a decomposition reaction into binary phases. The high-temperature behaviour of the $REPdSn$ ($RE = La, Ce$) remains unclear.

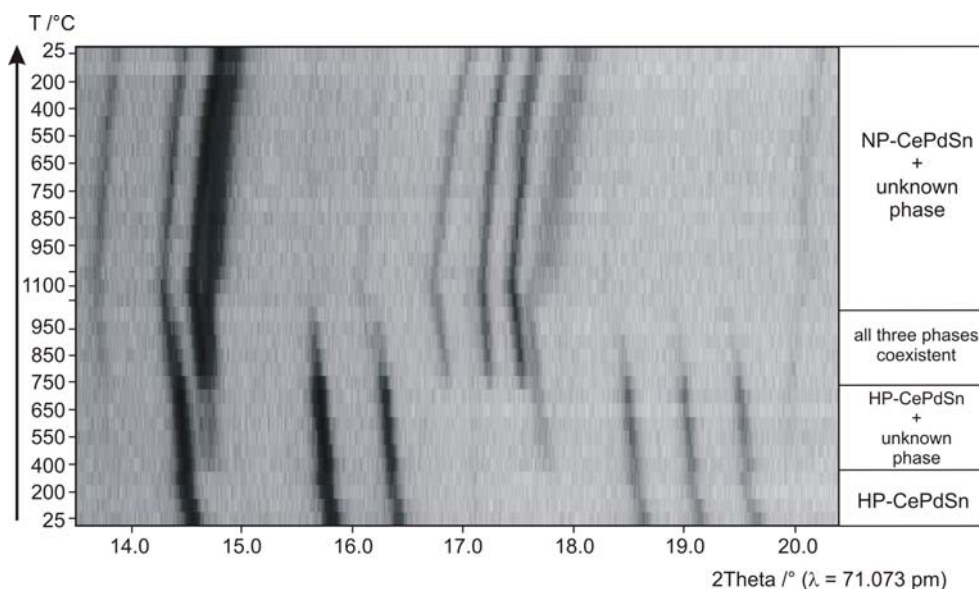


Figure 4.4-28: Temperature-programmed X-ray powder patterns of HP-CePdSn.

4.4.4.6 Magnetic Properties

Magnetic properties and heat capacity were measured on a bulk sample of HP-CePdSn in cooperation with Dr. S. Rayaprol, Universität Münster. Magnetic measurements were carried out in the temperature range 5–300 K on a QD-PPMS with a VSM insert. A small piece of the sample, glued to the platform of a pre-calibrated

heat capacity puck with *Apiezon N* grease, was used to measure heat capacity on the same PPMS.

The normal-pressure modification shows antiferromagnetic ordering at 7.5 K [292]. The susceptibility and resistivity data give clear indication for semiconducting-like Kondo behavior and a strong Ce 4*f*-conduction electron hybridization [257, 302, 303]. It was therefore desirable to study the magnetic behavior of the high-pressure modification also.

In Figure 4.4-29, the susceptibility ($\chi = M/H$) measured in an applied field of 10 kOe is plotted as a function of temperature down to 5 K. χ increases monotonously as T decreases. A small peak is observed in χ around 5 K, indicating an onset of antiferromagnetic ordering. The inverse susceptibility (χ^{-1}), plotted in the same figure, deviates from the Curie-Weiss law below 100 K, most likely due to crystal field splitting of the $J = 5/2$ ground state. From the linear region of χ^{-1} above 100 K, *i.e.*, in the paramagnetic region, the observed values of the paramagnetic Curie temperature (θ_p) and the effective Bohr magneton number (μ_{eff}) are -22.5(5) K and 2.55(1) μ_B/Ce atom, respectively. The negative sign of θ_p indicates antiferromagnetic interactions. The observed value of μ_{eff} is very close to the expected value of the free Ce^{3+} ion, 2.54 μ_B/mol cerium [274].

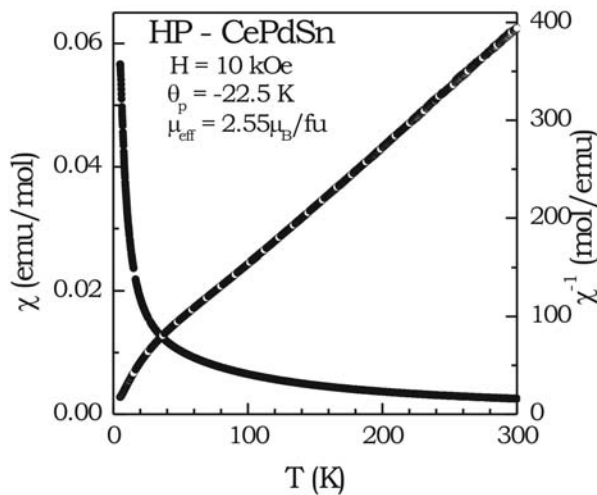


Figure 4.4-29: Susceptibility ($\chi = M/H$) and inverse susceptibility for HP-CePdSn, measured in an applied field of $H = 10$ kOe after zero field cooling.

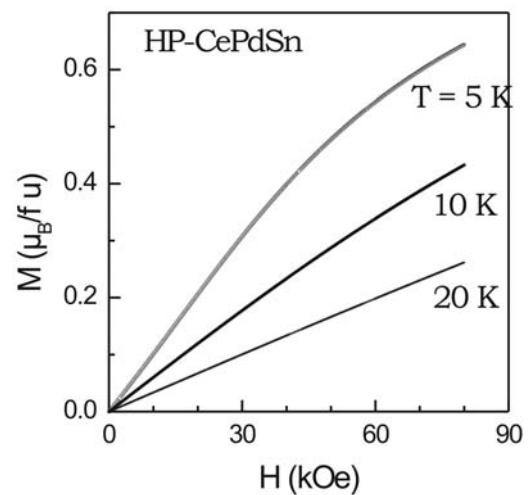


Figure 4.4-30: Magnetization (M) vs. varying field (H) for HP-CePdSn at $T = 5$, 10, and 20 K.

The magnetization as a function of field (M vs. H) for HP-CePdSn at $T = 5$, 10, and 20 K is shown in Figure 4.4-30. At $T = 5$ K, the magnetization M varies linearly with initial application of field and deviates as a curve above 30 kOe, clearly indicating the antiferromagnetic nature of magnetic ordering in HP-CePdSn. The magnetization M reaches a value of about 0.6 μ_B/Ce atom around 70 kOe. This value of satu-

ration magnetization is usually observed for similar cerium intermetallics [304, 305]. At 10 K, the magnetization M is still not linear with respect to field as it deviates from linearity above 30 kOe, indicating that the antiferromagnetic correlations persist up to this temperature. As expected, in the paramagnetic state of the compound, M varies linear with H (see the 20 K magnetization isotherm). The magnetic data thus exhibit that there is a clear transition from a paramagnetic state to an antiferromagnetic state in HP-CePdSn below 10 K. Another point worth noticing is that for all three temperatures the magnetization M is not hysteretic.

In Figure 4.4-31 the specific heat (C) data of HP-CePdSn measured down to 3 K is shown. The specific heat $C(T)$ undergoes a broad minimum in the temperature range 6–15 K, and exhibits a sharp peak around 5 K, indicating the antiferromagnetic transition temperature (T_N). Figure 4.4-31 also shows C measured in applied fields of 10 and 30 kOe. As expected for an antiferromagnet, the peak temperature slightly shifts to lower temperatures with increasing field.

In conclusion, cerium remains trivalent in the high-pressure modification, but there is a decrease of the magnetic ordering temperature from 7.5 (NP-CePdSn) to 5 K (HP-CePdSn). A similar decrease of the ordering temperature is observed in the sequence NP-CePdSn \rightarrow CePdSnH ($T_N = 5.0(2)$ K) [302]. Here, hydrogenation acts as a 'negative' pressure, decreasing the J_{cf} interactions. In contrast, for HP-CePdSn a switch in structure type (TiNiSi \rightarrow ZrNiAl) and a significant decrease in the Ce–Pd distances is observed, enabling stronger Ce (4*f*)–Pd (4*d*) hybridisation.

Finally, we draw back to the high-pressure resistivity studies by *Iga et al.* [303]. Their experiments under hydrostatic pressures up to 8 GPa at room temperature in a cubic-anvil device were indicative for disappearance of the magnetic transition in CePdSn at pressures higher than 6 GPa (transformation to a nonmagnetic Kondo lattice). At this point it remains unclear, if there is any structural phase transition under these room temperature conditions (in contrast, HP-CePdSn orders magnetically).

With the transition metal nickel, as already mentioned in the introduction of this Chapter, a group of very interesting compounds has been characterized. Therefore our interest in possible high-pressure phases was enormous. The following

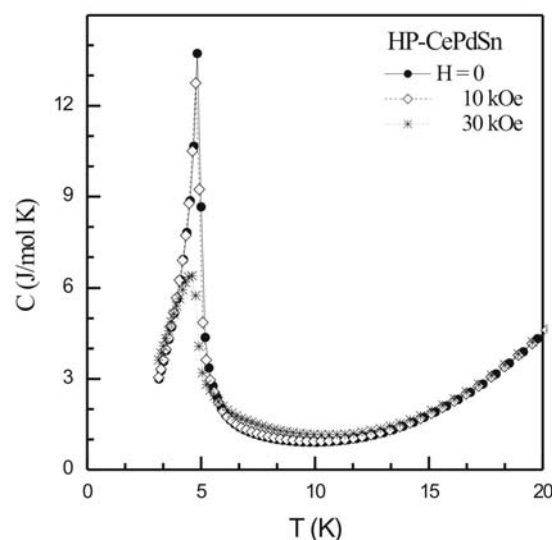


Figure 4.4-31: Specific heat (C) measured for HP-CePdSn in applied fields of $H = 0$, 10, and 30 kOe.

Chapter deals with the high-pressure investigations of the compounds LaNiSn, CeNiSn, and SmNiSn.

4.4.5 The Stannides $RENiSn$ ($RE = La, Ce, Sm$)

4.4.5.1 Introduction

The CeT Sn ($T = Ni, Rh, Pd, Ag, Ir, Pt, Au$) stannides crystallize with different structure types. CeNiSn, CePdSn [300, 301], and CePtSn [249] reveal the orthorhombic TiNiSi type, CeRhSn [295] and CeIrSn [296] adopt the ZrNiAl type and CeAgSn [319] and CeAuSn [306] crystallize with the hexagonal NdPtSb type. For the isotopic series $RENiSn$ compounds with each rare-earth representative except Pm are known crystallizing in the orthorhombic TiNiSi type structure [301, 323]. Besides the structural characterization, these stannides have intensively been studied with respect to their interesting magnetic properties. Especially the cerium compound [247] has been investigated since it exhibits valence changes or valence instabilities, *i.e.* $[Xe] 4f^0$ vs. $[Xe] 4f^1$. In the SciFinder data base [307], already 208 entries can be found dealing with this valence fluctuating Kondo lattice system. Up to now, the general way to influence the magnetic behaviour of such intermetallic compounds is the hydrogenation of the materials. Intermediate-valent CeNiSn transforms for example to the 7.0 K ferromagnet CeNiSnH_{1.8} [299]. High-pressure treatment of such compounds is another possibility to change the rare-earth coordination and influence the magnetic behaviour. We started our investigations with the probably most interesting cerium compound. Further on, the lanthanum and samarium compounds moved in our focus.

4.4.5.2 Syntheses

For the precursor preparation of NP- $RENiSn$ ($RE = La, Ce, Sm$) see Chapter 4.4.3.2. Several high-pressure / high-temperature experiments were performed to realize the HP- $RENiSn$ ($RE = La, Ce, Sm$) compounds with ZrNiAl type structure. A survey of the different approaches is given in Table 4.4-14.

Table 4.4-14: Experimental details of the high-pressure / high-temperature experiments.

Sample	Assembly	Max. pressure	Temperature program	Product
LaNiSn	14/8	5.5 GPa	↗ 1150 °C/15 min, → 1150 °C/16 min, ↓ 800 °C/1 min, ↘ 800 to 700 °C/300 min, ↓ RT	LaNi ₂ Sn ₂
CeNiSn	14/8	7.5 GPa	↗ 1150 °C/15 min, → 1150 °C/15 min, ↓ 800 °C/1 min, ↘ 800 to 700 °C/210 min, ↓ RT	HP-CeNiSn NP-CeNiSn
SmNiSn	14/8	10.5 GPa	↗ 1150 °C/20 min, → 1150 °C/10 min, ↓ 900 °C/1 min, ↘ 900 to 700 °C/180 min, ↓ RT	HP-SmNiSn

↗ : increase of temperature in x min, → : constant temperature for x min, ↘ : decrease of temperature in x min, ↓ : quenching of the sample

4.4.5.3 Crystal Structure Analysis

The samples were characterized by powder patterns on a STOE Stadi P or on a Huber Guinier powder diffractometer with CuK α_1 radiation ($\lambda = 154.06$ pm, Ge monochromator). A comparison with the Ce-Ni-Sn compounds listed in the "Search Match" database [73] revealed a probable transformation of NP-LaNiSn (TiNiSi type) into LaNi₂Sn₂ as main product. The RENi₂Sn₂ compounds (RE = La–Sm) were first described by Skolozdra *et al.* [308], some of them crystallize with the tetragonal structure of CaBe₂Ge₂ type, however, two allotropic forms are known for CeNi₂Sn₂ and LaNi₂Sn₂ [309], where annealing causes monoclinic distortion. A transformation of NP-LaNiSn into the ZrNiAl type was not evident up till now.

In the case of NP-CeNiSn (TiNiSi type) [310, 311] a partial transformation into ZrNiAl type HP-CeNiSn was observable. Figure 4.4-32 shows the powder pattern of the mixture of NP- and HP-CeNiSn with assigned reflections. Experiments indicated that higher synthetic pressures apparently favour the formation of CeNi₂Sn₂ which was detectable in the powder pattern at pressures above 7.5 GPa and in the case of LaNi₂Sn₂ already at pressures of 5.5 GPa. EDX analysis of a flat grinded sample using a Leica 420i scanning electron microscope with CeO₂, nickel, and tin as standards confirmed the 1:2:2 atomic ratio (Figure 4.4-33).

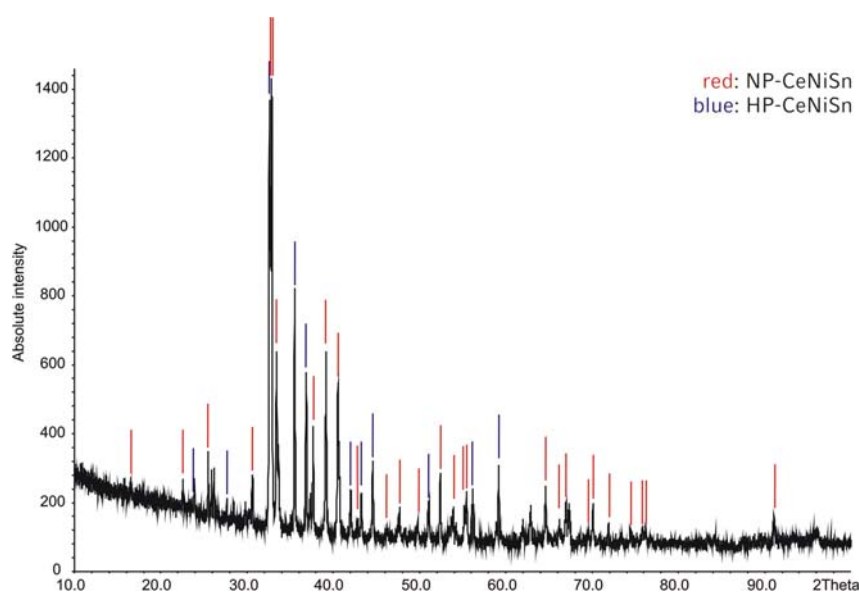
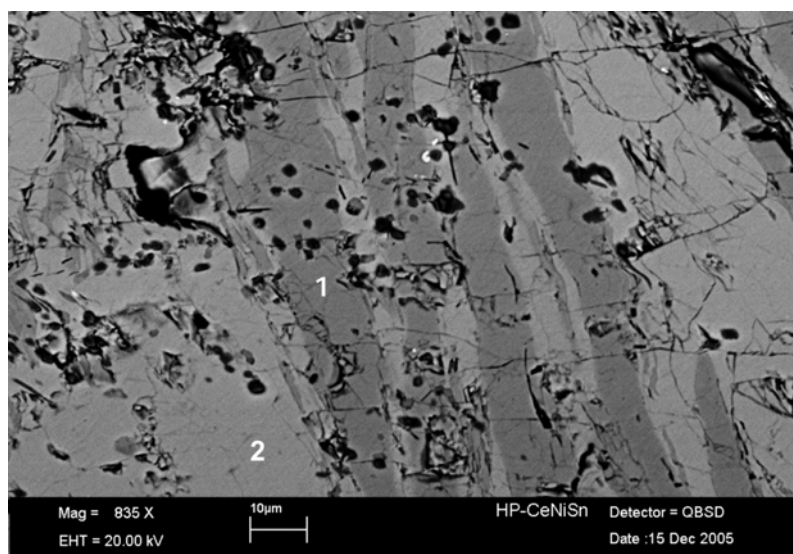


Figure 4.4-32: Powder pattern of the mixture NP-CeNiSn and HP-CeNiSn with marked reflections used for the cell refinement.



Phase	Weight %			Atom %		
	Ce	Ni	Sn	Ce	Ni	Sn
1	29.40(68)	22.31(58)	48.29(69)	21.05	38.12	40.12
1	29.87(65)	22.18(56)	47.95(66)	21.42	37.98	40.60
2	45.02(67)	18.54(54)	36.45(63)	34.03	33.44	32.53

Figure 4.4-33: EDX analysis of a flat grinded Ce-Ni-Sn sample confirming the two phases HP-CeNiSn (2) and CeNi_2Sn_2 (1).

The transformation of NP-SmNiSn into HP-SmNiSn at conditions mentioned in Table 4.4-14 succeeded in a X-ray pure ZrNiAl type high-pressure phase. Unfortunately, the single crystal quality of the two ZrNiAl analogue cerium and samarium compounds is still too bad and it was not possible to isolate suitable single crystals until now. So the diffraction patterns of HP-CeNiSn and HP-SmNiSn were indexed with the program ITO [70] on the basis of a hexagonal unit cell. The lattice parameters (Table 4.4-15) were obtained from least-square fits of the powder data. Further attempts to fully characterize the *RENiSn* compounds are still in progress.

In the previous Chapters a structural transformation from the TiNiSi type to the ZrNiAl type under high-pressure / high-temperature conditions was observable. In the following we were interested in a second structure type, also AlB_2 related, which shows a comparable situation concerning a structural change depending on the rare-earth size. We were successful with the discovery of the hexagonal NdPtSb type. Our experiments started with ErAgSn, in which Er is just too large to adopt the denser ZrNiAl type structure. The results of the performed high-pressure experiments are presented in the following.

Table 4.4-15: Refined cell parameters of HP-CeNiSn and HP-SmNiSn

	HP-CeNiSn	HP-SmNiSn
Molar mass ($\text{g}\cdot\text{cm}^{-3}$)	317.52	327.76
Space group		<i>P62m</i>
Lattice parameters		
a (pm)	744.6(2)	735.1(2)
c (pm)	406.29(8)	398.14(9)
Volume (nm^3)	0.195	0.186

4.4.6 The Stannide ErAgSn

4.4.6.1 Introduction

The equiatomic stannides $REAgSn$ (RE = rare-earth element) crystallize with different structures types, depending on the size of the rare-earth element. Under normal-pressure conditions, the $REAgSn$ stannides with $RE = Y, La-Nd, Sm,$ and $Gd-Er$ adopt the NdPtSb type structure, space group $P6_3mc$. Furthermore, EuAgSn with divalent europium adopts the KHg_2 type, space group $Imma$, and YbAgSn crystallizes into the YbAgPb structure, space group $P6m2$. A literature overview on these stannides is given in [316].

In the cases of smaller rare-earth elements, *i.e.* Tm, Lu, and Sc, other structure types occur. Samples of TmAgSn and LuAgSn annealed at 970 K show the hexagonal ZrNiAl type with two crystallographically independent tin sites, both in trigonal prismatic coordination [316]. The scandium atoms are too small for this structure type, and consequently the TiFeSi superstructure forms for ScAgSn. This superstructure was unambiguously determined by a combination of X-ray diffraction, ^{45}Sc , and ^{119}Sn solid-state NMR spectroscopy [312].

The previous Chapters of this thesis revealed that the crystal chemistry of such equiatomic $RETSn$ stannides, where different structure types occur within one series, can effectively be modified by applying high-pressures. Thus, the stabilization of metastable high-pressure phases means that the phase transitions are in most cases reconstructive.

This strategy was now applied to the $REAgSn$ stannides. In this series, the structural transformation occurs between the erbium [313-315, 319, 325-327] and the thulium [316] compound with a switch from the NdPtSb [317, 318] to the ZrNiAl [264, 265, 322] type.

4.4.6.2 Synthesis

Starting materials for the synthesis of NP-ErAgSn were ingots of erbium, silver wire, and tin granules, all with a stated purity better than 99.9%. The arc-melting procedure of the precursor was the same as previously described for the other intermetallic precursor materials. For further information see Chapter 2.1 and 4.4.3.2.

The intermetallic precursor was compressed in a 14/8-assembly to a pressure of 11.5 GPa in 3.5 hours and heated to 1150 °C in the following 20 min. After holding this temperature for 10 min, the sample was cooled down to 900 °C in 1 min. To

enhance the crystallinity of the sample, an annealing period of three hours followed, accompanied by a slow decrease of the temperature from 900 to 700 °C. Afterwards, the sample was cooled down to room temperature within 1 min. After decompression (10.5 hours), the recovered experimental octahedron was broken apart and the sample carefully separated from the surrounding boron nitride.

NP-ErAgSn and HP-ErAgSn are stable in air over months. Single crystals exhibit metallic lustre while ground powders are dark grey.

The single crystals investigated on the diffractometers and the bulk samples of the two stannides were studied by energy dispersive analyses of X-rays (EDX) using a scanning electron microscope. The experimentally observed compositions were all close to the ideal ones and no impurity elements were observed.

4.4.6.3 Crystal Structure Analysis

Both samples (precursor and high-pressure / high-temperature treated sample) were characterized through powder diffraction patterns using $\text{CuK}\alpha_1$ radiation. The hexagonal lattice parameters (Table 4.4-16) were refined from the powder data. The correct indexing was ensured through comparison of the observed patterns with calculated ones [256] taking the atomic positions obtained from the structure refinements. The single crystal and powder lattice parameters matched well. The normal-pressure phases are in good agreement with the literature data [313-315, 319].

Well-shaped single crystals were selected from the mechanically fragmented samples. The crystals were first investigated by Laue photographs on a Buerger camera (white molybdenum radiation; imaging plate technique, Fujifilm, BAS-1800) in order to check the quality for the data collection. Intensity data of NP-ErAgSn and HP-ErAgSn were collected at room temperature by use of a four-circle diffractometer (CAD4) with graphite monochromatized $\text{AgK}\alpha$ ($\lambda = 56.086$ pm; for a better differentiation between Ag/Sn) radiation and a scintillation counter with pulse height discrimination. The scans were taken in the $\omega/2\theta$ mode and empirical absorption corrections were applied on the basis of psi-scan data, accompanied by spherical absorption corrections. All relevant crystallographic data and details of the data collections are listed in Table 4.4-16.

The diffractometer data set of NP-ErAgSn was compatible with the space group $P6_3mc$. Since the Guinier powder data already revealed isotypism to the NdPtSb type, the atomic parameters of isotypic YAgSn [316] were taken as starting parameters. The HP-ErAgSn data set revealed no systematic extinctions in agreement with the space group $P6_2m$. In this case, the atomic parameters of isotypic LT-TmAgSn

[316] were taken as starting values. Subsequently, the two structures were successfully refined using SHELXL-97 [80] (full-matrix least-squares on F^2) with anisotropic atomic displacement parameters for all atoms. Since silver and tin differ only by three electrons, the silver and tin site occupancy parameters were refined in a separate series of least-squares cycles, in order to check for deviations from full occupancy and / or mixed occupied sites (99.8(6)% Ag and 99.8(6)% Sn for NP-ErAgSn; 99.4(5)% Ag, 101.8(8)% Sn1, and 100.2(5)% Sn2 for HP-ErAgSn). All positions were fully occupied and in the final cycles the ideal occupancy parameters were assumed again. Final difference Fourier syntheses revealed no significant residual peaks. Refinement of the correct absolute structures was ensured through refinement of the *Flack* parameters [266, 267]. Both structures revealed twinning by inversion (see BASF values in Table 4.4-16). The positional parameters and interatomic distances of the refinements are listed in Table 4.4-17 and Table 4.4-18.

Table 4.4-16: Crystal data and structure refinement for NP-ErAgSn and HP-ErAgSn.

Empirical formula	NP-ErAgSn	HP-ErAgSn
Molar mass (g·mol ⁻¹)	393.82	464.13
Crystal system		hexagonal
Space group	<i>P6₃mc</i>	<i>P6₂m</i>
Radiation		CuK α_1 ($\lambda = 154.06$ pm)
Powder-diffraction data		
<i>a</i> (pm)	466.3(1)	728.7(2)
<i>c</i> (pm)	729.0(2)	445.6(1)
Volume (nm ³)	0.1373	0.2049
Single crystal diffractometer		CAD4
Radiation		MoK α ($\lambda = 71.073$ pm)
Formula units per cell	<i>Z</i> = 2	<i>Z</i> = 3
Temperature (K)		293
Calculated density (g·cm ⁻³)	9.53	9.57
Crystal size (μm^3)	25 x 25 x 65	20 x 30 x 60
Absorption coefficient (mm ⁻¹)	24.5	24.7
F(000)	330	495
θ Range	3° to 30°	2° to 29°
Range in <i>hkl</i>	$\pm 8, \pm 8, \pm 12$	$\pm 12, \pm 12, \pm 7$
Total no. reflections	2239	4811
Independent reflections	347 ($R_{\text{int}} = 0.0593$)	488 ($R_{\text{int}} = 0.0673$)
Reflections with $I > 2\sigma(I)$	298 ($R_{\sigma} = 0.0274$)	475 ($R_{\sigma} = 0.0249$)
Data / parameters	347 / 12	488 / 15
Absorption correction		psi-scan
Transm. ratio (max / min)	1.39 (0.606 / 0.435)	1.68 (0.595 / 0.355)
Goodness-of-fit (F^2)	1.110	1.025
Final <i>R</i> indices ($I > 2\sigma(I)$)	<i>R</i> 1 = 0.0179 <i>wR</i> 2 = 0.0422	<i>R</i> 1 = 0.0178 <i>wR</i> 2 = 0.0392
<i>R</i> Indices (all data)	<i>R</i> 1 = 0.0233 <i>wR</i> 2 = 0.0439	<i>R</i> 1 = 0.0192 <i>wR</i> 2 = 0.0397
BASF	0.20(3)	0.49(2)
Extinction coefficient	0.013(2)	0.0067(7)
Larg. diff. peak and hole (e·Å ⁻³)	1.69 / -1.97	3.26 / -0.99

Table 4.4-17: Atomic coordinates and anisotropic displacement parameters (pm^2) for NP-ErAgSn and HP-ErAgSn. U_{eq} is defined as one third of the trace of the orthogonalized U_{ij} tensor. The anisotropic displacement factor exponent takes the form: $-2\pi^2[(ha^*)^2U_{11}+\dots+2hka^*b^*U_{12}]$. $U_{13} = U_{23} = 0$.

Atom	Wyckoff position	x	y	z	U_{11}	U_{22}	U_{33}	U_{12}	U_{eq}
NP-ErAgSn									
Er	2a	0	0	0.99553(8)	81(1)	U_{11}	78(2)	40(1)	80(1)
Ag	2b	$\frac{2}{3}$	$\frac{1}{3}$	0.30633(14)	94(4)	U_{11}	147(5)	47(2)	112(3)
Sn	2b	$\frac{2}{3}$	$\frac{1}{3}$	0.71554(9)	70(3)	U_{11}	91(4)	35(1)	77(3)
HP-ErAgSn									
Er	3f	0.56941(5)	0	0	102(1)	69(1)	88(1)	34(1)	90(1)
Ag	3g	0.24468(8)	0	$\frac{1}{2}$	97(2)	125(3)	166(3)	63(1)	126(1)
Sn1	1a	0	0	0	120(2)	U_{11}	88(3)	60(1)	109(2)
Sn2	2d	$\frac{2}{3}$	$\frac{1}{3}$	$\frac{1}{2}$	76(1)	U_{11}	74(2)	38(1)	76(1)

4.4.6.4 Crystal Structure Description

As an example, the structures of NP- and HP-ErAgSn are displayed in Figure 4.4-34 and Figure 4.4-3 bottom, respectively. NP-ErAgSn crystallizes into the NdPtSb type structure [317], a ternary ordered version of the well known AlB_2 type [318]. The structure of NP-ErAgSn was investigated by *Baran et al.* [319] on the basis of neutron powder diffraction data. The here presented single crystal data confirm this structural model; however, the lattice parameters and the positional parameters have been determined with significantly higher precision. Also it was possible to clearly distinguish the silver and tin atoms, leading to the ordered NdPtSb type arrangement. The silver and tin atoms build up a slightly puckered network of condensed Ag_3Sn_3 hexagons (Figure 4.4-34) with Ag–Sn distances of 277 pm, close to the sum of the covalent radii of 274 pm [273]. These Ag_3Sn_3 hexagons are rotated by 60° in every other layer, leading to an AB AB stacking sequence. Consequently, every silver (tin) atom has a fourth tin (silver) contact in the neighboring layer at the longer Ag–Sn distance of 298 pm. We

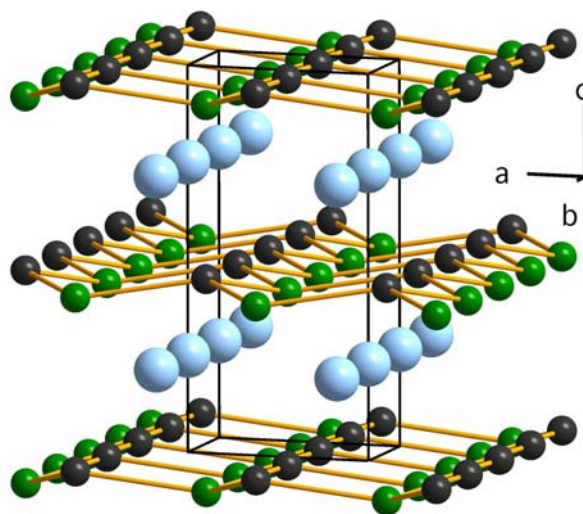


Figure 4.4-34: The structure of NP-ErAgSn. The erbium, silver, and tin atoms are drawn as light blue, black, and green spheres, respectively. The two-dimensional [AgSn] networks are emphasized.

can thus assume significant covalent Ag–Sn intralayer bonding, while the interlayer bonding is much weaker and the Ag_3Sn_3 network has a pronounced two-dimensional character. This is in agreement with electronic structure calculations in the isotypic series of REAuGe germanides [320]. For further crystal chemical details on such AlB_2 related superstructures, the reader should be referred to a recent review [318].

Under the high-pressure / high-temperature conditions NP-ErAgSn transforms to HP-ErAgSn with ZrNiAl type structure. Figure 4.4-3 bottom displays the ZrNiAl type structure for the isotypic REPtSn representatives. But in contrast to the REPtSn phases, in HP-ErAgSn, tin occupies the two platinum sites and silver the single tin sites of REPtSn . In the high-pressure modification, each silver atom has now four tin neighbors at Ag–Sn distances in the range 281–285 pm in a strongly distorted tetrahedral coordination, thus leading to a three-dimensional [AgSn] network. This network leaves distorted hexagonal channels, which are filled by the erbium atoms (Figure 4.4-3 bottom). Due to the reconstructive phase transition from NP-ErAgSn to HP-ErAgSn, there is no direct crystallographic relation between the two structures. The Sn1 atoms in HP-ErAgSn have trigonal prismatic silver coordination. The triangular faces of these Sn1Ag_6 prisms have an edge length of 309 pm, slightly longer than the Ag–Ag distance in *fcc* silver (289 pm) [321].

Besides the change in silver coordination and an increase in density (from 9.53 to 9.57 g/cm^3), the most pronounced difference between NP-ErAgSn and HP-ErAgSn concerns the erbium coordination. The coordination number (CN) increases from CN 14 for NP-ErAgSn (6 Ag + 6 Sn + 2 Er) to CN 15 for HP-ErAgSn (5 Sn + 6 Ag + 4 Er). In agreement with the pressure-coordination rule and the pressure-distance paradoxon, the Er–Ag (303 vs. 325 pm) and Er–Er (365 vs. 375 pm) distances are larger in the high-pressure modification. On the other hand, the Er–Sn distances are shorter in HP-ErAgSn (311 and 314 pm vs. 313 and 338 pm).

Table 4.4-18: Interatomic distances (pm), calculated with the lattice parameters taken from X-ray powder data of NP-ErAgSn and HP-ErAgSn. All distances within the first coordination spheres are listed.

normal-pressure				high-pressure			
NP-ErAgSn				HP-ErAgSn			
Er:	3	Ag	302.5(1)	Er:	4	Sn2	310.6(1)
	3	Sn	313.4(1)		1	Sn1	313.8(1)
	3	Sn	337.9(1)		2	Ag	325.0(1)
	3	Ag	351.9(1)		4	Ag	352.1(1)
	2	Er	364.5(1)		4	Er	374.7(1)
	6	Er	466.3(1)				
Ag:	3	Sn	277.2(1)	Ag:	2	Sn2	280.8(1)
	1	Sn	298.3(2)		2	Sn1	285.4(1)
	3	Er	302.5(1)		2	Ag	308.8(2)
	3	Er	351.9(1)		2	Er	325.0(1)
				4	Er	352.1(1)	
Sn:	3	Ag	277.2(1)	Sn1:	6	Ag	285.4(1)
	1	Ag	298.3(2)		3	Er	313.8(1)
	3	Er	313.4(1)	Sn2:	3	Ag	280.8(1)
	3	Er	337.9(1)		6	Er	310.6(1)

4.4.7 Discussion

The NP-RETSn ($RE = \text{La-Nd, Sm, Er}$; $T = \text{Ni, Pd, Pt, Ag}$) stannides crystallize as presented in the previous Chapters of this thesis with different AlB_2 related structure types. With La, Ce, Pr, Nd, Sm, or Eu as rare-earth metal components and platinum as transition metal component, these stannides crystallize with the orthorhombic TiNiSi type structure [263], while those with the smaller rare-earth elements adopt the hexagonal ZrNiAl type [264, 265, 322]. Gadolinium and the following smaller rare-earth elements are most likely too small for a TiNiSi like structural arrangement under normal-pressure conditions. With palladium as transition metal compound the corresponding change in structure type ($\text{TiNiSi} \rightarrow \text{ZrNiAl}$) takes place with holmium which can also adopt the TiNiSi type as well as the ZrNiAl type structure [323]. This change in crystal structure seems to be driven by the size (lanthanoide contraction) and the compressibility of the rare-earth elements.

It was now possible, to stabilize the ZrNiAl type structure for the rare-earth atoms larger than Gd with the help of the parameter pressure. This change in structure type is a reconstructive phase transition and the high-pressure samples can be quenched and characterized under ambient pressure conditions. That these phases are in fact metastable high-pressure compounds could proper be shown with tem-

perature-programmed *in-situ* X-ray diffractometry. Between 500–900 °C the high-pressure phases fully transformed back into the normal-pressure modification.

Due to the reconstructive type of the phase transition a significantly different coordination for the rare-earth cations in the normal- and high-pressure arrangement was observed. Each rare-earth atom has six nearest rare-earth neighbors, but in different geometry and with distinctly different *RE–RE* distances. Also the rare-earth-platinum coordination is different, *i.e.* six platinum neighbors in the normal-pressure and five ones in the high-pressure modification. The different rare-earth coordination is the main reason for the differing magnetic properties of both modifications. Magnetic properties were measured for the four high-pressure phases HP-CePtSn, HP-PrPtSn, HP-NdPtSn, and HP-CePdSn. All four stannides showed trivalent rare-earth cations over the whole temperature range (2–300 K). The experimental magnetic moments were close to the values for the free RE^{3+} cations. Latest results of HP-CePtSn exhibited a magnetic ordering at a temperature of 2.11 K and for HP-PrPtSn only short range magnetic ordering below 10 K was observable. For HP-NdPtSn spin-glass behavior was detected at temperatures below the freezing temperature of 4.5 K. HP-CePdSn showed antiferromagnetic ordering at temperatures lower than the Néel-temperature of 5 K.

It is interesting to compare the cell volumes per formula unit of the *REPtSn* stannides. The HP-modification of CePtSn has a slightly smaller cell volume (68.66 \AA^3) than NP-CePtSn with 69.31 \AA^3 . The change in structure type under ambient pressure conditions sets in for the gadolinium compound [272] with a much smaller cell volume of 64.84 \AA^3 . As it is evident from Figure 4.4-35 the transformation is accompanied by a densification effect of less than 1% in volume. The most evident difference between the two structural modifications (the NP and the HP forms) concerns the rare-earth coordination, *i.e.* $d(\text{Ce–Ce})$ in NP-CePtSn $\sim 4.12 \text{ \AA}$ and $d(\text{Ce–Ce})$ in HP-CePtSn $\sim 4.02 \text{ \AA}$. Thus a significant reduction during this high-pressure structure transformation was observed. Due to the electronic structure of the rare-earth elements (filling of *4f* orbitals), the compressibility of the cerium atoms as compared to the Pt and Sn atoms (filling of *d* or *p* orbitals) is more pronounced leading to a slightly smaller radius in the high-pressure modification. The course of the cell volumes of the normal-pressure and high-pressure phases nicely reflects the lanthanoide contraction. Both curves are almost parallel. As expected for the trivalent cerium atoms of both CePtSn modifications, the plot of the cell volumes shows no anomaly. In the course of the systematic investigation on high-pressure and/or high-temperature *RETSn* stannides, we were also interested in temperature induced phase transitions. Studies by *Riecken et al.* revealed that the yttrium, gadolinium, and the terbium compound show a similar phase transition, which nicely

rounds up these investigations [324]. The TiNiSi type high-temperature (HT) modifications of YPtSn, GdPtSn, and TbPtSn were obtained by rapidly quenching arc-melted samples. Annealing for five days at 800 °C resulted in a transformation to the ZrNiAl type low-temperature modifications again. The cell volumes per formula unit of the high-temperature phases are included in Figure 4.4-35, too.

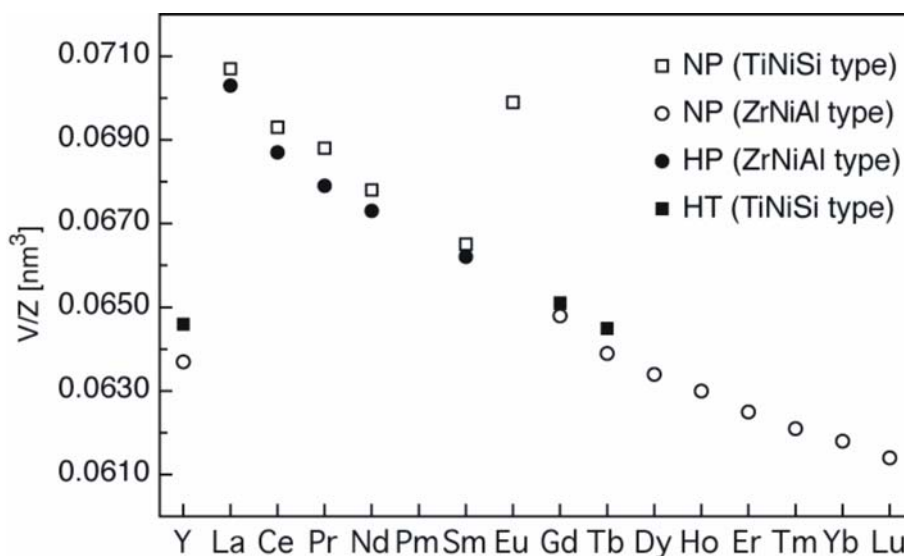


Figure 4.4-35: Plot of the cell volumes per formula unit of the normal-pressure, high-pressure, and high-temperature modifications of the $REPtSn$ stannides.

The Pt-Sn network of both structure types is a very strong and not much flexible network. With varying rare-earth cations the Pt-Sn distances still remain unaffected. Starting with lutetium at normal-pressure conditions we observe the ZrNiAl type structure up to the gadolinium. For larger rare-earth cations the Pt-Sn network seems to be too small and a structural transformation into the TiNiSi type takes place. This structural transformation can be prevented through applying high-pressure. So it is possible to stabilize the ZrNiAl type for rare-earth cations larger than gadolinium. In contrast to these results it is also possible to stabilize the less dense structure type. But therefore we need kinetic energy and the obtained phases (HT-YPtSn, HT-GdPtSn, HT-TbPtSn) are quenched high-temperature phases.

A second AIB_2 related structure type is the NdPtSb type structure [317, 318]. This strategy was now applied to the $REAgSn$ stannides. In this series, the structural transformation occurs between the erbium [313-315, 319, 325-327] and the thulium [316] compound with a switch from the NdPtSb to the ZrNiAl type. The investigations showed that ErAgSn forms a ZrNiAl type high-pressure modification (the structure of the higher homologue TmAgSn) and a quenched TmAgSn sample shows the NdPtSb type. The results are displayed again in a plot of the cell volumes per formula unit (Figure 4.4-36).

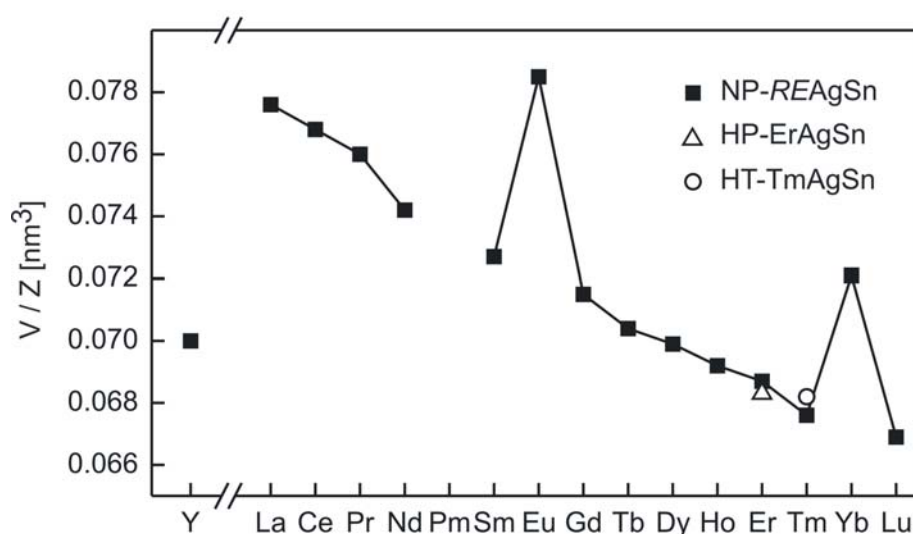


Figure 4.4-36: Plot of the cell volumes per formula unit of the normal-pressure, high-pressure, and high-temperature modifications of the $REAgSn$ stannides.

Summing up, the unique series of $RETSn$ stannides are the first two series of equiatomic intermetallic compounds, where high- and low-temperature modifications were observed besides high- and normal-pressure modifications. Under normal pressure conditions, the size of the rare-earth element determines the switch in structure type. Here one can consider the decreasing size of the rare-earth element as an internal pressure parameter. The $RETSn$ stannides with the larger rare-earth elements can transform only upon applying external pressure. In contrast, the $ZrNiAl$ type $REPtSn$ stannides with the highest cell volumes can transform to the $TiNiSi$ type by application of high-temperature. Furthermore, $NdPtSb$ type $ErAgSn$ transforms to the $ZrNiAl$ type at high-pressures and $ZrNiAl$ type $TmAgSn$ transforms to the $NdPtSb$ type at high-temperature conditions. Keeping these results in mind, the system was changed again and the main group element germanium was introduced instead of tin. In the following Chapters these results are presented.

4.4.8 The System RE-Ag-Ge

4.4.8.1 Introduction

Binary interactions of rare-earth elements with Ge and Ag are well known leading to a series of binary compounds, whereas information on the corresponding ternary alloys or intermetallic phases are still rare. When the heavy fermion superconductor CeCu_2Si_2 was discovered, the interest in the physical properties of the isotypic homologue CeAg_2Ge_2 grew. In the context of these investigations systematic phase analyses of the system Ce-Ag-Ge were performed from *Ferro et al.* and published in two review articles [328, 337]. Therein strong similarities between the RE-Cu-Ge and the RE-Ag-Ge systems are shown. Similar stoichiometries and crystal structures are often formed in these two series. In the following a short summary about existing compounds is given. With respect to isotypic copper compounds the transition metal component (T) is written in a general form and not only restricted to silver.

REAgGe: The structures found for these phases correspond to the types AlB_2 , CaIn_2 (or NdPtSb), and Fe_2P (or ZrNiAl). The structures in brackets are ternary ordered variants of the analogous compounds. In a number of cases, deviations from the ideal stoichiometry as well as solid solution formation have been reported. The 1:1:1 compounds with silver were described with several rare-earth cations. For the light lanthanoids (La, Ce, and Pr) the phases adopt an ordered variant of the hexagonal CaIn_2 type, the NdPtSb type, while for the other rare-earth's the hexagonal ZrNiAl type was observed [329-331, 336]. This structural change, depending on the size of the rare-earth cations, was the reason for the following high-pressure investigations.

For neodymium, a certain off-stoichiometry was observed ($\sim\text{NdAg}_{1.1}\text{Ge}_{0.9}$) [332]. Finally, AlB_2 type phases were described for La, Ce, Pr, and Nd, for compositions close to $\text{REAg}_{0.7-0.8}\text{Ge}_{1.3-1.2}$ [329, 332]. Divalent rare-earth cations like Eu were identified in the systems $\text{EuAg}_{1.1}\text{Ge}_{0.9}$ (orthorhombic CeCu_2 type) [333, 334] and in $\sim\text{EuAg}_{0.8}\text{Ge}_{1.1}$ (hexagonal AlB_2 type) [334].

The interesting different physical properties of the *REAgGe* phases were studied by various authors. *Pecharsky et al.* measured magnetic susceptibility and heat capacity for LaAgGe and CeAgGe and described an antiferromagnetic ordering transition for CeAgGe below 4.8 K [336]. Later, *Ferro et al.* revealed rather a soft ferromagnetic nature below 6.8 K. These ferromagnetic interactions enhance by a substi-

tution of Ge by Si ($\text{CeAgGe}_{1-x}\text{Si}_x$; $x_{\text{Si}} = 0.1, 0.33, 0.5, 0.67, 0.75$) [337]. Besides the most intensive investigated 1:1:1 phases, which were used as precursor materials for the experiments in this thesis, the following additional compounds exist.

RE₃T₄Ge₄: Compounds in this stoichiometry generally adopt the $\text{Gd}_3\text{Cu}_4\text{Ge}_4$ type structure, which occurs also in different ternary systems [346]. Isostructural compounds are formed with Sn instead of Ge and in some cases with $T = \text{Mn, Fe, Ni, Pd, etc.}$ With Ag and Ge, this structure exists with the larger lanthanoides, specifically from La to Gd with the exception of Eu and Y [337]. In the course of the high-pressure investigation of the Ce-Ag-Ge system in this thesis, the corresponding compound $\text{Ce}_3\text{Ag}_4\text{Ge}_4$ was observed as a byproduct. Further structural details concerning this structure type can be found later on in Chapter 4.4.8.8.

RE₂TGe₂: Besides Cu as transition metal the compound exists also with Ag for the rare-earth atoms $RE = \text{La, Ce, Pr, Nd, Sm, Gd, and Eu}$ [328 and ref. therein]. All these compounds were described as “line” compounds without any variations in stoichiometry, with the exception of Eu for which a composition range $\text{EuAg}_{2-2.25}\text{Ge}_{2-1.75}$ has been proposed [335]. High-pressure experiments started with the 1:1:1 CeAgGe precursor resulting in the formation of CeAg_2Ge_2 as a X-ray detectable byproduct in varying concentrations. Similar observations were already made in the Ce-Ni-Sn system (see Chapter 4.4.5), in which higher synthetic pressures obviously favour the formation of the 1:2:2 stoichiometry. In the literature, two more phases are known, which are described briefly in the following.

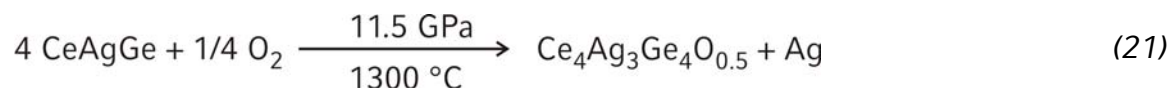
RE₂TGe₆ and RE_TGe₂: With $T = \text{Ag}$, the compounds RE_2TGe_6 are formed with the lanthanoides from La to Gd except Eu [368]. Next to the structural characterisation, magnetic properties were determined for these compounds, too. Phases of the stoichiometry RE_TGe_2 with crystal structures related to the orthorhombic CeNiSi₂ type are formed with copper and several other transition elements T . A corresponding silver representative is not known up to now.

In the preceding experiments concerning the stannides, a structural transformation from two different structure types (TiNiSi, NdPtSb) into the denser ZrNiAl type under high-pressure / high-temperature conditions was observed. This transformation is determined by the size of the rare-earth cations. The following experiments with CeAgGe revealed a surprising partial oxidation of the precursor material

and resulted in an intermetallic matrix with embedded [OCe₂Ce_{2/2}] tetrahedra chains.

4.4.8.2 Synthesis of Ce₄Ag₃Ge₄O_{0.5}

The germanide oxide Ce₄Ag₃Ge₄O_{0.5} was synthesized under high-pressure / high-temperature conditions starting from NdPtSb type CeAgGe [336-338] as a precursor compound. Since elemental silver was detected in the X-ray powder diagram of the reaction product, the following reaction scheme (equation (21)) under conditions of 11.5 GPa and 1300 °C can be formulated:



Starting materials for the synthesis of the CeAgGe precursor were ingots of the rare-earth metal, silver wire, and a germanium bar. Details about the precursor preparation can be found in Chapter 2.1 of this thesis.

The carefully milled intermetallic precursor was compressed to a pressure of 11.5 GPa in 3.5 hours and heated to 1250–1300 °C in the following 10 min. After holding this temperature for 10 min, the sample was cooled down to 900 °C in 1 min. To enhance the crystallinity of the sample, an annealing period of five hours followed, accompanied by a slow decrease of the temperature from 900 °C to 700 °C. Afterwards, the sample was cooled down to room temperature within 1 min. After decompression (10.5 hours), the recovered experimental octahedron was broken apart, and the sample carefully separated from the surrounding boron nitride.

The polycrystalline sample of Ce₄Ag₃Ge₄O_{0.5} is silvery with metallic lustre and stable in moist air over weeks. Powdered samples are dark gray. EDX analysis of the elements Ce, Ag, and Ge at single crystals revealed: Ce: 44.3% (47.40%) (theoretical values in brackets); Ag: 27.1% (27.37%); Ge: 25.6% (24.56%). To detect the small oxygen content and possible nitrogen contamination, the O/N-content was analyzed by an IR/thermal conductivity detection performed by the company Pascher (Remagen, Germany). The amount of oxygen showed a value of 0.65%, which fits well to the expected theoretical value of 0.68%. Only traces of nitrogen were detected.

Additionally, comparable experiments at similar conditions (see Table 4.4-19) were carried out with LaAgGe. From the powder diffraction pattern an oxidation to

$\text{La}_4\text{Ag}_3\text{Ge}_4\text{O}_{0.5}$ was evident. Unfortunately, it was not possible to isolate a suitable single crystal for a single crystal structure determination. An indexing of the powder pattern for the clarification lattice parameters was not possible as well.

Table 4.4-19: Experimental details for the synthesis of $\text{La}_4\text{Ag}_3\text{Ge}_4\text{O}_{0.5}$

Precursor	Assem- bly	Max. pressure	Temperature program	Product
LaAgGe	14/8	12.2 GPa	↗ 1200 °C/15 min, → 1200 °C/10 min, ↓ 800 °C/1 min, ↘ 800 to 650 °C/240 min, ↓ RT	$\text{La}_4\text{Ag}_3\text{Ge}_4\text{O}_{0.5}$

↗ : increase of temperature in x min, → : constant temperature for x min, ↘ : decrease of temperature in x min, ↓ : quenching of the sample

In the following, the way of the crystal structure analysis for $\text{Ce}_4\text{Ag}_3\text{Ge}_4\text{O}_{0.5}$ is described.

4.4.8.3 Crystal Structure Analysis of $\text{Ce}_4\text{Ag}_3\text{Ge}_4\text{O}_{0.5}$

The sample was characterized by a powder pattern from on a Huber Guinier powder diffractometer with $\text{CuK}\alpha_1$ radiation ($\lambda = 154.06$ pm, Ge monochromator). To ensure correct indexing, the observed pattern was compared with calculated ones [57], taking the atomic positions obtained from the single crystal structure refinement. The lattice parameters were then refined through least-squares fits. The single crystal and powder lattice parameters were in good agreement. Figure 4.4-37 shows the powder patterns of the HP-phase in comparison with the simulation derived from the single crystal data. According to the presented reaction scheme (equation 21), the silver reflections are marked with red lines in the powder pattern. It is also evident that next to the oxidized phase $\text{Ce}_4\text{Ag}_3\text{Ge}_4\text{O}_{0.5}$ another phase, a non oxidized one, occurs. In cooperation with N. Behrmann (during her bachelor works) it was possible to characterize this byproduct on the basis of single crystal data. The data of the byproduct $\text{Ce}_3\text{Ag}_4\text{Ge}_4$ are given later on in Chapter 4.4.8.8. Also a discussion concerning the different attempts to avoid the formation of the byproduct is given in Chapter 4.4.8.11.

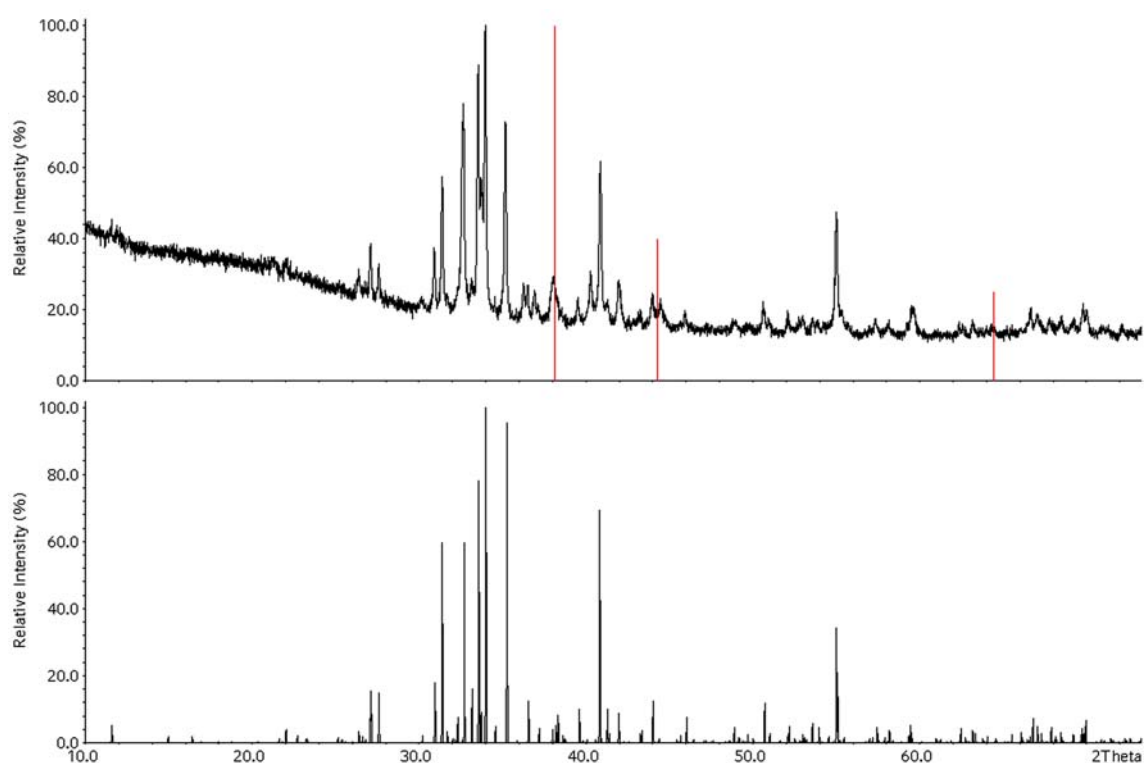


Figure 4.4-37: Recorded powder pattern of $\text{Ce}_4\text{Ag}_3\text{Ge}_4\text{O}_{0.5}$ (top) in comparison to the simulation (down) derived from single crystal data. The silver reflections are marked with red lines.

Small, irregularly shaped single crystals of $\text{Ce}_4\text{Ag}_3\text{Ge}_4\text{O}_{0.5}$ were selected from the high-pressure treated sample by mechanical fragmentation. The crystals were first investigated by Laue photographs in a Buerger camera (white molybdenum radiation; imaging plate technique, Fujifilm, BAS-1800) in order to check the quality for intensity data collection. Intensity data of a suitable crystal of $\text{Ce}_4\text{Ag}_3\text{Ge}_4\text{O}_{0.5}$ were collected at room temperature by use of a Kappa CCD diffractometer (Bruker AXS / Nonius, Karlsruhe) equipped with a rotating anode. An absorption correction based on multi-scans [339] was applied to the data set. All relevant crystallographic data and details of the data collections are listed in Table 4.4-20.

Analysis of the data set was consistent with the space group $Pnma$. The starting atomic positions were deduced from automatic interpretations of *Direct methods* with SHELXS-97 [79] and the structure was refined using SHELXL-97 (full-matrix least-squares on F^2) [80] with anisotropic atomic displacement parameters for all sites. The occupancy parameters were refined in a separate series of least-squares cycles in order to check for the correct composition. Thus, all sites except the oxygen site O1 were fully occupied within one standard deviation. The structure refinement clearly revealed occupancy of 52(2)% for the oxygen position. As careful analyses of the data set did not reveal any superstructure reflections and any diffuse scattering, the oxygen atoms statistically occupy the tetrahedral sites. The structural

refinement without a half occupied oxygen position at the tetrahedral site resulted in remarkably higher residuals (e.g. $R1 = 0.0270$ with oxygen and $R1 = 0.0340$ without oxygen ($I > 2\sigma(I)$). In the last cycles, the ideal occupancies were assumed again. Final difference Fourier synthesis revealed no significant residual peaks (see Table 4.4-20). The positional parameters, anisotropic displacement parameters, and interatomic distances are listed in Table 4.4-21 and Table 4.4-22.

Table 4.4-20: Crystal data and structure refinement for Ce₄Ag₃Ge₄O_{0.5}.

Empirical formula	Ce ₄ Ag ₃ Ge ₄ O _{0.5}
Molar mass (g·mol ⁻¹)	1182.5
Crystal system	orthorhombic
Space group	<i>Pnma</i> (No. 62)
Single crystal diffractometer	Kappa CCD
Radiation	MoK _α (λ = 71.073 pm)
Single crystal data	
<i>a</i> (pm)	2088.50(5)
<i>b</i> (pm)	440.35(1)
<i>c</i> (pm)	1114.29(2)
Volume (nm ³)	1.0248(4)
Powder data	
<i>a</i> (pm)	2087.3(4)
<i>b</i> (pm)	439.9(1)
<i>c</i> (pm)	1113.8(2)
Volume (nm ³)	1.0228(3)
Formula units per cell	<i>Z</i> = 4
Temperature (K)	293(2)
Calculated density (g·cm ⁻³)	7.68
Crystal size (mm ³)	0.02 × 0.02 × 0.02
Detector distance (mm)	30
Scan time / degree (min)	140
Scan step (°)	1.10
Absorption coefficient (mm ⁻¹)	34.5
F(000)	2020
θ Range (°)	3.13 to 32.03
Range in <i>hkl</i>	-30/+31, ±6, ±16
Total no. reflections	3459
Independent reflections	1986 (<i>R</i> _{int} = 0.0303)
Reflections with <i>I</i> > 2σ(<i>I</i>)	1503 (<i>R</i> _σ = 0.0455)
Data / parameters	1986 / 75
Absorption correction	multi-scan [339]
Goodness-of-fit (<i>F</i> ²)	1.045
Final <i>R</i> indices (<i>I</i> > 2σ(<i>I</i>))	<i>R</i> 1 = 0.0270 <i>wR</i> 2 = 0.0430
<i>R</i> Indices (all data)	<i>R</i> 1 = 0.0470 <i>wR</i> 2 = 0.0467
Extinction coefficient	0.00012(2)
Larg. diff. peak and hole (e·Å ⁻³)	2.36 / -2.11

Table 4.4-21: Atomic coordinates and anisotropic displacement parameters (pm²) for Ce₄Ag₃Ge₄O_{0.5}, U_{eq} is defined as one third of the trace of the orthogonalized U_{ij} tensor. The anisotropic displacement factor exponent takes the form: $-2\pi^2[(ha^*)^2U_{11}+\dots+2kha^*b^*U_{12}]$. U_{12} , $U_{23} = 0$.

Atom	Wyckoff position	x	y	z	U_{11}	U_{22}	U_{33}	U_{13}	U_{eq}
Ce1	4c	0.21375(2)	¼	0.45848(3)	95(2)	84(2)	113(2)	-1(1)	97(1)
Ce2	4c	0.03195(2)	¼	0.37003(3)	103(2)	96(2)	106(2)	-2(2)	102(1)
Ce3	4c	0.39643(2)	¼	0.36594(3)	92(2)	80(2)	129(2)	10(2)	101(1)
Ce4	4c	0.84974(2)	¼	0.79251(3)	94(2)	141(2)	110(2)	-5(2)	115(1)
Ge1	4c	0.71052(3)	¼	0.70192(6)	111(4)	85(4)	121(3)	-17(3)	106(2)
Ge2	4c	0.67748(3)	¼	0.48522(6)	110(4)	94(4)	112(3)	-5(3)	105(2)
Ge3	4c	0.49712(4)	¼	0.67924(6)	111(4)	83(4)	123(4)	2(3)	106(2)
Ge4	4c	0.39204(4)	¼	0.01736(7)	112(4)	96(4)	223(4)	-11(3)	144(2)
Ag1	4c	0.59572(3)	¼	0.84665(5)	179(3)	132(3)	143(3)	-6(2)	152(2)
Ag2	4c	0.28068(3)	¼	0.17013(5)	210(3)	116(3)	131(3)	-27(2)	152(2)
Ag3	4c	0.54582(3)	¼	0.44184(5)	141(3)	126(3)	160(3)	-28(2)	142(2)
O1*	4c	0.1390(5)	¼	0.2983(9)	230(6)	230(6)	280(6)	-60(5)	240(4)

*: half occupied O1 site

4.4.8.4 Crystal Structure Description

The already mentioned tetrahedra are formed of the Ce1, Ce2, and Ce4 atoms at Ce–O distances ranging from 237 to 243 pm in excellent agreement with the Ce–O distance of 239 pm in the tetrahedra of cubic CeO₂ [340]. The structural motif of chains of corner-sharing Ce₄O tetrahedra is also known from the structures of Ca₃AlAs₃ [341, 342] and Sm₃NS₃ [343, 344], which exhibit one dimensional [AlAs₃]⁶⁻ or [NSm₃]⁶⁺ tetrahedra chains, respectively. Figure 4.4-38 gives a view of the tetrahedra chain including the exact Ce–O bond length. These [OCe₂Ce_{2/2}] chains with statistically distributed oxygen atoms at the tetrahedral site are embedded in an intermetallic [CeAg₃Ge₄] matrix.

The three-dimensional [CeAg₃Ge₄] network has structural building units, which are well known from various rare-earth-transition metal-silicides and germanides. All three crystallographically independent silver atoms have got four germanium neighbours at Ag–Ge distances ranging from 263 to 289 pm, slightly longer than the sum of the coval-

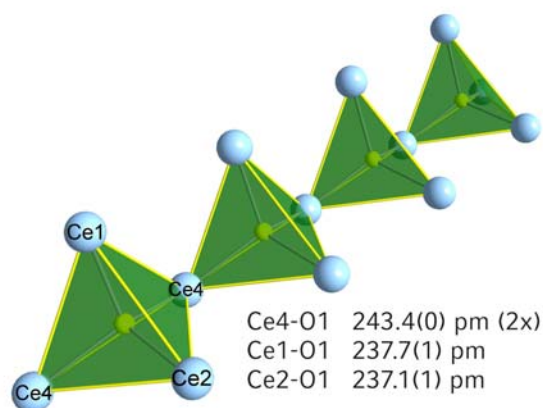


Figure 4.4-38: [OCe₂Ce_{2/2}] tetrahedra chain embedded in a [CeAg₃Ge₄] intermetallic matrix (not shown).

lent radii of 256 pm [273]. Within this network, we observed various weak Ag–Ag contacts (319–340 pm Ag–Ag), slightly longer than the Ag–Ag distance in *fcc* silver (289 pm) [321]. The structure contains four crystallographically independent germanium sites. While the Ge3 and Ge4 atoms are isolated, the Ge1 and Ge2 atoms build Ge₂ dumb-bells with a Ge1–Ge2 distance of 251 pm, a little longer than in elemental germanium (245 pm) [321]. The substructure, built up by the silver and germanium atoms, leaves slightly distorted pentagonal prismatic voids, which are filled with Ce3 atoms (Figure 4.4-39).

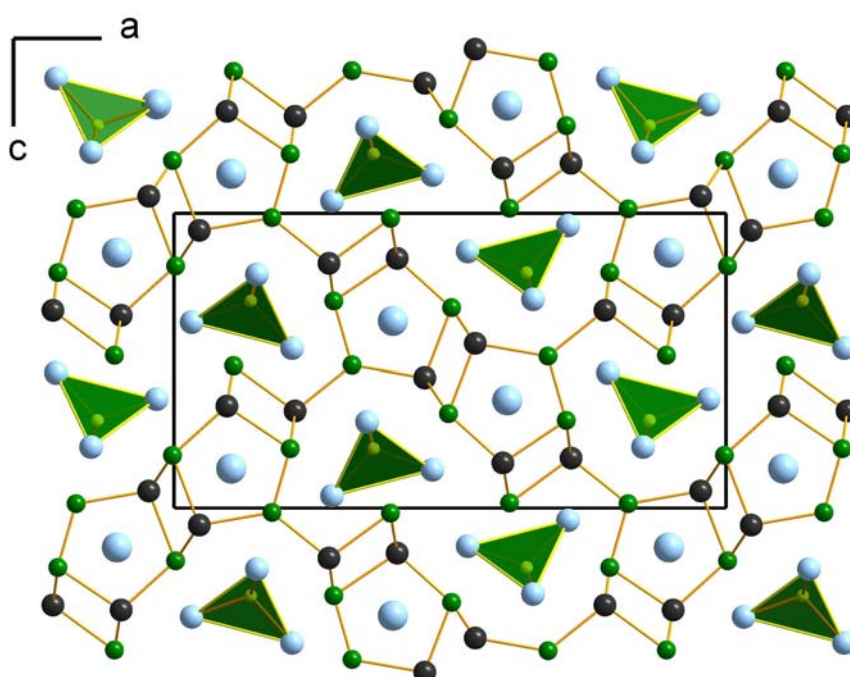


Figure 4.4-39: Projection of the $\text{Ce}_4\text{Ag}_3\text{Ge}_4\text{O}_{0.5}$ structure onto the *ac* plane. Cerium, silver, and germanium atoms are drawn as light blue, black, and green spheres, respectively. The three-dimensional $[\text{CeAg}_3\text{Ge}_4]$ network and the chains of corner-sharing, oxygen centered $[\text{OCe}_2\text{Ce}_{2/2}]$ tetrahedra are emphasized.

These prisms are condensed *via* Ag_2Ge_2 rhombs, a structural motive frequently observed in related intermetallic structures. It is worthwhile to note that similar structural features, with almost similar interatomic distances, were recently observed in the $\text{Gd}_3\text{Cu}_4\text{Ge}_4$ type structure of $\text{Ce}_3\text{Ag}_4\text{Ge}_4$ (Figure 4.4-44) [345]. Interestingly, this $\text{Ce}_3\text{Ag}_4\text{Ge}_4$ phase was always observed as a byproduct (around 40%) during the synthesis of $\text{Ce}_4\text{Ag}_3\text{Ge}_4\text{O}_{0.5}$. In contrast to the results of *Szytuła et al.*, who presented neutron diffraction data on polycrystalline samples, the crystallinity of $\text{Ce}_3\text{Ag}_4\text{Ge}_4$ prepared under HP / HT conditions allowed us to perform a single crystal structure determination giving precise structural data (see Chapter 4.4.8.8).

Table 4.4-22: Interatomic distances (pm), calculated with the powder lattice parameters in $\text{Ce}_4\text{Ag}_3\text{Ge}_4\text{O}_{0.5}$. All distances of the first coordination sphere are listed.

Ce1–Ge4	318.5(1) 2x	Ce2–Ge3	311.8(1) 2x	Ce3–Ge2	315.7(1) 2x	Ce4–Ge1	307.6(1)
Ce1–Ge2	322.3(1) 2x	Ce2–Ge4a	317.0(1) 2x	Ce3–Ge3	316.7(1) 2x	Ce4–Ge3	309.2(2)
Ce1–Ag2a	322.6(1) 2x	Ce2–Ge4b	317.8(1)	Ce3–Ge1	322.4(1) 2x	Ce4–Ge2	312.6(1) 2x
Ce1–Ge1	324.5(1) 2x	Ce2–Ag1a	342.5(1)	Ce3–Ag3a	323.1(1)	Ce4–Ag3	351.5(1) 2x
Ce1–Ag1	328.4(1)	Ce2–Ag1b	346.5(1) 2x	Ce3–Ag1	323.6(1) 2x	Ce4–Ag2	352.5(1) 2x
Ce1–Ag2b	350.2(1)	Ce2–Ag3	348.6(1)	Ce3–Ag2	325.5(1)	Ce4–Ce2	377.0(1) 2x
Ce1–Ce4	379.6(1)	Ce2–Ce4	377.0(1) 2x	Ce3–Ag3b	329.8(1) 2x		
						Ce1–O1	237.0(10)
						Ce2–O1	237.3(10)
						Ce4–O1	243.2(4) 2x
Ge1–Ge2	251.0(1)	Ge2–Ag2	276.3(1)	Ge3–Ag3a	273.1(1) 2x	Ge4–Ag1	268.3(1) 2x
Ge1–Ag2	262.7(1) 2x	Ge2–Ag3	279.0(2)	Ge3–Ag1	277.7(1)	Ge4–Ag2	288.1(1)
Ge1–Ag1	288.8(1)	Ge2–Ce4	312.6(1) 2x	Ge3–Ag3b	283.3(1)	Ge4–Ce2a	317.0(1) 2x
Ge1–Ce3	322.4(1) 2x	Ge2–Ce3	315.7(1) 2x	Ge3–Ce4	309.2(2)	Ge4–Ce2b	317.8(1)
Ge1–Ce1	224.5(1)	Ge2–Ce1	322.3(1) 2x	Ge3–Ce2	311.8(1) 2x	Ge4–Ce1	318.5(1) 2x
				Ge3–Ce3	316.7(1) 2x		

4.4.8.5 Thermal Behaviour

These investigations were performed on a STOE Stadi P powder diffractometer ($\text{MoK}\alpha$; $\lambda = 71.073$ pm) with a computer controlled STOE furnace. The sample was enclosed in an argon filled quartz capillary and heated from room temperature to 500 °C in 100 °C steps and from 500 °C to 1100 °C in 50 °C steps. Afterwards the sample was cooled down to 500 °C in 50 °C steps, and below 500 °C in 100 °C steps. At each temperature a diffraction pattern was recorded over the angular range $12.5^\circ \leq 2\theta \leq 21^\circ$. Figure 4.4-40 shows the temperature-programmed X-ray powder diffractograms. $\text{Ce}_4\text{Ag}_3\text{Ge}_4\text{O}_{0.5}$ remained stable up to a temperature of 650 °C. Exceeding this temperature, $\text{Ce}_4\text{Ag}_3\text{Ge}_4\text{O}_{0.5}$ decomposed into $\text{Ce}_3\text{Ag}_4\text{Ge}_4$. The decomposition was completed at 800 °C remaining stable after cooling down to room temperature.

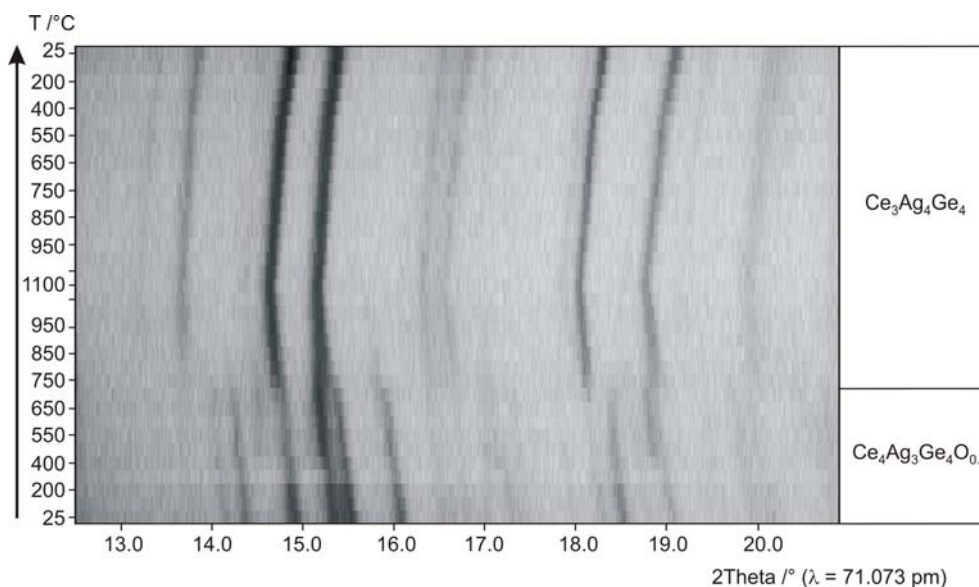


Figure 4.4-40: Temperature-programmed X-ray powder patterns, following the decomposition reaction of the metastable high-pressure phase $\text{Ce}_4\text{Ag}_3\text{Ge}_4\text{O}_{0.5}$.

4.4.8.6 Magnetic Properties

We were very interested in the magnetic properties of this new oxygen containing intermetallic compound. Unfortunately, as already mentioned, the compound was not obtained as a single phase product. Nevertheless, we performed first magnetic measurements on small amounts of the bulk material. The magnetic susceptibility ($\chi = M/H$, $T = 5\text{--}300$ K) and heat capacity (C_p , $3\text{--}100$ K) were measured on a Quantum Design-PPMS using the VSM and HC options, respectively. $\chi(T)$ was measured in a field of 10 kOe, and the Curie-Weiss law was fitted in the linear region (100–300 K) of the χ^{-1} vs. T plot. Figure 4.4-41 shows the inverse magnetic susceptibility of the sample. We observed Curie-Weiss behaviour above 100 K with an experimental magnetic moment of $2.42 \mu_B/\text{Ce}$ atom, close to the value of $2.54 \mu_B$ for the free Ce^{3+} ion, clearly indicating trivalent cerium in the bulk [274]. The negative Weiss constant of -8.6 K is indicative for antiferromagnetic ordering, as was evident from low-temperature specific heat data (3.2 K magnetic ordering temperature) (see Figure 4.4-42). The measurements gave no sign of a possible multi phase sample. Especially due to the fact, that the byproduct $\text{Ce}_3\text{Ag}_4\text{Ge}_4$ is described in the literature as revealing a ferromagnetic-like behaviour below 10 K [345]. The investigation of *Szytuła et al.* showed Curie-Weiss characteristics above 50 K. The so derived paramagnetic Curie temperatures and effective magnetic moments of $\text{Ce}_3\text{Ag}_4\text{Ge}_4$ were equal to -15.3 K and $2.50 \mu_B$. In addition to that, the low-temperature magnetization showed a ferromagnetic-like behaviour with a character-

istic rise below 10 K and a pronounced difference between the zero-field-cooled (ZFC) and field-cooled (FC) curves observed below about 7 K. However, the absolute value of the remanent magnetization (0.25 emu/g) at 1.72 K in a field of 0.05 T was rather small as for a ferromagnet. Collected neutron diffraction data did not evidence magnetic ordering in $\text{Ce}_3\text{Ag}_4\text{Ge}_4$ so the ground state of this compound remains a puzzle and one might consider the anomalies as resulting from some impurity contributions. Further investigations concerning the purity and the magnetic properties of the compounds are in progress.

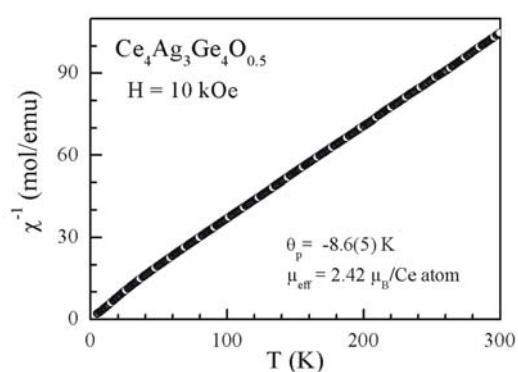


Figure 4.4-41: Plot of χ^{-1} vs. T measured in a field of 10 kOe for $\text{Ce}_4\text{Ag}_3\text{Ge}_4\text{O}_{0.5}$.

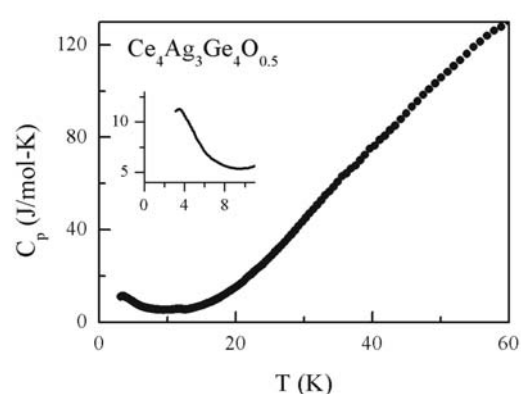


Figure 4.4-42: The C_p as a function of T . The inset shows the low temperature (< 10 K) features on an expanded scale. The onset of magnetic ordering below 3.2 K is clearly visualized in the inset.

4.4.8.7 Electronic Structure Calculation

To substantiate the claims regarding the properties and bonding, Prof. Dr. D. Johrendt performed DFT band structure calculations, using the LMTO-ASA program [286, 287] and the COHP [291] method for bond analysis.

The calculations resulted in metallic properties and in a magnetic ground state, compatible with one unpaired $4f$ electron per cerium in good agreement with the current magnetic data. The COHP analysis (Figure 4.4-43) revealed all bonds saturated, *i.e.* the Fermi level lies in an essentially nonbonding regime just between bonding and antibonding states, therefore $\text{Ce}_4\text{Ag}_3\text{Ge}_4\text{O}_{0.5}$ is close to a valence compound. The integrated COHP allowed to compare the bond strength, giving the sequence $\text{Ge-Ge} > \text{Ce-O} > \text{Ag-Ge}$. Thus, even though the major part of the bonding energy certainly originates from the Ag-Ge and the Ge-Ge bonds, also the strong Ce-O bonds within the $[\text{OCe}_2\text{Ce}_{2/2}]$ tetrahedra are very important for the stability of the structure.

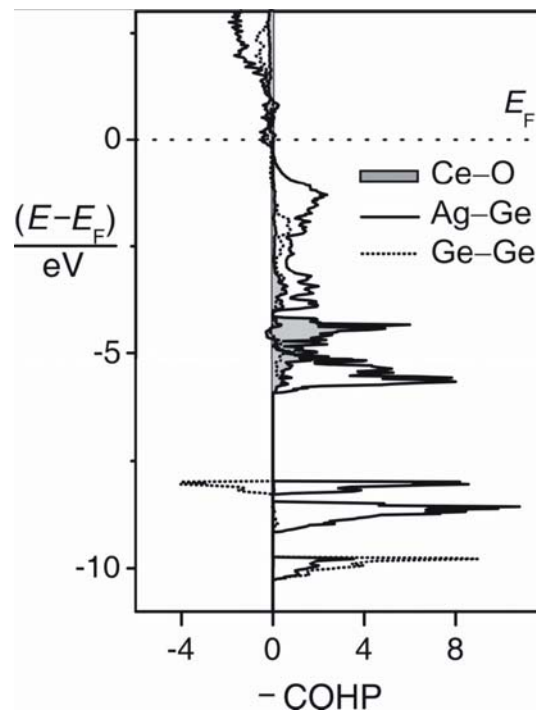


Figure 4.4-43: Crystal Orbital Hamilton Population (COHP) diagram of $\text{Ce}_4\text{Ag}_3\text{Ge}_4\text{O}_{0.5}$.

4.4.8.8 Synthesis of $\text{Ce}_3\text{Ag}_4\text{Ge}_4$

As already described in the experimental part of $\text{Ce}_4\text{Ag}_3\text{Ge}_4\text{O}_{0.5}$ (see Chapter 4.4.8.2) the appearance of a second unknown phase in the powder pattern was observed. Several experiments to minimize or to avoid the byproduct $\text{Ce}_3\text{Ag}_4\text{Ge}_4$ have been carried out during the bachelor work of N. Behrmann. One experiment, which had the intention to raise the oxygen content by use of a ball milled CeAgGe precursor with a large oxygen contaminated surface, surprisingly resulted in a X-ray pure sample of the non-oxidized compound $\text{Ce}_3\text{Ag}_4\text{Ge}_4$. The surplus cerium was not detectable in the powder pattern.

The precursor material CeAgGe was three times for three minutes ball milled in an argon filled glove box and afterwards exposed to the atmosphere over night. This material was used for the high-pressure / high-temperature experiments. Details concerning the experiment are listed in the following table.

Table 4.4-23: Experimental details of the $\text{Ce}_3\text{Ag}_4\text{Ge}_4$ synthesis.

Precursor	Assembly	Max. pressure	Temperature program	Product
CeAgGe	14/8	11.5 GPa	↗ 1300 °C/10 min, → 1300 °C/10 min, ↓ 900 °C/1 min, ↘ 900 to 650 °C/300 min, ↓ RT	$\text{Ce}_3\text{Ag}_4\text{Ge}_4$

↗ : increase of temperature in x min, → : constant temperature for x min, ↘ : decrease of temperature in x min, ↓ : quenching of the sample

4.4.8.9 Crystal Structure Analysis

Small, irregularly shaped single crystals of the compound $\text{Ce}_3\text{Ag}_4\text{Ge}_4$ were first examined through a Buerger precession camera. The single crystal intensity data were collected at room temperature by use of a Kappa-CCD (Bruker AXS / Nonius, Karlsruhe) diffractometer equipped with a rotating anode (graphite monochromatized MoK_α ($\lambda = 71.073$ pm) radiation). An absorption correction based on multi-scans [339] was applied to the data set. All relevant crystallographic data and details of the data collections are listed in Table 4.4-24. The analysis of the data set was consistent with space group *Immm*. The starting atomic positions were deduced from automatic interpretations of *Direct methods* with SHELXS-97 [79] and all atoms were refined using SHELXL-97 (full-matrix least-squares on F^2) [80] with anisotropic atomic displacement parameters for all sites. The final difference Fourier syntheses revealed no significant residual peaks. The positional parameters of the refinement and anisotropic displacement parameters are listed in Table 4.4-25. Interatomic distances are summarized in Table 4.4-26.

Table 4.4-24: Crystal data and structure refinement for Ce₃Ag₄Ge₄

Empirical formula	Ce ₃ Ag ₄ Ge ₄
Molar mass (g·mol ⁻¹)	1142.2
Crystal system	orthorhombic
Space group	<i>Immm</i> (No. 71)
Single crystal diffractometer	Kappa CCD
Radiation	MoK _α ($\lambda = 71.073$ pm)
Single crystal data	
<i>a</i> (pm)	1482.19(9)
<i>b</i> (pm)	714.08(4)
<i>c</i> (pm)	447.02(3)
Volume (nm ³)	0.473(5)
Powder data	
<i>a</i> (pm)	1480.62(7)
<i>b</i> (pm)	713.36(6)
<i>c</i> (pm)	446.74(9)
Volume (nm ³)	0.472(1)
Formula units per cell	<i>Z</i> = 2
Temperature (K)	293(2)
Calculated density (g·cm ⁻³)	8.04
Crystal size (mm ³)	0.02 × 0.03 × 0.03
Detector distance (mm)	30
Scan time / degree (min)	25
Scan step (°)	2.0
Absorption coefficient (mm ⁻¹)	34.7
F(000)	980
θ Range (°)	3.17 to 27.45
Range in <i>hkl</i>	-19/+18, ± 8 , ± 5
Total no. reflections	527
Independent reflections	330 (<i>R</i> _{int} = 0.0192)
Reflections with <i>I</i> > 2 σ (<i>I</i>)	306 (<i>R</i> _{σ} = 0.0254)
Data / parameters	330 / 23
Absorption correction	multi-scan [339]
Goodness-of-fit (<i>F</i> ²)	1.149
Final <i>R</i> indices (<i>I</i> > 2 σ (<i>I</i>))	<i>R</i> 1 = 0.0202 <i>wR</i> 2 = 0.0417
<i>R</i> Indices (all data)	<i>R</i> 1 = 0.0236 <i>wR</i> 2 = 0.0443
Extinction coefficient	0.0005(1)
Larg. diff. peak and hole (e·Å ⁻³)	1.4 / -1.1

Table 4.4-25: Atomic coordinates and anisotropic displacement parameters (pm^2) for $\text{Ce}_3\text{Ag}_4\text{Ge}_4$. U_{eq} is defined as one third of the trace of the orthogonalized U_{ij} tensor. The anisotropic displacement factor exponent takes the form: $-2\pi^2[(ha^*)^2U_{11}+\dots+2kha^*b^*U_{12}]$. U_{13} , $U_{23} = 0$. The values in brackets are from X-ray diffraction data from ref. [345].

Atom	Wyckoff position	x	y	z	U_{11}	U_{22}	U_{33}	U_{12}	U_{eq}
Ce1	2d	$\frac{1}{2}$	0	$\frac{1}{2}$	90(4)	85(5)	99(4)	0	91(2)
Ce2	4e	0.12981(4) [0.1328(7)]	0	0	74(3)	128(4)	80(3)	0	94(2)
Ag1	8n	0.33253(4) [0.3339(5)]	0.19323(8) [0.194(1)]	0	154(3)	126(4)	164(3)	-42(2)	148(2)
Ge1	4f	0.21632(7) [0.222(1)]	$\frac{1}{2}$	0	92(5)	197(7)	82(5)	0	124(3)
Ge2	4h	0	0.18010(5) [0.183(3)]	$\frac{1}{2}$	89(5)	98(6)	119(6)	0	102(3)

4.4.8.10 Crystal Structure Description

The analysis of the diffraction data confirmed that the sample crystallized in the structure of the $\text{Gd}_3\text{Cu}_4\text{Ge}_4$ type (S.G. *Immm*) first examined by *Rieger et al.* [346]. In 2006 *Szytuła et al.* published a paper analysing the magnetic, electronic, and transport properties of $\text{Ce}_3\text{Ag}_4\text{X}_4$ ($\text{X} = \text{Ge}, \text{Sn}$) obtained by arc melting under normal-pressure conditions. Crystallographic information was derived from polycrystalline samples *via* neutron diffraction experiments. Herein the first single crystal diffraction data of $\text{Ce}_3\text{Ag}_4\text{Ge}_4$ are presented.

The crystal structure of $\text{Ce}_3\text{Ag}_4\text{Ge}_4$ is built up from a three-dimensional $[\text{Ag}_4\text{Ge}_4]$ network, which contains structural building units well known in intermetallic compounds. A comparison with the oxygen containing phase $\text{Ce}_4\text{Ag}_3\text{Ge}_4\text{O}_{0.5}$ shows certain similarities (Figure 4.4-39). The only silver atom has got four germanium neighbours at Ag–Ge distances, ranging from 263–279 pm, slightly longer than the sum of the covalent radii of 256 pm [273]. Within this network we observe strong Ag–Ag contacts (276 pm Ag–Ag) shorter than the Ag–Ag distance in *fcc* silver (289 pm) [321]. The structure contains two crystallographically independent germanium sites, in which Ge1 is isolated and two Ge2 atoms build Ge_2 dumb-bells with a Ge2–Ge2 distance of 257 pm, a little longer than in elemental germanium (245 pm) [321] and in $\text{Ce}_4\text{Ag}_3\text{Ge}_4\text{O}_{0.5}$ (251 pm), respectively. The substructure, built up by the silver and the germanium atoms consists of pentagonal prisms. Two of them are condensed *via* two Ge_2 dumb-bells forming a pentagonal double prism. The double prisms are further on condensed *via* four Ag_2Ge_2 rhombs, a structural motive frequently observed in related intermetallic structures and also found in $\text{Ce}_4\text{Ag}_3\text{Ge}_4\text{O}_{0.5}$.

Inside the pentagonal prisms and the larger channels, formed through the connection of the prisms, the rare-earth cations are located. Figure 4.4-44 gives a projection of the $\text{Ce}_3\text{Ag}_4\text{Ge}_4$ structure onto the ab plane.

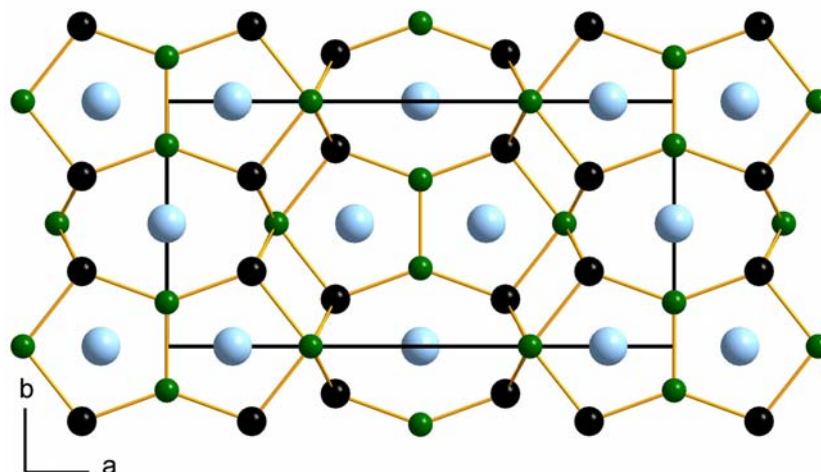


Figure 4.4-44: Projection of the $\text{Ce}_3\text{Ag}_4\text{Ge}_4$ structure onto the ab plane. Cerium, silver, and germanium atoms are drawn as light blue, black, and green spheres, respectively. The three-dimensional $[\text{Ag}_4\text{Ge}_4]$ network is emphasized.

The larger eight-membered ring channels, which are built up of alternating silver and germanium atoms, are filled with the Ce1 atoms. These Ce1 atoms are in the first coordination sphere octahedrally coordinated from six germanium atoms (319–320 pm) and in the second coordination sphere surrounded from eight silver atoms in a distances of 361 pm. In Figure 4.4-45 the coordination sphere of Ce1 is displayed. All Ce2 atoms are pentagonal prismatic coordinated from six germanium (319–322 pm) and four silver atoms (318 pm).

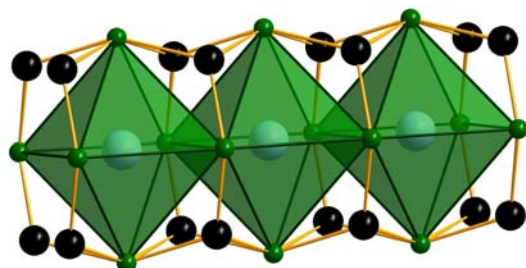


Figure 4.4-45: First and second coordination sphere of the Ce1 atoms.

Table 4.4-26: Interatomic distances (pm) calculated with the single crystal lattice parameters in $Ce_3Ag_4Ge_4$. All distances of the first coordination sphere are listed.

Ce1–Ge2	319.3(1) 4x	Ce2–Ag1a	317.6(1) 4x	Ge1–Ag1a	272.3(1) 4x	Ge2–Ge2	257.0(2)
Ce1–Ge1	320.3(2) 2x	Ce2–Ge1	319.1(1) 2x	Ge1–Ag1b	278.4(1)	Ge2–Ag1	263.9(1) 2x
Ce1–Ag1	361.1(1) 8x	Ce2–Ge2	321.5(1) 4x	Ge1–Ce2	319.1(1) 2x	Ge2–Ce1	319.3(1) 2x
		Ce2–Ag1b	330.3(1) 2x	Ge1–Ce1	320.3(2)	Ge2–Ce2	321.5(1) 3x

The following discussion points out the problems of a phase pure synthesis of $Ce_4Ag_3Ge_4O_{0.5}$ and gives a short overview of other oxygen containing intermetallics.

4.4.8.11 Discussion

The oxidation of intermetallic phases to metal oxides under ambient pressure conditions is well known from the research of Hoppe, Yvon, Schuster, and Jung [347-355]. But only a few intermetallic oxides were established, in which crystal structure considerations and chemical analysis revealed the presence of significant oxygen concentrations. For example, the phases $RE_{12}Fe_{32}O_x$ with $x \leq 2$ ($RE = Y, Gd, Tb, Dy, Ho, \text{ and } Er$) [356] and Zr_3NiO [357] represent oxygen-stabilized, transition metal intermetallic compounds with octahedrally coordinated oxygen atoms. Another interesting compound with octahedrally coordinated oxygen atoms is the phase $Th_4Fe_{17}P_4O_{1-x}$ synthesized in a tin flux by the *Jeitschko* group [358]. The oxygen content of these phases was first detected in the course of the structure determination and to exclude the possibility of the interstitial atoms being nitrogen or carbon, freshly broken surfaces of the crystals were investigated *via* EDX. Furthermore, the *Nowotny* phases with $D8_8$ type structure are stabilized by the presence of small amounts of carbon, boron, oxygen, or nitrogen [359-361]. While the former mentioned phases were synthesized under ambient pressure conditions, the germanide oxide $Ce_4Ag_3Ge_4O_{0.5}$ was synthesized under high-pressure / high-temperature conditions, starting from NdPtSb type CeAgGe as precursor compound. Considering the trivalent and monovalent oxidation states for the cerium and silver atoms, closed-shell Ge^{4-} and Ge_2^{6-} dumb-bells, and a half occupied oxygen site, the following ionic formula splitting $(4Ce^{3+})^{12+}(3Ag^+)^{3+}(2Ge^{4-})^8-Ge_2^{6-}(1/2O^{2-})^-$ can be assumed. The COHP analysis of $Ce_4Ag_3Ge_4O_{0.5}$ already confirmed the valence compound character. Nevertheless, $Ce_4Ag_3Ge_4O_{0.5}$ should be regarded as a metallic compound possessing an ionic $[OCe_2Ce_{2/2}]$ string inside of a metallic matrix. A similar bonding pattern occurs in a variety of subnitrides, e.g. isolated Ba_6N octahedra in a sodium matrix of $Na_{16}Ba_6N$ [362, 363]. *Simon* described these interesting phases with the catchphrase "salt in a metal" because the segregation of the sodium

atoms between the subnitride clusters reminds directly of the distribution of Rb atoms between Cs_{11}O_3 clusters in $\text{Rb}_x\text{Cs}_{11}\text{O}_3$ ($x = 1, 2, 7$) [362]. In alkali metal suboxides the O atoms are always surrounded octahedrally by metal atoms and the octahedra may be linked *via* common faces to larger clusters. In $\text{Ce}_4\text{Ag}_3\text{Ge}_4\text{O}_{0.5}$ the O atoms are tetrahedrally coordinated and linked to chains *via* corners. From this point of view the compound can also be regarded as a rare-earth metal suboxide embedded in an intermetallic matrix.

The largest effort was set on a phase pure synthesis of the compound $\text{Ce}_4\text{Ag}_3\text{Ge}_4\text{O}_{0.5}$. Unfortunately, up to now the formation of the side product $\text{Ce}_3\text{Ag}_4\text{Ge}_4$ could not be prevented. Strictly connected to this problem was the question, from which source the amount of oxygen derived from. Did the oxygen come from the atmosphere or from an oxygen surface contamination of the precursor material. At first a surface contamination was the most probable origin in our eyes. That was the reason for experiments with a ball-milled precursor, which was exposed to the air overnight. The experiments resulted as described in a X-ray pure formation of $\text{Ce}_3\text{Ag}_4\text{Ge}_4$. A ball-milled powder can be filled much denser in the boron nitride crucible and the included air volume is minimal. If oxygen derived from the air is responsible for the oxidation of the intermetallic phase a coarsely ground precursor could be surrounded by a larger gas volume inside of the crucible. In addition to that, the assembly was mounted under an oxygen gas flow to raise the oxygen concentration. A significant change in product composition was unfortunately not ascertainable.

Furthermore, experiments with a modified precursor material in the ideal stoichiometric ratio $\text{Ce}:\text{Ag}:\text{Ge} = 4:3:4$ or the attempt to reach the ideal stoichiometry starting from the 1:1:1 precursor and addition of small amounts of CeO_2 and GeO_2 did not succeed. Thermal decomposition of KClO_3 under high-pressure / high-temperature conditions through generating reactive oxygen was used to oxidize the precursor material. The only identified oxidized species was Ce_2O_3 , while the remaining intermetallic phase was identified to be CeAg_2Ge_2 .

As mentioned in the introduction of the *RE*-Ag-Ge germanides, a third compound with a 1:2:2 stoichiometric ratio appeared occasionally in this system. The formation of this phase was generally observed in a pressure range of 7.5 to 11.5 GPa and was always accompanied by the formation of $\text{Ce}_3\text{Ag}_4\text{Ge}_4$.

These first experiments revealed that there still exist certain difficulties in the synthesis of the new oxidized intermetallic phase $\text{Ce}_4\text{Ag}_3\text{Ge}_4\text{O}_{0.5}$. Several phases seem to be stable in a small area of the ternary phase diagram, only accessible through varying temperature, pressure, and tempering times, which makes it so

challenging. Into the bargain, the origin of the small amount of oxygen remains unclear. But the appearance of such a material under high-pressure / high-temperature conditions is an exciting product of this technique and must not be a single incident. Due to the trivalency of the Ce atoms the existence of isotypic phases with neighbouring rare-earth elements is probable. A corresponding lanthanum phase was already evident from the powder diffraction pattern (see Figure 4.4-46). Also an increase to other monovalent transition metals like Cu^{I} or Au^{I} could be promising because in ternary germanides a lot of polyanionic networks with comparable structural building units are known. First experiments with CeAuGe were carried out. The results are presented in the following.

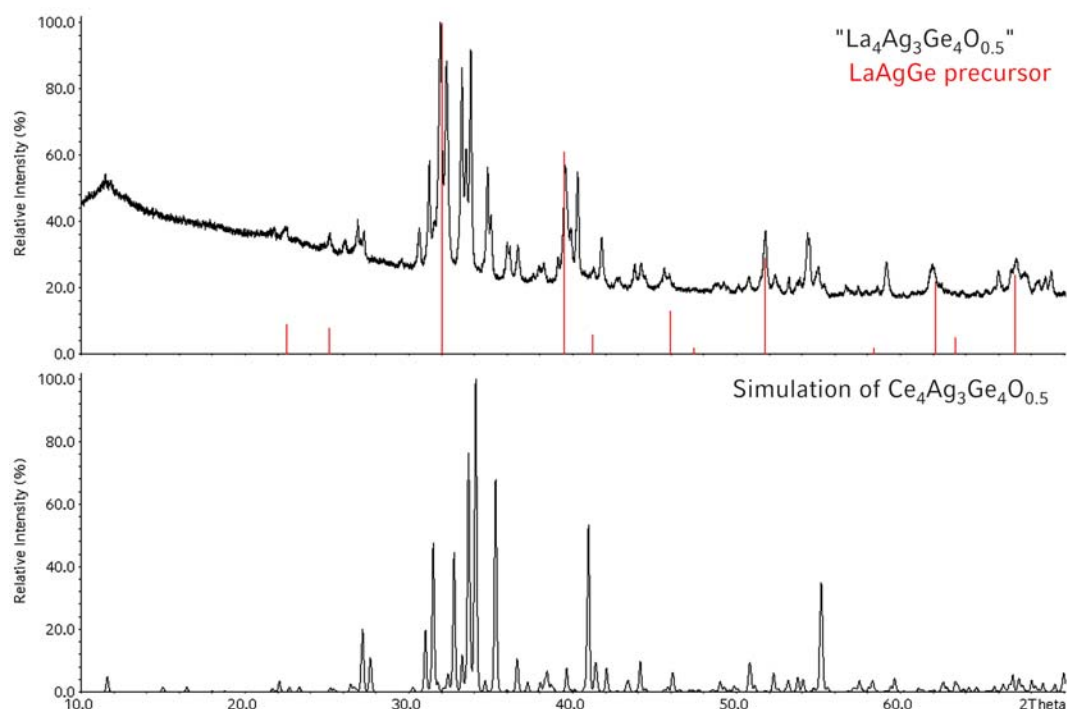


Figure 4.4-46: Recorded powder pattern of " $\text{La}_4\text{Ag}_3\text{Ge}_4\text{O}_{0.5}$ " (top) in comparison to the $\text{Ce}_4\text{Ag}_3\text{Ge}_4\text{O}_{0.5}$ simulation (down) derived from single crystal data. The educt reflections are marked with red lines.

4.4.9 The System RE-Au-Ge

4.4.9.1 Introduction

Cerium based intermetallic compounds have attracted synthetical chemists and physicists in the last years, due to their large variety of unusual physical properties (already mentioned in the introduction 4.4.1). Little information exists about the Ce-Au-Ge system. Only four ternary germanides were characterized up to now.

The compound with the 1:1:1 stoichiometric ratio was first identified and studied by *Rossi et al.* [364] and some years later the crystal structure of the CeAuGe compound was confirmed by *Pöttgen et al.* on the basis of single crystal data [365]. CeAuGe crystallizes in the well known hexagonal NdPtSb type structure. A more detailed description of the structure can be found in this thesis in Chapter 4.4.6.4. Investigations of the magnetic properties revealed long range ferromagnetic ordering below a Curie temperature of 10.0(2) K. In most cases, the derived local magnetic moments, associated with the stable trivalent state of the cerium ions, order antiferromagnetically like in CeAgGe (see Chapter 4.4.8). CeAuGe is one of a handful cerium compounds which show ferromagnetism.

A second AIB₂ related compound with statistically distributed gold and germanium atoms on the B₂ site was realized with the compound CeAu_{0.75}Ge_{1.25} [366]. In this compound ferromagnetic ordering at 6.0(5) K was observed, too.

Neutron-scattering studies on CeAu₂Ge₂ showed isotypy to the tetragonal ThCr₂Si₂ type structure [367]. Intensive investigations of the magnetic structures of the corresponding silver and ruthenium compounds were also presented in this paper.

Ce₂AuGe₆ was reported to crystallize with a Ce₂CuGe₆ type structure [368]. From this type of compound, all rare-earth representatives except promethium and lutetium were synthesized and identified *via* powder analysis. All these phases were synthesized under normal-pressure conditions. First high-pressure investigations were performed by *Schwarz et al.*, who investigated CeAuGe in a diamond anvil cell (DAC) at room temperature conditions up to a pressure of 15 GPa [369]. X-ray diffraction patterns of CeAuGe revealed a structural transformation from the NdPtSb type into the well known TiNiSi type structure. These first experiments aroused our interest to perform multianvil high-pressure / high-temperature experiments with subsequent analysis of tangible samples on the basis of single crystal data.

4.4.9.2 Synthesis of $\text{Ce}_7\text{Au}_{13.34(2)}\text{Ge}_{9.66(2)}$

Starting from a 1:1:1 Ce-Au-Ge precursor synthesized by the arc melting technique (see Chapter 2.1), multianvil high-pressure experiments were performed, which led to a new phase in the ternary Ce-Au-Ge phase diagram with the composition $\text{Ce}_7\text{Au}_{13.34(2)}\text{Ge}_{9.66(2)}$. For the precursor preparation cerium ingots, gold wire (\varnothing 1mm), and a germanium bar were used as starting materials.

The carefully milled intermetallic precursor was compressed to a pressure of 9.5 GPa in 2.5 h and heated to 1200–1250 °C in the following 15 min. After holding this temperature for 10 min, the sample was cooled down to 900 °C in 1 min. To enhance the crystallinity of the sample, an annealing period of 420 min followed, accompanied by a slow decrease of the temperature from 900 °C to 550 °C. Afterwards, the sample was cooled down to room temperature within 1 min. After decompression (8 h), the recovered experimental octahedron was broken apart, and the sample carefully separated from the surrounding boron nitride.

The polycrystalline sample of $\text{Ce}_7\text{Au}_{13.34(2)}\text{Ge}_{9.66(2)}$ is silvery with metallic lustre and stable in moist air over weeks. Powdered samples are dark gray. A comparison of the powder pattern recorded from the bulk material with the simulation derived from the crystal structure determination revealed that $\text{Ce}_7\text{Au}_{13.34(2)}\text{Ge}_{9.66(2)}$ is only a minor phase. The main product of this experiment is still unknown. Two independently selected single crystals of good quality led to the new phase in the Ce-Au-Ge phase diagram.

EDX analysis of the surface of a flat grinded sample revealed three different phases (see Figure 4.4-47 and Table 4.4-27). One major phase with a more or less 1:1:1 stoichiometry and two minor phases, whereas one showed the expected Ce:Au:Ge = 7:13:10 (measured: Ce:Au:Ge = 6.40:13.35:9.83) atomic ratio. For the third compound, a hitherto unknown composition of Ce:Au:Ge = 5:15:3 was evident.

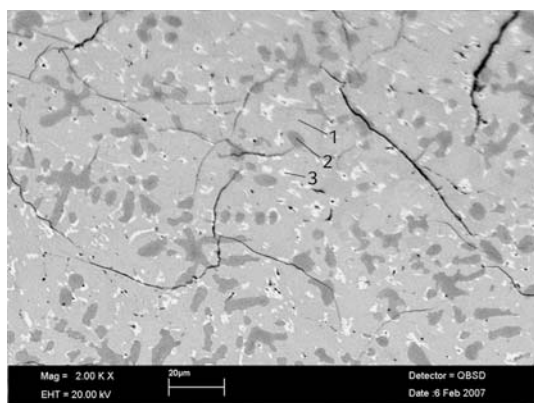


Figure 4.4-47: EDX analysis of a flat grinded bulk sample of the Ce-Au-Ge system.

Table 4.4-27: Results of the EDX analysis: (1) $\sim\text{Ce}_7\text{Au}_{13}\text{Ge}_{10}$, (2) $\sim\text{CeAuGe}$, (3) $\sim\text{Ce}_5\text{Au}_{15}\text{Ge}_3$.

Phase/ spectra	Ge / at%	Ce / at%	Au / at%	Altogether / at%
1/1	33	23	44	100.00
1/2	34	21	45	100.00
1/3	33	21	46	100.00
2/1	36	34	30	100.00
2/2	34	33	33	100.00
2/3	37	33	30	100.00
3/1	14	22	64	100.00
3/2	13	22	65	100.00

4.4.9.3 Crystal Structure Analysis

Small, irregularly shaped single crystals of $\text{Ce}_7\text{Au}_{13.34(2)}\text{Ge}_{9.66(2)}$ were selected from the high-pressure treated sample by mechanical fragmentation. The crystals were first investigated by Laue photographs in a Buerger camera (white molybdenum radiation; imaging plate technique, Fujifilm, BAS-1800) in order to check the quality for intensity data collection. Intensity data of a suitable crystal of $\text{Ce}_7\text{Au}_{13.34(2)}\text{Ge}_{9.66(2)}$ were collected at room temperature by use of a Kappa CCD diffractometer (Bruker AXS / Nonius, Karlsruhe) equipped with a rotating anode. An absorption correction based on multi-scans [339] was applied to the data set. All relevant crystallographic data and details of the data collections are listed in Table 4.4-28.

Analysis of the data set was consistent with space group *Pbam*. The starting atomic positions were deduced from automatic interpretations of *Direct methods* with SHELXS-97 [79] and all atoms were refined using SHELXL-97 (full-matrix least-squares on F^2) [80] with anisotropic atomic displacement parameters for all sites. The occupancy parameters were refined in a separate series of least-squares cycles in order to check for the correct composition. Thus, all sites were fully occupied within one standard deviation. But the Ge1/Au10 and the Ge5/Au9 site showed mixed occupancy and were refined coupled, using the commands EADP and EXYZ. The structure refinement clearly revealed occupancy of 97.2(3)% germanium and 2.8(3)% gold for the mixed site Ge1/Au10. In the case of the Ge5/Au9 site 85.7(4)% germanium and 14.3(4)% gold were distributed thereon. Final difference Fourier synthesis revealed no significant residual peaks (see Table 4.4-28). The positional

parameters, anisotropic displacement parameters, and interatomic distances are listed in Table 4.4-29 and Table 4.4-30.

Table 4.4-28: Crystal data and structure refinement for $\text{Ce}_7\text{Au}_{13.34(2)}\text{Ge}_{9.66(2)}$

Empirical formula	$\text{Ce}_7\text{Au}_{13.34(2)}\text{Ge}_{9.66(2)}$
Molar mass ($\text{g}\cdot\text{mol}^{-1}$)	4310.2
Crystal system	orthorhombic
Space group	<i>Pbam</i> (No. 55)
Single crystal diffractometer	Kappa CCD
Radiation	$\text{MoK}\alpha$ ($\lambda = 71.073$ pm)
Single crystal data	
<i>a</i> (pm)	1571.9(3)
<i>b</i> (pm)	1780.3(4)
<i>c</i> (pm)	443.58(9)
Volume (nm^3)	1.241(1)
Formula units per cell	<i>Z</i> = 2
Temperature (K)	293(2)
Calculated density ($\text{g}\cdot\text{cm}^{-3}$)	11.53
Crystal size (mm^3)	$0.03 \times 0.02 \times 0.02$
Detector distance (mm)	30
Scan time / degree (min)	30
Scan step ($^\circ$)	2.0
Absorption coefficient (mm^{-1})	102.5
F(000)	3538
θ Range ($^\circ$)	3.46 to 30.00
Range in <i>hkl</i>	-21/+22, -24/+25, ± 6
Total no. reflections	3501
Independent reflections	2017 ($R_{\text{int}} = 0.0240$)
Reflections with $I > 2\sigma(I)$	1770 ($R_\sigma = 0.0272$)
Data / parameters	2017 / 96
Absorption correction	multi-scan [339]
Goodness-of-fit (F^2)	1.047
Final <i>R</i> indices ($I > 2\sigma(I)$)	$R1 = 0.0207$ $wR2 = 0.0455$
<i>R</i> Indices (all data)	$R1 = 0.0271$ $wR2 = 0.0470$
Extinction coefficient	0.00007(2)
Larg. diff. peak and hole ($\text{e}\cdot\text{\AA}^{-3}$)	1.87 / -2.47

Table 4.4-29: Atomic coordinates and anisotropic displacement parameters (pm^2) for $\text{Ce}_7\text{Au}_{13.34(2)}\text{Ge}_{9.66(2)}$. U_{eq} is defined as one third of the trace of the orthogonalized U_{ij} tensor. The anisotropic displacement factor exponent takes the form: $-2\pi^2[(ha^*)^2U_{11}+\dots+2kha^*b^*U_{12}]$. $U_{13}, U_{23} = 0$.

Atom	Wyckoff position	x	y	z	U_{11}	U_{22}	U_{33}	U_{12}	U_{eq}
Ce1	4g	0.33792(3)	0.18209(3)	0	79(2)	103(3)	72(3)	10(2)	85(2)
Ce2	4h	0.15895(3)	0.95867(3)	1/2	65(2)	96(3)	66(2)	5(2)	76(2)
Ce3	4g	0.41515(3)	0.75895(3)	0	75(2)	123(3)	108(3)	6(2)	102(2)
Ce4	2c	1/2	0	0	89(3)	147(4)	102(4)	31(3)	113(2)
Au1	4h	0.19614(3)	0.14983(2)	1/2	117(2)	136(2)	169(2)	-25(2)	141(1)
Au2	4h	0.43005(3)	0.27717(2)	1/2	134(2)	107(2)	119(2)	-11(2)	120(1)
Au3	4g	0.24582(2)	0.85711(2)	0	133(2)	121(2)	89(2)	20(2)	114(1)
Au4	4h	0.36733(2)	0.89163(2)	1/2	84(2)	129(2)	224(2)	8(2)	145(1)
Au5	4h	0.35034(2)	0.04985(2)	1/2	103(2)	105(2)	99(2)	-15(2)	102(1)
Au6	2a	0	0	0	216(3)	559(5)	168(3)	183(3)	315(2)
Au7	4h	0.03149(3)	0.09674(3)	1/2	93(2)	187(2)	51(3)	24(2)	264(2)
Ge1/Au10	4g	0.42783(6)	0.35868(6)	0	125(5)	113(6)	90(6)	21(4)	109(4)
Ge5/Au9	4g	0.15257(6)	0.08395(5)	0	181(5)	124(5)	81(5)	-12(3)	129(3)
Ge2	4h	0.52170(7)	0.86089(6)	1/2	72(4)	95(5)	248(6)	0(4)	138(2)
Ge3	4h	0.24939(7)	0.28351(6)	1/2	113(5)	80(5)	75(5)	1(4)	89(2)
Ge4	4g	0.29410(7)	0.99691(6)	0	114(5)	133(5)	80(5)	-50(4)	109(2)

4.4.9.4 Crystal Structure Description

The compound $\text{Ce}_7\text{Au}_{13.34(2)}\text{Ge}_{9.66(2)}$ crystallizes in a new orthorhombic structure type with an interesting cluster unit and a string consisting of gold rhombs proceeding along the c axis. Figure 4.4-48 gives a projection of the Au-Ge network structure onto the ab plane with the central cluster unit circumscribed. The Au/Ge mixed sites are emphasized through different colours. Structural building units, well known from intermetallic phases like pentagonal and hexagonal prisms or rhombs, can be identified in the structure of $\text{Ce}_7\text{Au}_{13.34(2)}\text{Ge}_{9.66(2)}$.

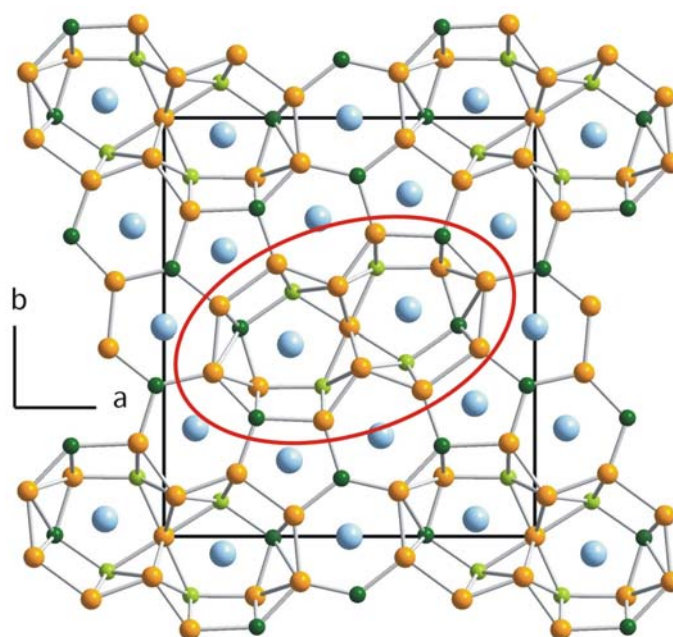


Figure 4.4-48: Projection of the $\text{Ce}_7\text{Au}_{13.34(2)}\text{Ge}_{9.66(2)}$ crystal structure onto the ab plane. Cerium, gold, germanium, and gold/germanium mixed sites are emphasized as light blue, orange, dark green, and light green, respectively.

Two pentagonal prisms, edge-linked *via* two Au6 atoms form the central building unit of the cluster, which are shown separately with labelled atoms in Figure 4.4-49. Four edges of each pentagonal prism were capped by the Au1, Au2, Au5, and Ge3 atoms and three square faces are capped from Au4 and two Au7 atoms. Within the Au-Ge cluster we have Au-Ge distances covering the large range from 256 to 312 pm. In the centre of the cluster, the Ce2 atoms are located.

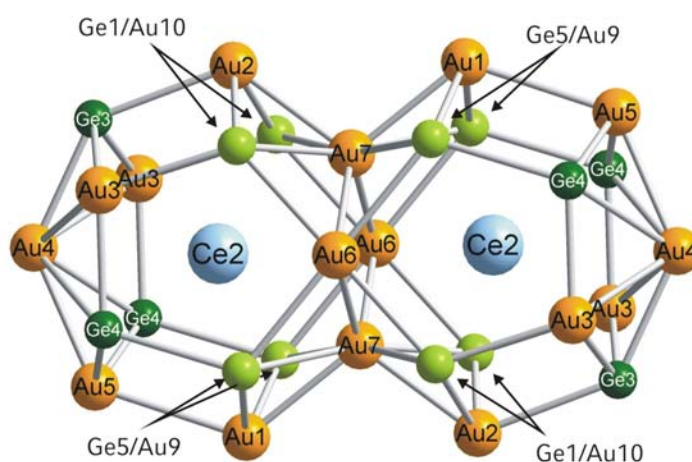


Figure 4.4-49: Cluster unit of $\text{Ce}_7\text{Au}_{13.34(2)}\text{Ge}_{9.66(2)}$ with labeled atoms.

The other rare-earth atoms can be found in pentagonal or hexagonal prismatic coordination, which are formed through the direct interconnection of the cluster units or a connection of two clusters *via* Ge2 atoms. The structure contains five crystallographically independent germanium sites. Two of them are mixed sites with mainly germanium occupation (Ge1/Au10: 97.2(3)% / 2.8(3)%; Ge5/Au9: 85.7(4)% / 14.3(4)%). Between Ge5 and Ge4, one can find the shortest Ge–Ge contacts (271 pm), which are quite longer than the Ge–Ge distances in Ge₂ dumb-bells (Ce₄Ag₃Ge₄O_{0.5}: Ge–Ge = 251 pm; Ce₃Ag₄Ge₄: Ge–Ge = 257 pm) already discussed in connection with the Ce–Ag–Ge phases (see Chapter 4.4.8.4 and 4.4.8.10). In the centre of the large cluster, a string of gold rhombs, built up from the Au6 and Au7 atoms, is visible (see Figure 4.4-50). The Au6–Au7 distances of 285 pm inside the rhombs are slightly shorter than in elemental gold (288 pm) [370], whereas the Au7–Au7 distance with 358 pm is quite longer and only van-der-Waals interactions can be assumed. Strong Au–Au contacts with 6s electron participation can be found in elemental gold (Au_x), gaseous Au₂, or in gold clusters. The Au–Au bond distances vary in a wide range: Au₂ = 250 pm, Au^{II}–Au^{II} ≈ 260 pm, Au_x = 288 pm, Au^I···Au^I = 275–340 pm, > 340 pm van-der-Waals effects [370]. In the [Au_{13.34(2)}Ge_{9.66(2)}] network the Au–Au distances range between 260–300 pm, whereas the shortest distances of 260 pm and 265 pm are between Au1 and the Ge5/Au9 sites as well as between Au2 and the Ge1/Au10 mixed sites. Further distances can be found in Table 4.4-30.

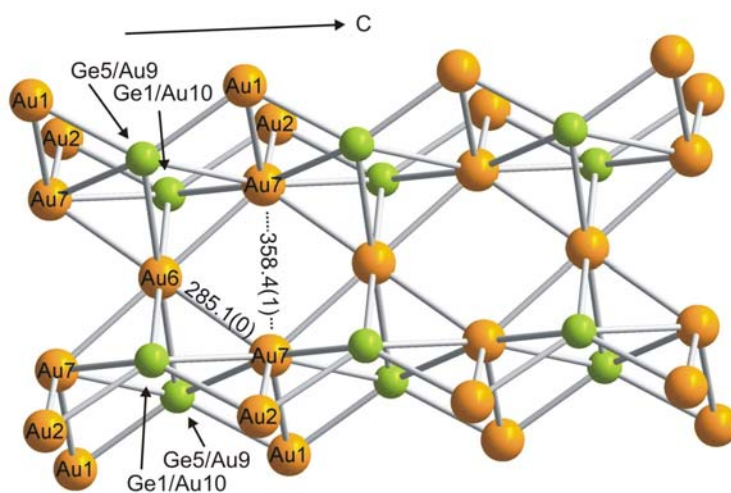


Figure 4.4-50: String of Au6/Au7 rhombs parallel to the *c* axis.

Figure 4.4-50 gives a view of the string of corner-linked gold rhombs running along the c axis. Such a string of connected rhombs is already known from other intermetallic compounds. For example, the Ni atoms in $Y_4Ni_{11}In_{20}$ show such a structural building unit surrounded by indium atoms [371]. The Ni–Ni distances of 259 and 286 pm, however, are slightly longer than in elemental fcc nickel (249 pm) [321] and reflect a comparable situation as described before for the Au₆/Au₇ rhombs. A second variation of this two dimensional string of rhombs is realized in the compounds $RE_4Pd_{10}In_{21}$ ($RE = La-Nd, Sm$), in which the string is built up from palladium and indium atoms [372]. The linkage of the several rhombs takes place *via* the indium atoms.

To represent intermetallic phases in a clear way and to raise the recognition factor, a special trigonal prismatic illustration form has been applied. The structure is separated into germanium centred trigonal prisms as shown in Figure 4.4-51. Though three different types of prisms are formed: *(i)* prisms with only cerium atoms at the corners, *(ii)* prisms consisting of four cerium and two gold atoms, and *(iii)* prisms with four gold and two cerium atoms at the corners. Among each other, the prisms are connected by common edges forming large rings of 10 prisms. In their centre, a unit of six condensed prisms is located. The central units and the large rings of prisms are shifted against each other along c by $\frac{1}{2}$.

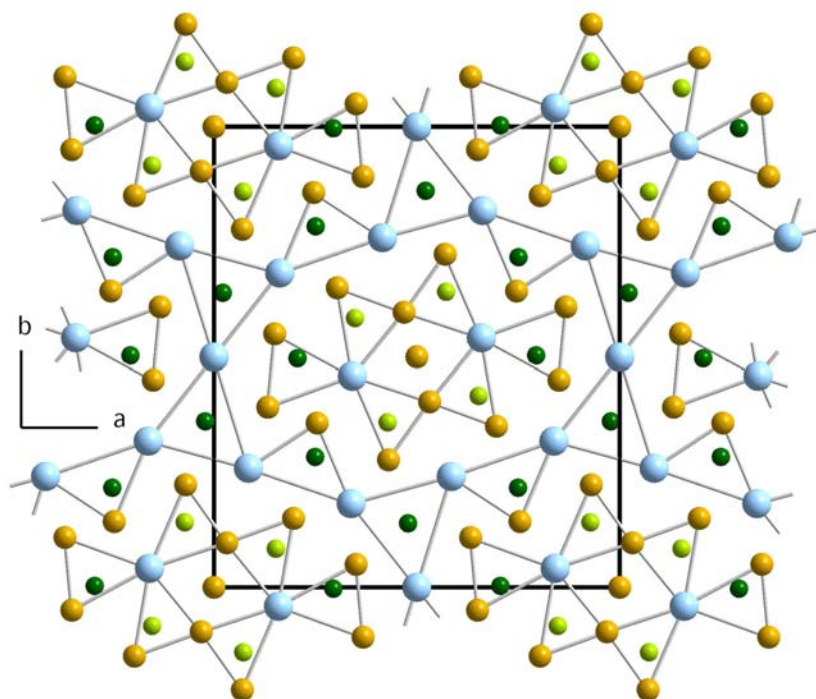


Figure 4.4-51: Crystal structure of $Ce_7Au_{13.34(2)}Ge_{9.66(2)}$. View onto the ab plane. Ge and Ge/Au centered prisms are illustrated to rise the recognition factor.

Table 4.4-30: Interatomic distances (pm), calculated with the lattice parameters taken from X-ray single crystal data of $\text{Ce}_7\text{Au}_{13.34(2)}\text{Ge}_{9.66(2)}$.

Ce1–Au2	314.3(1) 2x	Ce2–Ge4	314.6(1) 2x	Ce3–Au3	318.4(1)	Ce4–Ge4	323.7(1) 2x
Ce1–Ge3	318.1(1) 2x	Ce2–Au9	314.7(1) 2x	Ce3–Au10	323.7(2)	Ce4–Ge2	334.2(1) 4x
Ce1–Au1a	319.6(1) 2x	Ce2–Ge5	314.7(1) 2x	Ce3–Ge1	323.7(2)	Ce4–Au5	335.3(1) 4x
Ce1–Ge2	322.1(1) 2x	Ce2–Au7	315.2(1)	Ce3–Au9	329.2(2)	Ce4–Au4	360.4(1) 2x
Ce1–Au5	324.0(1) 2x	Ce2–Au10	315.4(1) 2x	Ce3–Ge5	329.2(2)		
Ce1–Ge4	336.8(2)	Ce2–Ge1	315.4(1) 2x	Ce3–Ge2	331.9(1) 2x		
Ce1–Au3	338.2(1)	Ce2–Au3	317.1(1)	Ce3–Au4	332.6(1) 2x		
				Ce3–Au2	335.5(1) 2x		
				Ce3–Au1	342.8(1)		
						Ge4–Au5	256.7(1) 2x
Ge1–Au2	265.1(1)					Ge4–Au9	271.1(2)
Ge1–Au3	273.0(2)	Ge2–Au5	256.3(2)	Ge3–Au3	257.7(1) 2x	Ge4–Ge5	271.1(2)
Ge1–Au6	276.0(2)	Ge2–Au2	257.2(2)	Ge3–Au4	265.9(2)	Ge4–Au4	312.4(1)
Ge1–Au7	286.4(1) 2x	Ge2–Ce1	322.1(1) 2x	Ge3–Ce1	318.1(1)	Ge4–Ce2	314.6(1)
Ge1–Ce2	315.4(1) 2x	Ge2–Ce3	331.9(1)	Ge3–Ce3	343.5(1) 2x	Ge4–Ce4	323.7(2)
Ge1–Ce3	323.7(2)	Ge2–Ce4	334.2(1) 2x	Ge3–Ce2	343.5(1)	Ge4–Ce1	336.8(2)
Ge5–Au1	260.1(1)	Au1–Au9	260.1(1)	Au3–Au10	273.0(2)	Au6–Au10	276.0(2) 2x
Ge5–Ge4	271.1(2)	Au1–Au7	275.5(1)	Au3–Au4	299.1(1) 2x	Au6–Au9	282.6(1) 2x
Ge5–Au7	293.1(1)	Au1–Au5	300.7(1)			Au6–Au7	285.1(1) 4x
Ge5–Ce2	314.7(1) 2x			Au4–Au5	283.0(1)		
Ge5–Ce3	329.2(2)	Au2–Au10	265.1(1)	Au4–Au3	299.1(1)	Au7–Au2	275.4(1)
		Au2–Au7	275.4(1)			Au7–Au6	285.1(1) 4x
				Au5–Au4	283.0(1)	Au7–Au10	286.4(1) 2x
						Au7–Au9	293.2(1)

4.4.9.5 Discussion

The structures of normal-pressure CeAuGe and high-pressure CeAuGe both derive from the well-known aristotype AlB_2 by different distortions. Due to the fact that there is no direct group-sub group relation between the NdPtSb type and the TiNiSi type, as already seen for the TiNiSi \rightarrow ZrNiAl transition, the phase transition is assumed to be a first order type transition. Although the experiments performed from Schwarz *et al.* were in a pressure range achievable by multianvil synthesis, the here presented results are different. Schwarz *et al.* found the normal-pressure phase to be stable up to a maximum pressure of 8.7(7) GPa. At higher pressures, additional lines plus splitting of reflections were observed. The high-pressure phase remains stable up to pressures of 15.1(5) GPa, which was the upper limit in the experiments.

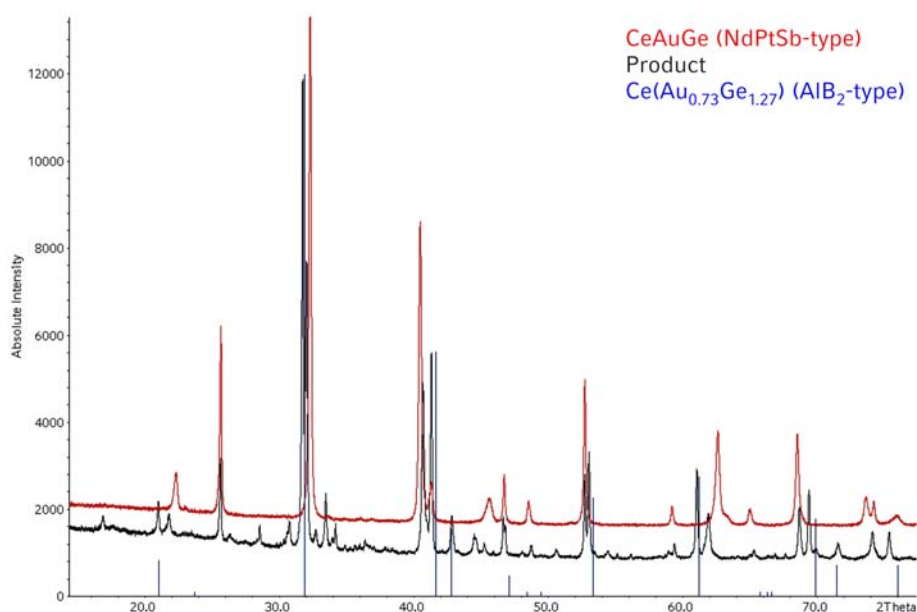


Figure 4.4-52: Powder diffraction pattern of the CeAuGe high-pressure experiment in comparison with the NdPtSb type CeAuGe as starting material and an AIB₂ type substitution variant.

Figure 4.4-52 gives a view of the powder pattern derived after the multianvil experiment. A comparison with the pattern of the starting material (NP-CeAuGe) and the AIB₂ substitution variant CeAu_{0.73}Ge_{1.27} showed some agreements but also shifted reflections, which do not harmonize with the NdPtSb type of NP-CeAuGe and the AIB₂ structure type. Without any single crystal data it is not possible to give a reliable prediction concerning the composition of the main phase. Since the Ce-Au-Ge experiments were the latest experiments in the context of this thesis, so far a full characterization was not possible. The two for X-ray single crystal diffraction selected single crystals of good quality revealed the new orthorhombic structure type of Ce₇Au_{13.34(2)}Ge_{9.66(2)}. One can see from the powder pattern that the phase Ce₇Au_{13.34(2)}Ge_{9.66(2)} is only a small byproduct, which makes it even more amazing that two crystals of this phase were selected. Apparently, the new compound crystallizes very well and maybe a phase pure synthesis is possible with an appropriate precursor. Experiments with a precursor in the correct stoichiometry prepared under ambient pressure *via* the arc melting procedure are planned. Furthermore, it is unclear, if the phase Ce₇Au_{13.34(2)}Ge_{9.66(2)} is also tangible at ambient pressure conditions. But the high synthesis pressures of 9.5 GPa, coordination numbers of 12 for the cerium atoms, and the existence of a network structure make a normal-pressure access extremely unlikely. A pure compound is also the precondition for further property measurements. The unusual properties especially of cerium compounds mainly arise from the hybridization of the moment carried out by the 4f electrons

with the conduction electrons. For this reasons the results of magnetic measurements are expected full of suspense.

These experiments clearly revealed that although high-pressure experiments have already been performed in the system Ce-Au-Ge a combination of high-pressures and high-temperatures can lead to completely new and exciting results. The systematic investigation of metastable ternary intermetallic phases synthesized under high-pressure / high-temperature conditions is still getting off the ground and a lot of new and interesting compounds will be discovered in the future. First hints of a further, gold richer new compound were given through the EDX investigation of the high-pressure sample.

4.5 Further Cooperations

Besides the strong cooperation with the group of Prof. Pöttgen in Münster, the European COST D30 network made it possible to cooperate with several other groups, namely Prof. G. Demazeau (ICMCB, CNRS Bordeaux), Prof. E. Moran (Departamento de Química Inorgánica I, Facultad de Ciencias Químicas, Madrid), Prof. J. P. Attfield (CSEC, Edinburgh), and Dr. J. A. Alonso (CSIC, Madrid). Beyond the COST D30 network, we cooperated with Prof. W. Scherer (Institut für Physik, Universität Augsburg). Owing to the special multianvil high-pressure facilities in Munich, a number of experiments at pressures exceeding the 8 GPa range were carried out to handle the other topics of the project. So experiments concerning the stabilization of oxides with mixed valences as well as to stabilize unusual oxidation states of transition metals were performed. The results of these experiments are summarized briefly in the following. For further information the reader is referred to the corresponding publications.

4.5.1 New preparation process for ^{57}Fe doped LaCuO_3 [373]

LaCuO_3 was for the first time prepared by *Demazeau et al.* [374] starting from a stoichiometric mixture of La_2CuO_4 and CuO as precursors and a high oxygen pressure treatment (6 GPa, 950 °C, 15 min) in a belt-type apparatus, using KClO_3 as *in-situ* oxygen source. Such a material is characterized by a rhombohedral structure and metallic character of conductivity in all temperature ranges due to the strong covalence of the $\text{M}^{3+}\text{-O}$ bond and the small structural distortion (Cu-O-Cu angle is close to 180°) [375].

A comparative study of the rhombohedral perovskites LaCuO_3 and LaNiO_3 (both characterized by Pauli paramagnetism) had evidenced that the differences between the magnitudes and thermal evolutions of their respective susceptibilities could be explained in terms of antiferromagnetic versus ferromagnetic superexchange enhancement and large versus small spin polarons associated with the excited states [376].

Mössbauer spectroscopy would be the method of choice to evaluate both, the valence state and the electronic configuration adopted by a transition metal through the isomer shift (δ) and the quadrupole splitting (Δ). Hence, such a physical characterization can also be applicable to study and to compare both LaCuO_3 and LaNiO_3 perovskites.

In the case of LaNiO_3 doped with ^{57}Fe (2%), the conventional preparation process occurred through the solid-state reaction $\text{La}_2\text{O}_3 + 2 \text{NiO} \cdot ^{57}\text{Fe}$ under gaseous O_2 pressure (100 MPa) at 900°C . For the LaCuO_3 matrix, the previous preparation method [376] ($\text{La}_2\text{CuO}_4 + \text{CuO} \cdot ^{57}\text{Fe}$ with KClO_3 as oxygen source) did not lead to a pure rhombohedral phase; consequently it was necessary to find a new preparation process for $\text{LaCu}_{0.98}^{57}\text{Fe}_{0.02}\text{O}_3$.

The new preparation process required two steps. The first one is the reaction between the precursors and the second one the oxidation of copper cations ($\text{Cu}^{2+} \rightarrow \text{Cu}^{3+}$). In order to reduce the number of steps, a new precursor $\text{La}_2\text{Cu}_2\text{O}_5 \cdot ^{57}\text{Fe}$ was selected. $\text{La}_2\text{Cu}_2\text{O}_5$ can be considered as the end member of the oxygen-defect perovskite series LaCuO_{3-x} [377]. The orthorhombic form of $\text{La}_2\text{Cu}_2\text{O}_5$ can be prepared through two different routes: a high-pressure synthesis from La_2O_3 and CuO [378], or the reduction of the tetragonal form of the $\text{LaCuO}_{3-\delta}$ perovskite [377, 379].

A pure phase $\text{LaCu}_{0.98}^{57}\text{Fe}_{0.02}\text{O}_3$ was obtained through a high-pressure oxidation process (11.5 GPa, $900^\circ\text{C} < T < 950^\circ\text{C}$) during 30 min using KClO_3 as *in-situ* oxygen source and a multianvil assembly (Walker-type) as high-pressure apparatus. The $\text{La}_2\text{Cu}_2\text{O}_5 \cdot ^{57}\text{Fe} \rightarrow \text{LaCuO}_3 \cdot ^{57}\text{Fe}$ transformation can be associated to a high-pressure diffusion of oxygen into the bulk of the vacant layers of the orthorhombic La_2CuO_5 matrix. Consequently, during the same process $[\text{CuO}_5]^{8-}$ square pyramids were transformed to $[\text{CuO}_6]^{9-}$ octahedra and the oxidation of copper cations took place. Figure 4.5-1 gives a view of the crystal structures of the $\text{La}_2\text{Cu}_2\text{O}_5 \cdot ^{57}\text{Fe}$ precursor and the corresponding transformed and oxidized $\text{LaCu}_{0.98}^{57}\text{Fe}_{0.02}\text{O}_3$ perovskite.

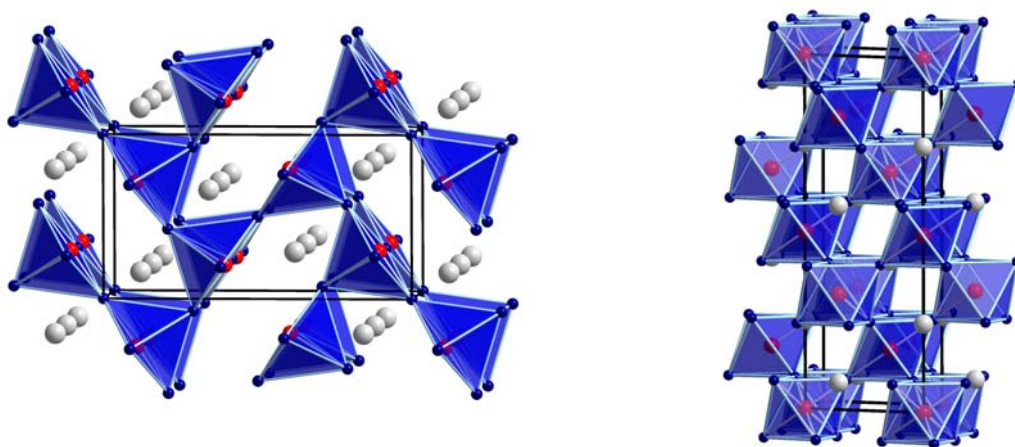


Figure 4.5-1: Left: crystal structure of $\text{La}_2\text{Cu}_2\text{O}_5 \cdot ^{57}\text{Fe}$ view along c ; Right: crystal structure of $\text{LaCu}_{0.98}^{57}\text{Fe}_{0.02}\text{O}_3$ view along b ; La: light grey spheres, Cu: red spheres and O: blue spheres.

In order to evaluate the role of the $\text{La}_2\text{Cu}_2\text{O}_5$ precursor structure on the LaCuO_3 synthesis, the preparation of LaCuO_3 from two different structural forms of $\text{La}_2\text{Cu}_2\text{O}_5$ (without Mössbauer probe) was studied. Using the monoclinic form (space group $C2/c$) [380] and KClO_3 as oxygen source, LaCuO_3 was not observed after a high-pressure treatment (6 GPa, 950 °C, 20 min). On the contrary, with the orthorhombic form (space group $Pbam$) as precursor and also KClO_3 , the formation of LaCuO_3 perovskite was observed under the same experimental conditions (6 GPa, 950 °C, 20 min).

Such results underline at first that the structure of the precursor plays an important role on the preparation conditions and secondly that if the same composition is used as precursor (orthorhombic $\text{La}_2\text{Cu}_2\text{O}_5$), the ^{57}Fe Mössbauer probe modifies drastically the preparation conditions (the pressure values must be essentially higher) probably due to the metallic character of the LaCuO_3 matrix. For matrixes characterized by insulating or semi-conducting properties, the doping with ^{57}Fe does not modify drastically the preparation process. LaCuO_3 , with metallic properties, appears as a specific case compared to LaNiO_3 . Mössbauer studies of both doped perovskites are in progress to explain such a different behaviour.

4.5.2 $\text{SrRu}_{1-x}\text{Cr}_x\text{O}_3$ perovskites: Solid solutions between two itinerant electron oxides [381]

Transition metal oxide perovskites are of enduring interest because of the properties that result from highly-correlated d -band electrons and strong electron-lattice couplings. SrRuO_3 and SrCrO_3 are notable as both are intrinsic metallic conductors. The electronic and magnetic properties of SrRuO_3 have been studied extensively. [382-384] An orthorhombic $Pbnm$ symmetry superstructure is found at 300 K due to tilting of the RuO_6 octahedra. SrCrO_3 has not been investigated so heavily as high-pressures are required to prepare this phase. The original study reported that SrCrO_3 is an undistorted cubic perovskite ($a_p = 3.818 \text{ \AA}$) [385].

Solid solutions between SrRuO_3 and SrCrO_3 are of potential interest to discover whether itinerant electron behaviour can be tuned between the two end-members, or whether insulating phases result from Cr/Ru disorder and charge transfer. It has recently been reported that $\text{SrRu}_{1-x}\text{Cr}_x\text{O}_3$ solid solutions up to $x = 0.15$ can be synthesised at ambient pressure and 1250–1370 °C [386-388]. Notably, this increases the Curie temperature up to $T_C = 188 \text{ K}$, whereas other substituents reduce the T_C of SrRuO_3 [386]. This has been attributed to a double-exchange interaction between minority spin t_{2g} -band electrons, resulting from partial $\text{Ru}^{4+} + \text{Cr}^{4+} \rightarrow \text{Ru}^{5+} + \text{Cr}^{3+}$ charge transfer [388]. An $x = 0.2$ sample was also prepared in the latter study at a

pressure of 3 GPa, but $\text{SrRu}_{1-x}\text{Cr}_x\text{O}_3$ solid solutions with higher Cr contents have not been reported. Here, a survey across the entire $\text{SrRu}_{1-x}\text{Cr}_x\text{O}_3$ series using appropriate pressures to stabilise the high x samples is presented. As well, variations of perovskite superstructure, magnetism, and electronic conductivity are presented.

Ceramic precursors for nominal $\text{SrRu}_{1-x}\text{Cr}_x\text{O}_3$ compositions were prepared from stoichiometric mixtures of SrCO_3 , RuO_2 , and Cr_2O_3 , pelletized and sintered at 950 °C in air for 12 hours. Single perovskite phase samples were obtained by re-heating samples with x up to 0.15 twice for 12 h at 1100 °C under flowing nitrogen. However, materials with $x > 0.2$ required high-pressure to stabilise perovskite phases. $\text{SrRu}_{1-x}\text{Cr}_x\text{O}_3$ samples with $x = 0.4$ and 0.6 were synthesised at 1000 °C and 3.5 GPa pressure in a piston cylinder apparatus. $x = 0.5, 0.8,$ and 1 samples were treated at 1100 °C and 10.5 GPa pressure, using a Walker-type, multianvil module.

Three different structure types were found for $\text{SrRu}_{1-x}\text{Cr}_x\text{O}_3$ perovskites as x changes from 0 to 1, and the properties of each group are described in the following in a brief way.

$x = 0-0.15$: The properties of these samples are very similar to those previously reported [386-388]. The samples have the $Pbnm$ superstructure of SrRuO_3 , and show an enhancement of T_C up to 188 K for $x = 0.10-0.15$ samples. These materials are band ferromagnets, with saturated moments of $\sim 1 \mu_B/\text{f.u.}$, and they show metallic conductivity with little temperature dependence down to 4 K.

$x = 0.40$: This sample showed a different pattern of X-ray diffraction peak splittings compared to the low doped $Pbnm$ and the higher x (cubic) materials. The splittings are consistent with a rhombohedral lattice distortion, and the X-ray data were fitted by an $R3c$ symmetry perovskite superstructure model. Magnetisation measurements between 4 and 320 K show a broad ferromagnetic transition with an onset at ~ 250 K for $\text{SrRu}_{0.6}\text{Cr}_{0.4}\text{O}_3$. The saturated moment of $\sim 0.15 \mu_B/\text{f.u.}$ is considerably less than that in the orthorhombic $x = 0-0.15$ materials. This sample is also semi-conducting showing that a metal-insulator boundary occurs in the $x = 0.2-0.4$ region of the $\text{SrRu}_{1-x}\text{Cr}_x\text{O}_3$ phase diagram (Figure 4.5-2).

$x = 0.5-1$: The materials in this range were all found to have undistorted, cubic $Pm3m$ perovskite cells. The $x = 0.5$ and $x = 0.6$ samples are semiconducting with resistivities comparable to the rhombohedral $x = 0.4$ material, whereas the $x = 0.8$ and 1 samples show that they are metallic, as reported previously [385]. Hence, a second insulator-metal transition occurs in the $x = 0.6-0.8$ interval of the $\text{SrRu}_{1-x}\text{Cr}_x\text{O}_3$ system. Magnetisation measurements in the 4-320 K range show an apparent ferromagnetic transition at 190 K for the $x = 0.5, 0.6,$ and 0.8 samples, but not for $x = 1$. The saturation moments are small ($< 0.1 \mu_B/\text{f.u.}$) and decrease with

increasing x . A further transition at 50 K is observed in the $x = 0.8$ sample, and is prominent in the magnetisation curve for SrCrO_3 . This was not reported in the previous study of the latter phase [385].

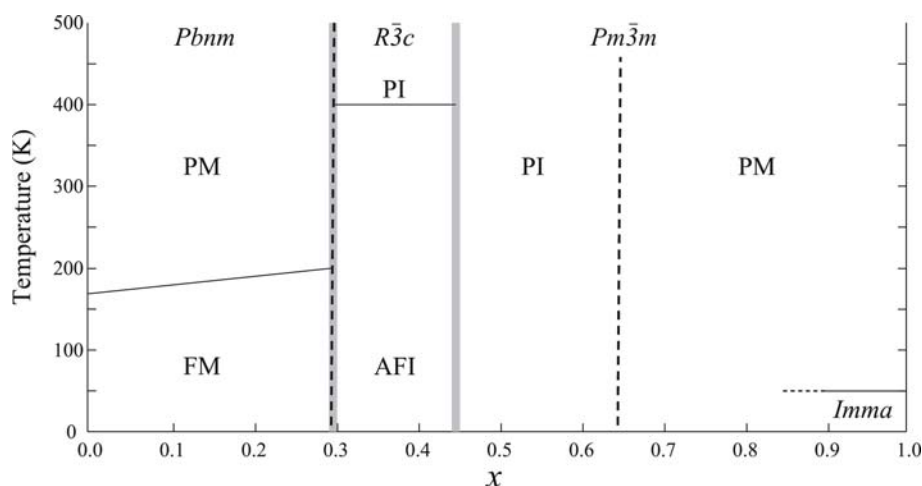


Figure 4.5-2: A schematic phase diagram for the $\text{SrRu}_{1-x}\text{Cr}_x\text{O}_3$ system based on the present results. Phase labels; P/F/AF = para-/ferro-/antiferro-magnetic; M/I = metallic/insulating. Approximate superstructure and metal-insulator transitions are shown as grey and broken lines, respectively [381].

This study has revealed that an entire range of $\text{SrRu}_{1-x}\text{Cr}_x\text{O}_3$ perovskite solid solutions can be prepared using high-temperatures and high-pressures. A substantial $\text{Ru}^{4+} + \text{Cr}^{4+} \rightarrow \text{Ru}^{5+} + \text{Cr}^{3+}$ charge transfer is evidenced by a volume-composition discontinuity near $x = 0.5$, as well as by enhancement of the ferromagnetic transition at low x . Three distinct electronic regimes are found. Low Cr-doped materials ($x < 0.3$) are itinerant-electron ferromagnets with an orthorhombic $Pbnm$ perovskite superstructure, as in SrRuO_3 , and show an enhancement of T_C from 160 to 190 K due to an additional $\text{Cr}^{3+}/\text{Cr}^{4+}$ double exchange. An insulation region is found for $0.3 < x < 0.7$ in which both rhombohedral and cubic structural phases occur. Antiferromagnetic G -type order with a high Néel temperature (~ 400 K) is found for the rhombohedral $x = 0.4$ phase. $0.7 < x < 1$ samples are cubic and Pauli paramagnetic, as typified by SrCrO_3 . However, low-temperature magnetic and structural transitions indicate that the ground state of SrCrO_3 is more subtle than previously reported, with a possible weak ferromagnetism arising from modifications of the Fermi surface. Further work is needed to clarify the nature of these correlated-electron states, and to investigate the phenomena, that may arise from phase co-existence or competition at the structural, magnetic, and electronic phase boundaries.

4.5.3 An organometallic *chimie douce* approach to new $\text{Re}_x\text{W}_{1-x}\text{O}_3$ phases [389]

As an electro-chromic material, applied e.g. as thin film for “smart windows”, and as gas sensors, crystalline WO_3 has found widespread interest. The thermodynamically most stable phase at room temperature is the monoclinic $\gamma\text{-WO}_3$ ($P2_1/n$) form, built up from tilted $[\text{WO}_6]^{6-}$ octahedra. A structural relationship *via* group-subgroup formalism to the cubic ReO_3 ($Pm3m$) has been shown, which represents the aristotype of the BO_3 perovskite family. Accordingly, it should be possible to form solid solutions of mixed $\text{Re}_x\text{W}_{1-x}\text{O}_3$ phases due to the structural resemblance of both parent oxides and the similar ionic radii of Re^{VI} (0.55 Å) and W^{VI} (0.6 Å) [141]. While WO_3 is an insulator, ReO_3 displays metallic behaviour with a specific conductivity in the same range as crystalline copper. However, up to now mixed $\text{Re}_x\text{W}_{1-x}\text{O}_3$ phases were only accessible in small quantities under extreme conditions at high-pressures and high-temperatures (6.5 GPa, 1200 °C) [390]. The here presented approach proposes a new organometallic *chimie douce* method which allows the synthesis of $\text{Re}_x\text{W}_{1-x}\text{O}_3$ phases in large quantities by a low temperature process at ambient pressure. But for doping concentrations $x > 0.12$ high-pressure / high-temperature conditions are still essential.

Mixed hydrated WO_3/ReO_3 phases are formed from sodium *meta*-tungstate containing the Keggin ion $[\text{H}_2\text{W}_{12}\text{O}_{40}]^{6-}$ and the organometallic precursor CH_3ReO_3 (**methyltrioxorhenium**; MTO) in diluted HCl at 100 °C. The new $\text{Re}_x\text{W}_{1-x}\text{O}_3 \cdot \text{H}_2\text{O}$ phases are obtained as dark green to black micro-crystalline platelets, in contrast to $\text{WO}_3 \cdot \text{H}_2\text{O}$, which shows a bright yellow colour when prepared under the same conditions. For x larger than 0.12, phase separation *via* ReO_3 formation is observed.

IR spectroscopic studies, dehydration behaviour analysed by TGA as well as magnetisation measurement and ESR investigations were used to follow the Re incorporation into the $\text{WO}_3 \cdot \text{H}_2\text{O}$ structure. Finally, a strong indication for the change in $\text{WO}_3 \cdot \text{H}_2\text{O}$ structure due to rhenium doping is found by X-ray powder diffractometry. The mixed hydrated phases are isotypic to the orthorhombic $\text{WO}_3 \cdot \text{H}_2\text{O}$ tungstite structure ($Pmnb$). *Rietveld* refinements reveal a widening of the $\text{WO}_3 \cdot \text{H}_2\text{O}$ structure by 1.5 pm in the c direction (from 5.1264(4) Å to 5.1416(1) Å) after Re doping ($x = 0.025$).

Due to the partial amorphous character, an analysis of the diffraction pattern of dehydrated $\text{Re}_x\text{W}_{1-x}\text{O}_3 \cdot \text{H}_2\text{O}$ was complicated. The resulting pattern closely resembles the ones found earlier for dehydrated $\text{WO}_3 \cdot \text{H}_2\text{O}$ phases which were reported to represent the hitherto unknown metastable form of cubic WO_3 [391]. However, a

direct comparison with the cubic diffraction pattern of highly crystalline $\text{Re}_{0.25}\text{W}_{0.75}\text{O}_3$ powder, obtained by bulk synthesis at 7.5 GPa and 1100 °C ($a = 3.7516(2)$ Å; Figure 4.5-3(c)), clearly reveals that the new $\text{Re}_x\text{W}_{1-x}\text{O}_3$ phases obtained by dehydration should be indexed rather by a monoclinic than by a cubic unit cell. Precise lattice parameters for the new monoclinic, $\gamma\text{-WO}_3$ analogue, $\text{Re}_x\text{W}_{1-x}\text{O}_3$ phase ($x = 0.025$, $a = 7.3165(4)$ Å, $b = 7.5131(4)$ Å, $c = 7.6911(5)$ Å, $\beta = 90.521(6)^\circ$, $P2_1/n$) could be obtained from *Rietveld* analysis of the annealed samples (720 °C, 1 d; Figure 4.5-3(b)).

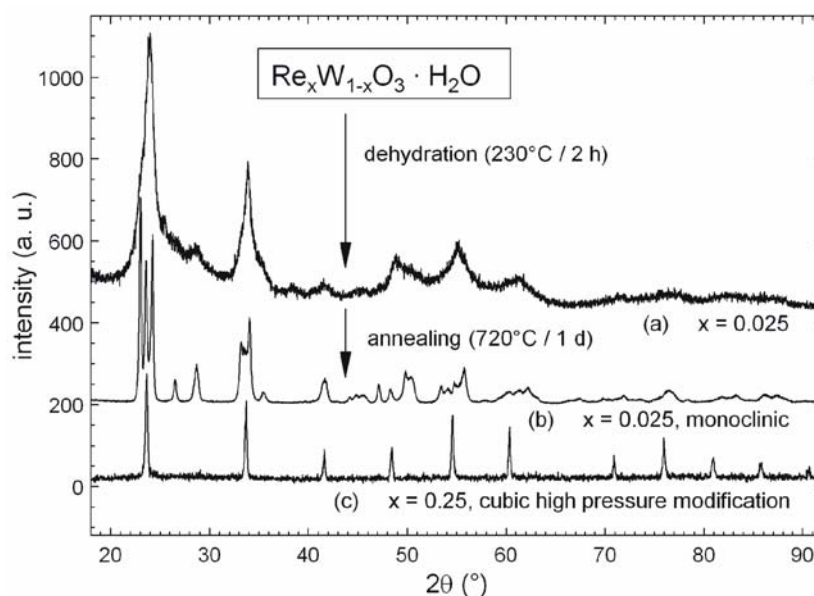


Figure 4.5-3: (a) X-ray powder diffraction pattern of dehydrated $\text{Re}_x\text{W}_{1-x}\text{O}_3 \cdot \text{H}_2\text{O}$ ($x = 0.025$) and (b) the annealed sample; (c) diffraction pattern of the cubic high-pressure modification of $\text{Re}_{0.25}\text{W}_{0.75}\text{O}_3$ [389].

As a result of these studies, a fast and simple *chimie douce* pathway to mixed Re/W trioxides has been opened as an alternative to ceramic routes. But it can also be concluded that doping concentrations greater than $x = 0.12$ as well as cubic phases of mixed Re/W trioxides still appear to remain a domain of high-pressure / high-temperature methods.

5 Prospects

Rare-Earth Borates

Due to the work of *Huppertz* and *Emme*, the field of rare-earth borates is a comparatively well investigated system under high-pressure / high-temperature conditions. The here introduced results concerning the synthesis and characterisation of the three new compounds δ - $RE(BO_2)_3$ ($RE = La, Ce$) and $Pr_4B_{10}O_{21}$ clearly reveal that the lower pressure range, which was neglected until then, is also a promising field for undiscovered new compounds. The field of existence seems to be very small, which can be seen at the *meta*-oxoborate examples, where three polymorphs exist in a small range of pressure. But exactly that is another chance for various new compounds, which are achievable through slight variations of the parameters pressure and temperature. The parameter pressure favours the formation of high-coordinated atoms and above 7 GPa we always observed $[BO_4]^{5-}$ tetrahedra as only remaining structural building unit. With the compound $Pr_4B_{10}O_{21}$ it was possible to synthesize an example, showing both structural building units, $[BO_3]^{3-}$ as well as $[BO_4]^{5-}$ groups, known in borates at a pressure of 3.5 GPa. Having two structural building units at one's disposal a much larger number of different compounds are possible to be formed. Therefore, also the lower pressure range is worth to be investigated much more intensively.

Furthermore, the extension of the experiments using metals from the transition metal groups led to various new compounds, as latest results of *Knyrim* reveal [392]. With the synthesis of β - NiB_2O_4 it was possible to realize a third compound exhibiting the rare structural feature of edge-sharing tetrahedra. But up till now, no NMR spectroscopic data concerning the chemical shift of ^{11}B atoms involved in the edge-linkages are known. For that reason, systematic enlargement into alkaline or alkaline-earth borates are planned.

Rare-Earth Germanates and Rare-Earth Borate Germanates

Initial high-pressure / high-temperature experiments to synthesize new compounds or high-pressure polymorphs quickly revealed that the commonly used experimental setup, especially concerning the BN crucible material, has to be changed. The reactivity of the crucible material and the rare-earth oxides was

higher than the reactivity with GeO_2 . Consequently, borate compounds were permanently detected in the powder patterns. The use of molybdenum or platinum capsules would find a remedy. But prospective high-pressure experiments in the field of germanates are promising due to the fact that germanium takes various different coordinations from tetrahedral to pyramidal or octahedral oxygen coordinations. Into the bargain, germanium is, as already mentioned in the general introduction, a highly compressible atom. This has been shown at the high-pressure synthesis of the $\text{RE}_2\text{Ge}_2\text{O}_7$ pyrochlore structures.

Furthermore, the field of rare-earth borate germanates is also very interesting, especially considering the various possibilities of building units ($[\text{BO}_3]^{3-}$, $[\text{BO}_4]^{5-}$, $[\text{GeO}_4]^{4-}$, $[\text{GeO}_5]^{6-}$, or $[\text{GeO}_6]^{8-}$ groups) and their different types of connection (via corners, edges, or faces). For that reason, this system is a good example to study the effects of high-pressure in the formation new compounds consisting of two or more different anionic building units. Interestingly, three-component systems from rare-earth oxides and two acid oxides like boron oxide and germanium oxide never form many ternary systems. High-pressure conditions could be the key to have synthetic access to these systems.

Gallium Oxonitrides

Nitride chemistry comprises an extensive field, and since the increasing interest in semiconducting materials with wide band gaps for industrial application, the research on nitrides and the anion-substituted oxonitrides focused on this class of materials that provides both, good optoelectronic and mechanical properties. In contrast to the well known phase diagram in the binary phase system Al_2O_3 and AlN there exist no systematic investigations on the respective phases in the system Ga_2O_3 and GaN . $\text{Ga}_{2.81}\text{O}_{3.57}\text{N}_{0.43}$ presented in this thesis was the first well-characterized crystalline gallium oxonitride phase after which *Soignard et al.* published a further crystalline phase prepared at high-pressures, showing that the competition in this new field has started.

After this preliminary experiments performed in this work, the area of research has been handed over to *S. Hering* who worked on this field during her diploma works and subsequent PhD thesis. Further goals of this project are the synthesis and characterization of new gallium oxonitrides under high-pressure / high-temperature conditions. This will be realized by different starting compositions, in which the starting mixtures and the elemental compositions of the starting precursors will be varied. That the choice of the correct precursor material is highly important was shown already in this thesis. An extension of the synthesis techniques, us-

ing laser heated diamond anvil cells to determine phase transitions and areas of stability, are planned. The systematic investigation of the stability fields of these new compounds should lead to a precise phase diagram, which does not exist until now. Also the synthesis and characterization of border phases like $\gamma\text{-Ga}_2\text{O}_3$ should not be neglected. In distance future, this systematic investigation can be expanded on the system $\text{InN}/\text{In}_2\text{O}_3$, entering a new high-density oxonitride system, in which no compounds exist until now. Following this way, unknown areas of stability with new crystal structures and material properties will be investigated.

Ternary intermetallic phases

The number of binary and ternary intermetallic compounds investigated under high-pressure conditions is of a manageable size. Systematic investigations at very high-pressures were carried out only occasionally. For the beginning of the project well investigated simple ternary 1:1:1 compounds of the *Pöttgen* group were selected for the following high-pressure experiments. During the last two years, many, mainly equiatomic stannides $RE\text{T}\text{Sn}$ were investigated. Besides the well investigated rare-earth platinum stannides, the corresponding Pd and Ni compounds were only synthesized for the rare-earth cations La and Ce. Especially CeNiSn is a promising compound, due to its possible mixed cerium valence state, resulting in interesting magnetic properties.

In the future, the experiments should be extended besides the stannides and germanides into the field of equiatomic silicides and the indium rich compounds $RE\text{T}\text{In}_2$. Within this series, the larger rare-earth compounds could be transformed well directed at high-pressure / high-temperature conditions into the structure types of the compounds consisting of the smaller rare-earth cations. In variation of the parameter pressure the fields of existence can be determined.

Besides the concrete investigation of the equiatomic phases, it is also possible to push the general phase analyses. A future aim could be the discovery of new compounds or substance classes of the general composition $RE_xT_y\text{Si}_z$, $RE_xT_y\text{Ge}_z$, or $RE_xT_y\text{Sn}_z$. Precursors for these experiments are available of the *Pöttgen* group.

Concerning the oxidation process of intermetallic phases under high-pressure conditions, the research is still at the beginning. With the compound $\text{Ce}_4\text{Ag}_3\text{Ge}_4\text{O}_{0.5}$ a new and very interesting new substance class has been developed. With lanthanum a corresponding representative was evident from the powder pattern. Further attempts to obtain single phase products of these compounds are of great interest, especially concerning subsequent reliable magnetic measurements. Furthermore,

the origin of the small oxygen amount remains unclear and additional experiments are necessary to clarify this question.

The exchange of Ag to Au in the Ce-T-Ge system resulted in a new compound of the composition $\text{Ce}_7\text{Au}_{13.34(2)}\text{Ge}_{9.66(2)}$ not known in the ternary phase diagram up to now. A lot of optimization in the precursor composition and the synthesis condition will be necessary to receive this compound as a pure compound. In addition to that, the main product during the synthesis of $\text{Ce}_7\text{Au}_{13.34(2)}\text{Ge}_{9.66(2)}$ is still unknown. In view of the large number of intermetallic phases at normal-pressure conditions and due to the fact that high-pressure investigations are still in its infancy, systematic research will produce a lot of interesting new compounds with maybe unusual properties or possible technical applications.

Further Cooperations

The financial support of the European Commission for the COST D30 program "Development of Materials Chemistry under High-Pressures" ends up in 2007 and a decision about a continuation period with new goals is still open.

The results presented in this thesis confirm the fruitful cooperations. Actually, two further projects concerning *(i)* Microstrain control of electronic phase separation in SrCrO_3 (submitted to *Nature Materials*) and *(ii)* Metamagnetism and metal-insulator transition of an Ir1212 cuprate obtained at high-pressure (in preparation), are in work.

6 Summary

6.1 Multianvil High-Pressure / High-Temperature Synthesis

The parameter pressure influences compounds, their atoms, and bonds as well as the synthesis procedures of materials in different ways. Pressure induced crystallisation but also pressure induced amorphisation has to be mentioned at this point. Therefore, the kinetics plays an important role, because, if the system under pressure has sufficient kinetics, a re-arrangement of the atoms resulting in a new high-pressure compound is possible. Generally, these structures are denser and often show higher coordination numbers than the starting compounds. A change in structure type can often be related to the compressibility of one kind of atoms of the compound or to the compressibility of the involved chemical bonds.

Technical facilities to apply high-pressures for materials chemistry has been developed and optimized during the last 50 years. Thereby, the octahedral multianvil technique represents the best combination of realizable pressures and sample size. Such a system was used for the following summarized experiments covering a broad field of different interesting chemical systems. These experiments, starting with rare-earth borates and rare-earth borate germanates, followed by gallium oxonitrides and phase transformations of ternary intermetallic phases under high-pressure conditions reflect the power and to some extent the creativity of the parameter pressure. The last part of this summary gives three further examples carried out in cooperation with other European groups dealing with perovskite solid solutions, high oxidized cuprates, and rhenium tungstates.

6.2 Rare-Earth Borates

α -Nd₂B₄O₉: (Chapter 4.1.3; page 45)

With the compound α -Nd₂B₄O₉, the new initial member of the former investigated series α -RE₂B₄O₉ (RE = Sm–Ho) characterized through edge-sharing [BO₄]⁵⁻ tetrahedra has been synthesized. Beside RE₄B₆O₁₅ (RE = Dy, Ho), this family of compounds is the second known example showing the rare structural feature of edge-linked [BO₄]⁵⁻ tetrahedra in borate crystal chemistry. Starting with a

stoichiometric mixture of $\text{Nd}(\text{OH})_3$ and B_2O_3 , the synthesis took place in an 18/11-assembly at 5.5 GPa and 950 °C. The structure was solved on the basis of single crystal data ($C2/c$, $Z = 20$, $a = 2570.8(5)$, $b = 440.30(9)$, $c = 2504.1(5)$ pm, $\beta = 99.82(3)^\circ$, $R1 = 0.0255$, $wR2 = 0.0550$ (all data)). The compound $\alpha\text{-Nd}_2\text{B}_4\text{O}_9$ is built up from corner as well as edge-sharing $[\text{BO}_4]^{5-}$ tetrahedra, resulting in a network structure. In Figure 6.2-1 the centro-symmetric fundamental building block (FBB) consisting of 18 corner-sharing and two edge-sharing tetrahedra is depicted. By connecting the FBB's via the single outer tetrahedra and the one tetrahedron of the five-membered ring, channels are formed in which the rare-earth atoms are positioned adopting coordinations from 8–11 oxygen atoms. MAPLE as well as Cycle-Class Spectra calculations confirmed the isotypy to the former investigated $\alpha\text{-RE}_2\text{B}_4\text{O}_9$ ($\text{RE} = \text{Sm-Ho}$) compounds.

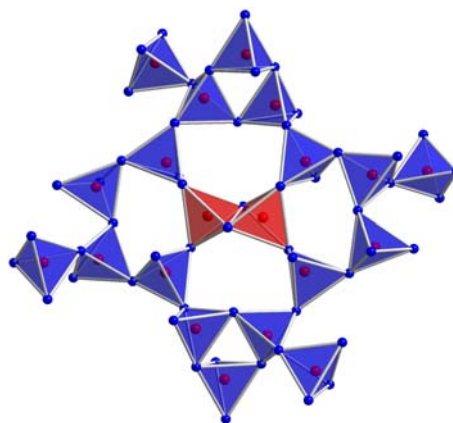


Figure 6.2-1: FBB of $\alpha\text{-Nd}_2\text{B}_4\text{O}_9$

$\beta\text{-Nd}(\text{BO}_2)_3$: (Chapter 4.1.4, page 54)

Polymorphism is a frequently observed phenomenon, especially among the rare-earth metal(III) *meta*-oxoborates. Four modifications α -, β -, γ -, and $\delta\text{-RE}(\text{BO}_2)_3$ are hitherto known as depending on the size of the rare-earth metal(III) cations and the synthetic conditions of pressure and temperature. During our investigations of the lower pressure range, the compound $\beta\text{-Nd}(\text{BO}_2)_3$ was synthesized at conditions of 3.5 GPa and 1050 °C. Single crystal structure analysis revealed isotypy to the already known rare-earth metal(III) *meta*-oxoborates $\beta\text{-RE}(\text{BO}_2)_3$ ($\text{RE} = \text{Sm-Lu}$, except Eu): $Pnma$, $Z = 16$, $a = 1618.2(4)$, $b = 748.71(9)$, $c = 1247.0(3)$ pm, $R1 = 0.0629$, $wR2 = 0.1023$ (all data). Higher pressures favour the formation of the denser γ modification. Due to the fact that $\beta\text{-RE}(\text{BO}_2)_3$ ($\text{RE} = \text{Tb, Dy}$) were synthesized at ambient pressure conditions and for the synthesis of the corresponding compounds with smaller rare-earth cations high-pressures were needed, it still remains unclear, if corresponding

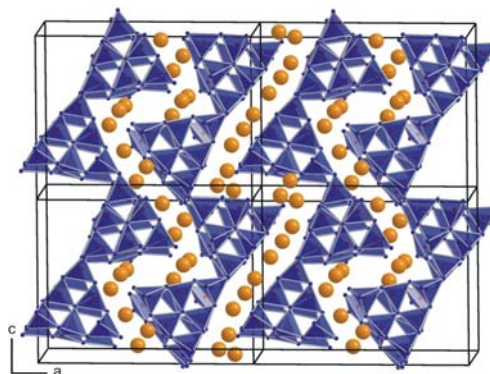


Figure 6.2-2: Crystal structure of the orthorhombic compound $\beta\text{-Nd}(\text{BO}_2)_3$; the rare-earth cations are shown as orange spheres. The $[\text{BO}_4]^{5-}$ tetrahedra are given in the polyhedral representation.

compounds with rare-earth atoms larger than Tb can be established at ambient pressures as well. The crystal structure of β -Nd(BO₂)₃ is built up from strongly corrugated layers of corner sharing [BO₄]⁵⁻ tetrahedra. 12 [BO₄]⁵⁻ tetrahedra are linked *via* common corners to one FBB of the B-O structure which results through interconnection of the FBB's in a layered structure (see Figure 6.2-2). Between the corrugated layers, the neodymium atoms are positioned.

δ -RE(BO₂)₃ (RE = La, Ce): (Chapter 4.1.5, page 60)

The new δ modification of lanthanum and cerium *meta*-oxoborate was discovered during our systematic investigations in the field of oxoborates, synthesized under moderate high-pressure conditions. δ -La(BO₂)₃ (\equiv δ -LaB₃O₆) and δ -Ce(BO₂)₃ (\equiv δ -CeB₃O₆) were obtained at high-pressure (RE = La: 5.5 GPa, RE = Ce: 3.5 GPa) and high-temperature (1050 °C both) conditions. The monoclinic compounds crystallize with four formula units in the space group *P*2₁/*c*, exhibiting lattice parameters of $a = 424.1(1)$, $b = 1171.2(2)$, $c = 731.1(2)$ pm, and $\beta = 91.2(1)^\circ$, $R1 = 0.025$, $wR2 = 0.038$ (all data) for the La representative and $a = 422.52(8)$, $b = 1169.7(2)$, $c = 725.2(2)$ pm, and $\beta = 91.33(3)^\circ$, $R1 = 0.0237$, $wR2 = 0.0445$ (all data) for the Ce compound, respectively. Due to the synthesis under high-pressure conditions, the structure exhibits exclusively [BO₄]⁵⁻ tetrahedra, which are connected *via* common corners (see Figure 6.2-3). Additionally, 1/6 of the oxygen atoms are bridging three boron atoms (O^[3]), leading to a network structure with ten-membered rings of [BO₄]⁵⁻ tetrahedra ($d(\text{B-O}) = 143\text{--}155$ pm), in which the RE³⁺ ions are coordinated by twelve oxygen atoms ($d(\text{La-O}) = 245\text{--}332$ pm, $d(\text{Ce-O}) = 243\text{--}333$ pm). Next to a discussion of the structure, infrared and temperature-dependent X-ray powder diffraction data were presented.

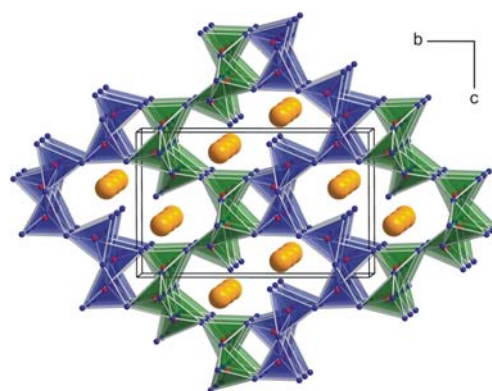


Figure 6.2-3: Crystal Structure of δ -RE(BO₂)₃ (RE = La, Ce), view along [100]; the rare-earth cations are shown as orange spheres. The [BO₄]⁵⁻ tetrahedra are given in the polyhedral representation.

Pr₄B₁₀O₂₁: (Chapter 4.1.6, page 73)

High-pressure chemistry at conditions of 3.5 GPa and 1050 °C led to the synthesis of the rare-earth borate Pr₄B₁₀O₂₁, whereas the larger rare-earth representatives La and Ce reacted at the same conditions to the just described δ -*meta*-oxoborate modification. With the synthesis of Pr₄B₁₀O₂₁, it was possible to add a new composition to the field of rare-earth oxoborates. The tetra-praseodymium(III)-

decaborate crystallizes monoclinically with four formula units in the space group $P2_1/n$ and lattice parameters of $a = 710.2(2)$, $b = 1948.8(4)$, $c = 951.6(2)$ pm, and $\beta = 93.27(3)^\circ$, $R1 = 0.0302$, $wR2 = 0.0558$ (all data). The boron–oxygen network (see Figure 6.2-1) consists of $[\text{BO}_4]^{5-}$ tetrahedra and $[\text{BO}_3]^{3-}$ groups; however, the $[\text{BO}_4]^{5-}$ groups represent the major part (80%) due to the high-pressure conditions during the synthesis. The praseodymium ions are coordinated by 10 and 12 oxygen atoms. Along with a detailed description of the crystal structure, temperature-programmed X-ray powder diffraction data are shown, demonstrating the metastable character of this compound. IR spectroscopy was used to confirm the existence of $[\text{BO}_3]^{3-}$ groups as well as $[\text{BO}_4]^{5-}$ groups in this structure.

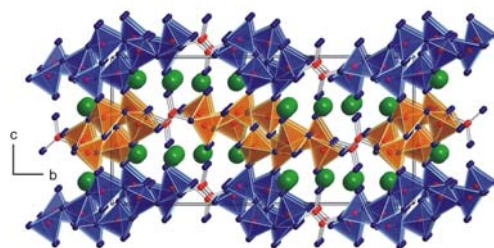


Figure 6.2-1: Crystal structure of $\text{Pr}_4\text{B}_{10}\text{O}_{21}$, view along $[100]$. The Pr cations are shown as green spheres, B as red spheres, and O as blue spheres.

6.3 Rare-Earth Borate Germanate

$\text{Ce}_6(\text{BO}_4)_2\text{Ge}_9\text{O}_{22}$: (Chapter 4.2.3, page 90)

The new monoclinic cerium borogermanate $\text{Ce}_6(\text{BO}_4)_2\text{Ge}_9\text{O}_{22}$ was synthesized under high-pressure and high-temperature conditions at 10.5 GPa and 1200 °C. Suitable single crystals were derived from flux synthesis in melted lead obtained through thermal decomposition of PbO. $\text{Ce}_6(\text{BO}_4)_2\text{Ge}_9\text{O}_{22}$ crystallizes with two formula units in the space group $P2_1/n$ with lattice parameters $a = 877.0(2)$, $b = 1079.4(2)$, $c = 1079.1(2)$ pm, and $\beta = 95.94(3)^\circ$, $R1 = 0.0584$, $wR2 = 0.0967$ (all data). As the parameter pressure favours the formation of compounds with cations possessing high coordination numbers, it was possible to produce simultaneously $[\text{BO}_4]^{5-}$ tetrahedra and $[\text{GeO}_6]^{8-}$ octahedra in one and the same borogermanate for the first time. The crystal structure is built up from corner- and edge-sharing $[\text{GeO}_6]^{8-}$ octahedra and $[\text{BO}_4]^{5-}$ tetrahedra forming corrugated layers which are interconnected by $[\text{BO}_4]^{5-}$ tetrahedra (see Figure 6.3-2). Furthermore, the cerium atoms,

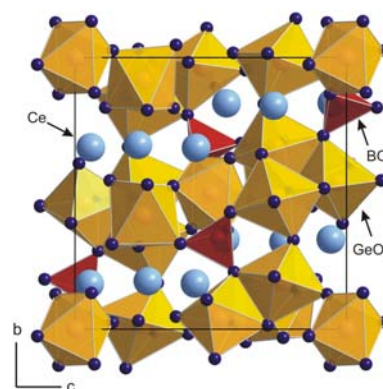


Figure 6.3-2: Crystal structure of $\text{Ce}_6(\text{BO}_4)_2\text{Ge}_9\text{O}_{22}$, view along $[100]$. The cerium cations are shown as light blue spheres and the oxygen atoms as dark blue spheres. The $[\text{GeO}_6]^{8-}$ octahedra and $[\text{BO}_4]^{5-}$ tetrahedra are given in the polyhedral representation.

which fill the remaining voids inside the polyhedral arrangement, show high coordination numbers (C.N.: 9 and 11). One oxygen site bridges one boron and two germanium atoms ($O^{[3]}$), which is observed here for the first time. Besides a structural discussion, temperature-dependent X-ray powder diffraction data were presented, demonstrating the metastable character of this high-pressure phase.

6.4 Gallium Oxonitrides

$Ga_{2.81}O_{3.57}N_{0.43}$: (Chapter 4.3.2, page 102)

Former investigations in the field of GaN-Ga₂O₃ ceramics suffered on low degrees of crystallinity. With the synthesis of Ga_{2.81}O_{3.57}N_{0.43}, it was possible to realize a characterizable, highly crystalline phase of the solid solution between the binary compounds GaN and Ga₂O₃ for the first time. The new compound Ga_{2.81}O_{3.57}N_{0.43} was crystallized under high-pressure / high-temperature conditions in a *spinel* type structure from a prestructured GaON ceramic, which was obtained from a single-source molecular precursor with the nominal chemical formula [Ga(O^tBu)₂NMe₂]₂ by thermal treatment in ammonia atmosphere. The optimized precursor-derived GaON ceramic stays nanocrystalline up to 600 °C and can be transformed at 7 GPa and 1100 °C into the crystalline phase Ga_{2.81}O_{3.57}N_{0.43}. Selected-area electron diffraction (SAED) patterns indicated a cubic face centered cell. Extinctions owing to a *d*-glide plane perpendicular to the 4-fold axis indicated space group *Fd3m* leading to a *spinel* type structure. On the basis of these results the crystal structure was refined on powder data: *Fd3m*, *Z* = 8, *a* = 826.4(1) pm. The structure, homogeneity, and nitrogen to oxygen ratio were determined using TEM coupled with an electron energy loss spectrometer (EELS) and an energy dispersive X-ray (EDX) spectrometer. The quantitative analysis of the two characteristic edges for nitrogen and oxygen resulted in a mean atomic ration of 0.12(2) (see Figure 6.4-1). These first experiments laid the foundation for a new DFG project actually continued by Dipl.-Chem. Stefanie Hering during her PhD thesis.

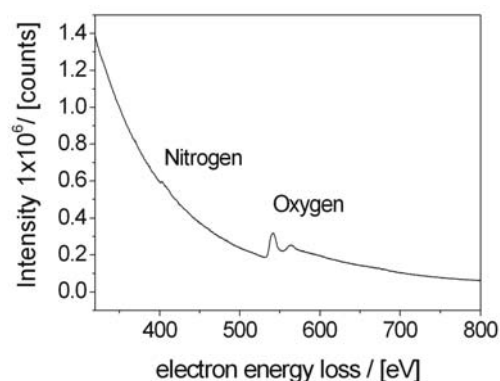


Figure 6.4-1: Electron energy loss spectroscopy performed on a spinel GaON crystal during TEM analysis.

6.5 Ternary Rare-Earth Transition Metal Stannides

RETSn ($RE = La-Nd, Sm; T = Pt$): (Chapter 4.4.3, page 114)

The NP-*RETSn* ($RE = La-Nd, Sm; T = Pt$) stannides crystallize with the orthorhombic *TiNiSi* type structure, while those with the smaller rare-earth elements adopt the hexagonal *ZrNiAl* type. Gadolinium and the following smaller rare-earth elements are most likely too small for a *TiNiSi* like structural arrangement under normal-pressure conditions. This change in crystal structure seems to be driven by the size of the rare-earth elements (lanthanoide contraction). In this work, it was possible to stabilize the *ZrNiAl* type structure for the rare-earth atoms larger than Gd with the help of the parameter pressure (9.2 to 13.5 GPa and 1000–1400 °C). This change in structure type is a reconstructive phase transition and the high-pressure samples can easily be quenched and characterized under ambient pressure conditions. All compounds, normal-pressure as well as high-pressure phases were investigated on the basis of single crystal data: e.g. NP-CePtSn: *Pnma*, $Z = 4$, $a = 746.89(9)$, $b = 462.88(4)$, $c = 801.93(7)$ pm, $R1 = 0.0249$, $wR2 = 0.0487$ (all data); HP-CePtSn: *P62m*, $Z = 3$, $a = 756.919(5)$, $c = 415.166(4)$ pm, $R1 = 0.0423$, $wR2 = 0.0546$ (all data). That these phases are in fact metastable high-pressure compounds could be shown properly with temperature-programmed *in-situ* X-ray diffractometry. Between 500–900 °C, the high-pressure phases fully transformed back into the normal-pressure modification. The different rare-earth coordination is the main reason for the differing magnetic properties of both modifications. Magnetic properties were measured for the three high-pressure phases HP-CePtSn, HP-PrPtSn, and HP-NdPtSn. All three stannides show trivalent rare-earth cations over the whole temperature range (2–300 K). The experimental magnetic moments are close to the values for the free RE^{3+} cations. Latest results of HP-CePtSn exhibited a magnetic ordering at a temperature of 2.11 K and for HP-PrPtSn only short range magnetic ordering below 10 K was observable. For HP-NdPtSn spin-glass behavior was detected at temperatures below the freezing temperature of 4.5 K.

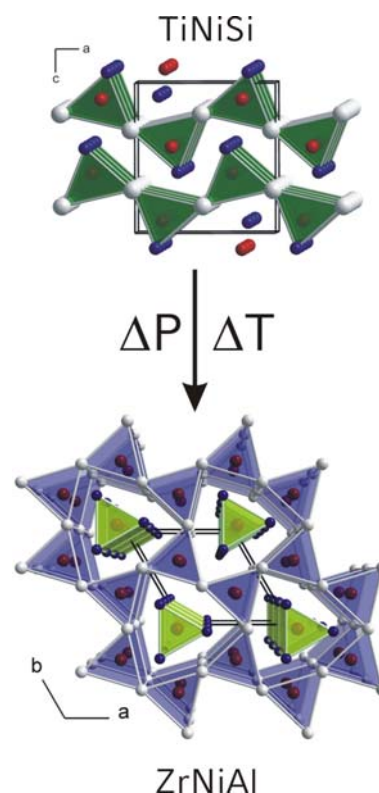


Figure 6.5-1: *TiNiSi* type transformation into *ZrNiAl* type under HP/HT conditions.

RETSn (RE = La, Ce; T = Pd): (Chapter 4.4.4, page 145)

With palladium as transition metal compound, the corresponding change in structure type at ambient pressure conditions (TiNiSi \rightarrow ZrNiAl) takes place with holmium, which can also adopt the TiNiSi type as well as the ZrNiAl type structure. For the two largest representatives lanthanum and cerium, an analogue structural transformation from TiNiSi \rightarrow ZrNiAl type at pressures of 10.5 GPa and 1100 °C was observed. Single crystal structure analysis confirmed the isotypy to the HP-REPtSn stannides: e.g. NP-CePdSn: *Pnma*, $Z = 4$, $a = 754.1(2)$, $b = 470.6(1)$, $c = 798.4(3)$ pm, $R1 = 0.0575$, $wR2 = 0.0336$ (all data); HP-CePtSn: *P62m*, $Z = 3$, $a = 760.03(5)$, $c = 416.06(3)$ pm, $R1 = 0.0189$, $wR2 = 0.0443$ (all data). HP-CePdSn shows anti-ferromagnetic ordering at temperatures lower than the Néel-temperature of 5 K. The high-temperature behaviour of LaPdSn and CePdSn is non-uniform.

RETSn (RE = La, Ce, Sm; T = Ni): (Chapter 4.4.5, page 156)

For the isotypic series of *RENiSn* compounds representatives with each rare-earth except Pm are known, crystallizing in the orthorhombic TiNiSi type structure at ambient pressure conditions. At high-pressure conditions (7.5 to 10.5 GPa, 1150 °C) the expected transformation into the ZrNiAl type was observed for CeNiSn and SmNiSn. Whereas HP-CeNiSn still contains an impurity of the normal-pressure modification, the transformation of SmNiSn succeeded in a pure sample. Due to the less availability of suitable single crystals, a detailed characterization of these phases was not possible until now. The lanthanum compound showed a different behaviour and mainly transformed into LaNi₂Sn₂. Nevertheless, further investigations on these compounds are still going on because of their interesting magnetic properties.

RETSn ($RE = Er; T = Ag$): (Chapter 4.4.6, page 160)

The NdPtSb type structure is a second AlB_2 related structure type and the knowledge gained from previous experiments in the TiNiSi \rightarrow ZrNiAl system were tried to adapt into this new system. In the *REAgSn* stannides, the structural transformation occurs between the erbium and the thulium compound with a switch from the NdPtSb to the ZrNiAl type (see Figure 6.5-2). The investigations showed that ErAgSn forms a ZrNiAl type high-pressure modification at pressures of 11.5 GPa and 1150 °C. Crystallographic data were derived from single crystal structure determination: NP-ErAgSn: $P6_3mc$, $Z = 2$, $a = 466.3(1)$, $c = 729.0(2)$ pm, $R1 = 0.0233$, $wR2 = 0.0439$ (all data); HP-ErAgSn: $P62m$, $Z = 3$, $a = 728.7(2)$, $c = 445.6(1)$ pm, $R1 = 0.0192$, $wR2 = 0.0397$ (all data). Interestingly, the TmAgSn compound (ZrNiAl type) transforms in a NdPtSb analogue metastable high-temperature form when rapidly quenched at ambient pressure conditions.

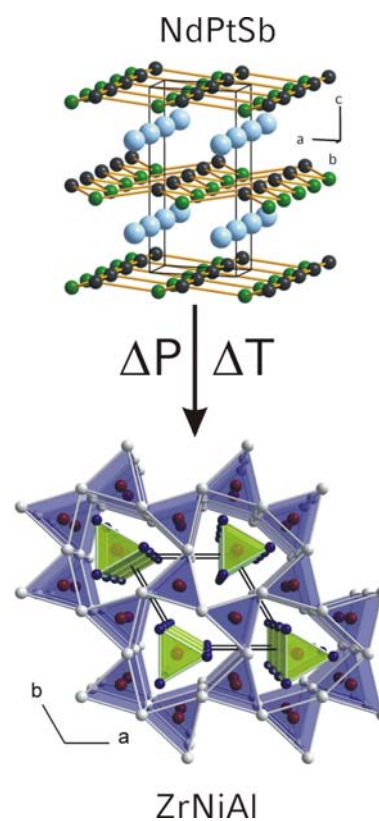


Figure 6.5-2: NdPtSb type transformation into ZrNiAl type under HP/HT conditions.

6.6 Ternary Rare-Earth Transition Metal Germanides

RE₄Ag₃Ge₄O_{0.5} ($RE = La, Ce$): (Chapter 4.4.8.2, page 172)

Experiments with the NdPtSb type Ce:Ag:Ge = 1:1:1 precursor at pressures of 11.5 GPa and temperatures of 1300 °C resulted in a surprising new compound of the composition Ce₄Ag₃Ge₄O_{0.5}. Here, for the first time a partial oxidation of an intermetallic phase under high-pressure / high-temperature conditions was observed. The oxygen atoms first appeared during the structural refinement and were confirmed in the following by an IR/thermal conductivity detection. The crystal structure ($Pnma$, $Z = 4$, $a = 2087.3(4)$, $b = 439.9(1)$, $c = 1113.8(2)$ pm, $R1 = 0.0470$, $wR2 = 0.0467$ (all data)) is built up of a three-dimensional [CeAg₃Ge₄] network which has structural building units, well known from various rare-earth transition metal silicides and germanides. Embedded into this intermetallic matrix is the oxi-

dic part of the structure, which consists of corner-linked $[\text{OCe}_2\text{Ce}_{2/2}]$ tetrahedra chains running along the b axis (see Figure 6.6-1). The tetrahedral oxygen site is half occupied and the oxygen atoms are statistically distributed. Another structural feature are Ge_2 dumb-bells with a Ge1–Ge2 distance of 251 pm, a little longer than in elemental germanium (245 pm). DFT band structure calculations resulted in metallic properties and in a magnetic ground state, compatible with one unpaired $4f$ electron per cerium in good agreement with the experimental data. The COHP analysis revealed that $\text{Ce}_4\text{Ag}_3\text{Ge}_4\text{O}_{0.5}$ is close to a valence compound and the bond strengths are given in the sequence $\text{Ge–Ge} > \text{Ce–O} > \text{Ag–Ge}$. Thus, the strong Ce–O bonds within the $[\text{OCe}_2\text{Ce}_{2/2}]$ tetrahedra are very important for the stability of the structure. Analysis of the powder pattern of the corresponding lanthanum compound revealed isotypism but up till now, no single crystal data are available to confirm this assumption.

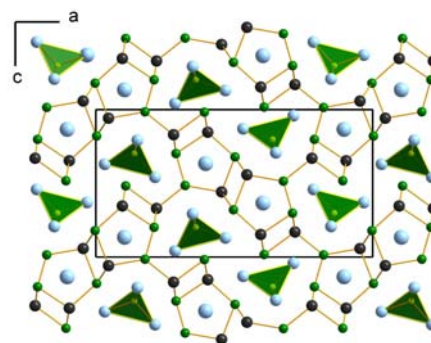


Figure 6.6-1: Projection of the $\text{Ce}_4\text{Ag}_3\text{Ge}_4\text{O}_{0.5}$ structure onto the ac plane.

$\text{Ce}_3\text{Ag}_4\text{Ge}_4$: (Chapter 4.4.8.8, page 182)

This compound was first identified as a steady byproduct during the synthesis of $\text{Ce}_4\text{Ag}_3\text{Ge}_4\text{O}_{0.5}$. A modification of the synthetic conditions (11.5 GPa, 1300 °C) and the CeAgGe precursor, which was inserted as ball milled powder, now resulted in a X-ray pure sample of $\text{Ce}_3\text{Ag}_4\text{Ge}_4$. Here, for the first time single crystal data of this compound were presented: $Immm$, $Z = 2$, $a = 1482.19(9)$, $b = 714.08(4)$, $c = 447.02(3)$ pm, $R1 = 0.0236$, $wR2 = 0.0443$ (all data). The crystal structure of $\text{Ce}_3\text{Ag}_4\text{Ge}_4$ is built up from a three-dimensional $[\text{Ag}_4\text{Ge}_4]$ network, which contains structural building units well known in intermetallic compounds. A structural comparison with the oxygen containing phase $\text{Ce}_4\text{Ag}_3\text{Ge}_4\text{O}_{0.5}$ shows certain similarities. Within this network, strong Ag–Ag contacts (276 pm Ag–Ag) shorter than the Ag–Ag distance in fcc silver (289 pm) and Ge_2 dumb-bells with a Ge2–Ge2 distance of 257 pm (little longer than in elemental germanium (245 pm) and in $\text{Ce}_4\text{Ag}_3\text{Ge}_4\text{O}_{0.5}$ (251 pm)) are observed.

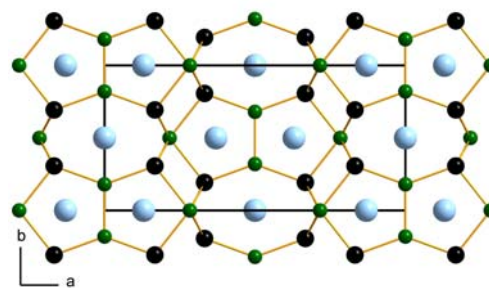


Figure 6.6-2: Projection of the $\text{Ce}_3\text{Ag}_4\text{Ge}_4$ structure onto the ab plane.

$Ce_7Au_{13.34(2)}Ge_{9.66(2)}$: (Chapter 4.4.9, page 190)

In ternary gold(I) germanides a lot of polyanionic networks with comparable structural building units as also found in silver(I) germanides are known. First experiments with CeAuGe (NdPtSb type structure) were carried out at 9.5 GPa and 1200–1250 °C resulting in a new ternary phase in the system Ce-Au-Ge. The compound $Ce_7Au_{13.34(2)}Ge_{9.66(2)}$ was isolated as a minor phase and the crystal structure was refined on the basis of single crystal data: *Pbam*, *Z* = 2, *a* = 1571.9(3), *b* = 1780.3(4), *c* = 443.58(9) pm, *R*1 = 0.0270, *wR*2 = 0.0470 (all data). Two sites show mixed occupation with mainly germanium placed on this positions (Ge1/Au10: 97.2(3)%/2.8(3)%; Ge5/Au9: 85.7(4)%/14.3(4)%). A striking structural feature is a gold-germanium cluster (see Figure 6.6-3) consisting of two edge-linked pentagonal prisms with capped faces and edges. In the centre of this cluster, two cerium atoms are located. Another remarkable building unit is a string of gold rhombs proceeding along the *c* axis with Au–Au distances (285 pm) comparable to elemental gold (288 pm). Such a string of connected rhombs is already known from a few other intermetallic compounds for example $Y_4Ni_1In_{20}$ exhibiting strings of Ni rhombs. Although, diamond anvil cell high-pressure experiments have already been performed in the system Ce-Au-Ge, the combination of high-pressures and high-temperatures can lead to remarkable new results.

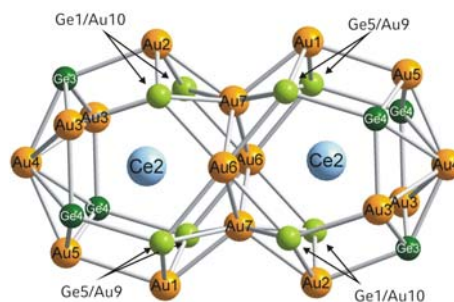


Figure 6.6-3: Cluster unit of $Ce_7Au_{13.34(2)}Ge_{9.66(2)}$

6.7 Further Cooperations

Due to the fact that our working group is embedded into an European COST project (Cooperation in the Field of Scientific and Technical Research), a lot of experiments were performed in cooperation with other groups treating various interesting questions concerning the effect of high-pressures in materials chemistry.

Demazeau et al. developed a new precursor for the synthesis of high oxidized lanthanum cuprates of the composition $LaCuO_3$ with a rhombohedral perovskite structure. This new preparation process at 11.5 GPa and $900\text{ °C} < T < 950\text{ °C}$ allows a ^{57}Fe doping of the sample for subsequent Mössbauer measurements.

In cooperation with *Attfield et al.* solid solutions of the perovskite system $SrRu_{1-x}Cr_xO_3$ were performed. Three distinct electronic regimes are found. Low Cr-

doped materials ($x < 0.3$) are itinerant-electron ferromagnets with an orthorhombic $Pbnm$ perovskite superstructure, as in SrRuO_3 , and show an enhancement of T_C from 160 to 190 K due to an additional $\text{Cr}^{3+}/\text{Cr}^{4+}$ double exchange. An insulation region is found for $0.3 < x < 0.7$ in which both the rhombohedral and cubic phases occur. Antiferromagnetic G -type ordering with a high Néel temperature ~ 400 K is found for the rhombohedral $x = 0.4$ phase. $0.7 < x < 1$ samples are cubic and Pauli paramagnetic, as typified by SrCrO_3 .

As a result of the studies of mixed Re/W trioxides in cooperation with *Scherer et al.* a fast and simple *chimie douce* pathway has been opened as an alternative to ceramic routes. But it can also be concluded that doping concentrations greater than $x = 0.12$ as well as cubic phases of mixed Re/W trioxides still appear to remain a domain of high-pressure / high-temperature methods.

7 Appendix

7.1 List of Abbreviations

$\bar{}$	Average	ICSD	Inorganic Crystal Structure Database
\sim	Circa	IR	Infrared
$^{\circ}$	Degree	J	Joule
$^{\circ}\text{C}$	Degree Celsius	K	Kelvin
χ	Susceptibility	M	Magnetization
λ	Wave length	M_{IRM}	Isothermal Relaxation Magnetization
μ_B	Effective Bohr magneton	min	Minute
μm	Micrometer	mg	Milligrams
ρ	Density	mm	Millimeter
σ	Standard deviation	NP	Normal-Pressure
\AA	Ångström	Oe	Oersted
atm.	atmosphere	Pa	Pascal
CCD	Charge Coupled Device	pm	Picometer
cm^{-1}	Wavenumber	PPMS	Physical Property Measurement System
CN	Coordination Number	PTFE	Polytetrafluorethylene
COHP	Crystal Orbital Hamilton Population	R_C	Rockwell hardness
C_P	Heat capacity	RE	Rare-Earth
CW	Curie-Weiss	RT	Room Temperature
d	Distance	sec	Second
DAC	Diamond Anvil Cell	sof	Site occupation factor
EDX	Energy Dispersive Analysis of X-ray	t	Tons
<i>et al.</i>	Et alii	T	Tesla
eq.	Equation	T	Temperature
eV	Electron Volt	TEM	Transmission Electron Microscope
FBB	Fundamental Building Block	T_C	Critical Temperature
FC	Field Cooled	T_F	Freezing Temperature
GooF	Goodness of Fit	T_N	Néel Temperature
H	Field	V	Volume
HP	High-Pressure	Z	Formula units
HT	High-Temperature	ZFC	Zero Field Cooled

7.2 Publications

The majority of the in this thesis presented results are already published in scientific papers or on poster presentations for conferences. A list of all published papers of this PhD thesis is given in the following.

7.2.1 Conference contributions

- (1) G. Heymann, H. Huppertz, *Multianvil High-Pressure / High-Temperature Synthesis, Structure, and Characterization of a new Sodium Rare-Earth Oxoborate $\text{Na}_3\text{Dy}_2(\text{BO}_3)_3$* , NRW Graduate School of Chemistry - University of Münster, 25. - 27.08.2004.
- (2) G. Heymann, H. Huppertz, *$\text{Ce}_6(\text{BO}_4)_2\text{Ge}_9\text{O}_{22}$: Ein neues Hochdruck-Borat-Germanat als Bindeglied zwischen Seltenerd Boraten und Germanaten*, Joint Conference of Deutsche Gesellschaft für Kristallographie, Deutsche Gesellschaft für Kristallwachstum und Kristallzüchtung und Nationalkomitee für Kristallographie der Österreichischen Akademie der Wissenschaften, Köln, 28.02. – 04.03.2005.
- (3) G. Heymann, T. Soltner, A. Haberer, H. Huppertz, *$\delta\text{-RE}(\text{BO}_2)_3$ ($\equiv \delta\text{-REB}_3\text{O}_6$, $\text{RE} = \text{La}, \text{Ce}$): Eine 4. Modifikation der Selten-Erd meta-Oxoborate*, 14. Jahrestagung der Deutschen Gesellschaft für Kristallographie, Freiburg, 03. – 06.04.2006.
- (4) J. F. Riecken, G. Heymann, R. Pöttgen, H. Huppertz, *High Pressure Phasetransformation of the Stannides RETSn ($\text{RE} = \text{La-Nd}$, $\text{T} = \text{Ni}, \text{Pd}, \text{Pt}$)*, 14. Jahrestagung der Deutschen Gesellschaft für Kristallographie, Freiburg, 03. – 06.04.2006.
- (5) J. F. Riecken, G. Heymann, R. Pöttgen, H. Huppertz, *High Pressure Phasetransformation of the Stannides RETSn ($\text{RE} = \text{La-Nd}$, $\text{T} = \text{Ni}, \text{Pd}, \text{Pt}$)*, 44th European High-Pressure Research Group Conference, Prague, 04. – 08.09.2006.

7.2.2 Papers

- (1) *High-pressure syntheses and crystal structures of $\beta\text{-RE}(\text{BO}_2)_3$ ($\text{RE} = \text{Nd}, \text{Sm}, \text{Gd}$)*
H. Emme, G. Heymann, A. Haberer, H. Huppertz, *Z. Naturforsch.* 62b (2007) 765.

- (2) δ -La(BO₂)₃ (\equiv δ -LaB₃O₆): A new high-pressure modification of lanthanum meta-oxoborate
G. Heymann, T. Soltner, H. Huppertz, *Solid State Sci.* 8 (2006) 821.
- (3) High-pressure Synthesis, Crystal Structure, and Properties of δ -Ce(BO₂)₃
A. Haberer, G. Heymann, H. Huppertz, *Z. Naturforsch.* 62b (2007) 759.
- (4) Pr₄B₁₀O₂₁: A new composition of rare-earth borates by high-pressure / high-temperature synthesis
A. Haberer, G. Heymann, H. Huppertz, *J. Solid State Chem.* 180 (2007) 1595.
- (5) Hochdrucksynthese und Kristallstruktur des neuen Borates Pr₄B₁₀O₂₁
A. Haberer, G. Heymann, H. Huppertz, *Z. Anorg. Allg. Chem.* 632 (2006) 2079.
- (6) Multianvil High-Pressure / High-Temperature Synthesis, Crystal Structure, and Thermal Behaviour of the Rare-Earth Borogermanate Ce₆(BO₄)₂Ge₉O₂₂
G. Heymann, H. Huppertz, *J. Solid State Chem.* 179 (2005) 393.
- (7) High-Pressure Synthesis of a Gallium Oxonitride with a Spinel-Type Structure
I. Kinski, G. Miehe, G. Heymann, R. Theissmann, R. Riedel, H. Huppertz, *Z. Naturforsch.* 60b (2005) 831.
- (8) The High-Pressure Modification of CePtSn - Synthesis, Structure, and Magnetic Properties
J. F. Riecken, G. Heymann, T. Soltner, R.-D. Hoffmann, H. Huppertz, D. Johrendt, R. Pöttgen, *Z. Naturforsch.* 60b (2005) 821.
- (9) Synthesis, Structure, and Properties of the High-Pressure Modifications of the Ternary Compounds REPtSn (RE = La, Pr, Sm)
J. F. Riecken, U. Ch. Rodewald, G. Heymann, S. Rayaprol, H. Huppertz, R.-D. Hoffmann, R. Pöttgen, *Z. Naturforsch.* 61b (2006) 1477.
- (10) Spin glass anomalies in HP-NdPtSn - structural, magnetic, and specific heat studies
G. Heymann, S. Rayaprol, J. F. Riecken, R.-D. Hoffmann, U. Ch. Rodewald, H. Huppertz, R. Pöttgen, *Solid State Sci.* 8 (2006) 1258.
- (11) The High-Temperature Phases HT-YPtSn, HT-GdPtSn, and HT-TbPtSn
J. F. Riecken, G. Heymann, H. Huppertz, R. Pöttgen, *Z. Anorg. Allg. Chem.* 633 (2007) 633.
- (12) Synthesis, Structure, and Properties of the High-Pressure Modification of CePdSn – a 5 K Antiferromagnet
G. Heymann, J. F. Riecken, S. Rayaprol, S. Christian, R. Pöttgen, H. Huppertz, *Z. Anorg. Allg. Chem.* 633 (2007) 77.
- (13) Dimorphic ErAgSn and TmAgSn – High-Pressure and High-Temperature Driven Phase Transitions

- C. P. Sebastian, G. Heymann, B. Heying, U. Ch. Rodewald, H. Huppertz, R. Pöttgen, *Z. Anorg. Allg. Chem.* in press.
- (14) *A novel preparation process for LaCuO₃ involving a high pressure oxidation of precursor derived from the perovskite structure: An appropriate route for doping with ⁵⁷Fe Mössbauer probe*
G. Demazeau, A. Baranov, G. Heymann, H. Huppertz, A. Sobolev, I. Presniakov, *Solid State Sci.* 9 (2007) 376.
- (15) *Charge transfer and antiferromagnetic insulator phase in SrRu_{1-x}Cr_xO₃ perovskites: Solid solutions between two itinerant electron oxides*
A. J. Williams, A. Gillies, J. P. Attfield, G. Heymann, H. Huppertz, M. J. Martínez-Lope, and J. A. Alonso, *Phys. Rev. B* 73 (2006) 104409.
- (16) *An organometallic chimie douce approach to new Re_xW_{1-x}O₃ phases*
C. Helbig, R. Herrmann, F. Mayr, E.-W. Scheidt, K. Tröster, J. Hanss, H.-A. Krug von Nidda, G. Heymann, H. Huppertz, W. Scherer, *Chem. Comm.* (2005) 4071.

7.3 CSD-Numbers

Further details of the crystal structure investigations may be obtained from the Fachinformationszentrum Karlsruhe, 76344 Eggenstein-Leopoldshafen, Germany (fax: (+49)7247-808-666; e-mail: crysdata@fiz-karlsruhe.de), on quoting the depository number:

• β -Nd(BO ₂) ₃	CSD-417645	• NP-NdPtSn	CSD-415953
• δ -La(BO ₂) ₃	CSD-415962	• HP-NdPtSn	CSD-415952
• δ -Ce(BO ₂) ₃	CSD-417721	• NP-SmPtSn	CSD-416897
• Pr ₄ B ₁₀ O ₂₁	CSD-417553	• HP-SmPtSn	CSD-416899
• Ce ₆ (BO ₄) ₂ Ge ₉ O ₂₂	CSD-391342	• NP-CePdSn	CSD-416970
• NP-LaPtSn	CSD-416896	• HP-CePdSn	CSD-417969
• HP-LaPtSn	CSD-416901	• NP-ErAgSn	CSD-417552
• NP-CePtSn	CSD-415491	• HP-ErAgSn	CSD-417551
• HP-CePtSn	CSD-415492	• Ce ₄ Ag ₃ Ge ₄ O _{0.5}	CSD-417492
• NP-PrPtSn	CSD-416898	• Ce ₃ Ag ₄ Ge ₄	CSD-417491
• HP-PrPtSn	CSD-416900		

7.4 Curriculum Vitae

Personal Details

10/17/1977 Born in Wolfratshausen / Bavaria, Germany, as first child of Wolf-Dietrich Heymann and Elisa Heymann, nee Rutten.
Citizenship: German
Marital status: unmarried

Education

1984 – 1988 Primary school education at the Isardamm Grundschule, Geretsried

1988 – 1997 High-School education at the Adalbert-Stifter Gymnasium, Geretsried

1997 Abitur

Aug. 1997 – Sept. 1998 Non-military service for conscientious objector at the Malteser Hilfsdienst, Wolfratshausen

Nov. 1998 – 2000 Undergraduate studies in Chemistry at the Ludwig-Maximilians-Universität, München

Nov. 2000 Preliminary Diploma

2000 – 2003 Graduate studies in Chemistry at the Ludwig-Maximilians-Universität, München

Jul. 2003 – Jan. 2004 Diploma thesis in the group of PD Dr. H. Huppertz at the Ludwig-Maximilians-Universität, München, entitled *“Hochdruck-/Hochtemperatur-Synthese, Struktur und Charakterisierung des neuen Oxoborates $\text{Na}_3\text{Dy}_2(\text{BO}_3)_3$ ”*

since Feb. 2004 Research assistant in the group of PD Dr. H. Huppertz at the Ludwig-Maximilians-Universität, München;
PhD thesis in inorganic solid-state chemistry, entitled *“Synthetic Investigations in Borates, Borate Germanates, Gallium Oxonitrides, and Intermetallic Phases at Extreme Conditions”*

7.5 References

- [1] P. F. McMillan, *Chem. Soc. Rev.* 35 (2006) 855.
- [2] M. Eremets, *High Pressure Experimental Methods*, Oxford University Press, Oxford (1996).
- [3] S. T. Weir, A. C. Mitchell, W. J. Nellis, *Phys. Rev. Lett.* 76 (1996) 1860.
- [4] H. Huppertz, *Z. Kristallogr.* 219 (2004) 330.
- [5] G. Demazeau, H. Huppertz, J. A. Alonso, R. Pöttgen, E. Moran, J. P. Attfield, *Z. Naturforsch.* 61b (2006) 1457.
- [6] F. Karau, W. Schnick, *Angew. Chem.* 118 (2006) 4617; *Angew. Chem. Int. Ed. Engl.* 632 (2006) 2093.
- [7] K. Landskron, H. Huppertz, J. Senker, W. Schnick, *Angew. Chem* 113 (2001) 2713; *Angew. Chem. Int. Ed. Engl.* 40 (2001) 2643.
- [8] P. Kroll, W. Schnick, *Chem. Eur. J.* 8 (2002) 3530.
- [9] A. Zerr, G. Miehe, G. Serghiou, M. Schwarz, E. Kroke, R. Riedel, H. Fuess, P. Kroll, R. Boehler, *Nature* 400 (1999) 340.
- [10] E. Soignard, M. Somayazulu, J. Dong, O. F. Sankey, P. F. McMillan, *J. Phys.: Condens. Matter* 13 (2001) 557.
- [11] W. Schnick, *Angew. Chem* 111 (1999) 3511; *Angew. Chem. Int. Ed. Engl.* 38 (1999) 3309.
- [12] H. He, T. Sekine, T. Kobayashi, H. Hirotsuki, I. Suzuki, *Phys. Rev. B* 62 (2000) 11412.
- [13] A. Y. Liu, M. L. Cohen, *Science* 245 (1989) 841.
- [14] V. L. Solozhenko, S. N. Dub, N. V. Novikov, *Diamond Relat. Mater.* 10 (2001) 228.
- [15] V. L. Solozhenko, D. Andrault, G. Fiquet, M. Mezouar, D. C. Rubie, *Appl. Phys. Lett.* 78 (2001) 1385.
- [16] H. Hubert, L. A. J. Garvie, P. R. Buseck, W. T. Petuskey, P. F. McMillan, *J. Solid State Chem.* 133 (1997) 356.
- [17] L. A. J. Garvie, H. Hubert, W. T. Petuskey, P. F. McMillan, P. R. Buseck, *J. Solid State Chem.* 133 (1997) 365.
- [18] H. Hubert, B. Devouard, L. A. J. Garvie, M. O'Keeffe, P. R. Buseck, W. T. Petuskey, P. F. McMillan, *Nature* 391 (1998) 376.
- [19] H. Hubert, L. A. J. Garvie, B. Devouard, P. R. Buseck, W. T. Petuskey, P. F. McMillan, *Chem. Mater.* 10 (1998) 1530.
- [20] J.-H. Park, J.-B. Parise, *Mater. Res. Bull.* 32 (1997) 1617.

- [21] J.-A. Lee, N.-K. Kim, *Mater. Lett.* 59 (2005) 32.
- [22] R. Escamilla, J. M. Gallardo-Amores, E. Morán, M. A. Alario-Franco, *J. Solid State Chem.* 168 (2002) 149.
- [23] R. D. Shannon, A. W. Sleight, *Inorg. Chem.* 7 (1968) 1649.
- [24] M. Hasegawa, T. Atou, J. V. Badding, *J. Solid State Chem.* 130 (1997) 311.
- [25] T. S. Snider, J. V. Badding, *Solid State Commun.* 131 (2004) 157.
- [26] J. B. Goodenough, J. A. Kafalas, J. M. Longo, *High Pressure Synthesis*, in P. Hagemuller (ed.): *Preparative Methods in Solid State Chemistry*, Chapt. 1, pp. 2-65, Academic Press, New York – London (1972).
- [27] R. Pöttgen, Th. Gulden, A. Simon, *GIT Labor-Fachzeitschrift* 43 (1999) 133.
- [28] D. Walker, M. A. Carpenter, C. M. Hitch, *Am. Mineral.* 75 (1990) 1020.
- [29] D. J. Frost, Personal Message.
- [30] H. Huppertz, *Habilitationsschrift*, Ludwig-Maximilians-Universität München (2003).
- [31] W. Wünschheim, H. Huppertz, PRESSCONTROL, A Program for Communication, Calibration, and Surveillance of a Hydraulic Press with Heating Device via RS232C Interfaces, Ludwig-Maximilians-Universität München (1999-2003).
- [32] E. Takahashi, H. Yamada, E. Ito, *Geophys. Res. Lett.* 9 (1982) 805.
- [33] I. C. Getting, G. L. Chen, J. A. Brown, *Pure Appl. Geophys.* 141 (1993) 545.
- [34] P. W. Bridgman, *Phys. Rev.* 48 (1935) 825.
- [35] V. E. Bean, S. Akimoto, P. M. Bell, S. Block, W. B. Holzapfel, M. H. Manghnani, M. F. Nicol, S. M. Stishov, *Physica* 139 & 140B (1986) 52.
- [36] F. P. Bundy, *Natl. Bur. Stand. Sp. Publ.* 326 (1971) 263.
- [37] P. W. Bridgman, *Phys. Rev.* 48 (1935) 893.
- [38] A. A. Giardini, G. A. Samara, *J. Phys. Chem. Solids* 26 (1965) 1523.
- [39] M. J. Duggin, *J. Phys. Chem. Solids* 33 (1972) 1267.
- [40] A. Yoneda, S. Endo, *J. Appl. Phys.* 51 (1980) 3216.
- [41] J. H. Chen, H. Iwasaki, T. Kikegawa, *High Press. Res.* 15 (1996) 143.
- [42] E. C. Lloyd, C. W. Becket, F. R. Boyd Jr. in *Accurate Characterization of the High-Pressure Environment* ed. E. C. Lloyd (Washington, DC: *Natl. Bur. Stand. (US) Sp. Publ.* 326 (1971) 1.
- [43] H. G. Drickamer, *Rev. Sci. Instr.* 41 (1970) 1667.
- [44] C. G. Homan, *J. Phys. Chem. Solids* 36 (1975) 1249.
- [45] M. I. McMahon, O. Degtyareva, R. J. Nelmes, *Phys. Rev. Lett.* 85 (2000) 4896.

- [46] K. Kusaba, L. Galoisy, Y. Wang, M. T. Vaughan, D. J. Weidner, *Pure Appl. Geophys.* 141 (1993) 643.
- [47] J. Camacho, I. Loa, A. Cantarero, K. Syassen, *J. Phys.: Condens. Matter* 14 (2002) 739.
- [48] A. San Miguel, A. Polian, M. Gautier, J. P. Itie, *Phys. Rev. B* 48 (1993) 8683.
- [49] R. J. Nelmes, M. I. McMahon, N. G. Wright, D. R. Allan, *J. Phys. Chem. Solids* 56 (1995) 545.
- [50] R. J. Nelmes, M. I. McMahon, N. G. Wright, D. R. Allan, *Phys. Rev. Lett.* 73 (1994) 1805.
- [51] R. Herman, C. A. Swenson, *J. Chem. Phys.* 29 (1958) 398.
- [52] A. K. Singh, *High Temp.-High Pressures* 12 (1980) 47.
- [53] R. A. Stager, H. G. Drickamer, *Phys. Rev. B* 133 (1964) A830.
- [54] A. S. Balchan, H. G. Drickamer, *Rev. Sci. Instr.* 32 (1961) 308.
- [55] R. A. Stager, H. G. Drickamer, *Phys. Rev.* 131 (1963) 2524.
- [56] S. Akimoto, T. Yagi, Y. Ida, K. Inoue, *High Temp.-High Pressures* 7 (1975) 287.
- [57] L. F. Vereshchagin, E. V. Zubova, V. A. Stupnikov, *High Temp.-High Pressures* 7 (1975) 149.
- [58] M. J. Walter, Y. Thibault, K. Wei, R. W. Luth, *Can. J. Phys.* 73 (1995) 273.
- [59] W. Massa, *Kristallstrukturbestimmung*, 4. Auflage, B. G. Teubner, Stuttgart, (2005).
- [60] C. Giacovazzo, H. L. Monaco, G. Artioli, D. Viterbo, G. Ferraris, G. Gilli, G. Zanotti, M. Catti, *Fundamentals of Crystallography*, IUCr Texts on Crystallography, 2nd Ed., Oxford University Press, New York, (2002).
- [61] J. Karle, *Angew. Chem.* 98 (1986) 611; *Angew. Chem. Int. Ed. Engl.* 25 (1986) 614.
- [62] H. Hauptman, *Angew. Chem.* 98 (1986) 600; *Angew. Chem. Int. Ed. Engl.* 25 (1986) 603.
- [63] Y. Amemiya, J. Miyahara, *Nature* 336 (1988) 89.
- [64] Basread, Raytest Isotopenmessgeräte GmbH, Straubenhardt.
- [65] TINA, v2.10g, Raytest Isotopenmessgeräte GmbH, (1993), Straubenhardt.
- [66] STOE WinXPOW, v1.2, STOE & CIE GmbH, Darmstadt, Germany, (2001).
- [67] P.-E. Werner, *TREOR90*, Universität Stockholm, (1990).
- [68] P.-E. Werner, *Z. Kristallogr.* 120 (1964) 375.
- [69] P.-E. Werner, L. Errikson, M. Westdahl, *J. Appl Crystallogr.* 18 (1985) 367.

- [70] J. W. Visser, *J. Appl. Crystallogr.* 2 (1969) 89.
- [71] A. Boultif, D. Louër, *J. Appl. Crystallogr.* 24 (1991) 987.
- [72] STOE WinXPOW THEO, v1.18, (2000).
- [73] WinXPOW Search, v1.22, (1999).
- [74] JCPDS, International Center for Diffraction Data, Swathmore, USA (1992).
- [75] STOE X-RED, v1.19, *STOE Data Reduction Programm*, STOE & Cie GmbH, Darmstadt, (1999).
- [76] STOE X-SHAPE, v1.06, *Crystal Optimisation for Numerical Absorption Correction*, STOE & Cie GmbH, Darmstadt, (1999).
- [77] W. Herrendorf, H. Bärnighausen, HABITUS - *Program for Numerical Absorption Correction*, University of Karlsruhe / Giessen, Germany, (1993/1997).
- [78] G. M. Sheldrick, XPREP, *Data Preparation & Reciprocal Space Exploration*, v6.12, Siemens Analytical X-ray Instruments, (1996).
- [79] G. M. Sheldrick, SHELXS-97, *Program for the Solution of Crystal Structures*, Universität Göttingen, (1997).
- [80] G. M. Sheldrick, SHELXL-97, *Program for Crystal Structure Refinement*, Universität Göttingen, (1997).
- [81] X-STEP32 Revision 1.05b, STOE + Cie GmbH, (1999).
- [82] A. L. Speck, PLATON, *A Multipurpose Crystallographic Tool*, Utrecht University, Utrecht, (2003).
- [83] K. Brandenburg, DIAMOND, *Program for X-ray Structure Analysis*, v3.0d, Crystal Impact GbR, Bonn, (2005).
- [84] P. F. Schmidt, *Praxis der Rasterelektronenmikroskopie und Mikrobereichsanalyse*, Expert Verlag, Renningen-Malmsheim, (1994), p.434 ff.
- [85] INCA, v4.02, Oxford Instruments Analytical Limited, (1998–2002).
- [86] OPUS, *Programm zur Auswertung von Schwingungsspektren*, v3.0.2, Bruker Optics GmbH, Karlsruhe, (1996).
- [87] R. Hoppe, *Angew. Chem.* 78 (1966) 52; *Angew. Chem. Int. Ed. Engl.* 5 (1966) 95.
- [88] R. Hoppe, *Angew. Chem.* 82 (1970) 7; *Angew. Chem. Int. Ed. Engl.* 9 (1970) 25.
- [89] R. Hübenthal, MAPLE, *Programm zur Berechnung des Madelunganteils der Gitterenergie*, v4, Universität Gießen, (1993).
- [90] L. Pauling, *J. Am. Chem. Soc.* 69 (1947) 542.
- [91] I. D. Brown, D. Altermatt, *Acta Crystallogr.* B41 (1985) 244.
- [92] N. E. Brese, M. O'Keeffe, *Acta Crystallogr.* B47 (1991) 192.

- [93] A. Trzesowska, R. Kruszynski, T. J. Bartczak, *Acta Crystallogr.* B60 (2004) 174.
- [94] R. Hoppe, *Z. Kristallogr.* 150 (1979) 23.
- [95] R. Hoppe, S. Voigt, H. Glaum, J. Kissel, H. P. Müller, K. Bernet, *J. Less-Common Met.* 156 (1989) 105.
- [96] W. E. Klee, *Z. Kristallogr.* 179 (1987) 67.
- [97] G. Thimm, S. Schumacher, W. Uhr, W. E. Klee, *TOPOLAN: Topological Analysis of Crystal Structures*, Universität Karlsruhe, (1993).
- [98] D. M. Schubert, *Borates in Industrial Use, Structure and Bonding* Vol. 105, Springer-Verlag, Berlin Heidelberg (2003).
- [99] J. Liebertz, S. Stähr, *Z. Kristallogr.* 165 (1983) 91.
- [100] C. Chen, B. Wu, A. Jiang, G. You, *Sci. Sin. B* 28 (1985) 235.
- [101] P. Becker, *Adv. Mater.* 10 (1998) 979.
- [102] D. A. Keszler, *Curr. Opin. Solid State Mater. Sci.* 4 (1999) 155.
- [103] J. S. Knyrim, P. Becker, D. Johrendt, H. Huppertz, *Angew. Chem.* 118 (2006) 8419; *Angew. Chem. Int. Ed.* 45 (2006) 8239.
- [104] R. J. Brotherton, *Encyclopedia of Inorganic Chemistry*, King RB (ed), John Wiley & Sons, Chichester, 1: 375 (1994).
- [105] G. E. Gurr, P. W. Montgomery, C. D. Knutson, B. T. Gorres, *Acta Crystallogr.* B26 (1970) 906.
- [106] Inorganic Crystal Structure Database, v1.0.0, Fachinformationszentrum Karlsruhe, (January 2007).
- [107] S. F. Bartram, *Proc. 3rd Conf. Rare Earth Res.*, Clearwater, Fla. (1964) 165.
- [108] J. H. Lin, M. Z. Su, K. Wurst, E. Schweda, *J. Solid State Chem.* 126 (1996) 287.
- [109] J. H. Lin, S. Zhou, L. Q. Yang, G. Q. Yao, M. Z. Su, *J. Solid State Chem.* 134 (1997) 158.
- [110] J. H. Lin, L. P. You, G. X. Lu, L. Q. Yang, M. Z. Su, *J. Mater. Chem.* 8 (1998) 1051.
- [111] H. Huppertz, B. von der Eltz, R.-D. Hoffmann, H. Piotrowski, *J. Solid State Chem.* 166 (2002) 203.
- [112] H. Emme, H. Huppertz, *Acta Crystallogr. C* 61 (2005) i117.
- [113] H. Huppertz, B. von der Eltz, *J. Am. Chem. Soc.* 124 (2002) 9376.
- [114] H. Huppertz, *Z. Naturforsch.* 58 b (2003) 278.
- [115] H. Huppertz, H. Emme, *J. Phys.: Condens. Matter* 16 (2004) S1283.

- [116] H. Emme, H. Huppertz, *Z. Anorg. Allg. Chem.* 628 (2002) 2165.
- [117] H. Huppertz, S. Altmannshofer, G. Heymann, *J. Solid State Chem.* 170 (2003) 320.
- [118] H. Emme, H. Huppertz, *Acta Crystallogr. C* 61 (2005) i23.
- [119] F. W. Roeßner, *Bachelorarbeit*, Ludwig-Maximilians-Universität München (2006).
- [120] H. Emme, M. Valldor, R. Pöttgen, H. Huppertz, *Chem. Mater.* 17 (2005) 2707.
- [121] J. S. Knyrim, H. Huppertz, *J. Solid State Chem.* 180 (2007) 742.
- [122] G. Canneri, *Gazz. Chim. Ital.* 56 (1926) 450.
- [123] J. Weidelt, *Z. Anorg. Allg. Chem.* 374 (1970) 26.
- [124] I. V. Tananaev, B. F. Dzhurinskii, I. M. Belyakov, *Izv. Akad. Nauk SSSR Neorg. Mater.* 2 (1966) 1791.
- [125] H. U. Bambauer, J. Weidelt, J.-St. Ysker, *Z. Kristallogr.* 130 (1969) 207.
- [126] I. V. Tananaev, B. F. Dzhurinskii, B. F. Chistova, *Izv. Akad. Nauk SSSR Neorg. Mater.* 11 (1975) 86.
- [127] I. V. Tananaev, B. F. Dzhurinskii, B. F. Chistova, *Inorg. Mat.* 11 (1975) 69.
- [128] V. I. Pakhomov, G. B. Sil'nitskaya, A. V. Medvedev, B. F. Dzhurinskii, *Inorg. Mater.* 8 (1972) 1107.
- [129] H. Müller-Bunz, T. Nikelski, Th. Schleid, *Z. Naturforsch.* 58 b (2003) 375.
- [130] G. D. Abdullaev, Kh. S. Mamedov, G. G. Dzhafarov, *Sov. Phys. Crystallogr.* 20 (1975) 161.
- [131] A. Goriounova, P. Held, P. Becker, L. Bohatý, *Acta Crystallogr. E* 59 (2003) i83.
- [132] W. H. Zachariasen, *Proc. Natl. Acad. Sci. U.S.A.* 17 (1931) 617.
- [133] M. Marezio, H. A. Plettinger, W. H. Zachariasen, *Acta Crystallogr.* 16 (1963) 390.
- [134] D. P. Shashkin, M. A. Simonov, N. V. Belov, *Sov. Phys. Crystallogr.* 16 (1971) 186.
- [135] M. Marezio, J. P. Remeika, P. D. Dernier, *Acta Crystallogr. B* 25 (1969) 955.
- [136] M. Marezio, J. P. Remeika, P. D. Dernier, *Acta Crystallogr. B* 25 (1969) 965.
- [137] H. Emme, H. Huppertz, *Chem. Eur. J.* 9 (2003) 3623.
- [138] H. Emme, H. Huppertz, *Acta Cryst. C* 61 (2005) i29.
- [139] J.-Y. Henry, *Mater. Res. Bull.* 11 (1976) 577.
- [140] R. Böhlhoff, H. U. Bambauer, W. Hoffmann, *Z. Kristallogr.* 133 (1971) 386.
- [141] R. D. Shannon, *Acta Crystallogr. A* 32 (1976) 751.

- [142] M. Ren, J. H. Lin, Y. Dong, L. Q. Yang, M. Z. Su, L. P. You, *Chem. Mater.* 11 (1999) 1576.
- [143] J. P. Laperches, P. Tarte, *Spectrochim. Acta* 22 (1966) 1201.
- [144] G. Blasse, G. P. M. van den Heuvel, *Phys. Stat. Sol.* 19 (1973) 111.
- [145] W. C. Steele, J. C. Decius, *J. Chem. Phys.* 25 (1956) 1184.
- [146] K. Machida, H. Hata, K. Okuno, G. Adachi, J. Shiokawa, *J. Inorg. Nucl. Chem.* 41 (1979) 1425.
- [147] M. Touboul, N. Penin, G. Nowogrocki, *J. Solid State Chem.* 150 (2000) 342.
- [148] C. E. Weir, R. A. Schroeder, *J. Res. Natl. Bur. Stand.* 86 A (1964) 465.
- [149] E. L. Belokoneva, V. A. Shuvaeva, M. Yu. Antipin, N. I. Leonyuk, *Zh. Neorg. Khim.* 41 (1996) 1097.
- [150] N. Hirosaki, S. Ogata, C. Kocer, *J. Alloys Compd.* 351 (2003) 31.
- [151] E. Zobetz, *Z. Kristallogr.* 160 (1982) 81.
- [152] C. Sieke, T. Nikelski, Th. Schleid, *Z. Anorg. Allg. Chem.* 628 (2002) 819.
- [153] I. Y. Nekrasov, R. A. Nekrasova, *Dokl. Akad. Nauk SSSR* 201 (1971) 179.
- [154] J.-St. Ysker, W. Hoffmann, *Naturwissenschaften* 57 (1970) 129.
- [155] G. K. Abdullaev, Kh. S. Mamedov, G. G. Dzhfarov, *Sov. Phys. Crystallogr.* 26 (1981) 473.
- [156] P. A. Arsen'ev, L. M. Kovba, Kh. S. Bagdasarov, *Chemistry of Rare Elements: Systems with Oxides of Group I and Group III Elements*, Nauka, Moscow (1983).
- [157] K. I. Portnoi, N. I. Timofeeva, *Rare-Earth Oxygen Compounds*, Metallurgiya, Moscow (1986).
- [158] L. N. Dem'yanets, A. N. Lobachev, G. A. Emel'chenko, *Germanates of Rare-Earth Elements*, Nauka, Moscow (1980).
- [159] I. A. Bondar', N. V. Vinogradova, L. N. Dem'yanets, *Chemistry of Rare-Earth Compounds: Silicates, Germanates, Phosphates, Arsenates, and Vanadates*, Nauka, Moscow (1983).
- [160] I. A. Bondar', M. A. Petrova, *Izv. Akad. Nauk SSSR, Neorg. Mater.* 6 (1970) 1285.
- [161] E. M. Levin, *J. Am. Ceram. Soc.* 57 (1974) 189.
- [162] B. M. Wanklyn, *J. Mater. Sci.* 8 (1973) 649.
- [163] K. K. Palkina, N. E. Kuz'mina, G. V. Lysanova, *Zh. Neorg. Khim.* 39 (1994) 184.

- [164] K. K. Palkina, N. E. Kuz'mina, B. F. Dzhurinskii, A. B. Pobedina, V. P. Sanygin, A. M. Kvardakov, *Russ. J. Inorg. Chem.* 46 (2001) 465.
- [165] A. B. Pobedina, M. G. Komova, B. F. Dzhurinskii, *Russ. J. Inorg. Chem.* 45 (2000) 1024.
- [166] K. K. Palkina, N. E. Kuz'mina, B. F. Dzhurinskii, A. B. Pobedina, V. P. Sanygin, A. M. Kvardakov, *Russ. J. Inorg. Chem.* 44 (1999) 1817.
- [167] K. K. Palkina, N. E. Kuz'mina, A. B. Pobedina, V. P. Sanygin, A. M. Kvardakov, B. F. Dzhurinskii, *Russ. J. Inorg. Chem.* 45 (2000) 1637.
- [168] A. A. Kaminskii, B. V. Mill, E. L. Belokoneva, A. V. Butashin, *Izv. Akad. Nauk SSSR, Neorg. Mater.* 26 (1990) 1105.
- [169] E. Antic-Fidancev, M. Lemaitre-Blaise, M. Taibi, J. Aride, A. Boukhari, P. Porcher, *J. Alloys Compd.* 275-277 (1998) 424.
- [170] E. L. Belokoneva, B. V. Mill, A. V. Butashin, A. A. Kaminskii, *Izv. Akad. Nauk SSSR, Neorg. Mater.* 27 (1991) 1700.
- [171] G. V. Lysanova, B. F. Dzhurinskii, M. G. Komova, V. I. Tsaryuk, I. V. Tananaev, *Inorg. Mater.* 25 (1989) 545.
- [172] M. Taibi, J. Airde, A. Boukhari, *Ann. Chim. Sci. Mat.* 23 (1998) 285.
- [173] A. Rulmont, P. Tarte, *J. Solid State Chem.* 75 (1988) 244.
- [174] A. A. Voronkov, Y. A. Pyantenko, *Sov. Phys. Crystallogr. Engl. Trans.* 12 (1967) 214.
- [175] J. McAdrew, T. R. Scott, *Nature* 4480 (1955) 509.
- [176] A. Gallegari, G. Giuseppeti, F. Mazzi, C. Tadini, *Neues Jahrb. Mineral., Monatsh.* H2 (1992) 49.
- [177] F. F. Foit, M. W. Phillips, G. V. Gibbs, *Am. Mineral.* 58 (1973) 909.
- [178] M. S. Dadachov, K. Sun, T. Conradsson, X. Zou, *Angew. Chem.* 112 (2000) 3820; *Angew. Chem. Int. Ed. Engl.* 39 (2000) 3674.
- [179] Y. Li, X. Zou, *Angew. Chem.* 117 (2005) 2048; *Angew. Chem. Int. Ed. Engl.* 44 (2005) 2012.
- [180] Z.-E. Lin, J. Zhang, G.-Y. Yang, *Inorg. Chem.* 42 (2003) 1797.
- [181] G.-M. Wang, Y.-Q. Sun, G.-Y. Yang, *Cryst. Growth Des.* 5 (2005) 313.
- [182] H.-X. Zhang, J. Zhang, S.-T. Zheng, G.-M. Wang, G.-Y. Yang, *Inorg. Chem.* 43 (2004) 6148.
- [183] H.-X. Zhang, J. Zhang, S.-T. Zheng, G.-Y. Yang, *Inorg. Chem.* 44 (2005) 1166.
- [184] B. F. Dzhurinskii, G. V. Lysanova, M. G. Komova, V. I. Chistova, E. G. Tselebrovskaya, *Russ. J. Inorg. Chem.* 36 (1991) 1991.

- [185] G. V. Lysanova, B. F. Dzhurinskii, M. G. Komova, O. V. Sorokina, B. I. Chistova, *Inorg. Mater.* 24 (1988) 190.
- [186] B. F. Dzhurinskii, A. B. Pobedina, K. K. Palkina, M. G. Komova, *Russ. J. Inorg. Chem.* 43 (1998) 1488.
- [187] A. B. Ilyukhin, B. F. Dzhurinskii, *Russ. J. Inorg. Chem.* 39 (1994) 530.
- [188] B. F. Dzhurinskii, G. V. Lysanova, M. G. Komova, L. Z. Gokhman, V. A. Krut'ko, *Russ. J. Inorg. Chem.* 40 (1995) 1699.
- [189] B. F. Dzhurinskii, A. B. Ilyukhin, *Russ. J. Inorg. Chem.* 45 (2000) 1.
- [190] G. A. Bandurkin, G. V. Lysanova, K. K. Palkina, V. A. Krut'ko, M. G. Komova, *Russ. J. Inorg. Chem.* 49 (2004) 213.
- [191] H. Emme, C. Despotopoulou, H. Huppertz, *Z. Anorg. Allg. Chem.* 630 (2004) 2450.
- [192] A. Neuhaus, *Chimia* 18 (1964) 93.
- [193] F. Goubin, Y. Montardi, P. Deniard, X. Rocquefelte, R. Brec, S. Jobic, *J. Solid State Chem.* 177 (2004) 89.
- [194] H. Bärnighausen, G. Schiller, *J. Less-Common Met.* 110 (1985) 185.
- [195] E. Zobetz, *Z. Kristallogr.* 191 (1990) 45.
- [196] F. C. Hawthorne, P. C. Burns, J. D. Grice, "Boron: Mineralogy, Petrology, and Geochemistry" *Rev. Mineral.* 33 (1996) 42.
- [197] J. R. Clark, *Amer. Mineral.* 49 (1964) 1549.
- [198] J. A. Konnert, J. R. Clark, C. L. Christ, *Amer. Mineral.* 55 (1970) 1911.
- [199] S. Ghose, C. Wan, *Amer. Mineral.* 62 (1977) 979.
- [200] J. Krogh-Moe, *Acta Chem. Scand.* 18 (1964) 2055.
- [201] A. Perloff, S. Block, *Acta Crystallogr.* 20 (1966) 274.
- [202] F. Pan, G. Shen, R. Wang, X. Wang, D. Shen, *J. Cryst. Growth* 241 (2002) 108.
- [203] D. L. Corker, A. M. Glazer, *Acta Crystallogr. Sect. B* 52 (1996) 260.
- [204] K.-I. Machida, G.-Y. Adachi, J. Shiokawa, *Acta Crystallogr. Sect. B* 36 (1980) 2008.
- [205] H. Huppertz, G. Heymann, *Solid State Sci.* 5 (2003) 281.
- [206] H. Huppertz, *Z. Naturforsch.* 58b (2003) 257.
- [207] H. Emme, M. Weil, H. Huppertz, *Z. Naturforsch., B: Chem. Sci.* 60 (2005) 815.
- [208] H. Emme, T. Nikelski, Th. Schleid, R. Pöttgen, M. H. Möller, H. Huppertz, *Z. Naturforsch.* 59b (2004) 202.
- [209] T. Nikelski, Th. Schleid, *Z. Anorg. Allg. Chem.* 629 (2003) 1017.

- [210] H. Emme, C. Despotopoulou, H. Huppertz, *Z. Anorg. Allg. Chem.* 630 (2004) 1717.
- [211] C. T. Prewitt, R. D. Shannon, *Acta Crystallogr. Sect. B* 24 (1968) 869.
- [212] O. Jarchow, K. H. Klaska, M. Ruks, B. Holtz, *Z. Kristallogr.* 211 (1996) 4.
- [213] A. A. Bolzan, C. Fong, B. J. Kennedy, C. J. Howard, *Acta Crystallogr. Sect. B* 53 (1997) 373.
- [214] K. Bluhm, Hk. Müller-Buschbaum, *J. Less-Common Met.* 147 (1989) 133.
- [215] F. Bertaut, A. Durif, *Compt. Rend.* 238 (1954) 2173.
- [216] K. Aurivillius, *Acta Crystallogr.* 9 (1956) 685.
- [217] Z. Lodziana, K. Parlinski, J. Hafner, *Phys. Rev. B* 63 (2001) 134106.
- [218] J. E. Lowther, T. Wagner, I. Kinski, R. Riedel, *J. Alloys Compd.* 376 (2004) 1.
- [219] P. Kroll, personal communication.
- [220] W. S. Jung, *Bull. Korean Chem. Soc.* 25(1) (2004) 51.
- [221] P. Foley, M. Zeldin, *Inorg. Chem.* 14 (1975) 2264.
- [222] H. Nöth, P. Konrad, *Z. Naturforsch.* 30b (1975) 681.
- [223] M. Valet, D. Hoffman, *Chem. Mater.* 13 (2001) 2135.
- [224] I. Kinski, F. Scheiba, R. Riedel, *Adv. Eng. Mater.* 7(10) (2005) 912.
- [225] T. Roisnel, J. Rodriguez-Carvajal, *Mater. Sci. Forum* 378-381 (2001) 118.
- [226] K. Pohl, *Naturwissenschaften* 55(2) (1968) 82.
- [227] J. McCauley, *J. Amer. Ceram. Soc.* 61 (1978) 372.
- [228] M. Puchinger, D. J. Kisailus, F. F. Lange, T. Wagner, *J. Cryst. Growth* 245 (2002) 219.
- [229] H. X. Willems, G. de With, R. Metselaar, R. B. Helmholtz, K. K. Petersen, *J. Mater. Sci. Lett.* 12 (1993) 1470.
- [230] R. S. Zhou, R. L. Snyder, *Acta Crystallogr., Sec. B: Structural Science* 47 (1991) 617.
- [231] E. Soignard, D. Machon, P. F. McMillan, J. Dong, B. Xu, K. Leinenweber, *Chem. Mater.* 17 (2005) 5465.
- [232] S. Hering, *Diplomarbeit*, Ludwig-Maximilians-Universität München (2007).
- [233] R. Demchyna, S. Leoni, H. Rosner, U. Schwarz, *Z. Kristallogr.* 221 (2006) 420.
- [234] H. Takamura, H. Katuka, Y. Goto, H. Watanabe, A. Kamegawa, M. Okada, *J. Alloys Compd.* 404-406 (2005) 372.
- [235] D. Santamaría-Pérez, J. Nuss, J. Haines, M. Jansen, A. Vegas, *Solid State Sci.* 6 (2004) 673.
- [236] H. Giefers, M. Nicol, *J. Alloys Compd.* 422 (2006) 132.
- [237] M. I. McMahon, R. J. Nelmes, *Chem. Soc. Rev.* 35 (2006) 943.

- [238] P. F. McMillan, *Chem. Soc. Rev.* 35 (2006) 855.
- [239] I. Shirovani, K. Takeda, C. Sekine, J. Hayashi, R. Nakada, K. Kihou, Y. Ohishi, T. Yagi, *Z. Naturforsch.* 61b (2006) 1471.
- [240] H. Kitô, T. Wada, H. Abe, *Physica B* 378-380 (2006) 1146.
- [241] H. Fukuoka, J. Kiyoto, S. Yamanaka, *J Solid State Chem.* 175 (2003) 237.
- [242] A. Wosylus, Yu. Prots, U. Burkhardt, W. Schnelle, U. Schwarz, Yu. Grin, *Solid State Sci.* 8 (2006) 773.
- [243] A. Wosylus, Y. Prots, U. Burkhardt, W. Schnelle, U. Schwarz, Y. Grin, *Z. Naturforsch.* 61b (2006) 1485.
- [244] S. Yamanaka, S. Maekawa, *Z. Naturforsch.* 61b (2006) 1493.
- [245] A. Szytuła, J. Leciejewicz, *Handbook of Crystal Structures and Magnetic Properties of Rare Earth Intermetallics*. CRC Press, Boca Raton, Florida (1994).
- [246] R. V. Skolozdra, *Stannides of rare-earth and transition metals*, in K. A. Gschneidner Jr. and L. Eyring (eds.) *Handbook on the Physics and Chemistry of Rare Earths*, North-Holland/Elsevier, Amsterdam, Vol. 24, Chapter 164, (1997) 399-517.
- [247] T. Fujita, T. Suzuki, S. Nishigori, T. Takabatake, H. Fujii, J. Sakurai, *J. Magn. Magn. Mater.* 108 (1992) 35.
- [248] E. Gaudin, B. Chevalier, B. Heying, U. Ch. Rodewald, R. Pöttgen, *Chem. Mater.* 17 (2005) 2693.
- [249] J. Sakurai, Y. Yamaguchi, S. Nishigori, T. Suzuki, T. Fujita, *J. Magn. Magn. Mater.* 90 & 91 (1990) 422.
- [250] M. Kolenda, J. Leciejewicz, N. Stuesser, A. Szytuła, A. Zygmunt, *J. Magn. Magn. Mater.* 145 (1995) 85.
- [251] H. Kadowaki, T. Ekino, H. Iwasaki, T. Takabatake, H. Fujii, J. Sakurai, *J. Phys. Soc. Jpn.* 62 (1993) 4426.
- [252] M. Bažela, M. Kolenda, J. Leciejewicz, N. Stuesser, A. Szytuła, A. Zygmunt, *J. Magn. Magn. Mater.* 140-144 (1995) 881.
- [253] D. T. Adroja, B. D. Rainford, *Physica B* 194-196 (1994) 363.
- [254] H. Kobayashi, F. E. Wagner, G. M. Kalvius, T. Takabatake, *Hyp. Int.* 93 (1994) 1515.
- [255] M. Divis, B. Janoušová, J. Rusz, V. Sechovský, M. Richter, I. Opahle, *J. Alloys Compd.* 376 (2004) 28.
- [256] K. Yvon, W. Jeitschko, E. Parthé, *J. Appl. Crystallogr.* 10 (1977) 73.

- [257] I. Higashi, K. Kobayashi, T. Takabatake, M. Kasaya, *J. Alloys Compd.* 193 (1993) 300.
- [258] D. Rafaja, V. Rejdák, B. Janoušová, P. Svoboda, V. Sechovský, *J. Alloys Compd.* 334 (2002) 50.
- [259] B. Janoušová, P. Svoboda, V. Sechovský, K. Prokeš, T. Komatsubara, H. Nakotte, S. Chang, B. Ouladdiaf, I. Císařová, *Appl. Phys. A: Mater. Sci & Processing* 74 (2002) S731.
- [260] B. Janoušová, V. Sechovský, T. Komatsubara, *Physica B* 671 (2003) 329.
- [261] T. Roisnel, J. Rodríguez-Carvajal, FULLPROF.2k v2.0 (2001) Laboratoire Léon Brillouin (CEA-CNRS), 91191 Gif-sur-Yvette Cedex (France).
- [262] J.-F. Béarar, P. Lelann, *J. Appl. Crystallogr.* 24 (1991) 1.
- [263] C. B. Shoemaker, D. P. Shoemaker, *Acta Crystallogr.* 18 (1965) 900.
- [264] P. I. Krypyakevich, V. Ya. Markiv, E. V. Melnyk, *Dopov. Akad. Nauk. Ukr. RSR, Ser. A* (1967) 750.
- [265] M. F. Zumdick, R.-D. Hoffmann, R. Pöttgen, *Z. Naturforsch.* 54b (1999) 45.
- [266] H. D. Flack, G. Bernadinelli, *Acta Crystallogr. A* 55 (1999) 908.
- [267] H. D. Flack, G. Bernadinelli, *J. Appl. Crystallogr.* 33 (2000) 1143.
- [268] Ch. D. Routsis, J. K. Yakinthos, E. Gamari-Seale, *J. Magn. Magn. Mater.* 110 (1992) 317.
- [269] R. Pöttgen, *Z. Naturforsch.* 51b (1996) 806.
- [270] J. Sakurai, K. Kegai, T. Kuwai, Y. Isikawa, K. Nishimura, K. Mori, *J. Magn. Magn. Mater.* 140-144 (1995) 875.
- [271] F. Canepa, S. Cirafici, *J. Alloys Compd.* 232 (1996) 71.
- [272] A. E. Dwight, W. C. Harper, C. W. Kimball, *J. Less-Common Met.* 30 (1973) 1.
- [273] J. Emsley, *The Elements*, Oxford University Press, Oxford (1999).
- [274] H. Lueken, *Magnetochemie*, Teubner, Stuttgart (1999).
- [275] D. Niepmann, R. Pöttgen, B. Künnen, G. Kotzyba, C. Rosenhahn, B. D. Mosel, *Chem. Mater.* 11 (1999) 1597.
- [276] Z. Hossain, L. C. Gupta, C. Geibel, *J. Phys.: Condens. Matter* 14 (2002) 9687.
- [277] B. Janoušová, V. Sechovsky, A. H. Lacerda, T. Komatsubara, *Czech. J. Phys.* 54 (Suppl. D) (2004) D319.
- [278] G. R. Stewart, *Rev. Mod. Phys.* 73 (2001) 797.
- [279] J. A. Mydosh, in 'Spin Glasses: An experimental Introduction' Taylor & Francis, (1993).
- [280] K. Binder, A. P. Young, *Rev. Mod. Phys.* 58 (1986) 801.

- [281] A. Szytuła, *Crystal Structures and Magnetic Properties of RTX Rare Earth Intermetallics*, Wydawnictwo Uniwersytetu Jagiellońskiego, Kraków (1998).
- [282] C. A. M. Mulder, A. J. van Duyneveldt, J. A. Mydosh, *Phys. Rev. B* 23 (1981) 1384.
- [283] D. Hüser, L. E. Wegner, A. J. van Duyneveldt, J. A. Mydosh, *Phys. Rev. B* 27 (1983) 1268.
- [284] G. E. Brodale, R. A. Fisher, W. E. Fogle, N. E. Philips, J. van Curen, *J. Magn. Magn. Mater.* 31-34 (1983) 1331.
- [285] D. L. Martin, *Phys. Rev. B* 21 (1980) 1902.
- [286] O. K. Andersen, O. Jepsen, *Tight-Binding LMTO*, v4.7, Max-Planck-Institut für Festkörperforschung, Stuttgart (1994).
- [287] O. Jepsen, M. Snob, O. K. Andersen, *Linearized Band Structure Methods and its Applications*, Springer Lecture Notes, Springer-Verlag, Berlin (1987).
- [288] H. L. Skriver, *The LMTO Method*, Springer-Verlag, Berlin (1984).
- [289] O. K. Andersen, O. Jepsen, *Solid State Commun.* 9 (1971) 1763.
- [290] W. R. L. Lambrecht, O. K. Andersen, *Phys. Rev. B* 34 (1986) 2439.
- [291] R. Dronskowski, P. Blöchl, *J. Phys. Chem.* 97 (1993) 8617.
- [292] D. T. Adroja, S. K. Malik, B. D. Padalia, R. Vijayaraghavan, *Solid State Comm.* 66 (1988) 1201.
- [293] D. Kußmann, R. Pöttgen, B. Künnen, R. Müllmann, B. D. Mosel, G. Kotzyba, *Z. Kristallogr.* 613 (1998) 356.
- [294] T. Takabatake, Y. Nakazawa, M. Ishikawa, *Jpn. J. Appl. Phys. Suppl.* 3 26 (1987) 547.
- [295] T. Schmidt, D. Johrendt, C. P. Sebastian, R. Pöttgen, K. Łątka, R. Kmieć, *Z. Naturforsch.* 60b (2005) 1036.
- [296] B. Chevalier, C. P. Sebastian, R. Pöttgen, *Solid State Sci.* 8 (2006) 1000.
- [297] J. F. Riecken, G. Heymann, T. Soltner, R.-D. Hoffmann, H. Huppertz, D. Johrendt, R. Pöttgen, *Z. Naturforsch.* 60b (2005) 821.
- [298] M. Lenkewitz, S. Corsépius, G. R. Stewart, *J. Alloys Compd.* 241 (1996) 121.
- [299] B. Chevalier, J.-L. Bobet, M. Pasturel, E. Bauer, F. Weill, R. Decourt, J. Etourneau, *J. Mater. Chem.* 15 (2003) 2181.
- [300] D. Rossi, V. Contardi, R. Marazza, D. Mazzone, G. Zanichchi, *Atti XVI Congr. Naz. di Chimica Inorganica*, Ferrara, September 12–16, Università degli Studi di Ferrara, Ferrara (1983) 240.
- [301] D. Rossi, R. Marazza, R. Ferro, *J. Less-Common Met.* 107 (1985) 99.

- [302] B. Chevalier, A. Wattiaux, J.-L. Bobet, *J. Phys.: Condens. Matter* 18 (2006) 1743.
- [303] F. Iga, M. Kasaya, H. Suzuki, Y. Okayama, H. Takahashi, N. Mori, *Physica B* 186-188 (1993) 419.
- [304] V. I. Zaremba, Ya. M. Kalychak, Yu. B. Tyvanchuk, R.-D. Hoffmann, M. H. Möller, R. Pöttgen, *Z. Naturforsch.* 57b (2002) 791.
- [305] R. Kraft, R. Pöttgen, D. Kaczorowski, *Chem. Mater.* 15 (2003) 2998.
- [306] D. Niepmann, R. Pöttgen, K. M. Poduska, F. J. DiSalvo, H. Trill, B. D. Mosel, *Z. Naturforsch.* 56b (2001) 1.
- [307] SciFinder Scholar v2005: <http://www.cas.org/SCIFINDER/SCHOLAR/>.
- [308] R. V. Skolozdra, V. M. Mandzyk, Y. K. Gorelenko, V. D. Tkachuk, *Fiz. Metalloved.* 52 (1981) 966.
- [309] A. Ślebarski, J. Pierre, K. Kaczmarek, *J. Magn. Magn. Mater.* 140-144 (1995) 893.
- [310] R. V. Skolozdra, O. E. Koretskaya, Yu. K. Gorelenko, *Inorg. Mater.* 20 (1984) 604.
- [311] T. Takabatake, F. Teshima, H. Fujii, S. Nishigori, T. Suzuki, T. Fujita, Y. Yamaguchi, J. Sakurai, D. Jaccard, *Phys. Rev. B.* 41 (1990) 9607.
- [312] C. P. Sebastian, L. Zhang, H. Eckert, C. Fehse, R.-D. Hoffmann, R. Pöttgen, *Inorg. Chem.* (2007) in press.
- [313] D. Mazzone, D. Rossi, R. Marazza, R. Ferro, *J. Less-Common Met.* 80 (1981) P47.
- [314] K. Łątka, E. A. Görlich, J. Gurgul, R. Kmieć, *Hyp. Int.* 126 (2000) 299.
- [315] C. P. Sebastian, S. Rayaprol, R. Pöttgen, *Solid State Commun.* 140 (2006) 276.
- [316] C. P. Sebastian, H. Eckert, C. Fehse, J. P. Wright, J. P. Attfield, D. Johrendt, S. Rayaprol, R.-D. Hoffmann, R. Pöttgen, *J. Solid State Chem.* 179 (2006) 2376.
- [317] G. Wenski, A. Mewis, *Z. Kristallogr.* 176 (1986) 125.
- [318] R.-D. Hoffmann, R. Pöttgen, *Z. Kristallogr.* 216 (2001) 127.
- [319] S. Baran, J. Leciejewicz, N. Stüsser, A. Szytuła, A. Zygmunt, Y. Ding, *J. Magn. Magn. Mater.* 170 (1997) 143.
- [320] R. Pöttgen, H. Borrmann, C. Felser, O. Jepsen, R. Henn, R. K. Kremer, A. Simon, *J. Alloys Compd.* 235 (1996) 170.
- [321] J. Donohue, *The Structures of the Elements*, Wiley, New York (U.S.A.) (1974).
- [322] A. E. Dwight, M. H. Mueller, R. A. Conner (Jr.), J. W. Downey, H. Knott, *Trans Met Soc. AIME* 242 (1968) 2075.
- [323] A. E. Dwight, *J. Less-Common Met.* 93 (1983) 411.

- [324] J. F. Riecken, G. Heymann, H. Huppertz, R. Pöttgen, *Z. Anorg. Allg. Chem.* 633 (2007) 869.
- [325] A. Adam, J. Sakurai, Y. Yamaguchi, H. Fujiwara, K. Mibu, T. Shinjo, *J. Magn. Magn. Mater.* 90 & 91 (1990) 544.
- [326] S. Baran, A. Szytuła, J. Leciejewicz, N. Stüsser, Y. F. Ding, A. Zygmunt, in: *Aperiodic'97, Proceedings of the International Conference on Aperiodic Crystals*, M. de Boissieu, J.-L. Verger-Gaugry, R. Currat (eds.), Alpe d'Huez, Aug. 27-31, p. 599-603, World Scientific, Singapore, (1997).
- [327] K. Łątka, R. Kmieć, J. Gurgul, *Mol. Phys. Rep.* 30 (2000) 94.
- [328] P. Riani, D. Mazzone, G. Zanicchi, R. Marazza, R. Ferro, *J. Phase Equilibria* 23 (2002) 7.
- [329] I. A. Savysyuk, E. I. Gladyshevskii, R. E. Gladyshevskii, *J. Alloys Compd.* 317-318 (2001) 340.
- [330] S. Baran, M. Hofmann, J. Leciejewicz, B. Penc, M. Slaski, A. Szytuła, *J. Alloys Compd.* 281 (1998) 92.
- [331] B. Gibson, R. Pöttgen, R. K. Kremer, A. Simon, K. R. A. Ziebeck, *J. Alloys Compd.* 239 (1996) 34.
- [332] O. V. Zaplatynsky, P. S. Salamakha, O. L. Sologub, O. S. Procyk, O. I. Bodak, *Polish J. Chem.* 70 (1996) 267.
- [333] R. Pöttgen, *Z. Naturforsch.* 50b (1995) 1071.
- [334] F. Merlo, M. Pani, M. L. Fornasini, *J. Alloys Compd.* 232 (1996) 289.
- [335] P. S. Salamakha, O. L. Sologub, O. I. Bodak, *Ternary Rare Earth Germanium Systems*, in K. A. Gschneidner Jr. and L. Eyring (eds.) *Handbook on the Physics and Chemistry of Rare Earths*, North-Holland/Elsevier, Amsterdam, Vol. 27, (1999) 1-223.
- [336] V. K. Pecharskii, K. A. Gschneidner Jr., O. I. Bodak, A. S. Protsyk, *J. Less-Common Met.* 168 (1991) 257.
- [337] E. Cordruwisch, D. Kaczorowski, A. Saccone, P. Rogl, R. Ferro, *J. Phase Equilibria* 20 (1999) 407.
- [338] B. J. Gibson, R. Pöttgen, R. K. Kremer, *Physica B: Condens. Matter.* 276-278 (2000) 734.
- [339] Z. Otwinowski, W. Minor, *Methods Enzymol.* 276 (1997) 307.
- [340] G. Brauer, H. Gradinger, *Z. Anorg. Allg. Chem.* 277 (1954) 89.
- [341] G. Cordier, H. Schäfer, *Angew. Chem.* 93 (1981) 474.
- [342] G. Cordier, G. Savelsberg, H. Schäfer, *Z. Naturforsch.* 37b (1982) 975.

- [343] F. Lissner, Th. Schleid, *Z. Anorg. Allg. Chem.* 619 (1993) 1771.
- [344] Th. Schleid, *Eur. J. Solid State Inorg. Chem.* 33 (1996) 227.
- [345] A. Szytuła, D. Kaczorowski, S. Baran, J. Hernández-Velasco, B. Penc, N. Stüßler, E. Wawrzyńska, K. Gofryk, *Intermetallics* 14 (2006) 702.
- [346] W. Rieger, *Monatsh. Chem.* 101 (1970) 449.
- [347] R. Hoppe, H. J. Röhrborn, *Naturwissenschaften* 12 (1961) 453.
- [348] R. Hoppe, H. J. Röhrborn, *Z. Anorg. Allg. Chem.* 327 (1964) 199.
- [349] R. Hoppe, *J. Solid State Chem.* 65 (1986) 127.
- [350] H.-D. Wasel-Nielen, R. Hoppe, *Z. Anorg. Allg. Chem.* 36 (1968) 359.
- [351] P. J. Yvon, R. B. Schwarz, C. B. Pierce, L. Bernadez, A. Conners, R. Meisner, *Phys. Rev. B* 39 (1989) 6690.
- [352] W. Schauerte, H.-U. Schuster, N. Knauf, R. Müller, *Z. Anorg. Allg. Chem.* 616 (1992) 186.
- [353] B. Cogel, H.-U. Schuster, *Z. Anorg. Allg. Chem.* 619 (1993) 1765.
- [354] H.-U. Schuster, J. Wittrock, *J. Therm. Anal.* 39 (1993) 1397.
- [355] A. Panahandeh, W. Jung, *Z. Anorg. Allg. Chem.* 629 (2003) 1651.
- [356] M. P. Dariel, M. R. Pickus, *J. Less-Common Met.* 50 (1976) 125.
- [357] R. Mackay, H. F. Franzen, *J. Alloys Compd.* 186 (1992) L7.
- [358] J. H. Albering, W. Jeitschko, *J. Solid State Chem.* 117 (1995) 80.
- [359] H. Nowotny, B. Lux, H. Kudielka, *Monatsh. Chem.* 87 (1956) 447.
- [360] E. Parthé, *Powder Metallurgy Bulletin* 8 (1957) 23.
- [361] E. Parthé, J. T. Norton, *Acta Crystallogr.* 11 (1958) 14.
- [362] G. J. Snyder, A. Simon, *Angew. Chem.* 106 (1994) 713; *Angew. Chem. Int. Ed. Engl.* 33 (1994) 374.
- [363] A. Simon, *Coord. Chem. Rev.* 163 (1997) 253.
- [364] D. Rossi, R. Marazza, R. Ferro, *J. Alloys Compd.* 187 (1992) 267.
- [365] R. Pöttgen, H. Borrmann, R. K. Kremer, *J. Magn. Magn. Mater.* 152 (1996) 196.
- [366] C. D. W. Jones, R. A. Gordon, F. J. DiSalvo, R. Pöttgen, R. K. Kremer, *J. Alloys Compd.* 260 (1997) 50.
- [367] A. Loidl, K. Knorr, G. Knopp, A. Krimmel, R. Caspary, A. Böhm, G. Sparn, C. Geibel, F. Steglich, A. P. Murani, *Phys. Rev. B* 46 (1992) 9341.
- [368] O. Sologub, K. Hiebl, P. Rogl, O. I. Bodak, *J. Alloys Compd.* 227 (1995) 37.
- [369] V. Brouskov, M. Hanfland, R. Pöttgen, U. Schwarz, *Z. Kristallogr.* 220 (2005) 122.

- [370] A. F. Holleman, E. Wiberg, N. Wiberg, *Lehrbuch der Anorganischen Chemie*, 102. Auflage, Walter de Gruyter, Berlin (2007) 1471f.
- [371] V. Hlukhyy, V. I. Zaremba, Y. M. Kalychak, R. Pöttgen, *J. Solid State Chem.* 177 (2004) 1359.
- [372] V. I. Zaremba, U. Ch. Rodewald, Ya. M. Kalychak, Ya. V. Galadzhun, D. Kaczorowski, R.-D. Hoffmann, R. Pöttgen, *Z. Anorg. Allg. Chem.* 629 (2003) 434.
- [373] G. Demazeau, A. Baranov, G. Heymann, H. Huppertz, A. Sobolev, I. Presniakov, *Solid State Sci.* 9 (2007) 376.
- [374] G. Demazeau, C. Parent, M. Pouchard, P. Hagemuller, *Mater. Res. Bull.* 7 (1972) 913.
- [375] D. B. Currie, M. T. Weller, *Acta Crystallogr.* C47 (1991) 696.
- [376] J. B. Goodenough, N. F. Mott, M. Pouchard, G. Demazeaux, P. Hagemuller, *Mater. Res. Bull.* 8 (1973) 647.
- [377] S. J. La Placa, J. F. Bringley, B. A. Scott, D. E. Cox, *Acta Crystallogr.* C49 (1993) 1415.
- [378] R. J. Cava, T. Siegrist, B. Hessen, J. J. Krajenski, W. F. Peck Jr., B. Batlogg, H. Takagi, J. V. Waszczak, L. F. Schneemeyer, H. W. Zanbergen, *Physica C* 177 (1991) 115.
- [379] M. Karppinen, H. Yamauchi, T. Ito, H. Suematsu, O. Fukunaga, *Mater. Sci. Eng.* B41 (1996) 59.
- [380] M. Karppinen, H. Yamauchi, H. Suematsu, K. Isawa, M. Nagano, R. Itti, O. Fukunaga, *J. Solid State Chem.* 130 (1997) 213.
- [381] A. J. Williams, A. Gillies, J. P. Attfield, G. Heymann, H. Huppertz, M. J. Martínez-Lope, J. A. Alonso, *Phys. Rev. B* 73 (2006) 104409.
- [382] J. M. Longo, P. M. Raccah, J. B. Goodenough, *J. Appl. Phys.* 39 (1968) 1327.
- [383] L. Klein, J. S. Dodge, C. H. Ahn, J. W. Reiner, L. Mieville, T. H. Geballe, M. R. Beasley, A. Kapitulnik, *J. Phys.: Condens. Matter* 8 (1996) 10111.
- [384] I. I. Mazin, D. J. Singh, *Phys. Rev. B* 56 (1997) 2556.
- [385] B. L. Chamberland, *Solid State Comm.* 5 (1967) 663.
- [386] L. Pi, A. Maignan, R. Retoux, B. Raveau, *J. Phys.: Condens. Matter* 14 (2002) 7391.
- [387] Z. H. Han, J. I. Budnick, W. A. Hines, B. Dabrowski, S. Kolesnik, T. Maxwell, *J. Phys.: Condens. Matter* 17 (2005) 1193.
- [388] B. Dabrowski, S. Kolesnik, O. Chmaissem, T. Maxwell, M. Avdeev, P. W. Barnes, J. D. Jorgensen, *Phys. Rev. B* 72 (2005) 054428.

-
- [389] C. Helbig, R. Herrmann, F. Mayr, E.-W. Scheidt, K. Tröster, J. Hanss, H.-A. Krug von Nidda, G. Heymann, H. Huppertz, W. Scherer, *Chem. Commun.* (2005) 4071.
- [390] A. W. Sleight, L. Gillson, *Solid State Commun.* 4 (1966) 601.
- [391] Cs. Balazsi, M. Farkas-Jahnke, I. Kotsis, L. Petras, J. Pfeiffer, *Solid State Ionics* 141-142 (2001) 411.
- [392] S. Knyrim, private communication.